ISBN 978-90-6464-751-2

Interfacial Interactions and Wettability Evaluation of Rock Surfaces for CO_2 Storage

N. Shojai Kaveh

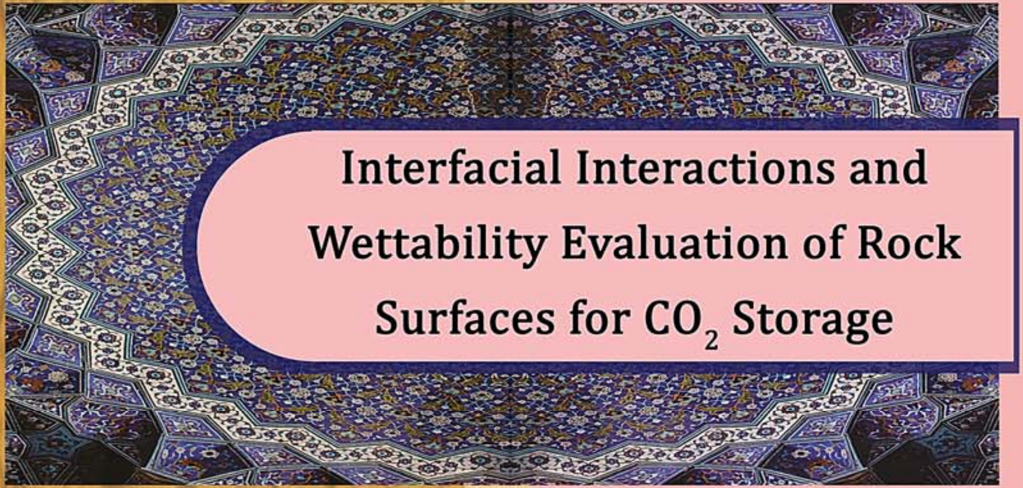

Interfacial Interactions and Wettability Evaluation of Rock Surfaces for CO_2 Storage

Narjes Shojai Kaveh

Interfacial Interactions and Wettability Evaluation of Rock Surfaces for CO$_2$ Storage

Narjes Shojai Kaveh

بررسی کنشهای متقابل بین سطحی و ترشوندگی سطح سنگ در فرایندهای ذخیره سازی دی اکسید کربن

نرجس شجاعی کاوه

Interfacial Interactions and Wettability Evaluation of Rock Surfaces for CO_2 Storage

PROEFSCHRIFT

ter verkrijging van de graad van doctor
aan de Technische Universiteit Delft,
op gezag van de Rector Magnificus prof. ir. K.C.A.M. Luyben,
voorzitter van het College voor Promoties,
in het openbaar te verdedigen op woensdag 12 maart 2014 om 12:30 uur

door

Narjes SHOJAI KAVEH

Master of Science in Chemical Engineering, Iran University of Science and Technology, Iran
Bachelor of Science in Process Engineering, Iran University of Science and Technology, Iran

geboren te Tehran, Iran.

Dit proefschrift is goedgekeurd door de promotor:
Prof. dr. W.R. Rossen

Copromotor: Dr. ir. K-H.A.A. Wolf

Samenstelling promotiecommissie:

Rector Magnificus,	voorzitter
Prof. dr. W.R. Rossen,	Technische Universiteit Delft, promotor
Dr. K.H.A.A. Wolf,	Technische Universiteit Delft, copromotor
Prof. dr. J.J.C. Geerlings,	Technische Universiteit Delft
Prof. dr. J. Bruining,	Technische Universiteit Delft
Prof. dr. ir. P.L.J. Zitha,	Technische Universiteit Delft
Dr. E.S.J. Rudolph-Flöter,	Technische Universität Berlin
Dr. C. Pentland,	Shell Global Solutions
Prof.dr.ir. J.D. Jansen,	Technische Universiteit Delft, reservelid

The research reported in this thesis was carried out as a part of the CATO-2 program (CO_2 capture, transport and storage in the Netherlands). Their financial support is gratefully acknowledged. The author wish to also thank GRASP program, founded by the European Commission, for awarded research fellowship through "Marie Curie Actions Program". The research was conducted in the Laboratory of Geoscience and Engineering at Delft University of Technology.

Published and distributed by: N. Shojai Kaveh
E-mail: nshojaikaveh@gmail.com
http://www.citg.tudelft.nl/shojaikaveh

Cover design: N. Shojai Kaveh
Cover illustrations: Shah Mosque in Isfahan; Grain and porosity distribution of Bentheimer;
Drawing of a Persian pattern on textile by my mother, Parvin Dokht Tajik.

Printed by: GVO drukkers & vormgevers B.V. | Ponsen & Looijen

ISBN: 978-90-6464-751-2

Just like a brief moment of joy, sorrow will go as well (Energy Conversion Law). However, there is no salve for wounds of losing parents and no end for our mourning.

زندگی ، شوق رسیدن به همان فردایی ست ، که نخواهد آمد

شاید این خنده که امروز ، دریغش کردی

آخرین فرصت همراهی با ، امید است....

سهراب سپهری

Dedicated to the memory of my lovely Mom

and to my beloved Dad

& my love, AMIN.

به یاد مهربانترین مهربانان، مادر نازنینم

و تقدیم به اسطوره زندگیم ، پدرم

و یار و یاور بی منتم ، امین

Propositions

accompanying the doctoral thesis

Interfacial Interactions and Wettability Evaluation of Rock Surfaces for CO_2 Storage

by Narjes Shojai Kaveh, 2014

1- “The value of an education is not the learning of many facts, but the training of the mind to think something that cannot be learned from textbooks.” -*Albert Einstein*

2- The coal rank is the main parameter that controls the degree of pressure dependency of the pure coal wettability- *Chapter 3 of this thesis*.

3- Contact angle variations with time in an unsaturated system cannot necessarily be attributed to wettability alteration of the surface; it can also reflect changes in bubble volume due to CO_2 dissolution in the aqueous phase- *Chapter 4 of this thesis*.

4- With dissolution, the bubble size continuously changes, so that a reliable and reproducible contact-angle determination is not guaranteed. As a consequence, a reliable contact-angle determination should be conducted using a pre-equilibrated (fully or quasi-saturated) aqueous phase to eliminate dissolution effects - *Chapter 4 of this thesis*.

5- The wetting properties of the surface as a function of pressure can be described by a surface-free-energy analysis, if a reliable relevant IFT and contact-angle data is available - *Chapter 5 of this thesis.*

6- Polishing the surface in contact-angle experiments is essential to minimize the surface roughness and by that reducing the hysteresis effect. However, neglecting the surface roughness in the experiments is too great a simplification of natural rock surfaces, from a physical point of view.

7- No experiment is a failure. At least it serves as a negative example.- *Prof. Hans Bruining*

8- The best way to check your knowledge about a scientific topic is trying to explain it to your grandmother.

9- “Scientific research can reduce superstition by encouraging people to think and view things in terms of cause and effect.”-*Albert Einstein*

10- **Sometimes** being quiet doesn’t mean confirmation or surrender; it may reflect disappointment by the level of understanding in your opponent.

These propositions are regarded as opposable and defendable, and have been approved as such by the promoter, Prof. dr. W.R. Rossen.

Stellingen

Behorende bij het proefschrift

Grensvlakinteracties en Bevochtigbaarheid Evaluatie van Gesteente-Oppervlakken voor CO_2 Opslag

van Narjes Shojai Kaveh, 2014

1- “De waarde van een opleiding is niet het leren van veel feiten, maar de training van de geest om iets te bedenken dat niet kan worden geleerd uit boeken” –*Albert Einstein*

2- De inkolingsgraad is de belangrijkste parameter die de mate van drukafhankelijkheid van de bevochtigbaarheid van pure steenkool bepaald - *Hoofdstuk 3 van dit proefschrift.*

3- Variaties van de contacthoek in de tijd bij een onverzadigd systeem kunnen niet noodzakelijkerwijs worden toegeschreven aan een verandering in de bevochtigbaarheid van het oppervlak; het kan ook het gevolg zijn van een veranderend gasbel volume doordat CO_2 oplost in de water fase - *Hoofdstuk 4 van dit proefschrift.*

4- De grootte van een gasbel verandert voortdurend tijdens het oplossingsproces, zodat een betrouwbare en reproduceerbare contacthoek bepaling niet kan worden gegarandeerd. Daarom moet de waterfase van tevoren in evenwicht worden gebracht (volledig of quasi-verzadigd) met het gas om een betrouwbare contacthoek bepaling uit te kunnen voeren, waarbij oplossingseffecten geen rol spelen – *Hoofdstuk 4 van dit proefschrift.*

5- De bevochtigende eigenschappen aan het oppervlak, als functie van de druk, kan worden beschreven door een oppervlakte-vrije-energie analyse indien betrouwbare en relevante grensvlakspanning en contacthoek gegevens beschikbaar zijn – *Hoofdstuk 5 van dit proefschrift.*

6- Polijsten van het oppervlak voor contacthoek experimenten is essentieel om de oppervlakteruwheid te minimaliseren en daardoor het hysterese-effect te verminderen. Echter, het verwaarlozen van de oppervlakteruwheid in een experiment is een te grote vereenvoudiging ten opzichte van natuurlijke gesteente oppervlakken in vanuit een fysiek oogpunt.

7- Geen enkel experiment is een mislukking. Het kan tenminste dienen als een negatief voorbeeld.- *Prof. Hans Bruining*

8- De beste manier om je kennis over een wetenschappelijk onderwerp te controleren is door te proberen het aan je grootmoeder uit te leggen.

9- “Wetenschappelijk onderzoek kan bijgeloof verminderen door mensen aan te moedigen om na te denken en dingen te bekijken in termen van oorzaak en gevolg.”-*Albert Einstein*

10- **Soms** betekent stil zijn geen bevestiging of toegeven, het kan ook teleurstelling weerspiegelen in het niveau van inzicht van je tegenstander.

Deze stellingen worden opponeerbaar en verdedigbaar geacht en zijn als zodanig goedgekeurd door de promotor, Prof. dr. W.R. Rossen.

CONTENTS

Summary ix

Samenvatting xi

Chapter 1: Introduction 1
1.1. General introduction 1
1.2. Storage mechanisms 2
1.3. Flue gas injection 3
1.4. Wettability and CCS 3
1.5. Wettability and contact angle determination 4
1.6. Research Objectives and Outline of the thesis 6
  1.6.1. Part I: CO_2 enhanced Coal bed methane 6
  1.6.2. Part II: Aquifers and depleted gas reservoirs 7
  1.6.3. Part III: Oil reservoir 7
References 9

Chapter 2: Contact-Angle Determination with the Captive Bubble Method: Experimental Procedure 11
2.1. Introduction 11
  2.2.2. Experimental set-up 14
2.3. Image analysis 17
  2.3.1. Microscopic image analysis 17
  2.3.3. Micro CT-Scan 18
  2.3.4. Bubble image analysis 18
    2.3.4.1. Sensitivity of the contact angle determination to the image analysis 21
2.4. Conclusions 25
References 26

Chapter 3: Contact-Angle Determination of Wet Coal System with Synthetic Flue gas and CO_2 27
Abstract 27
  3.1. Introduction 28
    3.1.1. CCS and CBM 28
    3.1.2. Coal Wetting properties 29
  3.2. Experimental 31
    3.2.1. Coal Samples 31
    3.2.2. Sample preparation 32

3.2.3. ExperimentaL procedure 33
3.2.4. Data interpretation 33
3.3. Image Analysis 34
3.3.1. Microscopic image analysis 34
3.3.2. Micro CT-Scan 36
3.4. Results and discussions 39
3.4.1. Effect of time on contact angle 39
3.4.2. CO_2 wetting behavior on a wet coal sample 41
3.4.2.1. High volatile bituminous (hvBb) coal 41
3.4.2.2. Semi-anthracite coal 43
3.4.3. Synthetic flue gas wetting behaviour on a wet coal sample 45
3.4.3.1. High volatile bituminous (hvBb) coal 45
3.4.3.2. Semi-anthracite coal 46
3.4.4. Comparison of results with respect to coal rank 48
3.4.4.1. Effect of coal surface charge 49
3.4.5. Implications for CO_2 storage in CBM 50
3.5. Conclusions 50
References 52

Chapter 4: Wettability Evaluation of CO_2-Water-Bentheimer Sandstone System: Dissolution, Interfacial Tension, Contact Angle and Bubble Size 55
Abstract 55
4.1. Introduction 56
4.2. Theoretical review 57
4.2.1. Contact angle and droplet/bubble size 57
4.2.2. Interfacial interactions of CO_2/water/rock or mineral systems 60
4.3. Experimental 62
4.3.1. Materials 62
4.3.2. Microscopic image analysis 64
4.3.3. Micro CT-Scan 64
4.3.4. Experimental set-up and procedure 65
4.4. Results and discussions 66
4.4.1. Experimental determination of interfacial tension 66
4.4.2. Contact-angle determination of CO_2 in unsaturated aqueous phase 69
4.4.2.1. CO_2 bubble dissolution 74
4.4.3. Contact-angle determination of CO_2 and flue gas in pre-equilibrated aqueous phase . 79
4.4.3.1. Surface roughness 83
4.4.3.2. Effect of gravity on bubble geometry 85
4.4.3.3. Effect of pressure on the contact angle in the Bentheimer/CO_2/water system 87
4.4.3.4. Effect of pressure on the contact angle in Bentheimer/flue gas/water system 89

4.5. Conclusions 91
Appendices: 93
Appendix 4.1: Mass-transfer model at the bubble interface 93
Appendix 4.2: Steady-state diffusion through the bubble variable area 94
Appendix 4.3: Rayleigh number calculation for a captive-bubble system 96
Appendix 4.4: Line-tension determination for a CO_2/water/Bentheimer system 97
Appendix 4.5: Theoretical analysis of gas captive bubble on a horizontal substrate 99
References 101

Chapter 5: Evaluation of Interfacial Interactions between Crude Oil-Water-Sandstone with CO_2 or Flue Gas using Surface Free Energy Analysis 105
Abstract 105
5.1. Introduction 106
5.2. Experimental 108
5.2.1. Materials 108
5.2.2. Methodology 108
5.3. Results and discussions 110
5.3.1. Effect of pressure 110
5.3.2. Evaluation of contact angles by Surface-free-energy analysis 114
5.3.4. Effect of bubble size 123
5.4. Conclusions 124
Appendix 5.1: Error analysis 126
References 127

Chapter 6: Conclusion 129
6.1. Part I: CO_2 enhanced Coal bed methane 129
6.2. Part II: Aquifers and depleted gas reservoirs 130
6.3. Part III: Oil reservoir 131
6.4. Recommendations 132

Nomenclature 133

Acknowledgements 137

List of Publications 141

About the Author 143

LIST OF FIGURES

Figure 1.1. Geological storage strategies overview 2

Figure 1.2. Interfacial interactions which control the flow behavior in porous media. 4

Figure 2.1. Drawing of three techniques of contact-angle determination 12

Figure 2.2. Schematic diagram of experimental set-up (Pendant-drop cell) 14

Figure 2.3. Side view of the open pendant-drop cell 15

Figure 2.4. Phase diagram of CO_2/H_2O system at a temperature of 318.15 K 17

Figure 2.5. The image processing procedure in the MATLAB routine. 20

Figure 2.6. Schematic illustrating the capturing of an image of a bubble 21

Figure 2.7. Image with focus on the bubble contour and on the surface 22

Figure 2.8. The bubble shape and gray values for images. 23

Figure 2.9. Image processing: importance of the baseline 23

Figure 2.10. The surface detection using the inflection points in the bubble shape 24

Figure 3.1. Side view of the pendant drop cell and top view of the sample holder. 33

Figure 3.2. Perpendicular view and 3-D side view of the WL sample surface. 35

Figure 3.3. 3-D side view of the surface of WL and SC sample. 35

Figure 3.4. Side view of the WL and SC samples after the experiment 36

Figure 3.5. Distribution of mineral-matter content. 37

Figure 3.6. Three-dimensional view of the void distribution. 38

Figure 3.7. CO_2 contact angle and dimensionless radius as a function of time 39

Figure 3.8. Synthetic flue gas contact angle and dimensionless radius as a function of time.. 39

Figure 3.9. Synthetic flue gas contact angle and dimensionless radius as a function of time.. 40

Figure 3.10. Stable contact angle as a function of pressure for CO_2- wet WL coal 42

Figure 3.11. Digital images of CO_2 bubble on the WL coal surface 42

Figure 3.12. Dimensionless density, CO_2 solubility in water, stable contact angle and sorption of CO_2 on wet WL coal at pressures ranging from atmospheric up to 20 MPa. 43

Figure 3.13. Stable contact angle as a function of pressure for the wet SC coal with CO_2. 43

Figure 3.14. Comparison of determined contact angle values for the CO_2- wet SC coal. 44

Figure 3.15. Dimensionless stable contact angle, sorption of CO_2 on wet SC coal, density and solubility of CO_2 at pressures ranging from atmospheric up to 20 MPa................................. 45

Figure 3.16. Stable contact angle as a function of pressure for flue gas- wet WL system....... 46

Figure 3.17. Stable contact angle as a function of pressure for the wet SC coal system with synthetic flue gas at a temperature of 318 K. 47

Figure 3.18. Digital images of gas bubble on the SC coal surface in the presence of water at 318 K and 5.25 MPa.. 47

Figure 3.19. Contact angle as a function of pressure for coal samples of different ranks. 48

Figure 4.1. Schematic of a captive bubble 58

Figure 4.2. 3-D side view of the contact surface of Bentheimer sandstone samples with different roughness values... 64

Figure 4.3. Three-dimensional view of side surfaces of the Bentheimer sample used. 65

Figure 4.4. Schematic of the modified Pendant-Drop Cell (PDC) experimental set-up.......... 65

Figure 4.5. Interfacial tension of CO_2/water as a function of pressure. 66

Figure 4.6. Normalized values of CO_2 density, the solubility of CO_2 in water and IFT at a constant temperature of 318 K as a function of pressure. 67

Figure 4.7. Comparison of experimentally determined IFTs for flue gas-water, CO_2/water and N_2/water systems at 318 K. 67

Figure 4.8. Density and interfacial tension variations with pressure in flue gas/water, CO_2/water and N_2/water systems at a constant temperature of 318 K. 68

Figure 4.9. Digital images of a buoyant gas bubble in a pre-saturated aqueous phase at a constant temperature of 318 K (±0.1 K) and various pressures. 69

Figure 4.10. Dynamic contact angle and Bubble radius at apex over time for different pressures and at a constant temperature of 318 K. 71

Figure 4.11. Sequential digital images of the captive CO_2–rich bubble on a Bentheimer surface at 0.58 MPa and 318 K 73

Figure 4.12. Evolution of the contact angle and bubble parameters with time at 0.58 MPa and 318 K. 74

Figure 4.13. Bubble radius as a function of time at various pressures and a constant temperature of 318 K.. 76

Figure 4.14. Bubble radius as function of time at various pressures 77

Figure 4.15. Evolution of bubble radius and contact angle over time at 0.58 MPa and 318 K in unsaturated, quasi-saturated and fully-saturated aqueous phase.. 80

Figure 4.16. Stable contact angle (fully-saturated system) as a function of pressure at a temperature of 318 K... 82

Figure 4.17. Stable contact angle as a function of the bubble radius at the apex at various pressures and a temperature of 318 K. 82

Figure 4.18. Bubble radius at the apex as a function of pressure at a temperature of 318 K... 83

Figure 4.19. Sequential digital images of the captive CO_2–rich bubble on the Bentheimer rock at 4.97 MPa and 318 K... 83

Figure 4.20. Stable contact angles for a less-polished surface as a function of pressure and bubble radius at apex at various pressures and a constant temperature of 318K. 84

Figure 4.21. Bubble volume as a function of the contact angle at a constant temperature of 318 K and pressures of 1.04 and 4.97 MPa... 85

Figure 4.22. Stable contact angle as a function of the Bond number for various bubble sizes, and Bond number as a function of the bubble radius, at a constant temperature of 318 K and two pressures of 1.04 MPa and 4.97 MPa 87

Figure 4.23. Contact angle as a function of pressure for bubbles with Bond numbers of about 0.2 (±0.02) for the Bentheimer/CO_2/water system at 318 K. 88

Figure 4.24. Sequential digital images of the captive CO_2 bubble with similar size. 89

Figure 4.25. Stable contact angle (in pre-CO_2 saturated aqueous phase) as a function of pressure at a temperature of 318 K.. 89

Figure 4.26. Stable contact angle as a function of the bubble radius at a constant temperature of 318 K and various pressures from 0.17 MPa to 13.9 MPa.. 90

Figure 4.27. Stable contact angle vs. bubble radius at four specific pressures. 90

Figure 4.2A.1. Mass balance in the r-direction for a captive bubble 94

Figure 4.3A.1. Contact angle versus bubble radius or the inverse length of the contact line.. 97

Figure 4.A4.1. Force balance in the z-direction for a captive bubble. 99

Figure 5.1. Digital photograph of the inside of the modified pendant-drop cell.................... 109

Figure 5.2. CO_2 contact angles for partially water-wet substrate, SB-1, and the oil-wet substrate, SB-5, as a function of pressure at a temperature of 318 K.. 110

Figure 5.3. Synthetic flue gas contact angles for partially water-wet substrate, SB-1, and the oil-wet substrate, SB-5, as a function of pressure at a temperature of 318 K. 111

Figure 5.4. Bentheimer Sandstone samples. 111

Figure 5.5. Digital images of CO_2 bubbles on an oil saturated-Bentheimer surface in the presence of CO_2-saturated aqueous phase at 318 K. 112

Figure 5.6. Schematic representation of work of adhesion in captive-bubble system. 114

Figure 5.7. CO_2 Contact angle as function of pressure for the oil-wet sample and water. 117

Figure 5.8. Synthetic flue gas contact angle as function of pressure for the oil-wet sample (SB-5) and water at a temperature of 318 K. 118

Figure 5.9. Calculated IFT-values versus pressure for CO_2/water/SB-5 system 119

Figure 5.10. Calculated IFT-values vs. pressure for CO_2/water/SB-1 system. 120

Figure 5.11. Dimensionless density, CO_2 solubility in water, IFT between CO_2 and water and the stable contact angle on oil-wet Bentheimer sandstone at a constant temperature of 318 K as function of pressure 121

Figure 5.12. Dependence of the stable contact angle as a function of bubble radius............ 123

LIST OF TABLES

Table 1.1. Estimation of storage capacity of the geological storage options 2

Table 3.1. Generic flue gas composition 28

Table 3.2. Proximate and ultimate analysis and coal petrology of coal samples used............. 32

Table 4.1. Synthetic mineral reconstruction of Bentheimer sandstone 63

Table 4.2. XRD analysis of Bentheimer sandstone 63

Table 4.3. Contact angle and other parameters of CO_2 gas bubble at various pressures and a constant temperature of 318 K 73

Table 4.4. Experimental and model parameters obtained from the description of the bubble radius as a function of time at various pressures and a temperature of 318 K. 78

Table 4.5. Parameters characterizing the experiments at 0.58 MPa in the unsaturated, quasi-saturated und fully-saturated system. 81

Table 5.1. Physical properties of the oil samples used in the experiments 107

Table 5.2. Summary of the experiments 108

Table 5.3. Results of the contact-angle prediction using the equation of state approach for the oil-wet substrate (SB-5)/ CO_2/ distilled water system 116

Table 5.4. Results of the contact-angle prediction using the equation of state approach for the oil-wet substrate (SB-5)/ synthetic flue gas/ distilled water system 116

Table 5.5. The calculated γ_{sl} and β_2 parameters with error analysis for oil-wet and water-wet systems 122

SUMMARY

> *"Nothing in life is to be feared, it is only to be understood. Now is the time to understand more, so that we may fear less."*
> ***- Marie Curie***
>
> *"If we knew what it was we were doing, it would not be called research, would it?"*
> ***- Albert Einstein***

To reduce CO_2 emissions into the atmosphere, different scenarios are proposed to capture and store carbon dioxide (CO_2) in geological formations (CCS). Storage strategies include CO_2 injection into deep saline aquifers, depleted gas and oil reservoirs, and unmineable coal seams. To identify a secure and proper strategy for CO_2 injection, the fluid displacement at reservoir conditions and thus the wettability of the geological formation need to be understood. Wettability has a strong effect on multiphase rock-fluid interactions and influences the efficiency of an immiscible displacement in the porous medium, the magnitude of irreducible water and residual oil saturations, the microscopic fluid distribution at pore scale in the porous medium, the capillary pressure and relative permeability curves and the electrical properties of the porous medium. Only a limited amount of literature refers to wetting properties of sedimentary rocks and minerals at high pressures and elevated temperatures. Hence, a reliable experimental method to determine the wettability is an important step towards understanding the physics of this phenomenon.

This thesis is a collection of experimental work on rock-fluid interactions and wettability behavior of the rock surface related to CO_2 storage. The captive-bubble technique is used to evaluate the wetting properties of different rock surfaces in the presence of CO_2 and/or synthetic flue gas. To mimic the in-situ conditions, experiments are performed at high pressures and elevated temperature (up to 16 MPa and at 318 K). In **Chapter 2** further details of the method, experimental set-up and procedure are provided.

In **Chapter 3** wetting properties of two coal samples with similar vitrinite content are evaluated as well as the effect of pressure and coal rank. The wettability of the coal is a function of coal rank, maceral content, ash content, heterogeneity of the coal surface, pressure, temperature and gas phase composition. This thesis shows that for reliable contact-angle determination the experiments should be conducted in fully–saturated aqueous phase, in order to minimize the effects of CO_2 dissolution on the wetting properties and changes of the aqueous phase composition. These criteria were not considered before in literature.

Dissolution of CO_2 in (immobile) formation water is one of the most important mechanisms to (permanently) store CO_2 (solubility trapping). Moreover, for most practical situations the

pressure and temperature conditions are such that dissolution of CO_2 in the formation water will increase the density of the formation water. This further enhances the storage capacity. However, dissolution is generally negatively correlated with salinity, and dissolution of CO_2 lowers the IFT of CO_2/water systems. Therefore, understanding of the wettability and dissolution behavior and the interplay with IFT is of importance for displacement behavior and storage capacity. In **Chapter 4** interfacial interactions and IFT between the gas phase and aqueous phase are studied at various pressures. Also, wetting properties of Bentheimer sandstone rock are investigated with an unsaturated aqueous phase, representing the short-term behavior, and with a saturated aqueous phase representing the long-term behavior. In addition, the dissolution behavior and mass transfer of a CO_2 bubble in a water/Bentheimer sandstone system are determined at various pressures.

Chapter 5 describes the contact angles, i.e. wettability, in systems with water, an oil-saturated rock, and carbon dioxide and/or synthetic flue gas. Two situations are considered: rock-system I is partially water-wet, whereas rock-system II is effectively oil-wet. For oil-wet rock, CO_2 must overcome a capillary barrier to invade the rock matrix in order to be able to displace the oil in a secondary drainage process. If the rock wettability alters from oil-wet to gas-wet, a positive value of capillary pressure is established. Therefore, the injected CO_2 will spontaneously imbibe from the fractures into the matrix blocks and oil will be expelled. This thesis shows that CO_2 can become the wetting phase for an oil-wet Bentheimer sandstone.

In addition, to describe the wetting properties of the surface as a function of pressure, a surface-free-energy analysis is used based on an equation of state (EOS). Following this approach, a modified equation of state is proposed in Chapter 5 to describe the contact angle of a liquid/gas/solid system at various pressures. The use of the equation of state method makes it possible to approach the experimental data quantitatively, if a number of reliable contact-angle and interfacial-tension measurements are available for a system of interest.

Finally, **Chapter 6** presents the overall conclusions of this project and an outlook for further work.

In this research, contact-angle determinations were performed using natural rock surfaces, which were not treated chemically. The output of this study is a step forward in understanding the displacement behavior of multiple phases in reservoirs. The results presented in this thesis can be used as input parameters in reservoir simulations dealing with CO_2 or flue gas storage.

SAMENVATTING

> *"Niets in het leven moet worden gevreesd, het moet alleen worden begrepen Nu is de tijd om meer te begrijpen, zodat we minder hoeven te vrezen. "*
> ***- Marie Curie***
>
> *"Als we wisten waar we mee bezig waren, zou het geen onderzoek worden, of wel?"*
> ***- Albert Einstein***

Om de CO_2-uitstoot in de atmosfeer te verminderen, worden verschillende scenario's voorgesteld voor kooldioxide afvang en opslag in geologische formaties (CCS). Opslagstrategieën zijn onder andere injectie van CO_2 in diepe zoutwater aquifers, uitgeputte gas- en oliereservoirs, en niet-ontginbare gasvoerende steenkoollagen. Voor het vinden van een veilige en goede strategie voor CO_2 injectie moet de vloeistofverplaatsing onder reservoircondities en daarmee de bevochtigbaarheid van de geologische formatie worden begrepen. Bevochtigbaarheid heeft een sterk effect op meer-fase gesteente/vloeistof interacties en beïnvloedt de efficiëntie van een niet-mengbaar verplaatsingsproces in het poreuze medium, alsmede de grootte van niet-reduceerbare water en rest-olie verzadigingen, de microscopische verdeling van de vloeistof op de porieschaal binnen het poreuze medium, de capillaire druk met de gerelateerde relatieve permeabiliteit curven en de elektrische eigenschappen van het poreuze medium. Slechts een beperkte hoeveelheid literatuur verwijst naar de bevochtigende eigenschappen van sedimentaire gesteentes en mineralen bij hoge drukken en verhoogde temperaturen. Vandaar dat een betrouwbare experimentele methode om de bevochtigbaarheid te bepalen een belangrijke stap is richting het begrijpen van de fysica van dit fenomeen.

Dit proefschrift is een beschrijving van experimenteel werk over gesteente-vloeistof interacties en bevochtigbaarheidsgedrag van het gesteente-oppervlak in relatie tot CO_2-opslag. De captive-bubble techniek wordt gebruikt om de bevochtigingseigenschappen van verschillende gesteente-oppervlakken te evalueren in de aanwezigheid van CO_2 en/of rookgas. Om de in-situ omstandigheden na te bootsen, worden experimenten uitgevoerd bij hoge druk en verhoogde temperatuur (tot 16 MPa en bij maximaal 318 K). In **Hoofdstuk 2** wordt nadere informatie verstrekt over de methode, experimentele opzet en procedure.

In **Hoofdstuk 3** worden bevochtigende eigenschappen van twee kolen monsters met een vergelijkbare vitriniet reflectie geëvalueerd samen met het effect van de druk en de inkolingsgraad. De bevochtigbaarheid van de kolen is een functie van de inkolingsgraad, maceraal inhoud, as-gehalte, heterogeniteit van het steenkooloppervlak, druk, temperatuur en gas-fasesamenstelling. Dit proefschrift blijkt dat experimenten moeten worden uitgevoerd in een volledig verzadigde waterfase om de effecten van CO_2 ontbinding op de bevochtigingseigenschappen en tevens de veranderingen van de waterfase te minimaliseren. Deze criteria zijn niet eerder overwogen in de literatuur.

Oplossing van CO_2 in (immobiel) formatiewater is een van de belangrijkste mechanismen om (blijvend) CO_2 op te slaan. In praktijk zijn de in-situ druk en temperatuur zodanig dat door sorptie van CO_2 in het formatiewater de dichtheid van het formatiewater zal toenemen; dit verbetert de opslagcapaciteit. Echter, oplossing is in het algemeen negatief gecorreleerd met het zoutgehalte en verlaagt de grensvlakspanning van CO_2/water systemen. Derhalve is begrip van het bevochtigbaarheids- en oplosgedrag en de wisselwerking met de grensvlakspanning van belang voor het verplaatsingsgedrag en de opslagcapaciteit.

In **Hoofdstuk 4** worden, bij verschillende drukken, grensvlak-interacties en de grensvlakspanning tussen de gas- en waterfase bestudeerd. Ook de bevochtigende eigenschappen van Bentheimer zandsteen met een onverzadigde waterfase worden bestudeerd. Deze studie vertegenwoordigt het korte-termijn gedrag. Zij wordt vergeleken met een verzadigde waterfase die het gedrag op lange termijn vertegenwoordigd. Bovendien worden het oplosgedrag en massaoverdracht van een CO_2 luchtbel in een water/Bentheimer zandsteen systeem bepaald bij verschillende drukken.

Hoofdstuk 5 beschrijft de contacthoeken, d.w.z. de bevochtigbaarheid, in systemen met water, een met olie verzadigd gesteente, en met kooldioxide en/of synthetische rookgas. Twee situaties worden beschouwd: gesteente-systeem I dat gedeeltelijk water-bevochtigd is, terwijl gesteente-systeem II effectief olie-bevochtigd is. Voor olie-bevochtigd gesteente moet CO_2 een capillaire barrière overwinnen om de gesteente-matrix binnen te dringen om de olie te kunnen verplaatsen in een secundair drainage proces. Verandering van de bevochtigbaarheid van olie-bevochtigd in gas-bevochtigd zal een positieve waarde van capillaire druk tot gevolg hebben en het geïnjecteerde CO_2 zal spontaan vanuit de scheuren in de matrixblokken worden opgenomen en de olie vervangen en verdringen. Dit proefschrift toont aan dat CO_2 de bevochtigingsfase voor een olie-bevochtigde Bentheimer zandsteen kan worden.

Om de bevochtigende eigenschappen van het oppervlak te beschrijven als functie van de druk wordt een oppervlakte-vrije-energie analyse gebruikt op basis van een toestandsvergelijking. Met deze benadering wordt een gemodificeerde toestandsvergelijking voorgesteld in hoofdstuk 5 om de contacthoek van een vloeistof/gas/vaste stof te beschrijven bij verschillende drukken. Het gebruik van de toestandsvergelijkingsmethode maakt het mogelijk om de experimentele gegevens kwantitatief te benaderen, indien aan een aantal betrouwbare metingen van contacthoek en grensvlakspanning beschikbaar zijn voor een gedefinieerd systeem.

Hoofdstuk 6 geeft tenslotte de algemene conclusies van dit project en de suggesties voor verdere werkzaamheden.

In dit onderzoek zijn contacthoek bepalingen uitgevoerd voor oppervlakken van natuurlijk gesteente die niet chemisch zijn behandeld. De uitkomst van dit onderzoek is een stap voorwaarts in het begrijpen van het verplaatsingsgedrag van meerdere fasen in reservoirs. De in dit proefschrift gepresenteerde resultaten kunnen worden gebruikt als invoerparameters in reservoirsimulaties voor opslag van CO_2 of rookgas.

CHAPTER 1

Introduction

1.1. GENERAL INTRODUCTION

Over the last decades, concerns about greenhouse gas emissions and global warming have been risen [1], as greenhouse gases increase the average temperature of the earth. The greenhouse effect is a natural phenomenon and without these gases the average temperature of the earth's surface would be about 33^{o}C colder than the current average of 14^{o}C [1-3]. One of the main concerns deals with the influence of humanity on this effect as a result of man-made greenhouse gas emissions. Also, the potential climate consequences of these emissions are under scrutiny. Since the beginning of the industrial revolution in 1750, the burning of fossil fuels has grown exponentially as a result of the ever increasing worldwide energy demand. At present, 40% of the CO_2 in the atmosphere can attributed to the burning of fossil fuels. CO_2 emissions produced by human activities, commonly referred to as anthropogenic emissions, have led to an increase in the atmospheric CO_2 concentration from 280 ppm in 1750 to 392.6 ppm in 2012 [4].

To control CO_2 emissions different options are proposed, such as reducing the consumption of carbon-based fuels, using carbon-free energy sources, e.g., solar power, wind power and geothermal energy, and capturing and storing carbon dioxide (CO_2) in geological formations (CCS). Storage strategies include CO_2 injection into deep saline aquifers [5, 6], (depleted) gas and oil reservoirs [7-10], and unmineable coal seams [11] (Fig. 1.1. [1]). Even though the volumetric CO_2 storage capacity is the highest in aquifers, CO_2 storage by means of CO_2-enhanced gas and oil recovery (CO_2-EGR and CO_2-EOR) or, potentially, enhanced-coal bed methane recovery (ECBM) could be more economically viable. CO_2 storage in depleted or almost depleted gas/oil reservoirs is an attractive option for CO_2 storage, because gas/oil recovery (EGR/ EOR) is enhanced, the underground and surface infrastructures are already available and the knowledge of the reservoir is quite extensive due to the data acquired during the exploitation stage [12].

Table 1.1 summarizes the estimations of storage capacity of the geological options with their highest level of maturity. The storage capacity includes storage options which are not economical [1].

Table 1.1. Estimation of storage capacity of the geological storage options [1]

Storage option	***Lower estimate of storage capacity (Gt CO_2)***	***Upper estimate of storage capacity (Gt CO_2)***	***Highest level of maturity***
Oil and gas fields	675*	900*	Economically feasible under specific conditions
Unmineable coal seams (ECBM)	3-15	200	Demonstration phase
Deep saline aquifers	1000	Uncertain, but possibly 10^4	Economically feasible under specific conditions

* Would increase by 25% by including ‘undiscovered’ oil and gas fields in the estimation.

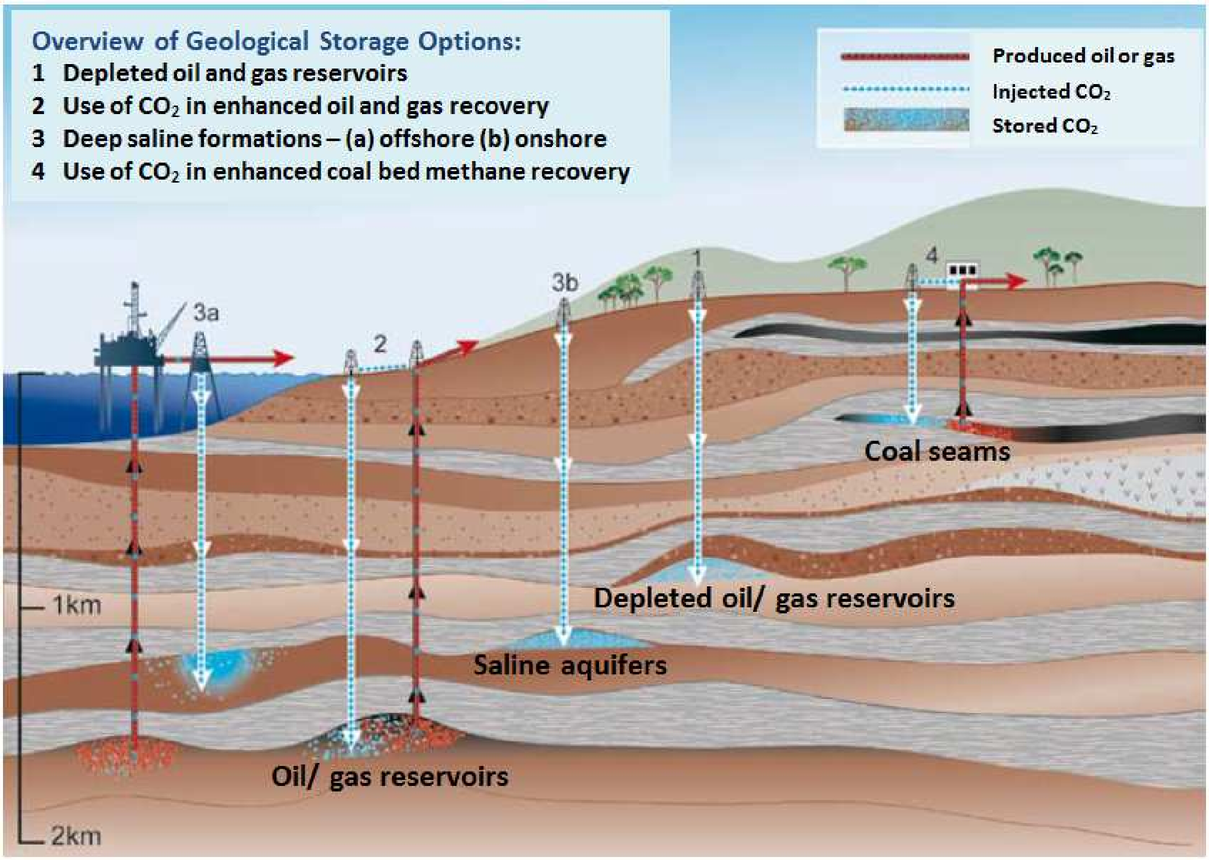

Figure 1.1. Geological storage strategies overview [1]

1.2. STORAGE MECHANISMS

CO_2 injection in deep geological formations, such as oil/gas reservoirs and saline aquifers, uses the same technologies developed in the oil and gas industries, like drilling and injection technologies, reservoir simulation and field monitoring. In depleted or almost depleted reservoirs the knowledge of the reservoir acquired during exploitation stage and the underground and surface infrastructure are mostly available.

In deep saline aquifers and oil/gas reservoirs, CO_2 injection takes places at depths of over 800 m (Fig.1.1), where CO_2 is in a liquid or supercritical phase. Here, CO_2 density is about 50% to 80% of the water density, which makes it more buoyant than other liquids present in the pore space [1]. Therefore, CO_2 penetrates through the porous medium until it reaches the top of the formation where it is trapped by an impermeable layer of cap-rock (structural/stratigraphic trapping). The cap-rock is supposed to act as the primary seal to prevent undesirable migration and leakage [13]. However, capillary leakage occurs when the pressure in the CO_2-rich phase increases above the capillary pressure of the cap-rock. This pressure is the minimum required pressure to initiate the displacement of brine within the cap-rock.

A part of the CO_2 moves through the porous medium and displaces reservoir fluid from the pores. Some of the CO_2 remains in the pore spaces as residual bubbles which are immobile (residual/capillary trapping).

Other trapping mechanisms are mineral trapping, where CO_2 reacts with minerals in the rock, and solubility trapping, where CO_2 dissolves in the aqueous phase. In general, different trapping mechanisms occur simultaneously [14-16].

At shallower depths than oil/gas reservoirs and saline aquifers, another type of trapping can occur, namely the adsorption of CO_2 onto coal or organic-rich shale, thereby replacing methane. In this case, as long as pressures and temperatures are stable, CO_2 remains trapped.

1.3. FLUE GAS INJECTION

Power plants are one of the major sources of CO_2 emission. The emitted flue gases mainly consist of nitrogen and CO_2 (Table 3.1) [17]. For depleted gas reservoirs and aquifers, CO_2 is separated from the flue gas prior to its injection for storage. This makes the process less energy efficient. Direct injection of flue gas into a reservoir eliminates the need for CO_2 separation prior to its injection into the field. Nevertheless, flue gas injection can reduce the structural trapping capacity for CO_2, which is undesirable for CCS volume efficiency. In ECBM, however, this process would be interesting and economically favorable since the flue gas strips methane, i.e. CO_2 and toxic contaminants get adsorbed at the coal surface while nitrogen and methane are produced. However, the injection of flue gas in coal seams causes the displacement of CO_2 by N_2 [18], early breakthrough of the nitrogen [19], and contamination of the methane-production stream. To implement this method on a field scale, this process needs to be investigated in more detail [20].

1.4. WETTABILITY AND CCS

In reservoir engineering, it has been well recognized that interfacial interactions, i.e. wettability, capillarity, interfacial tension and relative permeability, control the flow behavior and the displacement in porous media. These four parameters are interrelated and used as input parameters in reservoir simulations (Fig. 1.2). Particularly, surface rock wettability and interfacial tensions between two immiscible fluids have been recognized as the most important factors determining the residual saturation, the capillary-pressure and the relative-permeability functions [21-23].

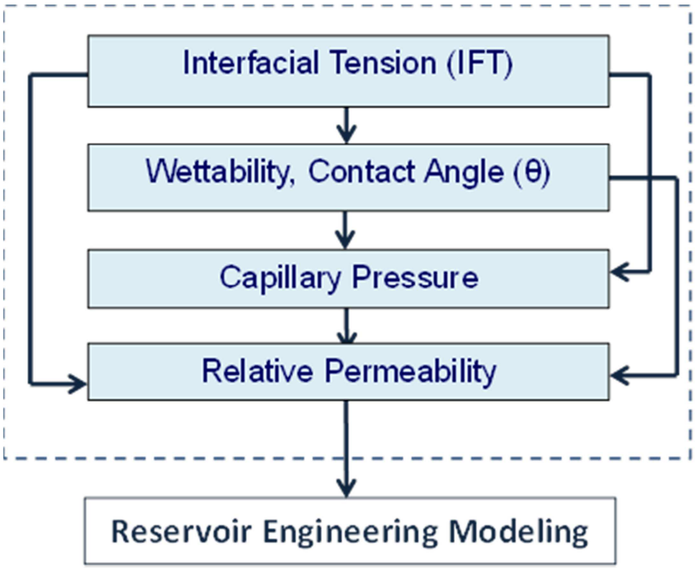

Figure 1.2. Interfacial interactions which control the flow behavior in porous media [21].

Wettability describes how immiscible fluids adhere to the rock surface and influences fluid flow. The fluid distribution in water-wet rocks is significantly different to that in oil/gas-wet rocks. In oil/gas-wet rocks, oil/gas wets the surface of the large pores and occupies small pores. Any reduction in IFT decreases capillary pressure and increases the capillary number. This causes the easier displacement of trapped oil/gas through the pore spaces. This means that the process of CO_2 storage in geological formations is influenced by gas-liquid-rock interfacial interactions [24-26]. The relation between the interfacial interactions (interfacial tension, capillarity and wettability) is represented by the Young-Laplace equation:

$$P_c = P_{nw} - P_w = 2\gamma_{aq,CO_2} \cos\theta / R \quad , \tag{1.1}$$

where P_c is the capillary pressure, P_{nw} and P_w are the pressures in the non-wetting and wetting phase, respectively, γ_{aq,CO_2} is the interfacial tension between the aqueous phase and the CO_2–rich phase, R is an effective pore radius corresponding to the narrowest pore throat along the entire CO_2 flow path [13], and θ is the contact angle related to reservoir wettability (determined through the densest phase, here the aqueous phase). The capillary pressure can be positive or negative, depending on the wetting phase, i.e. whether the contact angle is smaller or greater than 90°. Capillary trapping occurs when CO_2 is immobilized in the rock pores by capillary forces. This process depends on the wettability of the rock, the interfacial tension (IFT) between the CO_2-rich and the aqueous phase (brine) and the pore-size distribution (Eq. 1.1) [27, 28].

1.5. WETTABILITY AND CONTACT ANGLE DETERMINATION

Wettability of reservoir rocks is determined by a complex relationship of interfacial interactions between the rock, composed of a wide variety of minerals, and the reservoir fluids that occupy the irregular pore space. Experimentally, the wettability is only determined in the laboratory because no experimental method exists for *in-situ* measurements. Different techniques, either quantitative or qualitative, have been developed to evaluate the wettability of a rock-fluid system, namely the Amott test, the U.S. Bureau of Mines (USBM) test, and contact-angle measurements. The Amott and USBM methods give a quantitative value of the wettability of a core only at atmospheric conditions. The contact-angle method allows the determination of the wettability of a specific surface also at high pressures and elevated temperatures [29]. To avoid complications due to surface roughness and heterogeneity during the experiments and data processing, the experimental determination of the contact angle is commonly conducted on idealized and polished surfaces. Although the wettability determination on a polished or rough surface leads to an "*apparent contact angle*", this apparent contact angle is a good representative value of the average wettability of the real surface. Therefore, experimentally determined contact angles are widely used to characterize the wettability of complicated systems, in particular at high pressures and elevated temperatures [13, 28, 30].

For the characterization of the surface wettability by means of the contact angle, Young's equation is applied:

$$\gamma_{lv} \times cos\theta_Y = \gamma_{sv} - \gamma_{sl} \,, \tag{1.2}$$

where γ_{lv}, γ_{sv} and γ_{sl} are the interfacial tensions or surface energies between the aqueous phase and the gas phase, the solid and the gas phase, and the solid and the aqueous phase, respectively, and θ_Y is the Young's contact angle, which is a unique contact angle at equilibrium and is determined through the densest fluid phase. Commonly, the product $\gamma_{lv} \times cos\theta$ refers to the adhesion force [31], which is used in reservoir engineering for the calculation of the capillary number. Based on the capillary number, the residual saturations and relative permeabilities are determined [32].

However, in practice, many metastable states of a droplet/bubble on a solid exist, which might lead to an inequality of the experimentally determined contact angle, θ, with the Young's contact angle, θ_Y. In general, the contact angles formed by expanding and contracting a liquid droplet/gas bubble are described as the advancing contact angle θ_a and the receding contact angle θ_r, respectively. Differences in the receding and advancing contact angle result from surface roughness and/or heterogeneity [33]. The difference between the advancing and the receding angle is called the contact angle hysteresis (H):

$$H = \theta_a - \theta_r \tag{1.3}$$

On ideal surfaces, there is no contact angle hysteresis, and the experimentally determined contact angle is equal to Young's contact angle, θ_Y.

The contact angle between the three phases determines whether a reservoir rock is water-wet ($\theta<75^o$), intermediate-wet ($75^o<\theta<105^o$) or oil/gas-wet ($\theta>105^o$). The contact angle can be experimentally determined in a pendant/sessile drop cell that is adapted to allow the analysis of a captured bubble/sessile drop at a rock surface. The contact angle method is based on image analysis of high-resolution photographs of the droplet/bubble on the rock surface (Chapter 2).

1.6. RESEARCH OBJECTIVES AND OUTLINE OF THE THESIS

To identify a secure and proper strategy for CO_2 and flue gas injection, the fluid displacement at reservoir conditions and thus the wettability of the geological formation need to be understood. For instance, gas-wet cap-rock has a higher risk of CO_2 leakage due to lower capillary pressures [34]. In literature, many data can be found regarding CO_2 storage with focus on geochemical modeling, reservoir simulation, long-term reservoir integrity and risk assessment [14, 35]. Only a limited amount of literature refers to wetting properties of sedimentary rocks and minerals at high pressures and elevated temperatures [28, 30, 36-39]. Hence, a reliable experimental method to determine the wettability is a big step towards understanding the physics of this phenomenon.

This thesis is a collection of experimental work on the wettability behavior of the rock surface of different rank coals, Bentheimer sandstone and oil-saturated sandstone, in the presence of CO_2 and/or synthetic flue gas (80% N_2/20% CO_2). In addition, interfacial interactions between the gas phase and aqueous phase are studied at various pressures. To mimic the in-situ conditions, CO_2 experiments are performed at high pressures and elevated temperature (up to 16 MPa and at 318 K). Data on the contact angle are obtained for the evaluation of the wettability of different rock types because:

1. Data of contact angle and interfacial tension, particularly in the pressure range where CO_2 is a supercritical phase, are significant for the evaluation of the capillary trapping (Eq. 1.1) and,
2. When dealing with supercritical CO_2, wetting properties cannot be determined by the Amott-USBM method due to the fact that this method cannot be used at high pressure.

To determine the contact angle, experiments are conducted for different compositions of the aqueous phase, i.e. fully saturated and unsaturated with respect to CO_2. For the unsaturated aqueous phase, the injectivity and the gas distribution in the reservoir are influenced not only by matrix properties but also by the diffusion of CO_2 into the aqueous phase. However, after saturation of the aqueous phase, the gas distribution is mainly determined by the wetting properties of the rock. Additionally, before the method can be used in a field case, it is also important to evaluate the dissolution effects and the wettability for short and long periods. This can be done by conducting experiments with an unsaturated aqueous phase, representing the short-term behavior, and with a saturated aqueous phase representing the long-term behavior. To evaluate the wetting properties of rock surfaces the captive-bubble technique is used. The method, experimental set-up and procedure as well as image analysis method are explained in Chapter 2.

1.6.1. PART I: CO_2- ENHANCED COAL BED METHANE

Coal seam storage commonly takes place at depths where supercritical CO_2 sorbs to coal as a substitute gas for methane. The feasibility of this process is largely influenced by the fracture and matrix permeability of the coal bed and the wettability of the coal matrix. The wettability of the coal is a function of coal rank, maceral content, ash content, heterogeneity of the coal surface, pressure, temperature and gas phase composition. This thesis shows that for reliable contact-angle determination the experiments should be conducted in fully–saturated aqueous phase in order to minimize the effects of CO_2 dissolution on the wetting properties investigation and changes of the aqueous phase composition. These criteria were not considered before in literature. In Chapter 3 wetting properties of two coal samples with similar vitrinite content are evaluated as well as the effect of pressure and coal rank.

For the CATO-2 program, the outputs of this chapter include deliverables for work packages 3.2 (reservoir behavior).

1.6.2. PART II: AQUIFERS AND DEPLETED GAS RESERVOIRS

For a brine-saturated cap-rock, which consists of a low-permeability porous material, interfacial tension and contact angle data are the significant parameters for the evaluation of the capillary-sealing. Also, the amount of capillary-trapped CO_2 depends on the wettability of reservoir rocks. The wettability of the rock matrix has a strong effect on the distribution of phases within the pore space and thus on the entire displacement mechanism and storage capacity. Hence, reduction of the interfacial tension (IFT) may result in the mobilization of connate water (capillary trapping). In addition, dissolving CO_2 in (immobile) formation water is one of the most important mechanisms to (permanently) store CO_2 (solubility trapping). Moreover, for most practical situations the pressure and temperature conditions are such that dissolution of CO_2 in the formation water will increase the density of the formation water. This further enhances the storage capacity. However, dissolution is generally negatively correlated with salinity, and dissolution of CO_2 lowers the IFT of CO_2/water systems. Therefore, understanding of the wettability and dissolution behavior and the interplay with IFT is of importance for displacement behavior and storage capacity. In Chapter 4 wetting properties of Bentheimer sandstone rock are investigated with an unsaturated aqueous phase, representing the short-term behavior, and with a saturated aqueous phase representing the long-term behavior. In addition the dissolution behavior and mass transfer of a CO_2 bubble in a water/Bentheimer sandstone system are determined at various pressures.

For the CATO-2 program, the outputs of this chapter include deliverables for work packages 3.2 (reservoir behavior).

1.6.3. PART III: OIL RESERVOIR

Wettability has a significant effect on the performance of enhanced oil recovery techniques because of its effect on fluid saturations and flow behavior in porous media. For oil-wet rock, CO_2 must overcome a capillary barrier to invade the rock matrix in order to be able to displace the oil in a secondary drainage process. If the rock wettability alters from oil-wet to gas-wet, a positive value of capillary pressure is established. Therefore, the injected CO_2 will spontaneously imbibe from the fractures into the matrix blocks and oil will be expelled. Chapter 5 describes the contact angles, i.e. wettability, in systems with water, an oil-saturated rock, and carbon dioxide and/or synthetic flue gas. Two situations are considered: rock-system I is partially water-wet, whereas rock-system II is effectively oil-wet.

In addition, to describe the wetting properties of the surface as a function of pressure, a surface-free-energy analysis are used based on an equation of state (EOS). Following this approach, a modified equation of state is proposed to describe the contact angle of a liquid/gas/solid system at various pressures. The use of the equation of state method makes it possible to approach the experimental data quantitatively, if a number of reliable contact-angle and interfacial-tension measurements are available for a system of interest.

For the CATO-2 program, the outputs of this chapter include deliverables for work package 3.5 (additional benefits of CO_2 injection: CO_2/EOR).

Note from the author

The chapters of this thesis are stand-alone journal publications and hence can be read separately. Accordingly, some explanations and paragraphs may appear more than once.

REFERENCES

[1] IPCC, Carbon Dioxide Capture and Storage in: B. Metz, O. Davidson, H.d. Coninck, M. Loos, L. Meyer (Eds.) IPCC, 2005, pp. 431.

[2] H.L. Treut, R. Somerville, U. Cubasch, Y. Ding, C. Mauritzen, A. Mokssit, T. Peterson, M. Prather, Historical overview of climate change science, in: S. Solomon, D. Qin, M. Manning, Z. Chen, M. Marquis, K.B. Averyt, M. Tignor, H.L. Miller (Eds.), Cambridge University Press, 2008.

[3] S. Buckingham, M. Turner, Understanding Environmental Issues, SAGE Publications Ltd., 2008.

[4] Carbon Dioxide Information Analysis Center, in, U.S. Department of Energy (DOE), http://cdiac.ornl.gov/mission.html, 2012.

[5] A.E. Ofori, T.W. Engler, Effects of CO_2 Sequestration on the Petrophysical Properties of an Aquifer Rock, in: Canadian Unconventional Resources Conference, Society of Petroleum Engineers, Alberta, Canada, 2011.

[6] A. Chadwick, R. Arts, C. Bernstone, F. May, S. Thibeau, P. Zweigel, Best practice for the storage of CO_2 in saline aquifers- Observations and guidelines from the SACS and CO_2STORE Projects, British Geological Survey, Nottingham, 2007.

[7] R.J. Arts, C. Hofstee, V.P. Vandeweijer, M.P.D. Pluymaekers, D. Loeve, A. Kopp, W.J. Plug, The feasibility of CO_2 storage in the depleted P18-4 gasfield offshore the Netherlands (the ROAD project), International Journal of Greenhouse Gas Control, (2012) In press.

[8] R.J. Arts, A. Chadwick, O. Eiken, S. Thibeau, S. Nooner, Ten years of experience with CO_2 injection in the Utsira Sand at Sleipner (offshore Norway), First Break, 26 (2008) 65-72.

[9] D. Velasquez, O. Rey, E. Manrique, An overview of carbon dioxide sequestration in depleted oil and gas reservoirs in Florida, USGS Petroleum Province 50, in: Fourth LACCEI International Latin American and Caribbean Conference for Engineering and Technology (LACCEI'2006), Mayagüez, Puerto Rico, 2006.

[10] K. Damen, A. Faaij, F. van Bergen, J. Gale, E. Lysen, Identification of early opportunities for CO_2 sequestration—worldwide screening for CO_2-EOR and CO_2-ECBM projects, Energy, 30 (2005) 1931-1952.

[11] F.V. Bergen, P. Krzystolik, N.v. Wageningen, H. Pagnier, B. Jura, J. Skiba, P. Winthaegen, Z. Kobiela, Production of gas from coal seams in the Upper Silesian Coal Basin in Poland in the post-injection period of an ECBM pilot site, International Journal of Coal Geology, 77 (2009) 175-187.

[12] Z. Li, M. Dong, S. Li, S. Huang, CO_2 sequestration in depleted oil and gas reservoirs--caprock characterization and storage capacity, Energy Conversion and Management, 47 (2006) 1372-1382.

[13] P. Chiquet, D. Broseta, S. Thibeau, Wettability alteration of caprock minerals by carbon dioxide, Geofluids, 7 (2007) 112-122.

[14] B. Basbug, F. Gumrah, B. Oz, Simulating the Effects of Deep Saline Aquifer Properties for CO_2 Sequestration, (2007).

[15] A. Shariat, R.G. Moore, S.A. Mehta, K.C.V. Fraassen, K.E. Newsham, J.A. Rushing, Laboratory Measurements of CO_2-H_2O Interfacial Tension at HP/HT Conditions: Implications for CO_2 Sequestration in Deep Aquifers, in: Carbon Management Technology Conference, Carbon Management Technology Conference, Orlando, Florida, USA, 2012.

[16] H. Salimi, K.-H. Wolf, J. Bruining, The influence of capillary pressure on the phase equilibrium of the CO_2–water system: Application to carbon sequestration combined with geothermal energy, International Journal of Greenhouse Gas Control, 11, Supplement (2012) S47-S66.

[17] S. Mazumder, K.H. Wolf, CO_2 and Flue Gas Coreflood Experiments for Enhanced Coalbed Methane, in: SPE Asia Pacific Oil and Gas Conference and Exhibition, Society of Petroleum Engineers, Perth, Australia, 2008.

[18] R. Florenti, N. Aziz, D. Black, L. Nghiem, K. Baris, Recovery of stored gas in coal by nitrogen injection - a laboratory study, in: 10th Underground Coal Operators' Conference, University of Wollongong & the Australasian Institute of Mining and Metallurgy, Australia, 2010, pp. 217-228.

[19] S. Wo, J.T. Liang, Simulation Assessment of N_2/CO_2 Contact Volume in Coal and Its Impact on Outcrop Seepage in N_2/CO_2 Injection for Enhanced Coalbed Methane Recovery, in: SPE/DOE Symposium on Improved Oil Recovery, Society of Petroleum Engineers, Tulsa, Oklahoma, 2004.

[20] A. Syed, S. Durucan, J.-Q. Shi, A. Korre, Flue gas injection for CO_2 storage and enhanced coalbed methane recovery: Mixed gas sorption and swelling characteristics of coal, in: 11th International Conference for Greenhouse Gas Control Technologies, Kyoto, Japan, 2011.

[21] W.G. Anderson, Wettability Literature Survey- Part 1: Rock/Oil/Brine Interactions and the Effects of Core Handling on Wettability, SPE Journal of Petroleum Technology, 38 (1986) 1125-1144.

[22] N.R. Morrow, Wettability and Its Effect on Oil Recovery, SPE Journal of Petroleum Technology, (1990).

[23] G.J. Hirasaki, Wettability: Fundamentals and Surface Forces, SPE Formation Evaluation, 6 (1991) 217-226.

[24] B. Arendt, D. Dittmar, R. Eggers, Interaction of interfacial convection and mass transfer effects in the system CO_2–water, International Journal of Heat and Mass Transfer, 47 (2004) 3649-3657.

[25] D. Yang, Y. Gu, P. Tontiwachwuthikul, Wettability determination of the crude oil-reservoir brine-reservoir rock system with dissolution of CO_2 at high pressures and elevated temperatures, Energy and Fuels, 22 (2008) 2362-2371.

[26] C. Chalbaud, M. Robin, J.M. Lombard, F. Martin, P. Egermann, H. Bertin, Interfacial tension measurements and wettability evaluation for geological CO_2 storage, Advances in Water Resources, 32 (2009) 98-109.

[27] C.H. Pentland, S. Al-Mansoori, s. iglauer, B. Bijeljic, M.J. Blunt, Measurement of Non-Wetting Phase Trapping in Sand Packs, in: SPE Annual Technical Conference and Exhibition, Society of Petroleum Engineers, Denver, Colorado, USA, 2008.

[28] J. Mills, M. Riazi, M. Sohrabi, Wettability of common rock-forming minerals in a CO_2-brine system at reservoir conditions, in: International Symposium of the Society of Core Analysts, Austin, Texas, USA, 2011.

[29] W.G. Anderson, Wettability Literature Survey- Part 2: Wettability Measurement, SPE Journal of Petroleum Technology, 38 (1986) 1246-1262.

[30] D.N. Espinoza, J.C. Santamarina, Water-CO_2-mineral systems: Interfacial tension, contact angle, and diffusion-Implications to CO_2 geological storage

WATER RESOURCES RESEARCH, 46 (2010).

[31] A.W. Adamson, A.P. Gast, Physical chemistry of surfaces, 6th ed., A Wiley-Interscience Publication, 1997.

[32] D. Yang, Y. Gu, P. Tontiwachwuthikul, Wettability Determination of the Reservoir Brine−Reservoir Rock System with Dissolution of CO_2 at High Pressures and Elevated Temperatures, Energy & Fuels, 22 (2008) 504-509.

[33] D.Y. Kwok, A.W. Neumann, Contact angle measurement and contact angle interpretation, Advances in Colloid and Interface Science, 81 (1999) 167-249.

[34] P. Chiquet, D.F. Broseta, S. Thibeau, Capillary Alteration of Shaly Caprocks by Carbon Dioxide, in: SPE Europec/EAGE Annual Conference, Society of Petroleum Engineers, Madrid, Spain, 2005.

[35] L. Nghiem, P. Sammon, J. Grabenstetter, H. Ohkuma, Modeling CO_2 Storage in Aquifers with a Fully-Coupled Geochemical EOS Compositional Simulator, in: SPE/DOE Symposium on Improved Oil Recovery, Society of Petroleum Engineers, Tulsa, Oklahoma, 2004.

[36] M.B. Alotaibi, R.M. Azmy, H.A. Nasr-El-Din, Wettability Studies Using Low-Salinity Water in Sandstone Reservoirs, in, 2010.

[37] C. Chalbaud, M. Robin, S. Bekri, P. Egermann, Wettability impact on CO_2 storage in aquifers: visualisation and quantification using micromodel tests, pore network model and reservoir simulations, in: International Symposium of the Society of Core Analysts, Calgary, Canada, 2007.

[38] W. Jiamin, K. Yongman, J. Jongwon, Wettability alteration upon reaction with $scCO_2$: Pore scale visualization and contact angle measurements, in: Goldschmidt 2011, Prauge, Czech Republic, 2011.

[39] D. Yang, Interfacial Interactions of the Crude Oil-Reservoir Brine-Reservoir Rock Systems with Dissolution of CO_2 under Reservoir Conditions, in, University of Regina, Regina, SK, Canada, 2005.

CHAPTER 2

Contact-Angle Determination with the Captive Bubble Method: Experimental Procedure

This chapter describes the captive-bubble technique that is used in this study to evaluate the wetting properties of rock surfaces. The method, pendant-drop set-up, experimental procedure, and image analysis method are explained here.

2.1. INTRODUCTION

The wettability of reservoir rocks is determined by a complex relationship of interfacial interactions between the rock, composed of a wide variety of minerals, and the reservoir fluids that occupy the irregular pore space. Experimentally, wettability is only determined in the laboratory because no experimental method exists for *in-situ* measurements. Different techniques, either quantitative or qualitative, have been developed to evaluate the wettability of a rock-fluid system, namely the Amott test [1], the U.S. Bureau of Mines (USBM) test [2], and contact-angle measurements [3].

The difficulty with the Amott test arises when the spontaneous imbibition is low, i.e. if the rock surface is characterized by an intermediate wettability. The USBM method gives the average core wettability by determination of the areas underneath the positive and negative capillary pressure curves. The advantage of this method over the Amott method is that allows one to also quantify wettability of surfaces which are intermediate wet. However, the USBM method cannot be used to distinguish between different types of intermediate wettability. Additionally, the Amott and USBM methods determine the average wettability of a core at atmospheric conditions. However, the contact-angle method allows the determination of the wettability of a specific surface even at high pressures and elevated temperatures [4].

In general, the contact angle is not only the most universal measure of the wettability of a solid surface, but has also been widely used to characterize wettability phenomena of more complicated systems at high pressures and elevated temperatures. The contact angle and interfacial tension can be determined in a pendant/sessile drop cell which allows one to analyze the captured bubble/sessile drop at the rock surface. According to convention, a reservoir rock is considered to be water-wet when the contact angle of a water droplet on the rock surface is within the range between 0 and 75°. In case the contact angle is in the range between 75° and 105°, the surface is considered to be intermediate-wet. Finally, when the contact angle is in the range between 105° and 180°, the rock is oil-wet or gas-wet. Contact-angle determination is based on taking and analyzing high-resolution images which are used to determine either the contact angle or the vapor-liquid interfacial tension, or possibly both. It is worthwhile to mention that the experimentally observed apparent contact angle may or may not be equal to the Young contact angle as given in Young's equation (Chapter 1, Eq. 1.2). Chemical (mineral) heterogeneity and roughness of the surface induce so-called contact angle hysteresis [5] (Chapter 1).

In this study, contact-angle measurement was considered for the evaluation of the wettability because: 1) values of the contact angle and the interfacial tension, particularly in the pressure range where CO_2 is supercritical, are crucial for the evaluation of the capillary trapping [6], and 2) when dealing with supercritical CO_2, wetting properties cannot be determined by the Amott or USBM methods due to the fact that these methods cannot be used at high pressure.

Three different contact-angle determination techniques were considered in literature (Fig.2.1) [7], i.e., static sessile drop (Fig 2.1(a)), static captive bubble (Fig 2.1(b)) and dynamic captive bubble (Fig 2.1(c)).

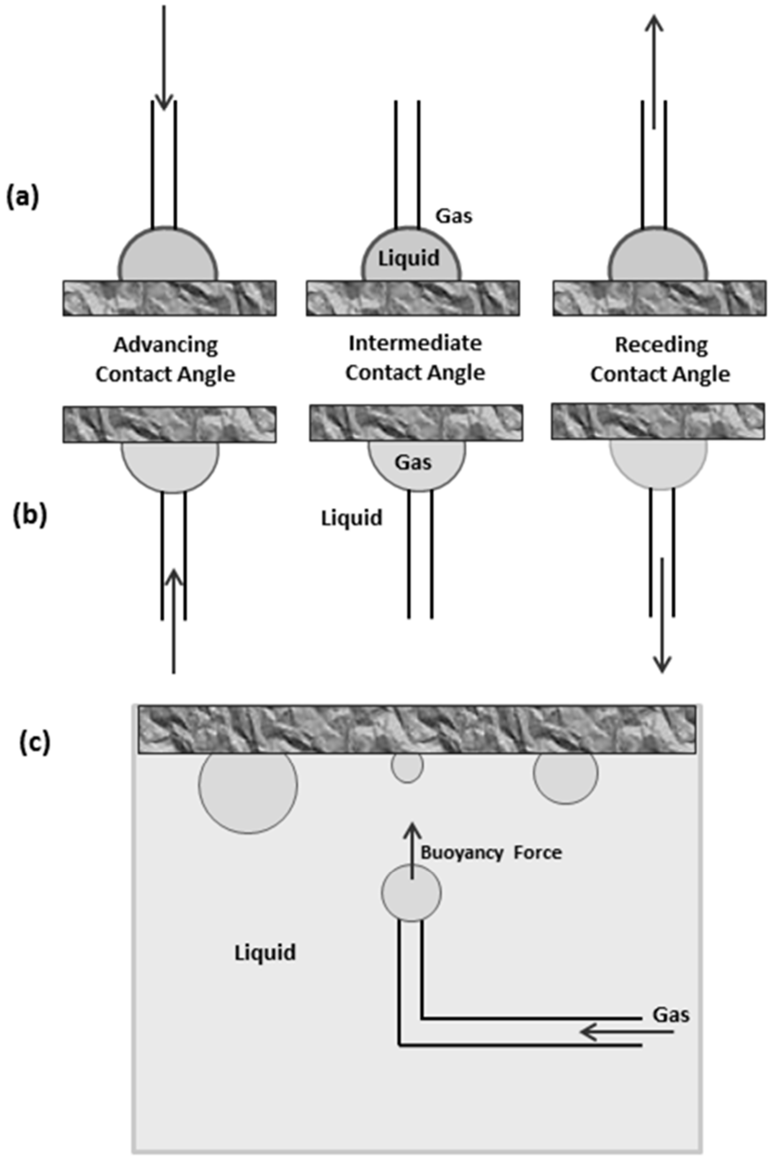

Figure 2.1. Drawing of three techniques of contact-angle determination: (a) static sessile drop; (b) static captive bubble; (c) dynamic captive bubble[7]

In static techniques, either captive-bubble or sessile-drop, the contact angle formed by shrinking and growing are represented to the receding contact angle, θ_r, and the advancing contact angle, θ_a, respectively (Fig. 2.1(a) and (b)). These angles are within a range with a maximum value, which corresponds to the advancing contact angle, and a minimum value, which is associated with the receding contact angle. The difference between the advancing angle and the receding angle is defined as the hysteresis (Chapter 1, Eq. 1.3) and the general conclusion is that it results from surface roughness and/or surface heterogeneity (Chapter 1).

In general, the dynamic captive-bubble technique is used to investigate the effect of bubble size on the contact angle [7]. In this technique, two different sets of contact-angle data are normally reported in the literature, i.e., equilibrium (stable) and transient (dynamic) contact angles. The transient contact angle gives information on the change, increase or decrease, of the contact angle in time while the stable contact angle refers to a constant contact angle with the system in equilibrium [8-11]. Even though the transient contact angle is an effective method to investigate the transient phenomena that occur at the interface, care must be taken in interpreting these results. For an unsaturated system, as found in other experiments [9, 10], the transient contact angle provides important information concerning the (interfacial) interactions between different phases, like dissolution, diffusion, and convective mass transfer. Indeed, the change in contact angle might be correlated with the contribution of the different mechanisms involved rather than the wettability alteration. In contrast, for a fully-saturated system, equilibrium has already been established and no further mass transfer occurs between the phases; therefore, the stable contact angle reveals the wetting properties of the system alone. For such a system, injection of a gas bubble into an equilibrated system, which consists of water and CO_2, induces an initial fluctuation of the determined contact angle. However, due to the fact that the overall composition is within the two-phase region, the release of a new gas bubble only leads to a small disturbance of the equilibrium that does not last long [8, 12]. Hence, after the system attains equilibrium, the contact angle should not change with time.

In this study all contact angle (CA) and interfacial tension (IFT) determinations were conducted in a modified pendant-drop (PD) cell, which was adapted to allow dynamic captive-bubble contact-angle measurements on rock surfaces. The determination of the contact angle is based on visual observation, i.e., by image capturing.

2.2. EXPERIMENTAL

2.2.1. SAMPLE PREPARATION

Unfortunately, no general procedure exists in literature concerning how smooth a solid surface should be to avoid the impact of surface roughness on the contact angle. In general, it is suggested to prepare the solid surface as smooth as possible. There are several methods for preparation of smooth solid surfaces, i.e., heat pressing, solvent casting, self-assembled monolayers, dip coating, vapor deposition and surface polishing. In this study in order to minimize the effect of surface roughness on the contact angle one side of the rock slabs was polished with a diamond paste with particle sizes from 10 to 250 μm. The rectangular samples used in this study were 30 mm by 6 mm by 12 mm. However, for coal and oil-saturated

Bentheimer samples extra actions have been taken as described in the Experimental sections of Chapters 3 and 5.

Afterward, the surface roughness was determined using a Leica 3D stereo explorer. Additionally, a Phoenix Nanotom scanner was used to determine the grain framework, as well as the voids distribution of the sample at the micro level (6 µm voxel size).

2.2.2. EXPERIMENTAL SET-UP

The pendant-drop setup has been used as a tool for the determination of contact angle and surface and interfacial tensions. The set-up was originally designed and constructed in the Dietz laboratory in 1989 [13]. The method is based on visual observation of a captive bubble on a rock surface at varying pressures up to 16 MPa and a constant elevated temperature of 318 K. A schematic drawing of the experimental set-up is given in Fig. 2.2.

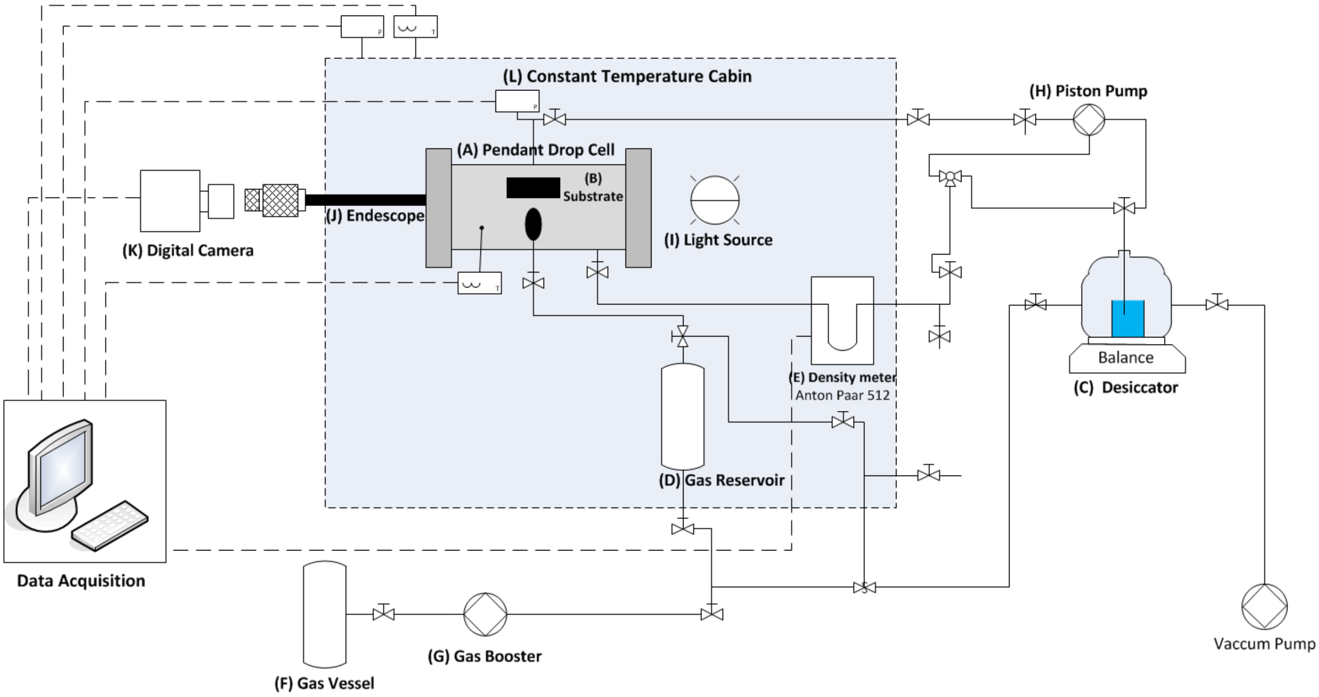

Figure 2.2. Schematic diagram of experimental set-up (Pendant-drop cell)

The pendant-drop cell (part A in Fig. 2.2) consisted of a steel cylinder with a wall thickness of 3.5 cm and a volume of 160 cm^3 that was suitable for use up to pressures of 60 MPa. Sapphire windows were used at the axial sides of the cell to allow visual observation. The sample (B) was positioned inside the cell using a specially designed holder. On the right side of the cell, a light source (I) provided a strong beam of light through one of the windows to illuminate the bubble in the cell. A monochromatic filter was placed in front of the light source to ensure a sharp image and to avoid chromatic aberration. The bubble was photographed through an endoscope (J) designed for this setup. For a sharp image between the phases, the endoscope was focused on the edge of the captured bubble. A Nikon D90 digital single lens reflex camera (K) with a resolution of 12.3 MP captured the bubble in real time on a monitor and created high-resolution images. As a calibration for the bubble size, the tip was photographed together with the bubble. The outside and inside diameters of the tip were 1.80 mm and 0.72 mm, respectively.

The degassed liquid phase, in this case double-distilled and demineralized water, was added from the top into the cell from the desiccator (C) by a Gibson™ single-piston, high-pressure displacement pump (H). A 10SC pump head provided a flow rate ranging from 0.05 to 10 ml/min and a pressure range from 0.1 to 60 MPa. The amount of injected water into the system was determined with a balance (Sartorius LA6200S) with an accuracy of ±0.01g. Fourteen needle valves were used to control the flow of the gas and liquid through the inlets and outlets. Gas was added through a needle at the bottom of the cell. In this way, the injected gas got immediately into contact with the liquid phase enhancing saturation of the liquid phase by the injected gas. The tube lines were arranged such that the mixture can be circulated to further enhance the mixing of the components and accelerate equilibrium. Within this circulation loop, a vibrating tube density meter (E) (Anton Paar K.G. DMA 512) was incorporated to allow determination of the density of the passing fluid. A constant density indicates that equilibrium has been reached. The accuracy of the density meter was 0.001 g/cm^3 in a temperature range between 273 and 323 K. To avoid temperature fluctuation during the experiment, the cell was placed in a constant temperature cabin (L) which was kept at constant temperature within ±1 K in the range from ambient+5 K up to 473 K. The temperature was measured in the oven and inside the cell, i.e. in the liquid bulk, close to the interface of the bubble, water and rock sample, by means of two calibrated thermometers, PT-100 and PT-8316, respectively (Fig. 2.3).

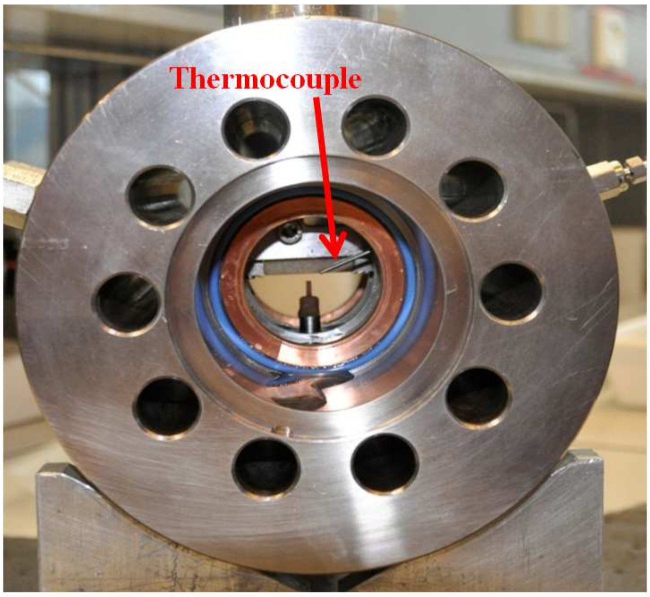

Figure 2.3. Side view of the open pendant-drop cell showing the location of the gas inlet tip and the thermocouple inside the cell

The gas supply system consisted of a gas booster (G) that pumped the gas, either CO_2 or synthetic flue gas, into the gas reservoir (D). Pressure transducers (Tradinco TS90064) monitored the pressure in the gas reservoir and the cell with an accuracy of 0.1% up to 40 MPa. The pressure change in the gas reservoir was used to determine the amount of injected CO_2 by applying an accurate equation of state (EOS), i.e., using Span-Wagner EOS

[14]. The composition of the water-CO_2 mixture together with phase-equilibrium data taken from literature [15] were used to verify system equilibrium (Fig. 2.4).

2.2.3. EXPERIMENTAL PROCEDURE

Before a series of experiments was performed, all of the components of the setup were cleaned with ethanol and distilled water to remove possible impurities. After evacuation and a helium leakage test up to 18 MPa, the cell was filled with double-distilled and demineralized water. The water level in the cell needed to be higher than the lower end of the substrate. The entire set up was pre-heated to a temperature of 318 K (±1 K), which was kept constant for all of the experiments.

The amount of CO_2 injected depended on which kind of aqueous phase needed to be established for the experiment. For a wettability study in an unsaturated aqueous phase, the initial aqueous phase was kept pure ($X_{CO_2}=0$). Therefore, the cell was filled with water up to the desired pressure, and a small amount of CO_2 was then added to the cell through a small needle at the bottom. For these experiments, the changes in contact angle were mainly attributed to the CO_2 dissolution rather than to the wetting properties of the Bentheimer substrate.

To investigate the wetting properties of Bentheimer sandstone, the experiments have to be performed in an aqueous phase that is fully-saturated with CO_2. Under such conditions, the effects of CO_2 dissolution and changes of the aqueous phase composition are minimal during the experiment. To ensure complete saturation of the aqueous phase, the mixture was circulated for at least five hours. Thereafter, the system was allowed to rest for at least one hour. The pressure and the temperature of the cell and the cabin, and the density of the mixture were continuously monitored during the experiments.

The phase diagram of the CO_2/water system in the region of high mole fractions of water at 318 K is depicted in Fig. 2.4. This diagram was used to determine whether the system was within the one-phase or the two-phase region at the given conditions. Once enough CO_2 had been injected, circulation was initiated to ensure the mixing of CO_2 and water and to achieve faster equilibrium. In this experiment, the overall composition of the mixture was determined through a material balance using the mass of water and the number of CO_2 moles determined by the Span-Wagner EOS [16]. When the pressure in the cell and the density of the aqueous phase reach a constant level, the system has reached equilibrium. In flue gas experiments, the aqueous phase was initially pre-saturated with CO_2 to accelerate the equilibrium time.

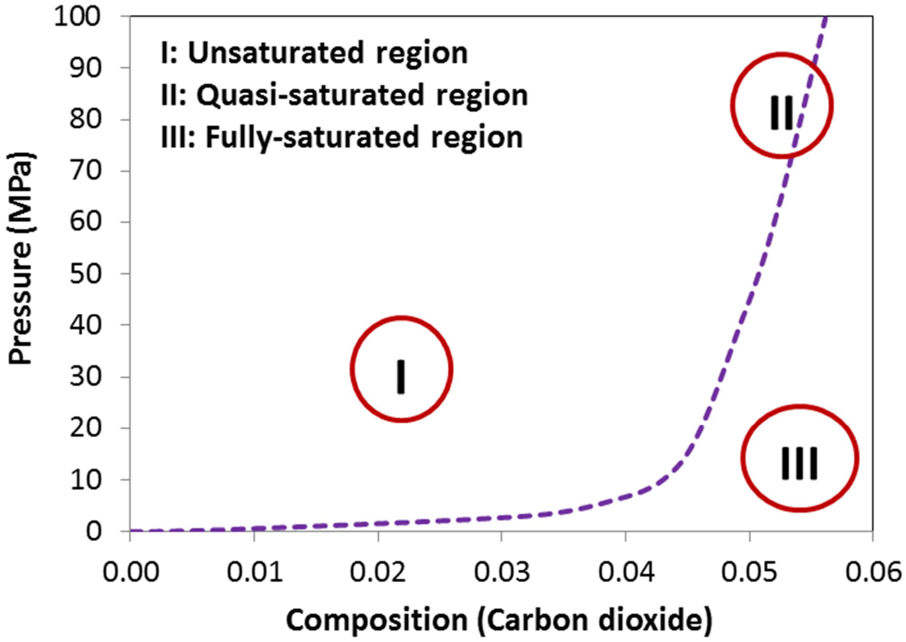

Figure 2.4. Phase diagram of CO_2/H_2O system at a temperature of 318 K. In this figure, only the H_2O-rich phase and part of the two-phase region are given. The two-phase region is situated on the right side of the curve, while the H_2O-rich one-phase region is located on the left side (Data from [15]).

After releasing a gas bubble from the tip and after a bubble had been captured beneath the substrate, images of the bubble were taken. These pictures were then processed in an image-analysis procedure which allowed determination of the contact angle at the specific pressure. Several pictures of the same bubble were taken in order to verify the reproducibility of the determined contact angle. Contact angles and interfacial tensions were determined using the KRÜSS™ drop-shape-analysis program (DSA4$^{©}$), analysing the pendant-drop shape [8, 17]. Thereafter, the pressure inside the cell was increased by adding more water (in unsaturated case) or gas (in fully-saturated case) to the cell.

2.3. IMAGE ANALYSIS

2.3.1. MICROSCOPIC IMAGE ANALYSIS

Prior to the contact-angle experiments, 2-D and 3-D microscopic images were taken from the surfaces using a Leica™ 3D stereo explorer. From the 3-D images, surface profiles were obtained, which were used for the P_a factor determination. The characterization of the surface roughness is based on the P_a factor, which is calculated according to an internationally recognized standard (EN ISO 4287), used to characterize the surface profiles. This standard is an international recognized standard used to characterize the surface profiles and defines values for the primary (P) profile. The P_a factor is the arithmetic mean of the absolute ordinate values Z(x) within a sampling length (l_p):

$$P_a = \frac{1}{l_p} \int_0^{l_p} |Z(x)|\, dx \tag{10}$$

The height (*Z*) is determined using a natural cubic spline function to describe the profile interpolating between discrete data. Larger P_a values are associated with rougher surfaces (i.e., the P_a value of a glass surface is about 0.01 μm). For different Bentheimer sandstone samples, the surface roughness was characterized by means of their P_a factors. The smoothest sample with the smallest P_a factor was selected for the experiments to minimize the effect of roughness on the determination of the contact angle.

It is worthwhile to mention that since this technique is designed for solid surfaces, it is not a complete characterization of the porous rock surface. For a porous Bentheimer, there are some holes on the surface where *Z* goes to very negative numbers. This technique cannot tell how deep the holes are and it transforms deep holes into shallow depressions. This method allows describing the roughness of the surface quantitatively. Based on a surface roughness analysis, the most proper and smoothest surface can be selected for the contact-angle experiments. This is an improvement in the sample preparation quality, in order to minimize the effect of surface roughness and hysteresis.

2.3.3. MICRO CT-SCAN

The distribution of mineral matter in the coal samples as well as the void distribution of the Bentheimer samples was determined at the micro level with a Phoenix Nanotom™ (180 kV/15 W nanofocus computed tomography (nano CT) system). The nano CT system consists of a high power nanofocus X-ray source, a precision object manipulator, a high resolution CCD detector and a computer for the control and re-construction of image slices. Digital geometry processing was used to generate a three-dimensional image of the inside of an object from a large series of two-dimensional X-ray images taken around a single axis of rotation. These two-dimensional X-ray images contained information on the position and density of absorbing features within the small samples [18].

2.3.4. BUBBLE IMAGE ANALYSIS

To determine the contact angle and interfacial tension, the Drop Shape Analysis (DSA4©) KRÜSS™ program was used to process the images [17]. To validate the results, images were also analyzed using an improved in-house MATLAB routine [19]. The results of both techniques were in a good agreement. However, for bubbles with a volume of less than 0.2 mm^3, the contact-angle determination is not reliable due to the limited pixel resolution and, thus, the high uncertainty in the bubble profile description.

For the image analysis with MATLAB routine, first the image was cropped to remove the part of the image that was not of interest (Fig. 2.5 (a)). The cropped image was converted into a grayscale (Fig. 2.5 (b)) and a binary image (Fig. 2.5 (c)); the binary image was transformed to an image containing a bubble profile and the surface (Fig. 2.5 (d)). From this image, the rock surface was determined by a linear regression over its corresponding data points and served as the baseline for the contact angle determination. The extracted bubble profile was split into two parts assuming an axis-symmetric shape for the bubble. Both halves of the bubble profiles were defined separately which allowed a better description of the surface and the bubble profile. The Young-Laplace equation in the orthogonal r, z directions was used to describe the bubble profiles (Fig. 2.5 (e)):

$$-\frac{\frac{d^2r}{dz^2}}{\left(1+\left(\frac{dr}{dz}\right)^2\right)^{3/2}}+\frac{1}{r\left(1+\left(\frac{dr}{dz}\right)^2\right)^{1/2}}=\frac{2}{R_0}+\frac{\Delta\rho g z}{\gamma_{lv}} \quad , \tag{2.1}$$

where R_0 is the radius of bubble at the apex, γ_{lv} and $\Delta\rho$ are the interfacial tension and the density difference between the gas and aqueous phases, respectively. For each side, an optimized set of parameters, ($2/R_0$) and ($\Delta\rho gz/\gamma_{lv}$), were obtained giving the respective best description. The values for both sides should be the same, unless hysteresis affects one side differently from the other. As a consequence, the difference of these parameters can be used as a criterion to judge the quality of the bubble and the bubble-profile description. Once the difference between the parameters describing the two halves of the bubble was accurate enough (at the 95% confidence level), the description of the bubble shape was accepted for subsequent determination of the contact angle. The contact angle was determined from the crossing of a tangent line to the bubble profile and the baseline describing the surface. In the last step, the calculated profile and baseline were compared with the original cropped picture (Fig. 2.5 (f)) to verify the descriptions.

The KRÜSS™ drop_shape-analysis program (DSA4$^{©}$) followed a similar principle as performed with the MATLAB routine, but in a shorter calculation time: first the bubble image was subjected to a gray-level analysis which gave an optically determined contour line around the phase boundary in the bubble image. In next step the bubble contour was described mathematically. For the analysis of the bubble profile several approaches were available, i.e., Young-Laplace method, circle method, conic section method and polynomial method. The contact angle was obtained from the angle between the fitter bubble-contour function and the rock surface which was the known baseline. The mathematical description of the baseline was a straight-line equation since the substrate was considered a flat surface. The Young-Laplace fit was the most proper method for symmetrical bubble shapes that were not influenced by distortions like contact with the needle or sample tilting. The symmetrical bubble can be mathematically characterized precisely by the Young-Laplace equation; therefore the best agreement between the theoretically and optically determined contours can be expected. The Young-Laplace method took the characteristic bubble shape under the influence of gravity into account with an improved iteration method [17]. This method was also used for determining the interfacial tension from the shape of a buoyant bubble. An additional advantage was that if the image scale was known, the real bubble dimensions, i.e., volume, contact surface and radius, could be determined.

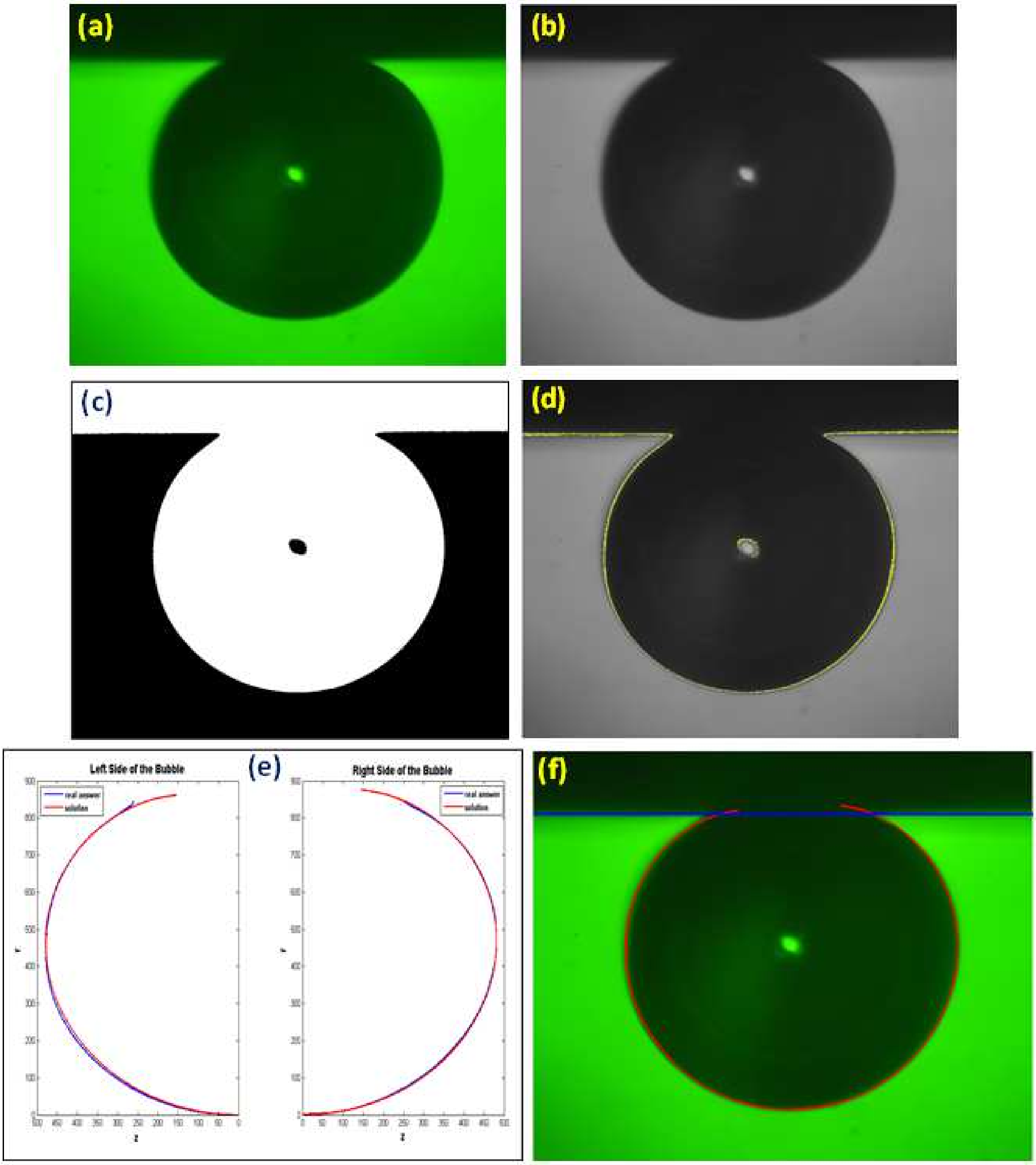

Figure 2.5. The image processing procedure in the MATLAB routine: (a) original cropped digital image, image converted to (b) grayscale, (c) binary image, (d) the bubble and surface outline, (e) description of left and right hand sides of bubble profile with Young–Laplace equation, (f) comparison of calculated profiles with the real image.

2.3.4.1. Sensitivity of the contact angle determination to the image analysis

Images of the bubble are taken and used as input for an image-analysis procedure, which allows determination of the contact angle and surface and interfacial tensions. Therefore, the visualization, i.e. light source, endoscope, camera, the image-evaluation and image-acquisition systems, are the crucial parameters of the experimental setup. In order to obtain reliable values of contact angle, it is important to have high-quality images in which the bubble profile is sharp, in focus and well-lit.

A few factors can cause discrepancies between the real 3-D system of bubble-surface and its 2-D image:

- Alignment of the camera, the endoscope and the rock surface;
- Aperture (field depth sharpness), ISO (image resolution/noise) and shutter speed (light and motion blur) of the camera;
- Light quality (monochromic, parallel);
- Focus point of the endoscope.

The effect of the first three factors can be mitigated by proper adjustment before or during the experimental run. However, the last factor is not easy to control, since most of the bubbles rest at different places on the surface, thus at different distances from the endoscope. As seen in Fig. 2.6, the edge of the rock and the bubble do not have the same distance from the endoscope and camera. Therefore, either the bubble profile or the surface contour is not in focus (Fig. 2.7). If the endoscope focuses on the bubble, the surface is closer to the lens and therefore the rays coming from the surface do not converge at the same place as the rays from the bubble.

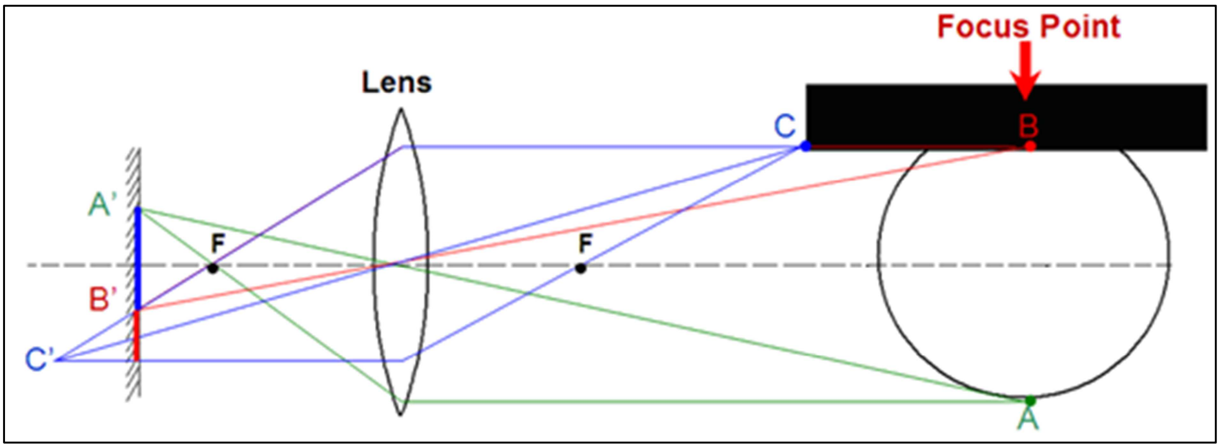

Figure 2.6. Schematic illustrating the capturing of an image of a bubble and the rock surface in the used pendant-drop experimental setup [19]

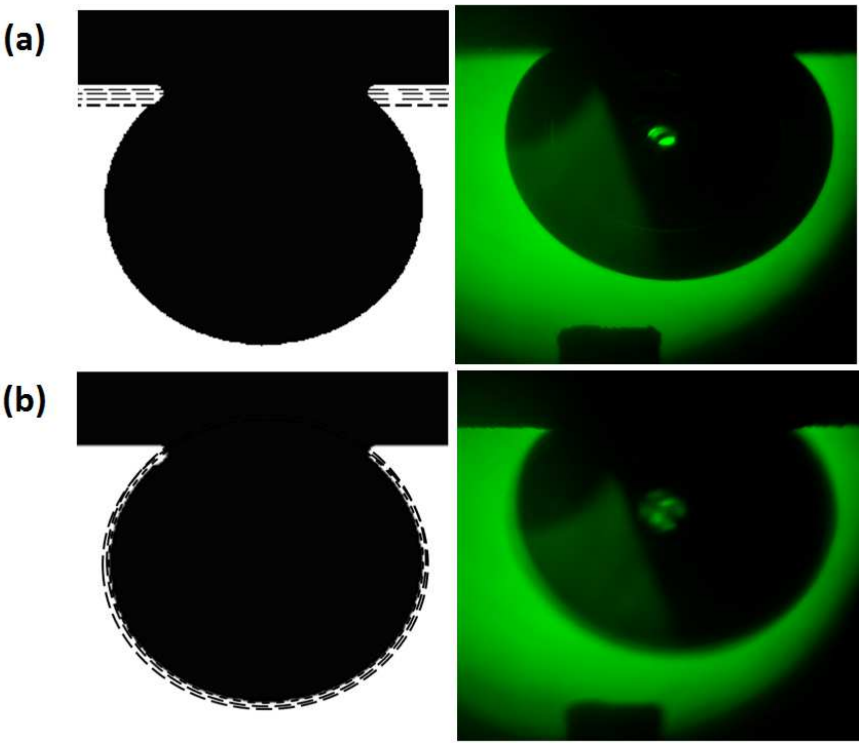

Figure 2.7. Image with focus (a) on the bubble contour and (b) on the surface. The left images are the schematic drawing of the case and the right ones are the digital photos from the system.

Figs. 2.8 (a-f) show images of the same bubble with focus on the bubble (Fig. 2.8 (a)) and the surface (Fig. 2.8(b)). The determined contact angles are given in the images and differ by about 26%. In Figs. 2.8(c) and (d), the positions of a virtual line across the bubble are shown, for which the gray values are given in Figs. 2.8(e) and (f). As can be seen for the image with the bubble in focus, the grey value change at the contour of the bubble is quite sharp and distinct, while for the other image with focus on the edge of the rock slab, the variation is less distinct. As a consequence, it is not possible to detect the “real” contour of the bubble accurately when using a bubble image with focus on the edge of the rock (Fig. 2.8(b)). The way in which the contour was described in the given example (Fig. 2.8(b)) means that the bubble volume is overestimated by about 16.6% and the contact angle by 25.8%. To minimize this error, one should focus on the bubble profile or the needle. However, as the centre of the bubble is not always in line with the centre of the needle, focusing on the needle might also introduce inaccuracies, although less than when focusing on the edge of the rock. From the discussion above, it is clear that images with a sharp bubble contour have a blurry surface, and vice versa. The exact position of the substrate surface and the baseline is a sensitive factor in contact-angle determination. Even a slight displacement of its position can cause variation of the determined contact angle by a few degrees; Fig. 2.9 illustrates this. If the line describing the surface, i.e. the baseline, is shifted parallel by 6 pixels in the direction of the y-axes (each pixel is about 8.47×10^{-2} mm), the contact angle changes from 26° to 24.4°. To avoid systematic errors during various measurements, the baseline should be adjusted separately for each measurement and bubble-shape analysis.

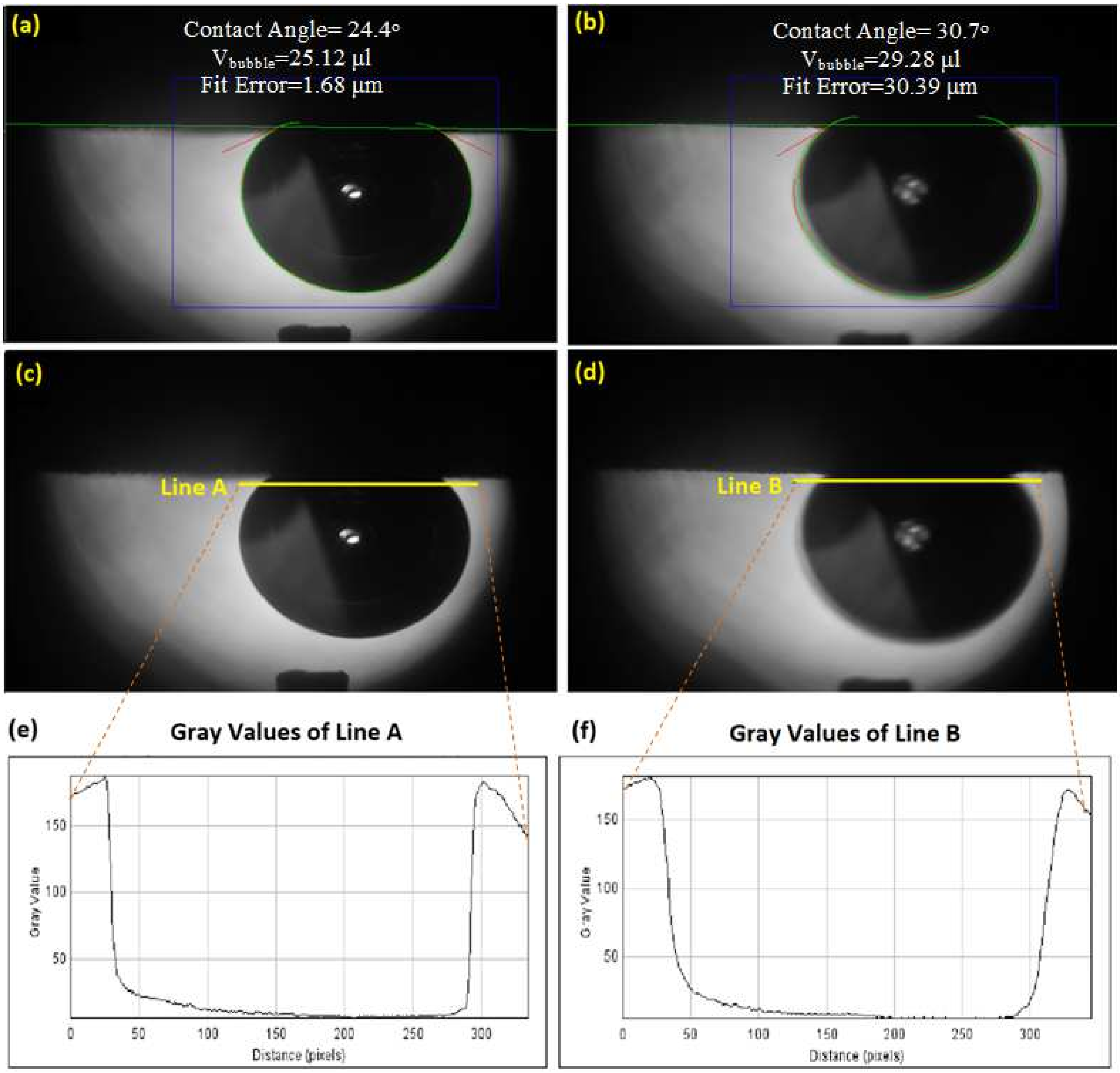

Figure 2.8. The bubble shape and gray values for images with (a, c, e) a sharp bubble contour and (b, d, f) a sharp surface edge. In (e) and (f) the gray values along the yellow lines given in (c) and (d) are displayed.

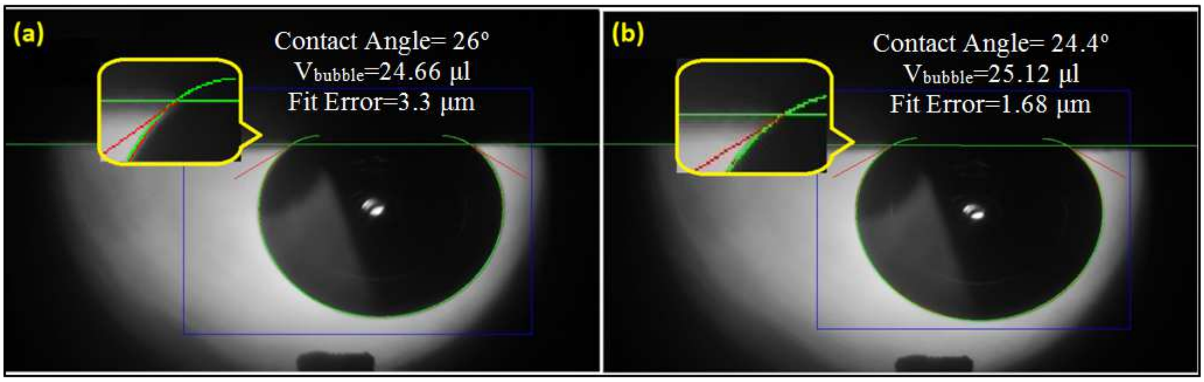

Figure 2.9. Image processing: importance of the baseline (line describing the surface) position on contact-angle determination. In (b), the line is 6 pixels above the line in (a) (parallel shift).

To allow an accurate detection of the baseline, the camera is tilted 1 to 2 degrees upwards (for captive bubbles). The image taken in this manner provides the onset of the mirror image of the bubble profile. Therefore, the baseline can be recognized precisely using the inflection points in the bubble shape which are formed by the transition between the bubble image and its mirror image (Fig. 2.10).

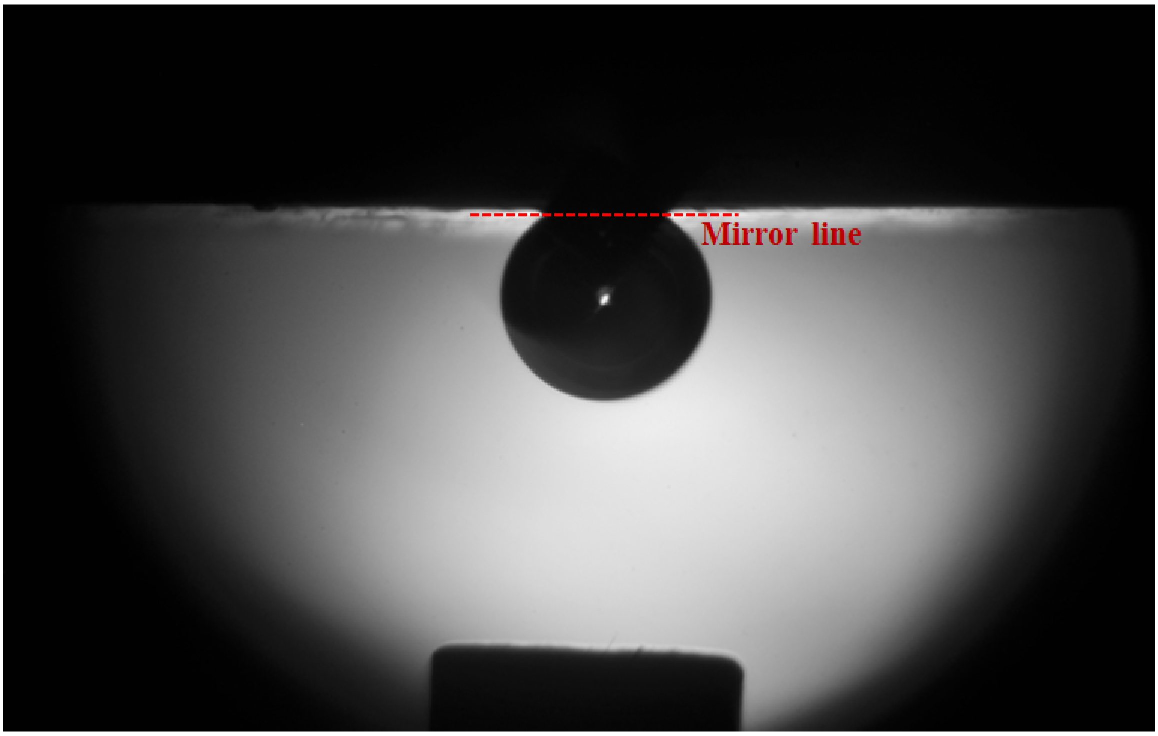

Figure 2.10. The surface detection using the inflection points in the bubble shape

Even with this method, the difficulties in detecting the correct position of the bubble contact with the rock surface in systems with small contact angles (<20°), such as strongly water-wet Bentheimer sandstone, or with large contact angles (>160°) may cause significant errors in the contact-angle determination.

2.4. CONCLUSIONS

- The pendant-drop set-up has been modified for captive-bubble experiments and improved for determination of contact angles and IFTs at high pressures (up to 30 MPa) and elevated temperatures (up to 333 K).

- An accurate procedure of contact-angle determination has been developed in order to minimize the effects of CO_2 dissolution on the wetting properties investigation and changes of the aqueous phase composition.

- Microscopic image analysis prior to the contact-angle experiments allows the characterization of a surface profile from the rock sample. A Leica™ 3D stereo explorer describes the roughness of the surface quantitatively. Based on a surface roughness analysis with a Leica 3D™ microscope, the most proper and smoothest surface can be selected for the contact-angle experiments. This is an improvement in the sample preparation quality, in order to minimize the effect of surface roughness and hysteresis.

- A revised experimental pendant-drop procedure in combination with a drop-shape analysis program allows accurate determination of IFTs and contact angles.

REFERENCES

[1] E. Amott, Observations Relating to the Wettability of Porous Rock., Trans. AIME 216 (1959) 156-162.

[2] E.C. Donaldson, R.D. Thomas, P.B. Lorenz, Wettability Determination and Its Effect on Recovery Efficiency, 9 (1969) 13-20.

[3] W.G. Anderson, Wettability Literature Survey-Part 2: Wettability Measurement, J. Pet. Technol., 37 (1986) 1246-1262.

[4] W.G. Anderson, Wettability Literature Survey- Part 2: Wettability Measurement, SPE Journal of Petroleum Technology, 38 (1986) 1246-1262.

[5] A.W. Neumann, R. David, Y. Zuo, Applied surface thermodynamics, in, CRC Press, 2011.

[6] P. Chiquet, D. Broseta, S. Thibeau, Wettability alteration of caprock minerals by carbon dioxide, Geofluids, 7 (2007) 112-122.

[7] J. Drelich, J.D. Miller, R.J. Good, The Effect of Drop (Bubble) Size on Advancing and Receding Contact Angles for Heterogeneous and Rough Solid Surfaces as Observed with Sessile-Drop and Captive-Bubble Techniques, Journal of Colloid and Interface Science, 179 (1996) 37-50.

[8] N. Shojai Kaveh, E.S.J. Rudolph, K.-H.A.A. Wolf, S.N. Ashrafizadeh, Wettability determination by contact angle measurements: hvbB coal–water system with injection of synthetic flue gas and CO_2, Journal of Colloid and Interface Science, 364 (2011) 237-247.

[9] N. Siemons, H. Bruining, H. Castelijns, K.-H. Wolf, Pressure dependence of the contact angle in a CO_2–H_2O–coal system, Journal of Colloid and Interface Science, 297 (2006) 755-761.

[10] D. Yang, P. Tontiwachwuthikul, Y. Gu, Dynamic Interfacial Tension Method for Measuring Gas Diffusion Coefficient and Interface Mass Transfer Coefficient in a Liquid, Industrial & Engineering Chemistry Research, 45 (2006) 4999-5008.

[11] N. Shojai Kaveh, K.H. Wolf, S.N. Ashrafizadeh, E.S.J. Rudolph, Effect of coal petrology and pressure on wetting properties of wet coal for CO_2 and flue gas storage, International Journal of Greenhouse Gas Control, 11 (2012) S91-S101.

[12] N. Shojaikaveh, c. berentsen, S.E.J. Rudolph-Floter, K.H. Wolf, W.R. Rossen, Wettability Determination by Equilibrium Contact Angle Measurements: Reservoir Rock- Connate Water System With Injection of CO_2, in: SPE Europec/EAGE Annual Conference, Society of Petroleum Engineers, Copenhagen, Denmark, 2012.

[13] R.J.M. Huijgens, The influence of interfacial tension on nitrogen flooding, in: Geotechnology, delft University of Technology, Delft, 1994.

[14] W. Wagner, R. Span, Special Equations of State for Methane, Argon, and Nitrogen for the Temperature Range from 270 to 350 K at Pressures up to 30 MPa, International Journal of Thermophysics, 14 (1993) 699-725.

[15] G.-S. Shyu, N.S.M. Hanif, K.R. Hall, P.T. Eubank, Carbon dioxide-water phase equilibria results from the Wong-Sandler combining rules, Fluid Phase Equilibria, 130 (1997) 73-85.

[16] R. Span, W. Wagner, A New Equation of State for Carbon Dioxide Covering the Fluid Region from the Triple-Point Temperature to 1100 K at Pressures up to 800 MPa, Journal of Physical and Chemical Reference Data, 25 (1996) 1509-1596.

[17] B. Song, J. Springer, Determination of Interfacial Tension from the Profile of a Pendant Drop Using Computer-Aided Image Processing: 1. Theoretical, Journal of Colloid and Interface Science, 184 (1996) 64-76.

[18] S.R. Stock, MicroComputed tomography : methodology and applications Taylor & Francis Group, LLC, 2009.

[19] A. Delavarmoghaddam, A new method for determination of contact angle of captive bubbles, in: Geotechnology Department, Delft University of Technology, Delft, 2009.

CHAPTER 3

Contact-Angle Determination of Wet Coal System with Synthetic Flue gas and CO_2*

ABSTRACT

The injection of carbon dioxide (CO_2) or flue gas into coal layers enhances coal-bed methane production (ECBM) and offers an option for CO_2 storage. The success of this process depends on different factors; among them wetting behavior of the coal plays an important role, which is a function of coal rank, ash content, heterogeneity of the coal surface, pressure, temperature and composition of the gas.

The wetting behavior can be evaluated from the contact angle of a gas bubble, CO_2 or flue gas, on a coal surface. In this chapter, contact angles of a synthetic flue gas, i.e. a 80/20 (mol%) N_2/CO_2 mixture and pure CO_2 on wet coal samples have been determined using a modified pendant-drop cell in a pressure range from 0.1 to 16 MPa and a constant temperature of 318 K. Two coal samples with similar vitrinite content were used, representing different coal ranks, a Selar Cornish (SC), as a semi-anthracite high rank coal and a Warndt Luisenthal (WL), as a high volatile bituminous (hvBb) medium-rank coal.

It was found that the contact angles of flue gas on the high volatile bituminous Warndt Luisenthal coal were generally smaller than those of CO_2. The contact angle of CO_2 changes from water-wet to gas-wet by increasing pressure above 8.5 MPa while the one for the flue gas changes from water-wet to intermediate-wet by increasing pressure above 10 MPa.

For the semi-anthracite Selar Cornish sample, the wettability alteration from intermediate-wet to gas-wet with CO_2 injection was observed at pressures above 5.7 MPa. Experimental results with synthetic flue gas revealed that the Selar Cornish coal is intermediate-wet at all pressures, and the contact angle slightly increases with increasing pressure.

Comparison between high rank (semi-anthracite) and medium (high volatile bituminous (hvBb)) coals confirms that hydrophobicity increases with the coal rank for samples with a similar bulk mineral content. The results of the contact angle experiments are input parameters for field-scale reservoir modeling.

KEYWORDS: CO_2; flue gas; storage; ECBM; wettability; contact angle; high volatile bituminous coal; semi-anthracite coal.

---

[*] ***Published in:***

- *International Journal of Greenhouse Gas Control, 11, Supplement (2012) S91-S101.*
- *Journal of Colloid and Interface Science, 364 (2011) 237-247.*

3.1. INTRODUCTION

3.1.1. CCS AND CBM

Laboratory studies as well as recent pilot field tests [1-7] demonstrate that CO_2 injection has the potential to enhance methane production from coal seams. The injection of carbon dioxide (CO_2), or possibly flue gas, into coal layers would allow to enhance the coal bed methane production (ECBM) as well as to store CO_2. Injection of CO_2 into coal reservoirs has enhanced the methane recovery up to 90% of the gas-initial-in place while conventional methods recover only about 50% by reservoir-pressure depletion [8].

Power plants are one of the major sources of CO_2 emission. The emitted flue gases mainly consist of nitrogen and CO_2 (see Table 3.1) [9]. For depleted gas reservoirs and aquifers, CO_2 is separated from the flue gas prior to its injection for storage; this makes the process less energy efficient. Direct injection of flue gas would eliminate the necessity of separation of the flue gas streams prior to the injection into the coal bed. This process would be interesting and economically favorable only if the flue gas injected into the coal seams is stripped; i.e. CO_2 and toxic contaminants get adsorbed at the coal surface while nitrogen and methane are produced. The subsequent separation of CH_4 and N_2 from the produced gas is considered as a challenge from the energy and technical points of view due to their similar behavior and physicochemical properties. Applicable separation technologies for this kind of gas mixtures are cryogenic distillation, membrane and PSA (pressure swing adsorption) [10]. Injection of flue gas (87.5% N_2 and 12.5% CO_2) in a micro-pilot in Alberta, Canada, showed an increase in injectivity [6]. However, the injection of flue gas causes the displacement of CO_2 by N_2 [11], early breakthrough of the nitrogen [12], and contamination of the methane-production stream. To implement this method in the field scale, the interactions between coal and flue gas, i.e. adsorption, swelling and wettability, need to be investigated in detail [13].

Table 3.1. Generic flue gas composition [9]

Components	Composition (mol%)
N_2	73.974
CO_2	10.9
O_2	3.00
CO	0.01
SO_2	0.106
H_2	9.0
CH_4	3.01

According to White [14], the global CBM resources are about 48% to 148% of the current global CH_4 reserves. As usually less than 60% of the original methane present in the coal beds is produced by primary recovery methods, there is considerable interest in enhancing the methane recovery by means of gas injection [2, 5]. Assuming that 50% of the global coal-bed methane resources can be produced, the proven global methane reserves would increase from 177 Tm^3 to 210-308 Tm^3 (+19 to 74%). Depending on the estimation, the CO_2 volume produced in a period between 10 to 33 years could be stored in all CBM reservoirs worldwide [14].

With injection of CO_2 into the coal seams, methane can be replaced by CO_2, since coal has a preferential sorption of CO_2 over methane, and consequently coal-bed methane recovery is enhanced. CO_2 injected into the reservoir flows through the cleat system, diffuses into the coal matrix and is sorbed by the coal micropore surfaces. As a consequence, gases with a lower affinity to coal,e.g., methane, are released [15]. Furthermore, when CO_2 is sorbed by the coal, the coal swells. The latter reduces the permeability and the injectivity by an order of a magnitude or more [16]. This effect might be counteracted by increasing the injection pressure [17]. CO_2 has been injected successfully in the Alberta Basin in Canada and in the Allison project at depths where the pressure is greater than the critical pressure of CO_2 [7].

3.1.2. COAL WETTING PROPERTIES

Coal-bed methane (CBM) is largely controlled by the interactions among CO_2, the reservoir fluid, the coal matrix and the ash. The success of this combined process depends on different parameters. One of these factors is CO_2-wetting behavior of the coal, which is a function of coal rank, ash content, heterogeneity of the coal surface, pressure, temperature, and composition of the gas [18, 19]. The maturity level of coal, which indicates the degree of coalification of the organic matter, is known as rank parameter and is estimated by measuring the moisture content, specific energy, and reflectance of vitrinite or volatile matter. Low-rank coal is usually distinguished by the calorific heating value and water content, whereas higher-rank coals are characterized by means of vitrinite reflectance, fixed carbon content and volatile matter content [20].

Coal mostly consists of inorganic minerals and organic macerals. Arnold and Aplan [21] found the biggest difference in the wetting behavior of the coal is between hydrophilic inorganic mineral inclusions and hydrophobic organic macerals. Furthermore, coal has a network of cleats and a matrix pore system ranging from macro pores (>50 nm) to meso pores (from 2 to 50 nm), micropores (from 0.4 to 2 nm) and the sub-micro pores (< 0.4 nm). This widely used pore-size classification, which was proposed by Dubinin (1960), was later accepted by IUPAC (International Union of Pure and Applied Chemistry) [20, 22]. The matrix blocks between the smallest cleat system have diameters of a few tens of microns [23]. In the large cleats, the main flow of the fluid occurs according to Darcy’s law. Diffusion-driven transport becomes increasingly more important in the denser network of micro-cleats. For a hydrophobic coal (gas-wet), it is expected that the micro-cleats are filled with gas, leading to a faster transport of the injected gas to the coal matrix than for a hydrophilic coal (diffusion coefficient of CO_2 in gas is about 1.7×10^{-7} m^2/s and independent of pressure [24]). For a hydrophilic (water-wet) coal, the micro-cleats are filled with water. In this case, the transport of the injected gas to the rock surface is limited by the diffusion of the gas through the aqueous phase. This leads to a slower transport of the injected gas within the coal matrix and micro-cleats network (the diffusion coefficient of CO_2 in water is 2×10^{-9} m^2/s at 10 MPa and 298 K [24]).

The wetting properties of coal play a critical role not only in CO_2 storage processes, but also in coal preparation and utilization processes, viz. froth flotation, oil agglomeration, dust abatement, and preparation of coal-water slurries [21, 25, 26]. Because of the heterogeneous structure of coal, at both macroscopic and microscopic levels, the results of wettability studies on coal surfaces change from sample to sample, even where the samples originate from the same block. Therefore, often a distribution of contact angles is provided instead of reporting one averaged contact angle [27]. It is also believed that the wettability of coal changes as a function of several parameters including the coal rank [28], chemical composition [29-31], mineral matter content [32-34], moisture level [35], porosity [36, 37], degree of oxidation [29, 31, 38, 39], and the pressure and temperature of the reservoir as well as the composition of the reservoir fluids [18, 19]. In addition, chemical heterogeneity due to the presence of different characteristic groups of components affect wetting behaviour. The presence of paraffinic hydrocarbons results in a strongly hydrophobic behaviour, aromatic hydrocarbons an intermediate-wet behaviour, and mineral components a strongly water-wet behaviour [37].

Previous studies, which concentrate on the wetting behavior of coal-water-air systems at atmospheric pressure using contact-angle measurements, revealed that dry coal is naturally hydrophobic [28, 39]. Its hydrophobicity varies from one sample to another because of variations in the composition of the coal, particularly in the coal rank. Coals become increasingly hydrophobic with increasing rank [28, 39, 40]. A comparative study of contact-angle experiments of air bubbles and droplets of either oil, flocculant or coagulant on flat polished coal surfaces immersed in water were carried out by Orumwens [41]. The experiments show a positive correlation between hydrophobicity and coal rank of vitrinite-rich coals. It can be concluded that the hydrophobicity of coal decreases with decreasing of fixed and total carbon content.

Gutierrez-Rodriguez et al. [28, 39] found that the hydrophobicity of a wide variety of coals decreases with decreasing rank, fixed carbon,and total carbon content, and with increasing oxygen and hydroxyl contents. Findings by Sakurovs and Lavrencic [40] also confirmed that coals become increasingly CO_2-wet with increasing pressure (gas density), and consequently, the penetration rate of CO_2 into the coal increases rapidly. Furthermore, they found that coals with high rank, low ash yield, or both were preferentially CO_2-wet at high pressures. However, coals with a high ash and high oxygen contents do not become CO_2-wet, even at high pressures. Comparison of a vitrinite-rich with a vitrinite-poor coal revealed that the growing of the contact angle with the pressure is more pronounced for a vitrinite-rich coal [40].

Murata (1981) performed contact-angle measurements on pressed pellets of pulverized coal at atmoshperic pressure. He concluded that the contact angles depend on the hydrogen and oxygen content of the coal.

Keller (1987) summarized the literature [25, 28, 39, 42] on surface properties of coal-water-air systems. Chi et al. (1988) found that the contact angle in a CO_2-water-coal system increases with pressure in the range from atmospheric up to 6.2 MPa. Additionally, it was observed that when the ash content increases, the coal becomes more water wet.

According to the literature [32, 33], the contact angle decreases with increasing mineral-matter content in the coal. Gosiewska et al. (2002) found that increasing the amount of mineral matter in the coal samples reduces the contact angle. The fact that the results are scattered implies that other factors may also be responsible for the variations, e.g. the size of the hydrophilic mineral inclusions [43].

So far, few experimental data have been reported on the wettability of different ranks of coals in the presence of CO_2 at high pressures and elevated temperatures [18, 40, 44, 45]. Furthurmore, there are no experimental data available on the wettability of coal against flue gas at high pressures. Siemons performed contact angle experiments by means of a modified pendant drop cell on two different ranks of wet coal using supercritical CO_2 at a temperature of 318 K and pressures ranging from 0.1 up to 12 MPa [20]. From these data, it can be concluded that for high-rank coals wetting alteration from water-wet to CO_2-wet occurs at a pressure as low as 0.27 MPa. For a medium-rank coal, this wetting alteration is observed for pressures above 8.7 MPa. It needs to be mentioned that during these experiments the water was not fully saturated with CO_2 and thus the composition of the aqueous phase varied with each experiment.

In this chapter, two coal samples have been used representing different ranks. The wettability behaviour of the wet coal samples against synthetic flue gas (20 mol% CO_2/ 80 mol% N_2) and pure CO_2 was investigated by means of contact-angle experiments. The experiments were carried out in a modified pendant-drop cell at a constant temperature of 318 K and pressures varying between 0.1 up to 16 MPa. The chosen pressures and temperature are representative for typical in-situ conditions [46]. The experiments were performed with an aqueous phase fully saturated with CO_2, in order to minimize the effect of dissolution of CO_2 and consequently changing the composition and properties of the aqueous phase during the experiment. In this work the effect of the coal composition on contact angle has not been studied and only the results of a high-rank coal have been compared to the results of a medium-rank coal. Micro CT images of the coal samples were taken to identify the distribution of the mineral content on the surface. The mineral matter content on the surface of the used coal samples was too low to allow a conclusive interpretation on its infuence in the wetting behavior. Furthermore, local effects of the variation of the maceral composition of the samples have not been investigated.

3.2. EXPERIMENTAL

3.2.1. COAL SAMPLES

Two coal samples with similar vitrinite content were used in this study, representing different coal ranks, a Selar Cornish (SC), as a semi-anthracite high-rank coal and a Warndt Luisenthal (WL), as a high volatile bituminous (hvBb) medium-rank coal. The Warndt Luisenthal samples were mined from the intra-mountain Saar basin in Western Germany and the Selar Cornish samples originate from the Selar colliery in South Wales Coalfield. Both samples were cored in the same direction and parallel to the bedding plane. The abbreviations SC and WL are respectively used to describe the experimental data for these coal samples. The results of the ultimate and proximate analysis of the coal samples are given in Table 3.2.

3.2.2. SAMPLE PREPARATION

For the contact-angle experiments, ten coal samples were prepared with dimensions of $30\times12\times6$ mm^3. The samples were drilled and cut from a larger coal block (> 0.25 m^3). The interpretation and the data processing of contact-angle measurements on coal surfaces is very critical due to the occurrence of surface oxidation, surface roughness, and chemical heterogenity [28, 37, 39]. In order to eliminate the effect of some systematic errors on the results, all blocks were treated in the same manner. First, the smoothest side of the coal sample was identified. The rougher side was then immersed in an epoxy solution, to be coated with a layer of epoxy, to increase the stability of the sample. This side of the substrate was not used for the contact-angle measurements. The other side of the sample (smoother) was appropriately polished and prepared according to the procedure of Drehlich et al. [47]. The coal samples were wet-polished with a series of abrasive papers with a grid ranging from 60 to 1200 µm, followed by polishing with 0.5 µm abrasive alumina powders and a fibrous cloth. Polishing was terminated with water rinsing and ultrasonic cleaning.

After preparation, 2-D and 3-D microscopic surface images were then taken from the samples to determine the surface roughness (LEICA 3D stereo explorer). Moreover, a Phoenix Nanotom scanner was used to determine the mineral matter distribution in the coal samples at the micro-level (Chapter 2).

As the final step of sample preparation, the coal samples were equilibrated at a relative humidity of 96 to 97% and a temperature of 303 K for at least 48 h (ASTM standard D 1412) to establish a water saturation representative of the reservoir conditions.

Table 3.2. *Proximate and ultimate analysis and coal petrology of coal samples used [20]*

Sample	Warndt Luisenthal	Selar Cornish
Rank	hvBb	Semi anthracite
R_{max} (%)	0.71	2.41
Vitrinite (%)	74.40	73.60
Liptinite (%)	15.60	0.00
Inertinite (%)	9.00	24.60
Minerals (%)	1.00	1.80
Volatile Matter (w.f.) (%)	40.50	10.40
Carbon (wt%)	81.30	85.70
Hydrogen (%)	5.58	3.36
Nitrogen (%)	1.88	1.56
Sulfur (%)	0.69	0.68
Oxygen (%)	5.47	5.58
H/C	0.82	0.47
O/C	0.05	0.05
Ash (w.f.) [%]	2.77	3.94-5.50
Fixed Carbon (d.a.f.) [%]	58.36	89.27

3.2.3. EXPERIMENTAL PROCEDURE

The experiments were conducted in a modified pendant-drop cell (PDC), which was adapted to allow captive-bubble contact-angle determination on real coal surfaces. The experiments were performed in a pressure range from 0.1 to 16 MPa and a constant temperature of 318 K. The coal sample was positioned inside the cell using a specially designed holder (Fig. 3.1). The detailed description of the experimental setup and procedure can be found in Chapter 2.

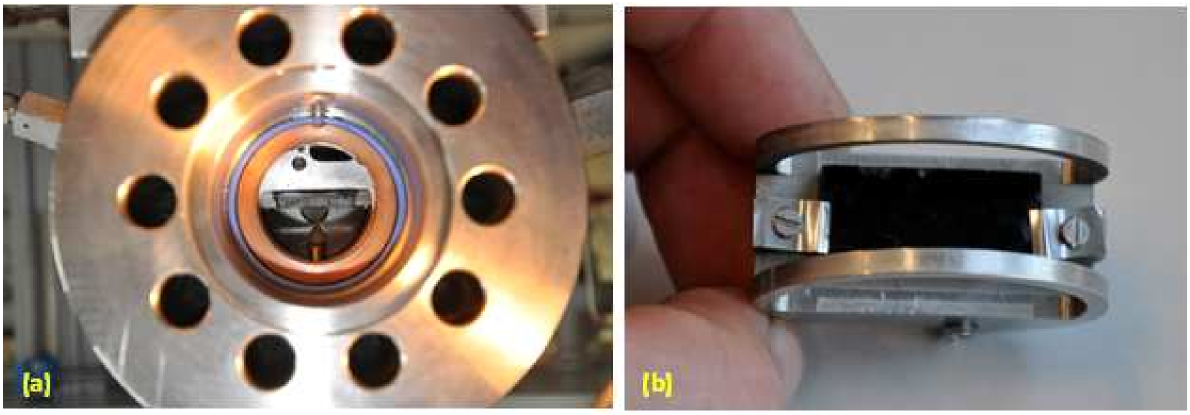

Figure 3.1. (a) side view of the pendant drop cell, (b) top view of the sample holder with a coal substrate.

3.2.4. DATA INTERPRETATION

In this study to allow comparison of contact angles at different pressures not only the contact angle but also the dimensionless radius of the bubble is given. The dimensionless radius is computed by normalizing all radii by the maximum bubble radius of this particular experimental run.

In this chapter I distinguish between a ‘non-stable contact angle’ and a ‘stable contact angle’. Initially, the contact angle changes with time until it reaches a constant value. A contact angle varying with time is called a ‘non-stable contact angle’; the final, constant value represents the ‘stable contact angle’. The non-stable contact angles show the effect of (aging) time, roughness and surface heterogeneity.

Releasing a gas bubble into the pre-saturated aqueous phase causes some disturbance which can initially be recognized by a change in the contact angle with time (more details provided in Chapter 4, section 4.4.3). When introducing a bubble of pure CO_2 or of the synthetic flue gas, there is mass transfer from the gas bubble to the aqueous phase and vice versa [48]. The driving force for this process is the difference in chemical potential of each specific component in the different phases. The time required to reach a stable value depends, e.g., on the concentration gradient of the phases (gas and liquid).

Because of the continuous change in the composition of the gas and liquid phases until the equilibrium has been reached, the bubble size and, consequently, the contact angle change. In this chapter the aging time is defined as the time required reaching a stable contact angle after introducing the gas bubble. It is assumed that stability is reached when the change in contact angle is less than that of the standard error of all values of an experimental run per 30 minutes.

3.3. IMAGE ANALYSIS

3.3.1. MICROSCOPIC IMAGE ANALYSIS

For the contact-angle experiments, it is of vital importance to have a coal sample with a very smooth surface. Prior to the contact angle experiments and after preparation of the sample blocks, 2-D and 3-D microscopic images were taken from the coal surfaces. From these images, profiles can be extracted allowing determination of the surface roughness. To identify the surface smoothness quality, a Leica 3D Stereo Explorer was used to determine the Cartesian surface values. The characterization of the surface is based on the so-called P_a factor, which is calculated according to the international standard of EN ISO 4287. A detailed description on determination of P_a value is given in Chapter 2.

The P_a factors determined for the smoothest samples of SC and WL coal surfaces before the experiments were 0.011 and 0.018 mm, respectively. After the contact-angle experiments, these values increased to 0.014 and 0.027 mm, respectively. In other words, the surface became rougher during the experiments. This increase in roughness is most likely due to the coal swelling and differential volume changes between coal and mineral matter [49] and/or dissolution of minerals. In addition, fast pressure reduction may cause matrix damage and, consequently, surface damage due to the fast escape of CO_2.

Figs. 3.2 (a) and (c) illustrate the perpendicular view of the WL substrate surface before and after the experiment, respectively. The different grey shades indicate the chemical heterogeneity and the ash content. The 3D side views of the WL substrate surface before and after the experiment are shown in Figs. 3.2 (b) and (d), respectively. From these pictures it can be observed that the cleats in the coal surface have become bigger after the experiment. This is mainly accounted to the swelling of coal due to diffusion of CO_2 into the coal matrix and differential volume changes between coal and mineral matter during the experiments.

Figs. 3.3 (a)-(d) show the side views of the SC and WL substrate surfaces before and after the experiment. As it can be seen, the surface of the WL substrate (Fig. 3a) is rougher than that of the SC sample (Fig. 3b) and became still rougher after the experiments (Figs. 3c and d).

Note: The surface reconstruction of the contact planes were conducted with the Leica Stereo Explorer directly after the experiments. Sometimes this gives spikes that are attributed to unwanted reflection of the water coming from the matrix.

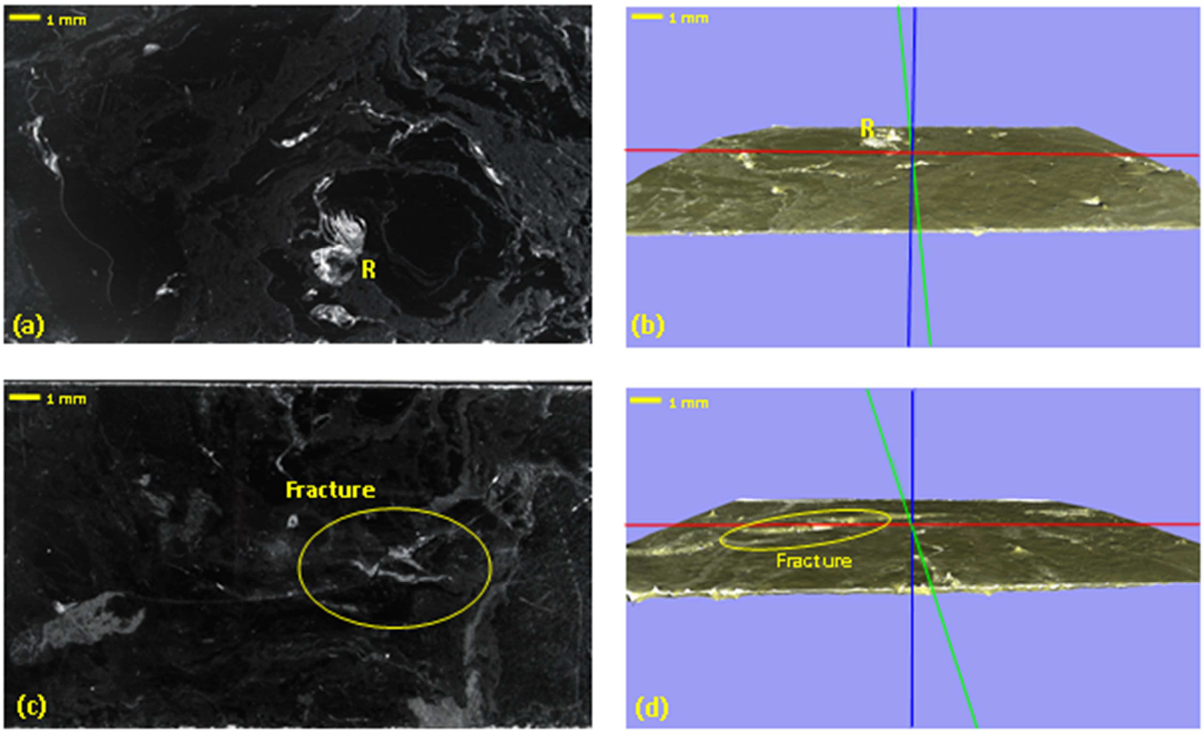

Figure 3.2. (a) Perpendicular view and (b) 3-D side view of the WL sample surface before experiments; (c) perpendicular view and (d) 3-D view of the WL sample surface after experiments. These images are taken from the same sample with a LEICA 3D stereo explorer. Point R is an artifact as a result of reflection. The blue, red and green lines give the orthogonal x, y, z directions used for determination of the P_a factor.

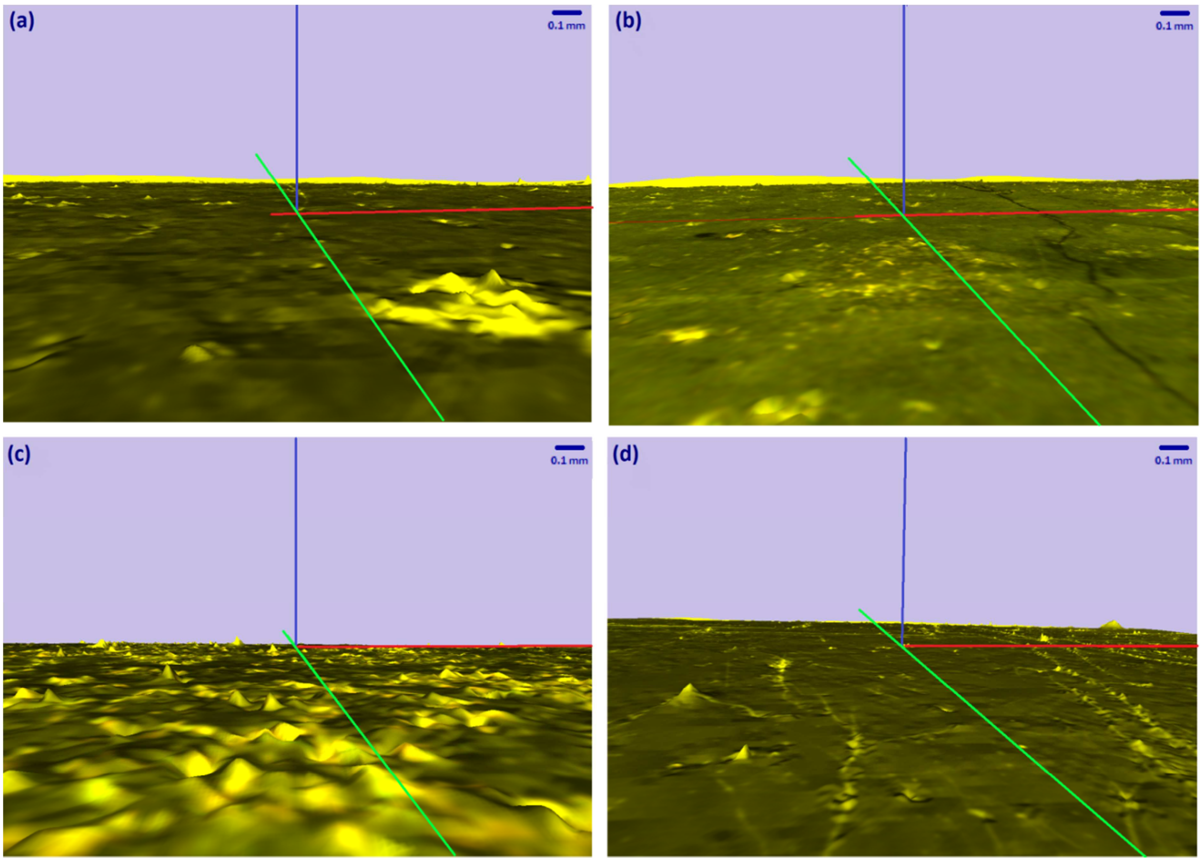

Figure 3.3. 3-D side view of the surface of (a) WL sample and (b) SC sample before the experiments and (c) WL sample and (d) SC sample after the experiments.

3.3.2. MICRO CT-SCAN

The mineral matter distribution in the coal samples at the micro level was determined by means of a Phoenix Nanotom™ micro CT scanner based on the density differences in the coal samples (180 kV / 15 W nanofocus computed tomography (nano CT) system). 2-D sections through the WL and SC reconstructed CT images after the experiments show the heavier minerals as red areas and the fracture network and cracks as blue areas; the green shades represent the coal matrix (Fig. 3.4). In this chapter, for clarification purposes, the original coal part represented by grey scales was replaced by green shades. This was only for visualization purposes and not for quantification. Meanwhile direct comparison between the green shades of two different images was not possible, because a different grey-scale calibrations were used for different images. The side of the samples coated with a stabilizing epoxy layer shows ellipse-shaped voids of various sizes.

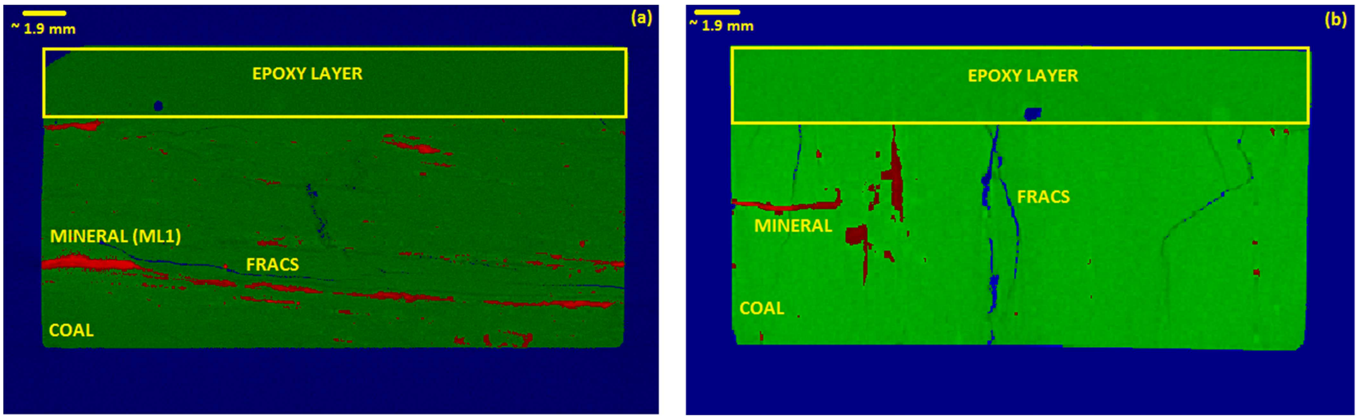

Figure 3.4. Side view of the (a) WL and (b) SC sample after the experiment, using a Phoenix Nanotom micro CT-scanner. The images have a 10µm resolution.

The distribution of mineral matter on the samples and contact surfaces is shown in Fig. 3.5. Although the mineral content of the used WL substrate is higher than the one of the used SC substrate (Figs. 3.5 (a) and (b)), it should be mentioned that it cannot explain differences in the wetting behavior of these two different kinds of coal. In order to examine the influence of the mineral content on the wetting behavior, the mineral content of the surface, on which the bubble sits, needs to be compared (Figs. 3.5 (c) and (d)). However, the analyses of the mineral-matter content of both contact surfaces shows that there are no considerable differences.

The spatial distributions of voids before and after experiments (Fig. 3.6) clearly show that a fracture pattern, comparable to a face/butt-cleat type of system, developed in the SC-sample (Figs. 3.6 (a) and (b)). The medium rank WL coal shows that the void volume increases sub-parallel to the coal layering (Figs. 3.6 (c) and (d)).

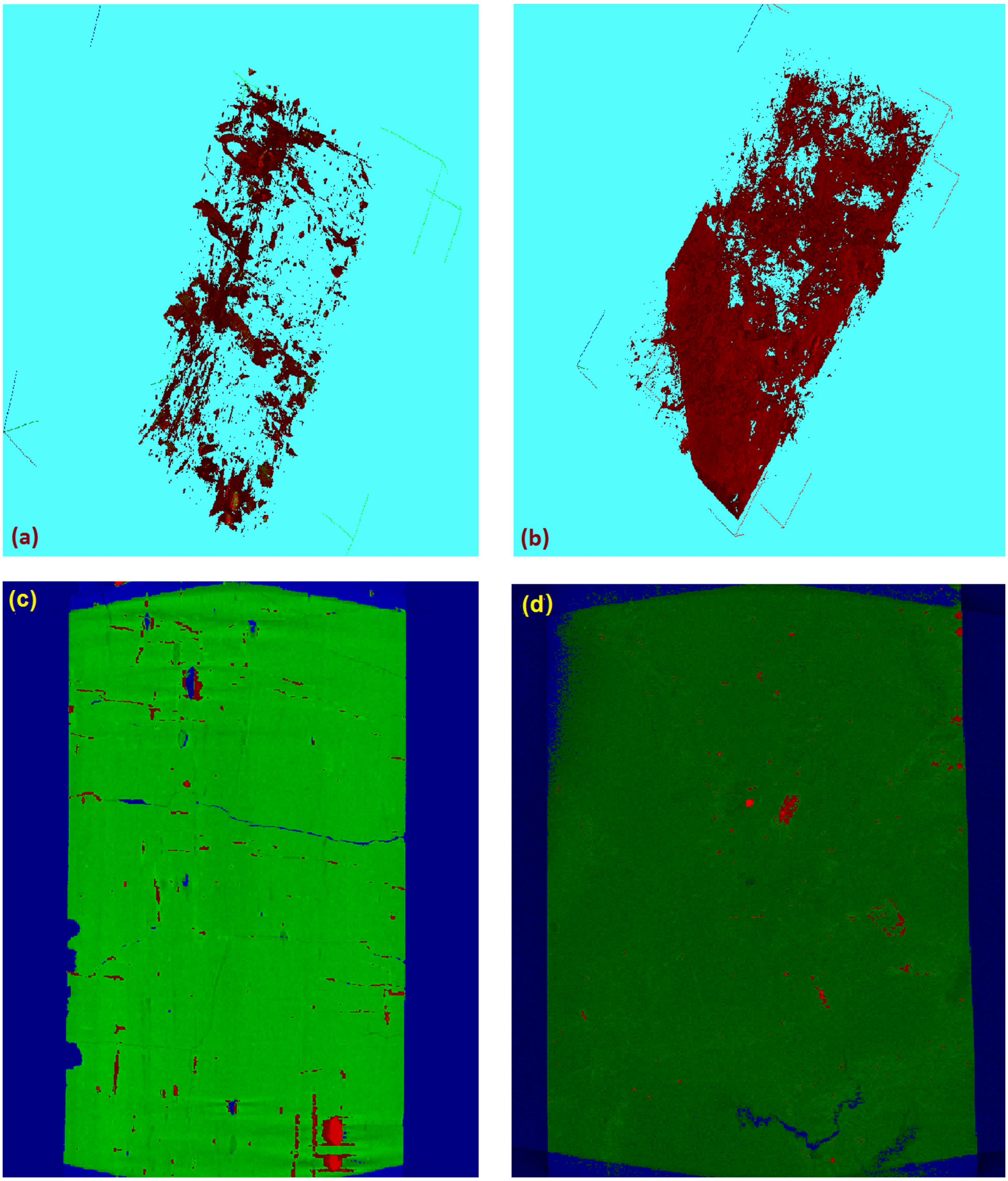

Figure 3.5. Distribution of mineral-matter content determined with the micro-CT scanner: (a) 3-D view of the SC sample, (b) 3-D view of the WL samples, (c) 2-D view of the SC contact surface, and (d) 2-D view of the WL contact surface. The red areas show the heavier minerals (i.e. silicates, carbonates, oxides, etc.) and blue areas show cracks.

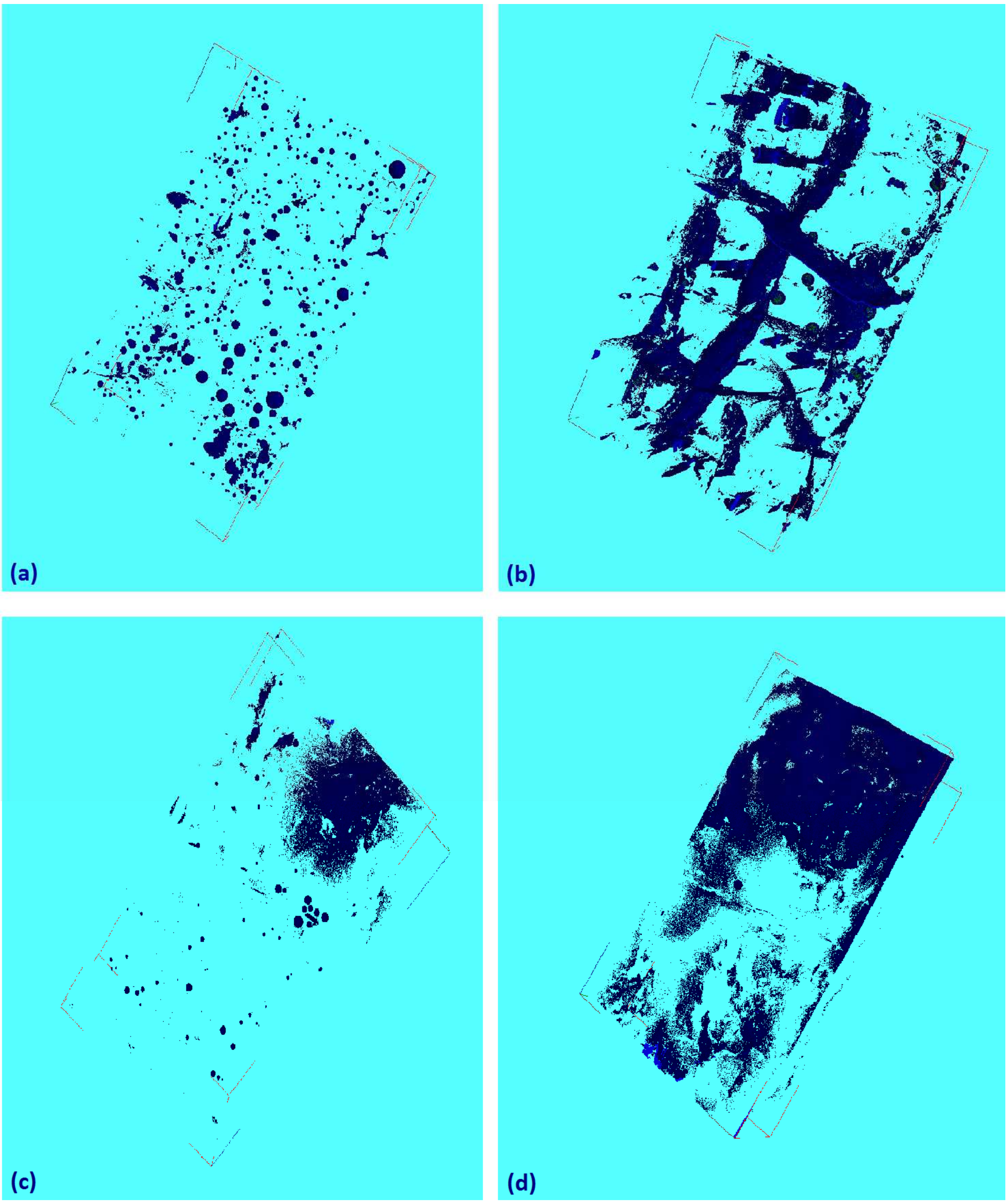

Figure 3.6. Three-dimensional view of the void distribution (dark blue) in (a) SC sample before the experiment, (b) SC sample after the experiment, (c) WL sample before the experiment and (d) WL sample after the experiment. Note that all obvious elliptic bubbles are in the epoxy. The resolution is 10μm.

3.4. RESULTS AND DISCUSSIONS

3.4.1. EFFECT OF TIME ON CONTACT ANGLE

Figs. 3.7- 3.9 show the contact angles and dimensionless radius of either the CO_2 or the synthetic flue gas bubble versus logarithm of time on a Warndt Luisenthal coal at a temperature of 318 K.

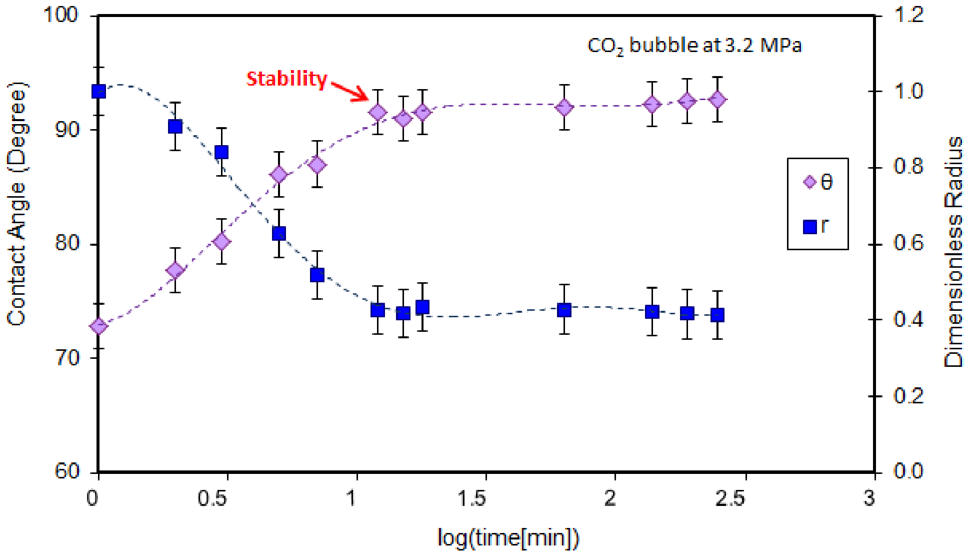

Figure 3.7. CO_2 contact angle (Θ) and dimensionless radius (r) as a function of time at 318 K and 3.2 MPa; Aging time=11 min. The lines are drawn to guide the eye.

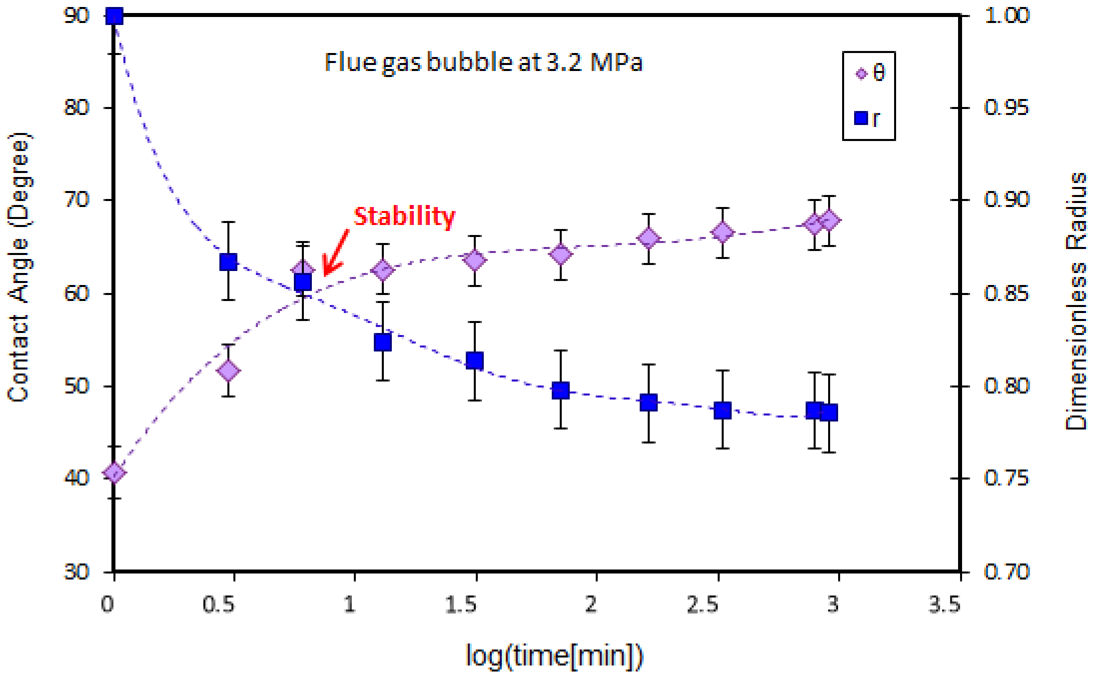

Figure 3.8. Synthetic flue gas contact angle (Θ) and dimensionless radius (r) as a function of time at 318 K and 3.2 MPa; Aging time=4 min. The lines are drawn to guide the eye.

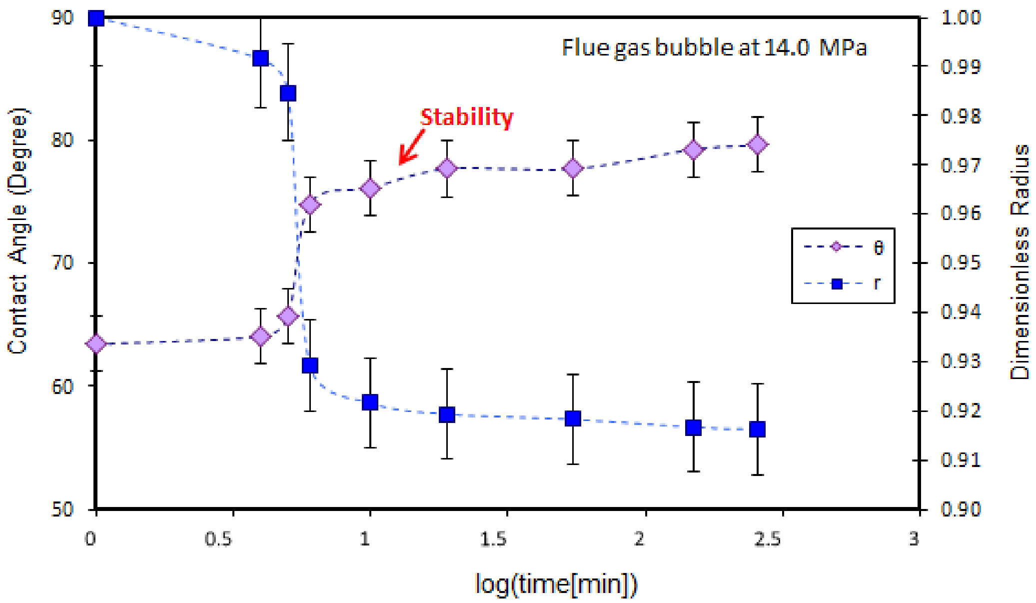

Figure 3.9. Synthetic flue gas contact angle (Θ) and dimensionless radius (r) as a function of time at 318 K and 14.0 MPa; Aging time=14 min. The lines are drawn to guide the eye.

The contact angle of a CO_2 bubble at 3.2 MPa and 318 K increases with time before it becomes stable after about 11 min at a value of 91°. In particular, shortly after the bubble has been released, the non-stable contact angle fluctuates (Fig. 3.7). This can be explained by the two parallel mass transfer processes; CO_2 transfers from the bubble into the liquid phase and water from the liquid phase into the gas bubble. The latter process induces an increase in the density of the gas bubble. This further causes a decrease in the bubble volume; which was observed during the experiments. Yang et al. [48] observed a similar phenomenon. They did similar experiments with CO_2 and carbonate rock samples, which is described as being intermediate-wet and having been drilled from the Weyburn oil reservoir. According to Yang et al. [48], the volume reduction of the bubble was not solely due to the mass transfer as described above, but also partly due to imbibition and sorption of CO_2 on the rock surface; in this case a carbonate [48]. In order to figure out whether these processes occurred during the current study, microscopic images of the coal surfaces were taken before and after the experiments (Fig. 3.2). From these images it is obsereved that indeed CO_2 is imbibed into the coal samples which leads to growth of the fractures in the coal surface during the experiment.

Fig. 3.8 illustrates the effect of residence time on the contact angle for the synthetic flue gas on Warndt Luisenthal coal at temperature of 318 K and 3.2 MPa pressure (the same conditions as for Fig. 3.7). A shorter aging time of about 4 min and a smaller contact angle of 63^o than the one for the pure CO_2 bubble were obtained at the same temperature and pressure. A possible explanation for this can be provided by referring to the smaller total amount of CO_2 in the synthetic flue gas mixture, expressed by a smaller partial pressure of CO_2, less sorption of CO_2 to the coal and very low solubility of N_2 in water. Thus, the required aging time is mainly determined by the concentration gradient of CO_2 in the bubble as well as in the liquid phase. Fig. 3.9 shows the evolution of the contact angle and the flue gas bubble radius at total pressure of 14.0 MPa, corresponding to a CO_2 partial pressure of 2.8 MPa. In this condition the stability time increases to 14 min, which is longer than that found for pure CO_2 in Fig. 3.7. This can be explained by the fact that at the total pressure of 14 MPa, the solubility of CO_2 in water is higher than that at 3.2 MPa. The fact that the contact angle for the flue gas at 14 MPa is about 78°, which is lower than that for CO_2 at 3.2 MPa, shows that the contact angle is not solely determined by the CO_2 content.

3.4.2. CO_2 WETTING BEHAVIOR ON A WET COAL SAMPLE

3.4.2.1. High volatile bituminous (hvBb) coal

Injection of a gas bubble into a pre-equilibrated system, which consists of water and CO_2, induces an initial fluctuation of the determined contact-angle values. However, due to the fact that the overall composition is within the two-phase region, the releasing of a new gas bubble only gives a small disturbance of the equilibrium which does not last long. There is a constant or stable contact angle at the end of each contact-angle measurement. The measured stable contact angles of the CO_2-water-hvBb coal system at a constant temperature of 318 K are depicted in Fig. 3.10. The contact angle, θ, increases with pressure: i.e. $\theta=(78.49^o\pm 3.4^o)+(0.34\times P\ [MPa])$. The square of the correlation coefficient, R^2 (Pearson's correlation), is equal to 0.94. The wetting behaviour of WL coal changes from intermediate-wet (contact angles between 75^o to 105^o) towards CO_2-wet with increasing pressure (contact angles larger than 105^0). This means that the coal surface becomes hydrophobic ($\theta \geq 105^o$) at pressures higher than 8.5 MPa and a temperature of 318 K. This wettability alteration versus pressure is also clearly visible from the images in Fig. 3.11.

The measured contact angles are of the same order of magnitude as the one determined by Siemons [20]. The wettability alteration was also detected from capillary pressure measurements, where at lower pressures water was the wetting phase while for pressures higher than 8.7 MPa CO_2 became the wetting phase [50].

Siemons found that the contact angle was constant at a value of about 85^o up to a pressure of 8.7 MPa. At a pressure of 10.0 MPa a contact angle of about 120^o was observed. For pressures higher than 10.0 MPa, the contact angle steadily increased up to about 140^o at a pressure of 15 MPa. A possible explanation for the difference in the contact-angle behavior might be attributed to the experimental conditions chosen by Siemons, where the CO_2/water solution was not pre-equilibrated and thus, the mass transfer of CO_2 and water could interfere with the measurement of the contact angle. This explanation is supported by the fact that the gas bubble disappeared in Siemons' experiments [20]. In the work presented here (Fig. 3.10), the experiments were conducted with a fully CO_2-saturated aqueous phase to eliminate the effect of any changes in the composition of the aqueous phase and to minimize the dissoluion effect. As a result, a continuous change of the contact angle versus pressure was observed without disappearance of the bubble.

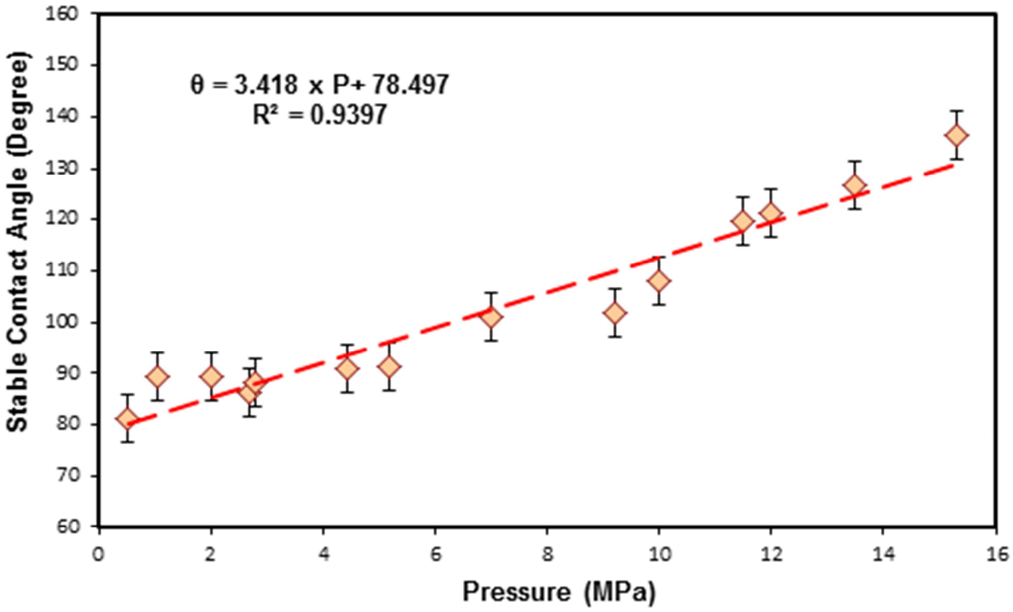

Figure 3.10. Stable contact angle as a function of pressure at 318 K for CO_2- wet WL coal system

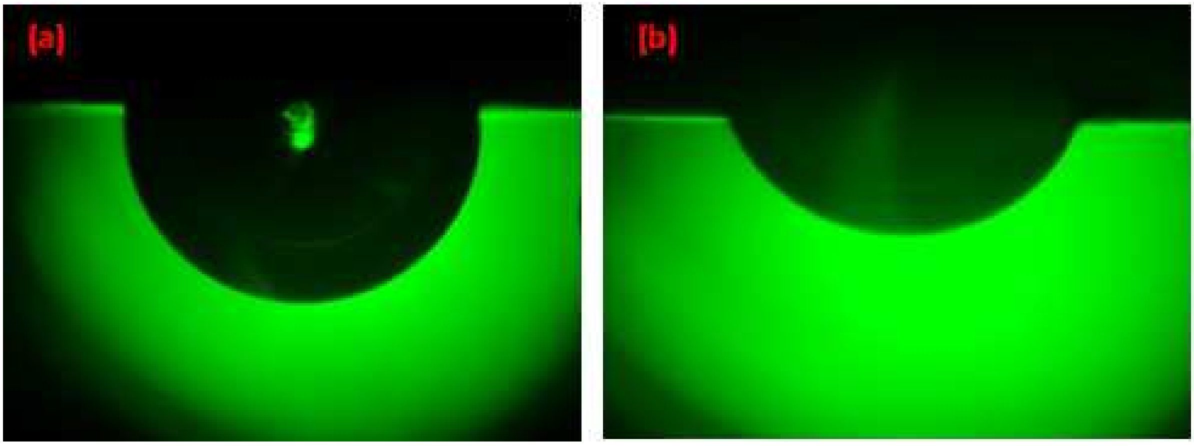

Figure 3.11. Digital images of CO_2 bubble on the WL coal surface in the presence of water as liquid phase at 318 K; (a) P=0.65 MPa and (b) P=11.0 MPa

According to Chun and Hebach [51, 52] the wettability alteration is mainly attributed to the formation of a CO_2-enriched aqueous phase. However, analysis of the CO_2 density [53], the solubility of CO_2 in water [54] and the sorption of CO_2 on wet WL coal [20] with increasing pressure shows that all these properties might be responsible for the wettability change (Fig. 3.12). The above-mentioned properties are depicted as relative properties in Fig. 3.12; therefore the value at a certain pressure is divided by the respective maximum value in the pressure range up to 20 MPa. The maximum of the CO_2 sorption on the coal sample and the wettability alteration from water-wet to gas-wet are observed in the same pressure range. In this pressure range, it can be observed that the density and the solubility of CO_2 strongly increase before they become almost constant at higher pressures; similar to the contact angle (Fig. 3.12). All these factors together might be summarized as a water film stability between the bubble and the surface as discussed by Siemons [20].

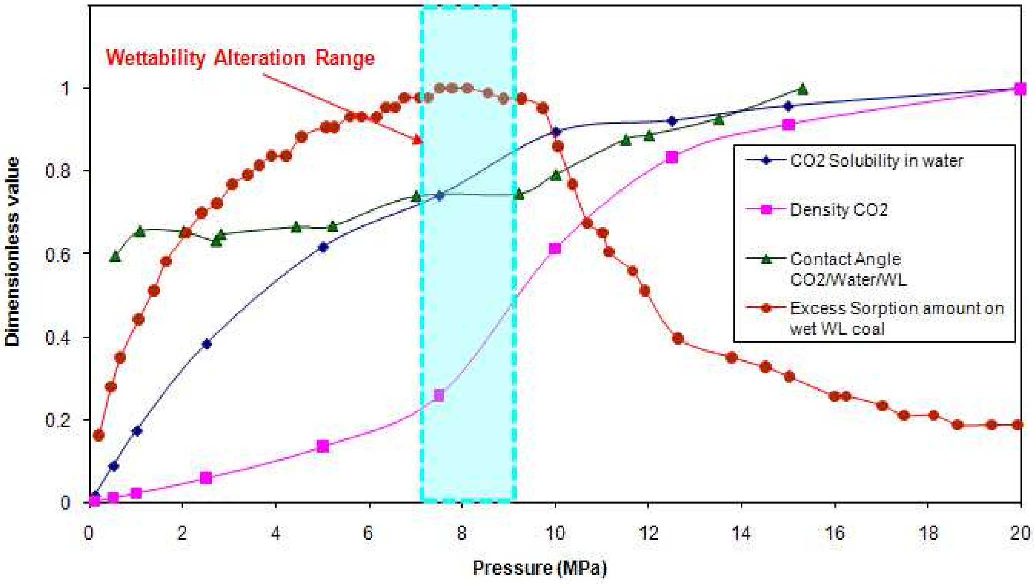

Figure 3.12. Dimensionless density [53], CO_2 solubility in water [54], stable contact angle (this work) and sorption of CO_2 on wet WL coal [20] at a constant temperature of 318 K and a pressure ranging from atmospheric up to 20 MPa.

3.4.2.2. Semi-anthracite coal

The contact angles of the CO_2/water/semi-anthracite coal system at a constant temperature of 318 K are depicted in Fig. 3.13. The contact angle (θ) can be described by a positive linear correlation (regression: $\theta=92.84^{o}(\pm 4.3^{o})+0.42\times P$ [MPa], $R^2 = 0.94$). The wetting properties of SC coal change from intermediate-wet towards CO_2-wet with increasing pressure at a temperature of 318 K. The coal surface becomes hydrophobic at pressures higher than 5.7 MPa. The implication on field scale could be that for CO_2 storage in semi-anthracite coal, the injection pressure has to overcome a pressure threshold of 5.7 MPa to wet the surface and thereby to enhance the storage capacity.

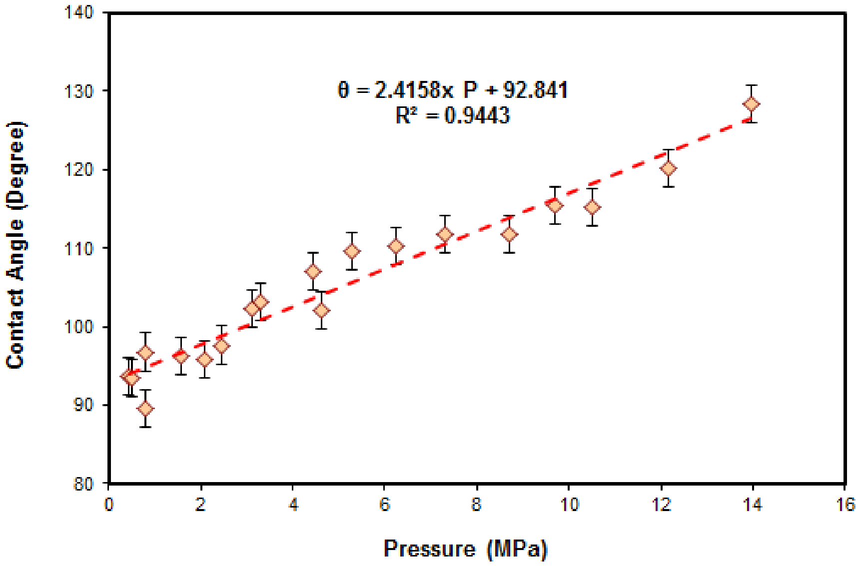

Figure 3.13. Stable contact angle as a function of pressure for the wet SC coal system with CO_2 at a temperature of 318 K. The dashed line gives the best linear fit through the data.

This behavior is partly in contrast with the contact-angle experiments of Siemons et al. [45] and the capillary-pressure experiments of Plug [50]. According to Plug's experiments the wettability of the same high-rank coal, SC, is CO_2-wet during primary imbibition experiments from low pressures up to 9 MPa. This is in agreement with the contact angle data of Siemons et al. [45]. Regarding the fact that both Plug and Siemons conducted their experiments using water which was not fully saturated with CO_2, one may attribute this observation to the dissolution of CO_2 in the aqueous phase. The comparison of the SC contact angles resulting from the work of Siemons et al. [45] and from this work (Fig. 3.14) shows that the values of Siemons are generally higher than those of this work. In Siemons' experiments the SC samples behave as CO_2-wet already at pressures above 0.26 MPa, with contact angles varying between 100 and 140 degree. The contact angles in this work show a relatively steady increase from 90 to 120 degree versus pressure. A possible explanation for the difference in the contact-angle behavior might be attributed to the different experimental conditions of the two studies. In the work of Siemons the solution of CO_2 and water was not pre-equilibrated and thus the mass transfer of CO_2 and water into the aqueous and the gas phase might have possibly interfered. This explanation is also supported by the fact that in the experiments conducted by Siemons the CO_2 bubble disappears within 60 min at low pressures and in about 20 to 30 min at high pressures and that the contact-angle data of Siemons strongly scatter upon increasing pressure [45]. Siemons et al. [45] showed that the disappearance of the CO_2 bubble was due to dissolution and not due to CO_2 sorption on the coal surface.

Throughout this research, the system was always carefully equilbrated before a CO_2 bubble was released for the measurement. This bubble was stable throughout the contact-angle determination at that specific pressure. It only disappeared when the pressure of the system was changed. However, even with this cautious method a very slight initial change in the contact angle was always observed caused by slight initial pressure fluctuations and/or mass transfer as mentioned above.

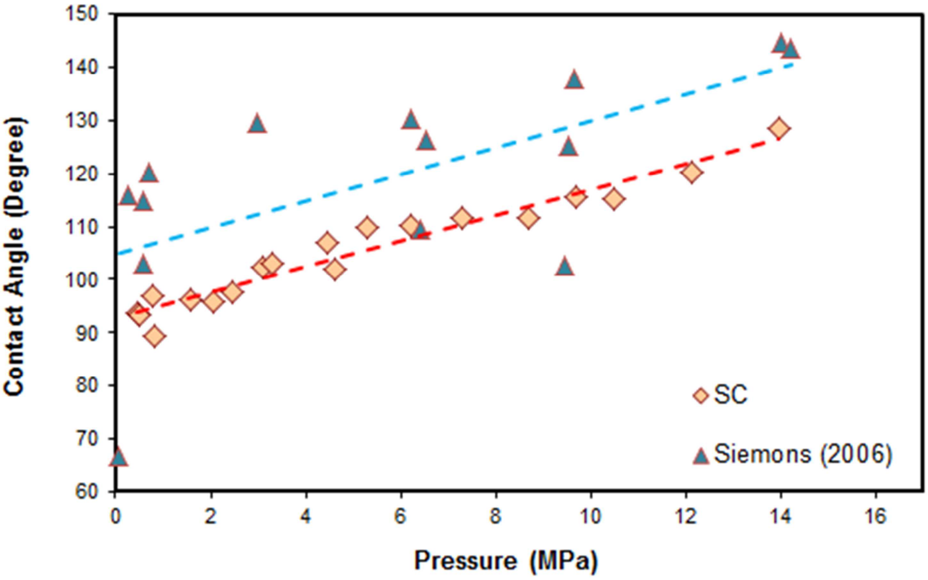

Figure 3.14. Comparison of determined contact angle values for the CO_2- wet SC coal system. Triangles display the work of Siemons et al. [45] for which the aqueous phase was not saturated with CO_2; diamonds give the data of this work in a pre-equilibrated aqueous phase. Lines are the best linear fits through the experimental data.

Fig. 3.12 shows the relation bewteen wettability of the wet WL system and the CO_2 density, the solubility of CO_2 in water, and the sorption of CO_2 on wet WL coal. The same relative properties have been plotted for the wet SC coal system (Fig. 3.15) and show that the wettability alteration and the maximum of the CO_2 sorption are also observed in the same pressure range as for the WL experiment. In contrast with the wet WL system, the change in the density and the CO_2 solubility in water do not coincide in the same pressure range. This leads to the conclusion that the sorption of CO_2 on the wet coal determines the wettability behavior rather than the CO_2 properties, such as density and solubility. The lower pressure range (light blue area) for wettability alteration in a wet SC-system is due to the higher coal rank.

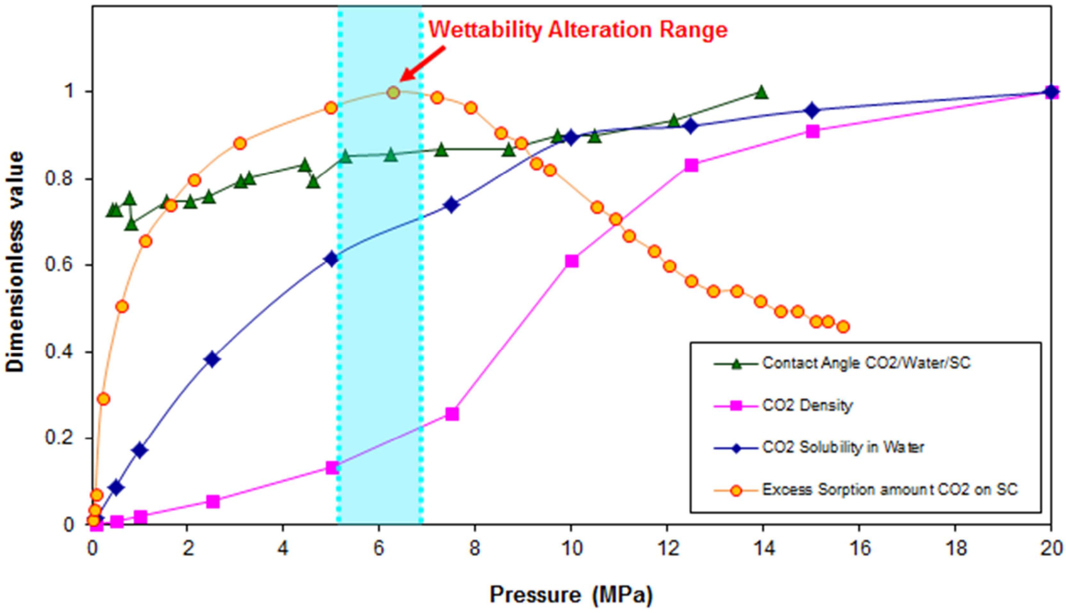

Figure 3.15. Dimensionless stable contact angle (this work), sorption of CO_2 on wet SC coal [20], density [53] and solubility of CO_2 [54] at a constant temperature of 318 K and pressures ranging from atmospheric up to 20 MPa. Values are relative values divided by the respective maximum value in the pressure range up to 20 MPa.

3.4.3. SYNTHETIC FLUE GAS WETTING BEHAVIOR ON A WET COAL SAMPLE

3.4.3.1. High volatile bituminous (hvBb) coal

The stable contact angles of the synthetic flue gas-water-hvBb coal system as a function of pressure at a temperature of 318 K are depicted in Fig. 3.16. In general, the contact angles of the flue gas on wet WL coal are smaller than those of CO_2. As it can be observed, the contact angle, θ, increases with pressure, starting with a contact angle of about 60^{o} at low pressures and a contact angle of about 89^{o} at 16.0 MPa. The linear relation $\theta = (60.51^{o} \pm 2.9^{o}) + (1.61\times \ P\ [\mathrm{MPa}])$ describes the change of the contact angle versus pressure with a square of the correlation coefficient, R^2, equal to 0.95. Thus, the wettability of WL coal changes from strongly water-wet (at low pressures) to intermediate-wet (at pressures higher than 10.5 MPa). This wettability alteration is found at higher total pressures than those for the CO_2 system. This can be explained in terms of the partial pressure of CO_2. It is worthwhile to note that the contact angles of the flue gas are of the same order of magnitude as the contact angles of the pure CO_2 system; if the absolute pressure of the CO_2 system is compared to the respective partial pressure of CO_2 in the flue gas system. Even though the contact angles are of the same order of magnitude, the contact angles of the flue gas bubbles are all smaller. This might be explained that in fact more CO_2 is dissolved in the aqueous phase because of the higher total pressure. In general, the sorption of nitrogen on coal and the solubility of nitrogen in water are much smaller than for CO_2. Therefore, the influence of nitrogen on the change of the contact angle is assumed to be small and the variations of the contact angle is dominated by the CO_2 behavior.

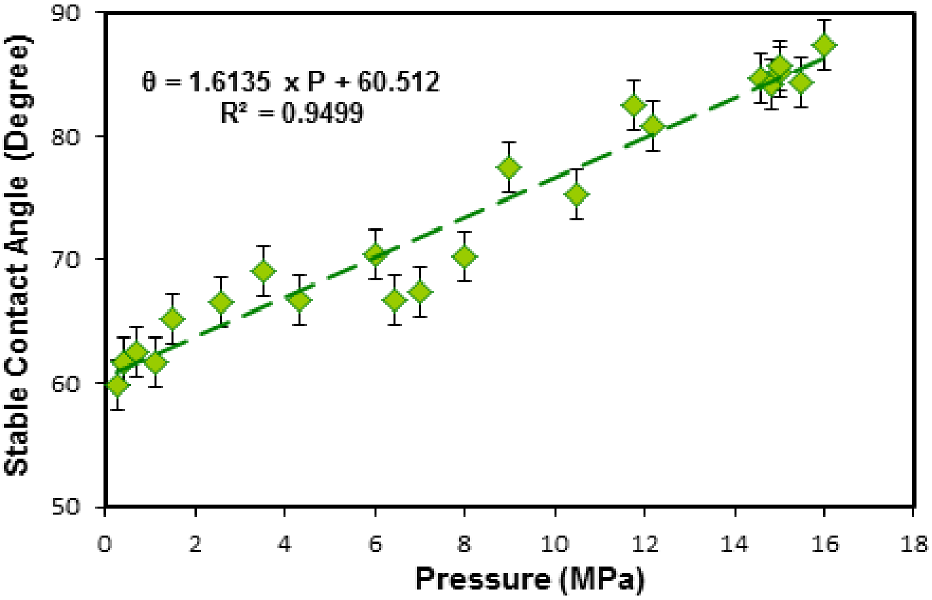

Figure 3.16. Stable contact angle as a function of pressure for flue gas- wet WL system at 318 K

3.4.3.2. Semi-anthracite coal

A series of experiments were performed to recognize the wetting properties of flue gas on a wet semi-anthracite coal. The stable contact angles of the synthetic flue gas/water/semi-anthracite coal system as a function of pressure at a constant temperature of 318 K are depicted in Fig. 3.17. Similar to the WL results, the contact angles of the flue gas on wet SC coal are smaller than those of CO_2. The experiments reveal that the wettability of Selar Cornish coal is intermediate-wet at all pressures. The increase in contact angle at low pressures is stronger (red dashed line) than that at pressures above 2.5 MPa (green dashed line). For pressures below 2.5 MPa, the contact angle increases with an inclination of about 2.88 degree/MPa, while for pressures above 2.5 MPa, it is 0.41 degree/MPa.

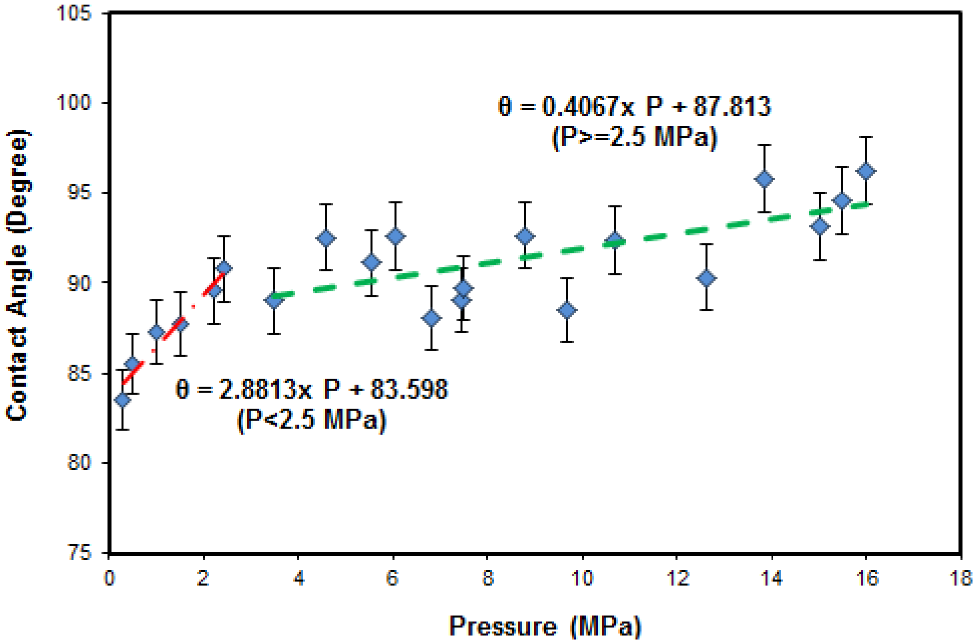

Figure 3.17. Stable contact angle as a function of pressure for the wet SC coal system with synthetic flue gas at a temperature of 318 K. The dashed line gives the best linear fit through the data and is used to guide the eye.

For the relevant in-situ pressures, it can be concluded that the contact angle slightly increases with increasing pressure. Thus, the wettability of SC coal with flue gas injection remains intermediate-wet at all pressures between 0.2 and 16 MPa. The contact angles of the flue gas bubbles are all smaller than those of the CO_2 bubbles. This is visible from the images shown in Fig. 3.18. This phenomenon could be explained by considering the ratio of 20 mol% CO_2 to 80 mol% N_2 in the flue gas bubble.

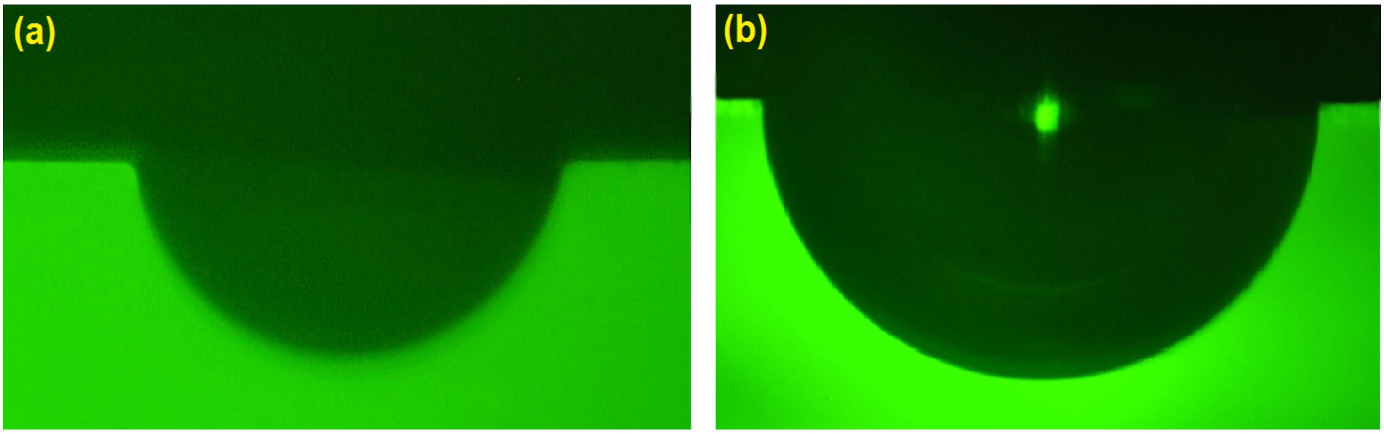

Figure 3.18. Digital images of gas bubble on the SC coal surface in the presence of water at 318 K and 5.25 MPa; (a) CO_2 bubble, $\theta_{avg.}\approx 104.1^o$, and (b) flue gas bubble, $\theta_{avg.}\approx 89.9^o$

3.4.4. COMPARISON OF RESULTS WITH RESPECT TO COAL RANK

The values of the determined contact angles for a high-rank and a medium-rank coal samples with similar vitrinite contents are given in Fig. 3.19.

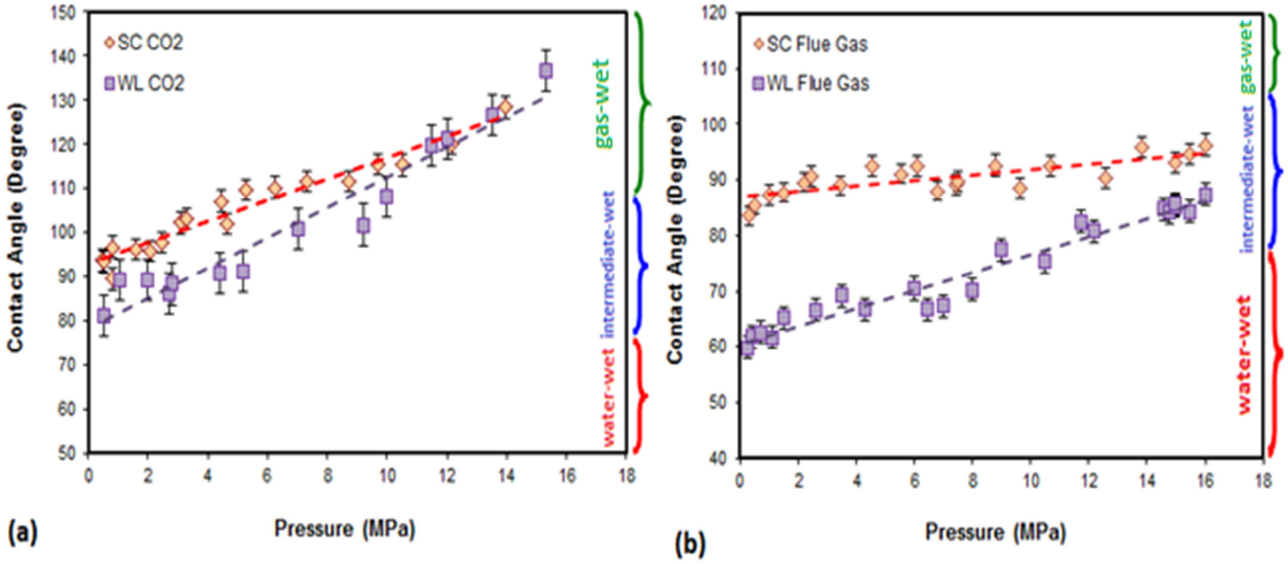

Figure 3.19. Contact angle as a function of pressure for coal samples of different ranks; against (a) CO_2 and (b) synthetic flue gas.

The following observations can be made from Fig. 3.19:

- For the hvBb rank WL sample and injection of pure CO_2, the wettability of the coal surface changes from intermediate-wet to CO_2-wet at 8.5 MPa.
- For the same WL sample when injecting the synthetic flue gas, the alteration from water-wet to intermediate-wet was observed at pressures above 10.5 MPa.
- For the semi-anthracite rank SC sample, it is found that the contact angle increases with pressure against pure CO_2 and the wettability alteration occurs at around 5.7 MPa.
- Experimental results with synthetic flue gas revealed that the wettability of Selar Cornish coal is intermediate-wet at all pressures and the contact angle only slightly increases with pressure.
- It is observed that hydrophobicity (the contact angle) of a coal sample increases with the coal rank and pressure, which confirms previous findings by Gutierrez-Rodriguez et al. [28] and Sakurovs and Lavrencic [40].
- For the semi-anthracite sample, the wettability alteration against CO_2 occurs at a lower pressure than that for the lower rank hvBb sample.
- The contact angles on the semi-anthracite Selar Cornish sample against flue gas are higher than those on Warndt Luisenthal coal.
- For the Selar Cornish coal sample the pressure slightly affects the wettability whehter CO_2 or flue gas has been injected. Warndt Luisenthal coal becomes apparently more

hydrophobic with increasing pressure. In other words, coal rank is a parameter that controls the degree of pressure dependency of the wettability.

- For the samples used in this work the mineral-matter contents in the contact surface are comparable. In this study, the WL coal sample contains more total mineral matter than the SC coal sample. However, the difference between mineral-matter content of the two coal surfaces is negligible. Although in general a coal with a higher content of mineral matter is more water-wet [43], the results of this study do not allow one to attribute the variations in the wettability of the used samples to the amount of mineral matter in the coal, because the mineral-matter content on the surface of the used coal samples was too low and similar.

3.4.4.1. Effect of coal surface charge

The observed wettability behavior of the coal ranks used in this work is related to the different surface chemistry of the coal samples. According to the DLVO theory [55, 56] and electric double layer effects, the wettability alteration and increase in contact angle are due to the decrease the stability of the water film on the surface. Any reduction in the negative surface charge of coal particles reduces the electrostatic repulsions and consequently decreases the stability of the water film covering the surface. However, electrochemical properties of the coal and the aqueous interface are mainly determined by coal functional groups and surface chemistry. Metoxy-, hydroxyl-, carboxyl- and carbonyl- groups are hydrophilic, while paraffin, graphite and naphtalene groups are hydrophobic [57]. Due to coalification, coal loses its hydrophilic functional groups and the coal structure enriches in aromatic carbon. Therefore, the content of phenolic groups decreases gradually with increasing coal rank. This leads to an increasing hydrophobicity with increasing rank [37]. The fact that the hvBb-rank coal (WL) is more water-wet is due to hydrophilic functional groups, mainly carboxylic and hydroxyl groups, which are more abundant in the hvBb rank coal [34, 39].

It is found that the maximum sorption of CO_2 on the coal types used in this study and wettability alteration occur in the same pressure range. The effect of pressure on the wettability of coal samples and its effect on the maximum sorption might be also explained by the difference in coal electrochemical properties. The increase of contact angle with pressure has been attributed to the decrease of surface charge under the acidic pH of CO_2–equilibrated water [58]. The pH of the aqueous phase influences the surface charge of the particles. In water/CO_2 solution, pH decreases from 7 to 3 by CO_2 dissolution in water. Wen [59] found that the negative surface charge of bituminous coal increases with increasing the pH and oxidation in air. The pH reduction leads to a decline in the negative surface charge of particles and thereby reduces the electrostatic repulsions and stability of the water film. The zeta potential and surface charge determination of coal particles are highly dependent on the functional groups, the coal type and coal rank. Consequently, it is expected that the point of zero charge, which corresponds to the minimum water film stability, occurs at different pH (and pressures) for different coal samples. According to the results (Fig. 3.19(a)) the minimum stability of the water film for the semi-anthracite rank SC and the hvBb-rank WL samples are around 5.7 MPa and 10.5 MPa, respectively. Moreover, the coal surface charge influences the adsorption of gas on the coal at different pH values [60]. This may explain the occurrence of the wettability alteration and maximum sorption in the same pressure range. To prove these findings, more investigations on the zeta potential and surface charge determination of these samples versus pH are needed.

3.4.5. IMPLICATIONS FOR CO_2 STORAGE IN CBM

To assess the displacement and capture efficiency commonly the so-called capillary number is used. A large capillary number means that by injecting CO_2 water is displaced easily during CO_2 capture [61]. The capillary number is defined as:

$$N_{ca} = \frac{\mu \times v}{\gamma_{wg} \times cos\theta} \tag{3.1}$$

where μ is the viscosity of the aqueous phase and v is the injection velocity of the gas. At a constant temperature, the equilibrium interfacial tension, γ_{wg}, between the aqueous and the gas phases of the CO_2-water system decreases with the pressure, which is associated with increasing solubility of CO_2 in water [48]. In addition, the water contact angle, θ, in the water-CO_2-coal system increases with pressure at a constant temperature (see Fig. 3.19(a)). As a consequence, cos θ decreases. Combining these observations, it can be concluded that the adhesion force (product of contact angle and interfacial tension) decreases with pressure at a constant temperature. Thus, with increasing pressure at constant temperature, the capillary number increases. This means that by injecting CO_2 at a higher pressure, it is easier to displace water through the cleat system of the coal. Hence, with increasing pressure, more CO_2 can be injected into the coal and the CO_2 storage capacity increases. Therefore, the alteration of the wettability of the coal from water-wet to intermediate or gas-wet increases the efficiency of the CO_2 storage. Comparison of the contact angles determined by CO_2 with those determined by synthetic flue gas shows that injection of pure CO_2 is more efficient for medium rank hvBb coal, since the nitrogen in the synthetic flue gas is not participating in the process. However, because the sorption on coal and the solubility in water for nitrogen are lower than those for CO_2, one might consider to inject the flue gas and use the medium (coal) as an in-situ separation unit [47- 49].

It is thus expected that the behavior found in this study is generally applicable to coals with the same rank and with similar compositions disregarding the ash content of the coal. However, other types of coal might show a different behaviour due to their different mineral/aliphatic/aromatic surface compositions.

3.5. CONCLUSIONS

Two coal types were studied with respect to their wetting properties when injecting CO_2 or flue gas at various pressures, ranging from 0.1 to 16 MPa, at a constant temperature of 318 K. The results show that at a given temperature and pressure the non-stable contact angle increases with time up to a constant value; the latter is the stable contact angle. The aging time (time to reach stability) was much shorter for the synthetic flue gas bubbles than for CO_2 bubbles. From this study it was found that:

- In general, the stable contact angles of CO_2 as well as the synthetic flue gas increase with pressure. The rate of increase is influenced by the coal rank and the gas bubble composition.
- When injecting CO_2, the wettability of the semi-anthracite coal surface changed from intermediate-wet to CO_2-wet at a pressure around 5.7 MPa. The implication on field scale could be that, for CO_2 storage in semi-anthracite coal, the reservoir pressure has to overcome a pressure threshold of 5.7 MPa to wet the surface and thereby to enhance the storage capacity.
- Results with injection of synthetic flue gas revealed that Selar Cornish coal is intermediate-wet at the investigated pressures and that the contact angle only slightly increases with pressure. For field-scale applications this implies that there is no pressure threshold to wet the surface with the flue gas.
- For both coal samples the contact angles of the flue gas bubbles are smaller than those of the CO_2 bubbles. Based on this wetting behavior, injection of pure CO_2 into SC and WL coal could be more efficient than injection of flue gas.
- For the synthetic flue gas, the contact-angle trend is dominated by the CO_2 behavior. Nitrogen does not dissolve in water and sorbs into the coal to a lesser degree than CO_2. The behavior of the synthetic flue gas system at a certain CO_2 partial pressure is comparable to the behavior of the CO_2 system at the same (total) pressure.
- The pressure has less effect on the contact angles on the semi-anthracite sample than on those on the Warndt Luisenthal sample independent whether CO_2 or flue gas has been injected.
- In general, the hydrophobicity of the coal samples increases with coal rank and pressure. This behavior can be related to the different surface chemistry and electrocchemical properties of the two coal samples used.
- The fact that the wettability of different coal ranks changes differently reveals that on field scale coal wettability is definitely important for the evaluation of the efficiency of CO_2 storage process.

REFERENCES

[1] K. Damen, A. Faaij, F. van Bergen, J. Gale, E. Lysen, Identification of early opportunities for CO_2 sequestration—worldwide screening for CO_2-EOR and CO_2-ECBM projects, Energy, 30 (2005) 1931-1952.

[2] M. Mazzotti, R. Pini, G. Storti, Enhanced coalbed methane recovery, The Journal of Supercritical Fluids, 47 (2009) 619-627.

[3] F.V. Bergen, P. Krzystolik, N.v. Wageningen, H. Pagnier, B. Jura, J. Skiba, P. Winthaegen, Z. Kobiela, Production of gas from coal seams in the Upper Silesian Coal Basin in Poland in the post-injection period of an ECBM pilot site, International Journal of Coal Geology, 77 (2009) 175-187.

[4] F.V. Bergen, H. Pagnier, P. Krzystolik, Field experiment of enhanced coalbed methane-CO_2 in the upper Silesian basin of Poland, Environmental Geosciences, 13 (2006) 201-224.

[5] P.v. Hemert, Manometric determination of supercritical gas sorption in coal in: Geotechnology, Delft University of Technology, Delft, 2009.

[6] M.J. Mavor, W.D. Gunter, J.R. Robinson, Alberta Multiwell Micro-Pilot Testing for CBM Properties, Enhanced Methane Recovery and CO_2 Storage Potential, in: SPE Annual Technical Conference and Exhibition, Society of Petroleum Engineers, Houston, Texas, 2004.

[7] W.D. Gunter, M.J. Mavor, J.R. Robinson, CO_2 storage and enhanced methane production: field testing at Fenn-Big Valley, Alberta, Canada, with application, in: 7th International Conference on Greenhouse Gas Control Technologies (GHGT-7), Vancouver, Canada, 2005, pp. 413-422.

[8] S.H. Stevens, J.A. Kuuskraa, R.A. Schraufnagel, Technology spurs growth of U.S. coalbed methane, Oil and Gas Journal, 94 (1996) 56-63.

[9] S. Mazumder, K.H. Wolf, CO_2 and Flue Gas Coreflood Experiments for Enhanced Coalbed Methane, in: SPE Asia Pacific Oil and Gas Conference and Exhibition, Society of Petroleum Engineers, Perth, Australia, 2008.

[10] L. Congmin, Z. Yaping, S. Yan, S. Wei, Z. Li, Enrichment of coal-bed methane by PSA complemented with CO_2 displacement, AIChE Journal, 57 (2011) 645-654.

[11] R. Florenti, N. Aziz, D. Black, L. Nghiem, K. Baris, Recovery of stored gas in coal by nitrogen injection - a laboratory study, in: 10th Underground Coal Operators' Conference, University of Wollongong & the Australasian Institute of Mining and Metallurgy, Australia, 2010, pp. 217-228.

[12] S. Wo, J.T. Liang, Simulation Assessment of N2/CO_2 Contact Volume in Coal and Its Impact on Outcrop Seepage in N_2/CO_2 Injection for Enhanced Coalbed Methane Recovery, in: SPE/DOE Symposium on Improved Oil Recovery, Society of Petroleum Engineers, Tulsa, Oklahoma, 2004.

[13] A. Syed, S. Durucan, J.-Q. Shi, A. Korre, Flue gas injection for CO_2 storage and enhanced coalbed methane recovery: Mixed gas sorption and swelling characteristics of coal, in: 11th International Conference for Greenhouse Gas Control Technologies, Kyoto, Japan, 2011.

[14] C.M. White, D.H. Smith, K.L. Jones, A.L. Goodman, S.A. Jikich, R.B. LaCount, S.B. DuBose, E. Ozdemir, B.I. Morsi, K.T. Schroeder, Sequestration of carbon dioxide in coal with enhanced coalbed methane recovery - A review, Energy and Fuels, 19 (2005) 659-724.

[15] C. Amorino, R. Bencini, R. Cara, D. Cinti, G. Deriu, V. Fandinò, A. Giannelli, M. Mazzotti, S. Ottiger, L. Pizzino, R. Pini, F. Quattrocchi, R.G. Sardu, G. Storti, N. Voltattorni, CO_2 geological storage by ECBM techniques in the Sulcis area (SW Sardinia Region, Italy), in: Second International Conference on Clean Coal Technologies for our Future (CCT), Castiadas, Sardinia, Italy, 2005.

[16] J. Shi, Q., S. Durucan, CO_2 Storage in Deep Unminable Coal Seams, Oil & Gas Science and Technology - Rev. IFP, 60 (2005) 547-558.

[17] J.W. Larsen, The effects of dissolved CO_2 on coal structure and properties, International Journal of Coal Geology, 57 (2003) 63-70.

[18] N. Shojai Kaveh, E.S.J. Rudolph, K.-H.A.A. Wolf, S.N. Ashrafizadeh, Wettability determination by contact angle measurements: hvbB coal–water system with injection of synthetic flue gas and CO_2, Journal of Colloid and Interface Science, 364 (2011) 237-247.

[19] N. Shojai Kaveh, K.H. Wolf, S.N. Ashrafizadeh, E.S.J. Rudolph, Effect of coal petrology and pressure on wetting properties of wet coal for CO_2 and flue gas storage, International Journal of Greenhouse Gas Control, 11, Supplement (2012) S91-S101.

[20] N. Siemons, Carbon Dioxide Transport and Retention in Coal, in: Geotechnology, Delft University of Technology, Delft, 2007.

[21] B.J. Arnold, F.F. Aplan, The hydrophobicity of coal macerals, Fuel, 68 (1989) 651-658.

[22] M.M. Dubinin, The potential theory of adsorption of gases and vapors for adsorbents with energetically nonuniform surfaces, Chemical Reviews, 60 (1960) 235-241.

[23] P.D. Gamson, B.B. Beamish, D.P. Johnson, Coal microstructure and micropermeability and their effects on natural gas recovery, Fuel, 72 (1993) 87-99.

[24] R.B. Bird, W.E. Stewart, E.N. Lightfoot, Transport phenomena, Wiley, New York, 1960.

[25] D.W. Fuerstenau, J. Diao, Characterization of Coal Oxidation and Coal Wetting Behavior by Film Flotation, Coal Preparation, 10 (1992) 1-17.

[26] J.S. Laskowski, Coal surface chemistry and its effects on fine coal processing, in: S.K. Kawatra (Ed.) High Eficiency Coal Preparation, SOC. Mining Metallurgy and Exploration, Littleton, 1995, pp. 163-176.

[27] D. Wei, S. Chander, R. Hogg, Distribution of Wettability of Coal, Coal Preparation, 10 (1992) 37-45.

[28] J.A. Gutierrez-Rodriguez, R.J. Purcell Jr, F.F. Aplan, Estimating the hydrophobicity of coal, Colloids and Surfaces, 12 (1984) 1-25.

[29] J.S. Laskowski, Coal Surface Chemistry and Its Role in Fine Coal Beneficiation and Utilization, Coal Preparation, 14 (1994) 115-131.

[30] G.A. Brady, A.W. Gauger, Properties of Coal Surfaces, Industrial & Engineering Chemistry, 32 (1940) 1599-1604.

[31] S.C. Sun, Hypothesis for different floatabilities of coals, carbons and hydrocarbon minerals, Trans. AIME, 199 (1954) 67-95.

[32] Y.B. He, J.S. Laskowski, Contact Angle Measurements on Discs Compressed From Fine Coal, Coal Preparation, 10 (1992) 19-36.

[33] F.F. Aplan, Coal Properties Dictate Coal Flotation Strategies, Mining Engineering, 45 (1993) 83 - 96.

[34] R.J. Crawford, D.W. Guy, D.E. Mainwaring, The influence of coal rank and mineral matter content on contact angle hysteresis, Fuel, 73 (1994) 742-746.

[35] M.G. Elyashevitch, Contact angles as a criterium of coal floatability, Trans. Donetsk Industrial Institute, 32 (1941) 225-235

[36] J. Drelich, J.S. Laskowskl, M. Pawuk, Improved Sample Preparation and Surface Analysis Methodology for Contact Angle Measurements on Coal (Heterogeneous) Surfaces, Coal Preparation, 21 (2000) 247-275.

[37] D.V.J. Keller, The contact angle of water on coal, Colloids and Surfaces, 22 (1987) 21-35.

[38] J.B. Gayle, W.H. Eddy, R.Q. Shotts, Laboratory investigation of the effect of oxidation on coal flotation, U.S. Dept. of the Interior, Bureau of Mines, Washington, D.C., 1965.

[39] J.A. Gutierrez-Rodriguez, F.F. Aplan, The effect of oxygen on the hydrophobicity and floatability of coal, Colloids and Surfaces, 12 (1984) 27-51.

[40] R. Sakurovs, S. Lavrencic, Contact angles in CO_2-water-coal systems at elevated pressures, International Journal of Coal Geology, 87 (2011) 26-32.

[41] F.F.O. Orumwense, Wettability of coal - A comparative study, Scandinavian Journal of Metallurgy, 30 (2001) 204-211.

[42] T. Murata, Wettability of coal estimated from the contact angle, Fuel, 60 (1981) 744-746.

[43] A. Gosiewska, J. Drelich, J.S. Laskowski, M. Pawlik, Mineral Matter Distribution on Coal Surface and Its Effect on Coal Wettability, Journal of Colloid and Interface Science, 247 (2002) 107-116.

[44] S.M. Chi, B.I. Morsi, G.E. Klinzing, S.H. Chiang, Study of interfacial properties in the liquid CO_2-water-coal system, Energy & Fuels, 2 (1988) 141-145.

[45] N. Siemons, H. Bruining, H. Castelijns, K.-H. Wolf, Pressure dependence of the contact angle in a CO_2–H_2O–coal system, Journal of Colloid and Interface Science, 297 (2006) 755-761.

[46] R.J.M. Huijgens, The influence of interfacial tension on nitrogen flooding, in: Geotechnology, delft University of Technology, Delft, 1994.

[47] J. Drelich, J.S. Laskowski, M. Pawlik, S. Veeramasuneni, Preparation of a coal surface for contact angle measurements, J. Adhesion Sci. Techno, 11 (1997) 1399-1431.

[48] D. Yang, Y. Gu, P. Tontiwachwuthikul, Wettability Determination of the Reservoir Brine−Reservoir Rock System with Dissolution of CO_2 at High Pressures and Elevated Temperatures, Energy & Fuels, 22 (2008) 504-509.

[49] E. Battistutta, P. van Hemert, M. Lutynski, H. Bruining, K.-H. Wolf, Swelling and sorption experiments on methane, nitrogen and carbon dioxide on dry Selar Cornish coal, International Journal of Coal Geology, 84 (2010) 39-48.

[50] W.-J. Plug, Measurements of capillary pressure and electric permittivity of gas–water systems in porous media at elevated pressures, in: Geotechnology, Delft University of Technology, Delft, 2007.

[51] B.-S. Chun, G.T. Wilkinson, Interfacial tension in high-pressure carbon dioxide mixtures, Industrial & Engineering Chemistry Research, 34 (1995) 4371-4377.

[52] A. Hebach, A. Oberhof, N. Dahmen, A. Kögel, H. Ederer, E. Dinjus, Interfacial tension at elevated pressures-measurements and correlations in the water + carbon dioxide system, Journal of Chemical and Engineering Data, 47 (2002) 1540-1546.

[53] R. Span, W. Wagner, A New Equation of State for Carbon Dioxide Covering the Fluid Region from the Triple-Point Temperature to 1100 K at Pressures up to 800 MPa, Journal of Physical and Chemical Reference Data, 25 (1996) 1509-1596.

[54] V.I. Baranenko, L.N. Fal'kovskii, V.S. Kirov, L.N. Kurnyk, A.N. Musienko, A.I. Piontkovskii, Solubility of oxygen and carbon dioxide in water, Atomic Energy, 68 (1990) 342-346.

[55] S. Levine, G.P. Dube, Interaction between two hydrophobic colloidal particles, using the approximate Debye-Huckel theory. I. General properties, Transactions of the Faraday Society, 35 (1939) 1125-1140.

[56] E.J.W. Verwey, J.T.G. Overbeek, Theory of the Stability of Lyophobic Colloids, Elsevier, 1948.

[57] H. Polat, S. Chander, Adsorption of PEO/PPO triblock co-polymers and wetting of coal, Colloids and Surfaces A: Physicochemical and Engineering Aspects, 146 (1999) 199-212.

[58] T.K. Tokunaga, DLVO-Based Estimates of Adsorbed Water Film Thicknesses in Geologic CO_2 Reservoirs, Langmuir, 28 (2012) 8001-8009.

[59] W.W. Wen, Electrokinetic behavior and flotation of oxidized coal, in, Pennsylvania State University, University Park, 1977.

[60] C. Moreno-Castilla, J. Rivera-Utrilla, M.V. López-Ramón, F. carrasco-Marín, Adsorption of some substituted phenols on activated carbons from a bituminous coal, Carbon, 33 (1995) 845-851.

[61] D. Yang, Interfacial Interactions of the Crude Oil-Reservoir Brine-Reservoir Rock Systems with Dissolution of CO_2 under Reservoir Conditions, in, University of Regina, Regina, SK, Canada, 2005.

CHAPTER 4

Wettability Evaluation of CO_2-Water-Bentheimer Sandstone System: Dissolution, Interfacial Tension, Contact Angle and Bubble Size[*]

ABSTRACT

The success of CO_2 storage in deep saline aquifers and depleted oil and gas reservoirs is largely controlled by interfacial phenomena amongst fluid phases and rock pore spaces. Particularly, the wettability of the rock matrix has a strong effect on capillary pressure, relative permeability and the distribution of phases within the pore space and thus on the entire displacement mechanism and storage capacity. Precise understanding of wettability behavior is therefore fundamental when injecting CO_2 into geological formations to sequestrate CO_2 and/or to enhance gas/oil production. In this chapter, the interfacial tensions and contact angles of Bentheimer sandstone/water/CO_2 or flue gas have been evaluated experimentally using the captive-bubble technique in the pressure range from 0.2 to 15 MPa. The experiments were conducted using different compositions of aqueous phase with respect to CO_2, i.e. unsaturated and fully saturated. In an unsaturated system, two dissolution regimes are observed. Based on a diffusion model, it is shown that, in the so-called short-time regime, the effective diffusion is about an order of magnitude larger than expected from the molecular diffusivity of CO_2 into water; this may be explained by density-driven natural convection. In the other regime, over longer times, molecular diffusion is the controlling mechanism for mass transfer. It has been shown that a reliable contact-angle determination needs to be conducted using a pre-equilibrated aqueous phase to eliminate dissolution effects. In the fully saturated aqueous phase, the Bentheimer sandstone/ water system is (and remains) water-wet even at high pressures against CO_2 and/or flue gas. In these systems, the data of the stable contact angle demonstrate a strong dependence on the bubble size, which can be explained by the buoyancy effect on bubble shape. However, the surface non-ideality and roughness have significant influence on the reliability of the contact-angle determination. For systems characterized by Bond numbers less than 0.9, the influence of the bubble radius on the contact angle becomes insignificant. The experimental results show that the phase transition of CO_2 from subcritical to supercritical has a negligible effect on the contact angle of the Bentheimer/CO_2/water system.

KEYWORDS: Wettability; Dissolution; CO_2; Bentheimer sandstone; Contact angle; Flue gas; Bubble size; Line tension; Bond number; Interfacial tension; Roughness.

---

[*] ***Presented partly in:***
- *SPE 154382, 2012.*

[*] ***Just Accepted in:***
- *Journal of Energy and Fuels, 2014.*

4.1. INTRODUCTION

CO_2 storage in depleted or almost depleted gas reservoirs is an attractive option for CO_2 sequestration and storage, because gas recovery is enhanced (EGR), the underground and surface infrastructures are already available and the knowledge of the reservoir is quite well characterized due to the data acquired during the exploitation stage [1].

In deep saline aquifers, CO_2 is initially stored as a gas or supercritical fluid (physical trapping). Part of the injected CO_2 remains in the reservoir either in the residual phase near the well or in pore spaces (residual/capillary trapping) and some in the mobile phase below the cap rock (structural/stratigraphic trapping). Other trapping mechanisms are mineral trapping, where CO_2 reacts with minerals in the rock, and solubility trapping, where CO_2 dissolves in the aqueous phase. In general, different trapping mechanisms occur simultaneously [2-4].

To identify the most secure and best strategy for CO_2 injection, not only the wettability and its relation to fluid distribution, but also the physics of the trapping mechanisms, need to be understood. Capillary trapping occurs when CO_2 is immobilized in the rock pores by capillary forces. This process depends on the wettability of the rock, the interfacial tension (IFT) between the CO_2-rich and the aqueous phase (brine) and the pore-size distribution (Chapter 1, Eq. 1.1) [5, 6]. For a brine-saturated caprock, which consists of a low-permeability porous material saturated with brine, interfacial-tension and contact-angle data are the crucial parameters for the evaluation of the capillary-sealing efficiency. The hypothesis is that the caprock acts as the primary seal to prevent undesirable migration and leakage. However, capillary leakage occurs when the pressure in the CO_2-rich phase increases above the minimum pressure which is required to initiate the displacement of brine within the caprock. The caprock sealing efficiency can thus be regarded as CO_2 storage capacity [7]. In the literature, a large amount of data related to research with respect to CO_2 storage in depleted gas reservoirs and aquifers can be found. Current focus is on geochemical modeling, aquifer and reservoir simulation, long-term reservoir integrity and risk assessment. Only a very limited amount of literature data with focus on wetting properties of aquifers and gas reservoirs at high pressures and elevated temperatures can be found [6, 8-12]. A reliable experimental method to determine the wettability is a big step towards understanding the physics of this phenomenon, which should subsequently lead to successful CO_2 storage. In the CCS field application, the amount of capillary-trapped CO_2 depends on the wettability of reservoir rocks.

The main purpose of the study at hand is to examine the wettability behavior of the system of Bentheimer sandstone/water in the presence of CO_2 at elevated pressure [20]. Data on the contact angle were considered for the evaluation of the wettability of this system because: 1) values of the contact angle and the interfacial tension, particularly in the pressure range where CO_2 is supercritical, are necessary for the evaluation of the capillary trapping (Chapter 1, Eq.1.1) [7], and 2) when dealing with supercritical CO_2, wetting properties cannot be determined by the Amott-USBM method due to the fact that this method cannot be used at high pressure. To this end, contact-angle measurements were conducted for different compositions of the aqueous phase, i.e. fully saturated and not fully-saturated (unsaturated) with respect to CO_2, at a constant temperature of 318 K and at pressures varying between 0.2 and 15 MPa. When the aqueous phase is not completely saturated with CO_2, the injectivity and the gas distribution in the reservoir are not only influenced by the rock properties but also by the diffusion of CO_2 into the aqueous phase. After the aqueous phase has been saturated with CO_2, the injectivity is mainly determined by the wetting properties of the rock. Before the method can be applied in the field, it is thus important to evaluate the dissolution effects and the wettability for short and long periods. This can be done by conducting experiments with an unsaturated aqueous phase, representing the short-term behavior, and with a saturated aqueous phase representing the long-term behavior.

In addition, the wettability behavior of the Bentheimer sandstone/water system has been evaluated for synthetic flue gas (80% N_2/20% CO_2). Direct injection of flue gas into a reservoir eliminates the need for CO_2 separation prior to its injection into the field. Moreover, nitrogen stripping can recover considerably more methane than reservoir pressure depletion alone [13, 14]. Nevertheless, flue gas injection can reduce the structural trapping capacity for CO_2 by reducing the density of CO_2. This reduction is undesirable for CCS volume efficiency. To understand this process in more detail, flue gas injection has been evaluated from a wettability point of view, which is missing in the literature. In this study, the interfacial tension and contact angle of a synthetic flue gas/water/Bentheimer sandstone system are determined at high temperature and elevated pressures.

4.2. THEORETICAL REVIEW

4.2.1. CONTACT ANGLE AND DROPLET/BUBBLE SIZE

The application of Young equation (Chapter 1, Eq. 1.2) requires well-defined conditions, such as an ideal and perfectly smooth solid surface. The Young contact angle, θ_Y, is exclusively determined by the liquid/solid, liquid/gas, and gas/solid interfacial properties. Therefore, it is a single and unique contact angle and independent of the mass and volume of the bubble/drop. However, extensive experimental results found in the literature show that, for some cases, the contact angle of a captive bubble/sessile droplet on a horizontal surface is not only a physical property of the gas, liquid and solid materials, but also varies with the bubble/droplet size [15-18]. To address this phenomenon, several explanations have been offered in the literature, i.e., surface roughness and hysteresis [15, 19], line tension [17, 20] and gravity effects on droplet/bubble geometry [21].

Good and Koo [18] presented the concept of line tension to explain the variation of the contact angle with drop size. The so-called line tension is defined as the excess Gibbs energy per unit length of the contact line between three coexisting phases. Including the concept of line tension, which gives the dependency of the contact angle on bubble size [15, 17, 18, 22, 23], leads to the modified Young equation:

$$\gamma_{lv} \times cos\theta + \frac{\sigma}{R} = \gamma_{sv} - \gamma_{sl} \ , \tag{4.1}$$

where σ is the line tension (J/m) and R is the radius (m) of the solid-liquid contact circle that is the cross-section of the bubble which is captured on the surface (Fig. 4.1). For an axisymmetric bubble on a homogeneous, smooth and horizontal surface, the three-phase contact line is a circle. If the bubble is extremely large (i.e., $R \rightarrow \infty$), the modified Young equation reduces to the original Young equation:

$$\gamma_{lv} \times cos\theta_{\infty} = \gamma_{sv} - \gamma_{sl} \ , \tag{4.2}$$

where θ_∞ is the contact angle for the bubble with $R \rightarrow \infty$. Combining Eqs. 4.1 and 4.2 yields to an expression describing the contact angle for a bubble with a finite radius:

$$cos\theta = cos\theta_\infty - \frac{\sigma}{R\gamma_{lv}} \tag{4.3}$$

The infinite contact angle and the line tension can be determined at a constant temperature and pressure from a plot of $cos\theta$ versus *1/R*.

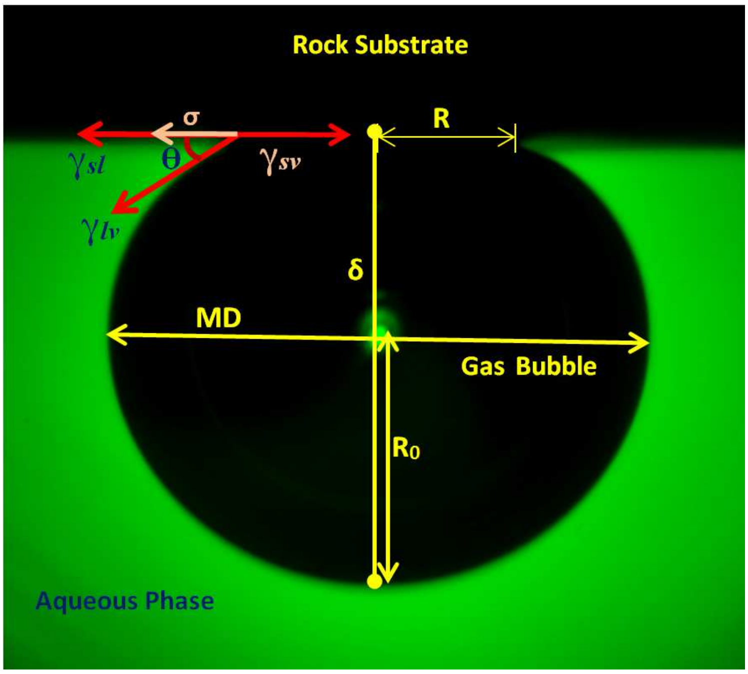

Figure 4.1. Schematic of a captive bubble explaining properties such as contact angle, interfacial tensions and dimensions of the bubble.

In the literature, there are a number of experimental studies on determining the line tension; however, the reported values vary widely in either magnitude or sign. This variation can be attributed to 1) typically small values of these parameters, in particular of the contact line length, which are used to determine the line tension, and/or 2) the fact that line tension is new introduced physical property that is difficult to measure and based on highly uncertain data [21, 24]. Moreover, incorporation of the line tension to describe the non-ideal (non-smooth or heterogeneous) surface is very complex and not straightforward [25]. The difficulties of contact-angle determination, i.e., contact-angle hysteresis and surface non-homogeneities, lead to the huge variation of line-tension values. Even a small amount of surface non-homogeneity can lead to a considerable overestimation of the line tension, which might even lead to a sign conversion. Values of the line tension found in the literature are both negative and positive and vary in the range of absolute values between 10^{-11} and 10^{-5} J/m. Recently, Liu et al. [26] reported that the linear relationship between $cos\theta$ and *1/R*, which is normally used for the line-tension determination, is incorrect at the nanometer scale. In addition, by using the roughness model, Lin et al. [15] showed that the experimentally observed fluctuations of apparent contact angles, which are more scattered than the prediction of the modified Young equation for a smooth surface (Eq. 4), are attributed to surface roughness. They concluded that the modified Young equation is inappropriate to interpret the contact angle and bubble size relation on a rough surface [15].

These contradictory results about the line-tension determination led to a search for other approaches, which can be also applicable for non-ideal and complex systems. The other explanation for addressing the contact-angle variation with droplet size might be provided by considering the effect of gravity on the droplet shape [21, 24]. Pethica and Pethica [27] and Leja and Poling [28] formulated a model explaining the influence of gravity on the contact angle. Vafaei and Podowski [21, 24] introduced models for two different droplet geometries. They showed that the contact angle for elongated droplets is size-independent and can be described by the original Young equation. According to their model, axisymmetric droplets are size-dependent and cannot satisfy the original Young equation [21, 24] but can be described by:

$$V = \frac{2\gamma_{lv}\pi R^2}{\rho_l g}\left(\frac{\rho_l g \delta}{2\gamma_{lv}} + \frac{1}{R_0} - \frac{\sin\theta}{R}\right) . \tag{4.4}$$

This approach is based on a liquid droplet surrounded by a gas phase. Eq. 4.4 represents a relationship between the volume of a droplet (*V*), the radius of the contact circle (*R*), the contact angle (θ), the radius of the curvature at the apex (R_0), the location of the apex (δ), and the properties of the droplet, such as density (ρ_l), and surface tensions between the coexisting phases (γ_{lv}) (Fig.4.1).

With this model, the contact angle of axisymmetric droplets can be predicted for a given mass of the droplet and any combination of components and mixtures forming the droplet and substrate:

$$\sin\theta = \left[\frac{3V}{\pi(2+\cos\theta_S)(1-\cos\theta_S)^2}\right]^{1/3} \frac{\sin^2\theta_S}{R} \quad , \tag{4.5}$$

where *V* is the volume of a droplet, *R* is the radius of the contact circle and θ_s is the contact angle for a spherical droplet, which is independent of the spherical droplet volume [21, 24]. θ_s is determined by extrapolating the determined contact angles at various droplet volumes to a droplet with zero volume.

The description of the effect of gravity on the contact angle of a liquid droplet surrounded by a gas phase is based on the two main forces acting on the droplet, i.e., the surface force and the gravity, which are considered to be independent of each other. If the gravity force dominates, the contact angle is influenced by the droplet volume. For a smaller droplet, the effect of gravity decreases and surface tension forces dominate; with decreasing droplet radius, the droplet shape asymptotically approaches a spherical shape. The contact angle for a spherical droplet is exclusively determined by the liquid/solid, liquid/gas, and gas/solid interfacial properties and the properties of the phases such as density, and is independent of the droplet volume, therefore fulfilling the Young equation.

To identify whether surface forces or gravity forces dominate, the Bond number is used. The Bond number is a dimensionless number described by:

$$Bo = \frac{\Delta\rho g L^2}{\gamma_{lv}} \tag{4.6}$$

where $\Delta\rho$ is the density difference between the liquid and the gas phase and *L* is characteristic length, which is the appropriate linear dimension. For bubble (droplet) systems, characteristic length is bubble diameter (*MD* in Fig. 4.1) [29]. A high Bond number indicates that the system is relatively unaffected by surface tension forces; a low number indicates that surface tension dominates. Intermediate numbers indicate a non-trivial balance between the two forces.

Nevertheless, there are still discussions surrounding whether the contact angle of a liquid on a solid is influenced by drop size and gravity. Herzberg and Marian [19] showed experimentally that the contact-angle variation with the drop size was generated by hysteresis rather than by gravity. In addition, Blokhuis et al. [30] showed analytically that the Young's contact angle is independent of the strength of the gravitational field.

Fujii and Nakae [31] quantitatively calculated the effect of gravity on the contact angle using a precise drop-shape model. They showed that gravity has no effect on the equilibrium contact angle. They concluded that the effect that Pethica and Pethica [27] and Leja and Poling [28] attributed to gravity, indeed originates from the difference between the droplet shape assumed in their models and the actual droplet shape. However, Sakai and Fujii [32] subsequently found that the solid–liquid tension was enhanced by gravity when gas was adsorbed at a rough solid interface. Accordingly, they concluded that the apparent contact angle on rough surfaces, which was considered not to be influenced by gravity in a previous publication [31], can be changed by gravity.

Letellier et al. [33] used another approach describing the equilibrium of a droplet on a solid substrate based on the concept of *non-extensive thermodynamics*. In this approach, the contact angle changes with the drop volume according to a power law. Letellier et al. [33] concluded that the non-extensive thermodynamics approach provides descriptions of all systems found in the literature, i.e. systems which are described by Young's law, modified Young's law, and by other methods such as Wenzel and Cassie–Baxter. The approach also allows the description of complex cases such as systems with rough and heterogeneous surfaces.

4.2.2. INTERFACIAL INTERACTIONS OF CO_2/WATER/ROCK OR MINERAL SYSTEMS

In the last decade, a few studies have focused on the wettability of CO_2-water-rock/mineral systems [6, 7, 12, 34-37]. A number of authors have published experimental data for interfacial tensions between an aqueous phase (with or without electrolytes) and CO_2 at reservoir conditions [3, 10, 38-44]. However, there are no experimental data available on the interfacial tension of flue gas and water in the literature. Published data on interfacial tensions (IFT) between CO_2–rich and aqueous phases (with or without electrolytes) were experimentally determined using different techniques, i.e., the pendant-drop method, the sessile-drop method and the capillary-rise technique. For the pendant-drop method, a small CO_2-bubble is released from a needle-like inlet into the CO_2-saturated aqueous phase at the desired pressure and temperature. The IFT is determined from the analysis of the drop shape and the density difference between the CO_2-rich and the aqueous phase ($\Delta\rho$). Literature data on the CO_2–water IFT are scattered and occasionally contradict each other, in particular those close to the critical point of CO_2. This can be explained by the strong dependency of the IFT on equilibration conditions, i.e., phase compositions and accounting for the CO_2 dissolution into the water phase, the presence of impurities and accuracy of the density difference between the CO_2-rich and the aqueous phases. Additionally, the image-analysis method used and the accuracy of the temperature measurement have an impact on the determined values. In particular, the position of the thermocouple in the equipment needs to be close to the bubble surface, so that the temperature is accurately determined [43].

Chalbaud et al. [10, 39] extensively studied interfacial tensions of brine-CO_2 systems at different pressures, temperatures and salinities that are representative of CO_2 storage operations. Their results show that reliable wettability data are crucial for the accurate design and optimization of CO_2 sequestration strategies [39]. They also studied wettability alterations using 2D glass micro-models allowing the tracking of fluid distribution at different pressures and temperature conditions and different wettability scenarios. They found that CO_2 does not wet a strongly hydrophilic porous medium, whereas CO_2 can wet a rock if the solid surface is oil-wet or intermediate-wet [10].

The wetting properties and the interfacial interactions between (reservoir) brine, carbonate reservoir rock, and CO_2-rich phase at various temperatures and pressures were studied by Yang et al. [34]. They applied an axisymmetric drop shape analysis (ADSA) technique for image analysis to determine the dynamic and equilibrium (static or stable) contact angles. They found that the dynamic contact angles remain almost constant at a given pressure and a constant temperature because the sessile brine drop was saturated with CO_2. It was also found that the equilibrium contact angle increases with pressure and decreases with temperature. It was assumed that this might be attributed to the fact that the solubility of CO_2 in the aqueous phase is higher at higher pressures and lower temperatures.

Espinoza and Santamarina [12] collected literature data and conducted a number of experiments at pressures up to 20 MPa and a temperature of 298 K to obtain data on interfacial tensions, contact angles and diffusion for systems with CO_2, saline water and different substrates (amorphous silica, calcite, silica coated with oil, and polytetrafluoroethylene (PTFE)). They found that the contact angles on amorphous silica and calcite substrates remained nearly constant with pressure while dissolved NaCl in the aqueous phase increased the contact angle by approximately 20° for SiO_2 and approximately 4° for $CaCO_3$ [12].

The contact angle of CO_2 on mineral samples consisting of quartz, orthoclase, labradorite, calcite and biotite was determined by Mills et al. using the captive bubble technique [6]. Their findings show strongly water-wet to water-wet conditions for all experiments for which CO_2 is in the gaseous or supercritical state (5.5-13.8 MPa at 313 K). Their data shows that mica and calcite substrates become more water-wet as pressure is reduced, whereas quartz and biotite substrates become more water-wet with increasing pressure. Comparison of the determined contact angles for N_2 and CO_2 bubbles shows that the system containing CO_2 is less water-wet than one containing N_2 at low pressure; no clear trend was observed with increasing pressure. Although they reported contact angles as a function of contact circle radius, they did not draw any conclusion with respect to this dependency.

Jung and Wan [36] studied the wettability alterations of silica surfaces, aqueous phase and CO_2 system under pressures from 0.1 to 25 MPa while the NaCl concentration in the aqueous phase varies from 0 to 5.0 M. They found that, at pressures higher than the critical pressure of CO_2 (larger than 7.39 MPa), the contact angle increases steeply with increasing pressure up to a pressure of 10 MPa. For pressures below the critical pressure and pressures above 10 MPa, the contact angle remained almost unchanged. They showed that the contact angle increased with ionic strength.

Ameri et al. confirmed that the phase transition of CO_2 from a subcritical gas to a supercritical gas affects the wettability of a hydrophobic Bentheimer Sandstone [45]. However, when CO_2 was either subcritical or supercritical, no significant influence of pressure on the wetting properties of the hydrophilic Bentheimer was observed.

Saraji et al. [37] showed that CO_2 phase change and pressure variation do not significantly influence the water receding contact angles on the quartz surface. However, the water advancing contact angles increased from 5^o to 12^o with increasing pressure and temperature. They concluded that supercritical CO_2 changes the wettability of the quartz surface towards less water-wet conditions compared to subcritical CO_2.

In our previous works, we have investigated the effect of pressure on the wettability behavior of two samples of coal of different rank and Bentheimer sandstone [35, 46, 47]. We observed that the supercritical CO_2 could alter the wettability of coal from intermediate-wet to CO_2-wet [46, 47]. However, no clear trend of contact angle with pressure was observed for CO_2-water-Bentheimer sandstone system [35].

Although the wettability of idealized quartz surfaces has been experimentally investigated by several researchers [6, 12, 37, 40], the results partly contradict each other, particularly concerning the effect of the transition of CO_2 from subcritical to supercritical and the influence of pressure on wettability. These disagreements are mainly due to differences in experimental set-ups and methods, the preparation and treatment of mineral plates, the presence of contaminants and mostly the equilibrium condition of the aqueous phase with respect to the dissolution of CO_2. Moreover, to the best of our knowledge, there is only a small amount of experimental data available for contact-angle determination on natural rock samples [34, 35, 45-47] due to the complexity of the experimental determination of the contact angle on natural rock. In addition, there is limited information of wettability in the presence of flue gas [46, 47] and hardly any data are available on the effect of dissolved CO_2 in the aqueous phase on the wettability of sandstone reservoirs at high pressures and elevated temperature. In our study, the contact-angle determinations have been performed using natural rock surfaces without any chemical treatment. The results of these experiments might be a step forward in understanding the displacement behavior of fluids in sandstone reservoirs. Ultimately, this leads to a more accurate estimation of the CO_2 storage capacity in depleted gas reservoirs and saline aquifers.

4.3. EXPERIMENTAL

4.3.1. MATERIALS

CO_2 with a purity of 99.7 mol% and a synthetic flue gas consisting of a mixture of 20 mol% CO_2 and 80 mol% N_2 were used (Linde Gas Benelux). Since the percentages of the other components (i.e. NO_x and SO_x) usually found in industrial flue gas are in the percentage to ppm range [47], they were ignored in order to establish a wettability behavior without complicating it by reacting systems.

The rock slabs were taken from a sawed Bentheimer sandstone block from the Bentheim-area (Germany). XRD and XRF analyses of the samples were used to reconstruct a qualitative and quantitative mineral composition (Tables 4.1 and 4.2). The samples are mainly composed of quartz (~96%), which is homogeneously distributed throughout the rock matrix.

The average porosity and permeability of Bentheimer sandstone were about 20% and around 2 to 3 Darcy, respectively. The rectangular samples used in this study were 30 mm by 6 mm by 12 mm. Prior to the experiment, one side of the rock slabs was polished with a diamond paste of 10 to 250-µm, in order to minimize the effect of surface roughness on the contact angle. After that, the surface roughness was determined using a LEICA 3D stereo explorer. Additionally, a Phoenix Nanotom scanner was used to determine the grain framework, as well as the voids distribution of the sample at the micro level (6 µm voxel size).

Table 4.1. Synthetic mineral reconstruction of Bentheimer sandstone

Mineral	***Conc. wt (%)***
Quartz	91.70
Kaolinite	2.50
Montmorillonite	0.18
Orthoclase	4.86
Dolomite	0.26
Calcite	0.15
Hematite	0.16
Rutile	0.03
Pyrite	0.01
Ca-Phosphate	0.07
Halite (NaCl)	0.03

Table 4.2. XRD analysis of Bentheimer sandstone

Compound Name	***Conc. wt (%)***	***Absolute Error (%)***
Al_2O_3	1.931	0.04
CaO	0.208	0.01
Cl	0.020	0.004
Co_3O_4	0.001	0.0008
Cr_2O_3	0.005	0.002
Fe_2O_3	0.172	0.01
K_2O	0.827	0.03
MgO	0.064	0.008
Na_2O	0.022	0.004
NiO	0.002	0.001
P_2O_5	0.030	0.005
PbO	0.003	0.002
SO_3	0.020	0.004
SiO_2	96.616	--
SrO	0.002	0.001
TiO_2	0.072	0.008
ZnO	0.002	0.001
ZrO_2	0.004	0.002

4.3.2. MICROSCOPIC IMAGE ANALYSIS

Prior to the wettability experiment, 2-D and 3-D microscopic images were taken from the surface using a LEICA 3D stereo explorer. From the 3-D images, surface profiles were obtained, which were used for the P_a factor determination. The characterization of the surface roughness is based on the P_a factor, which is calculated according to an internationally recognized standard (EN ISO 4287), used to characterize the surface profiles. A more detailed description on determination of P_a value is given in Chapter 2.

For different Bentheimer sandstone samples, the surface roughness was characterized by means of their P_a factors. The smoothest sample with the smallest P_a factor was selected for the experiments to minimize the effect of roughness on the determination of the contact angle. 3-D images of samples with different P_a factors are shown in Fig. 4.2.

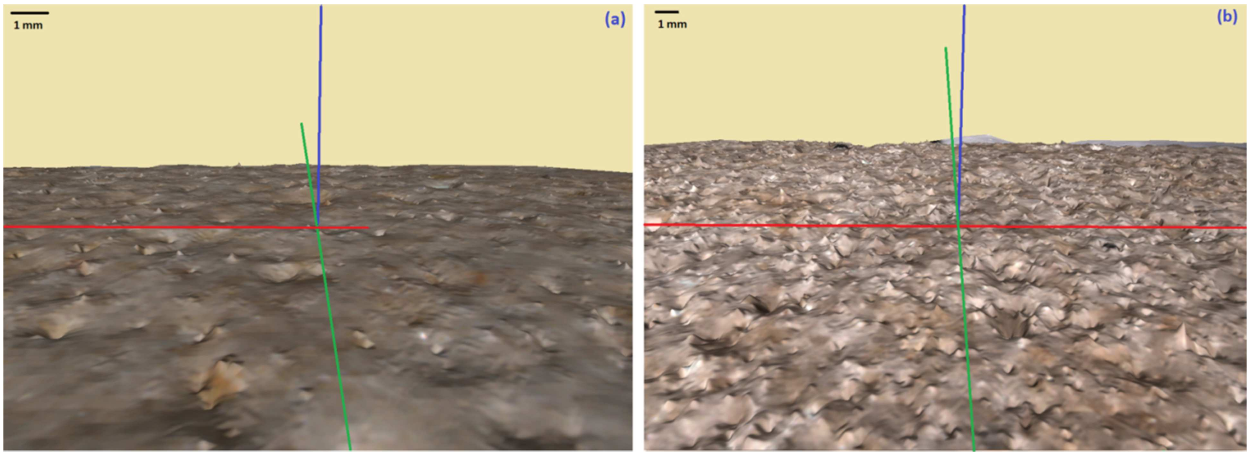

Figure 4.2. 3-D side view of the contact surface of Bentheimer sandstone samples with different roughness values (a) 0.032 mm and (b) 0.059 mm. The pictures were taken with a LEICA 3D stereo explorer. The blue, red and green lines give the orthogonal x, y, z directions used for the determination of factor P_a.

After the experiment, the surface roughness of the sample was again determined to investigate the degradation of the sample during the experiment. The P_a factor for the smoothest Bentheimer sample was 0.032 mm before and 0.035 mm after the experiment. The minor increase in surface roughness during the experiments could be within the accuracy range of the experimental method to determine the surface roughness or may have been the result of mineral reactions with water and CO_2. However, in comparison with samples of other rock types, like shale and coal, the increase in surface roughness was negligible. Therefore, it is considered that the roughness of Bentheimer sandstone remains constant during the experiments, even at high pressures.

4.3.3. MICRO CT-SCAN

The void distribution of the sample at the micro level was determined with a Phoenix Nanotom (180 kV/15 W nanofocus computed tomography (nanoCT) system. Fig. 4.3 shows the spatial distributions of voids and the surface roughness of the Bentheimer sandstone sample. In this figure, the effect of polishing of the surface is visible when the polished and unpolished sides of the substrate are compared.

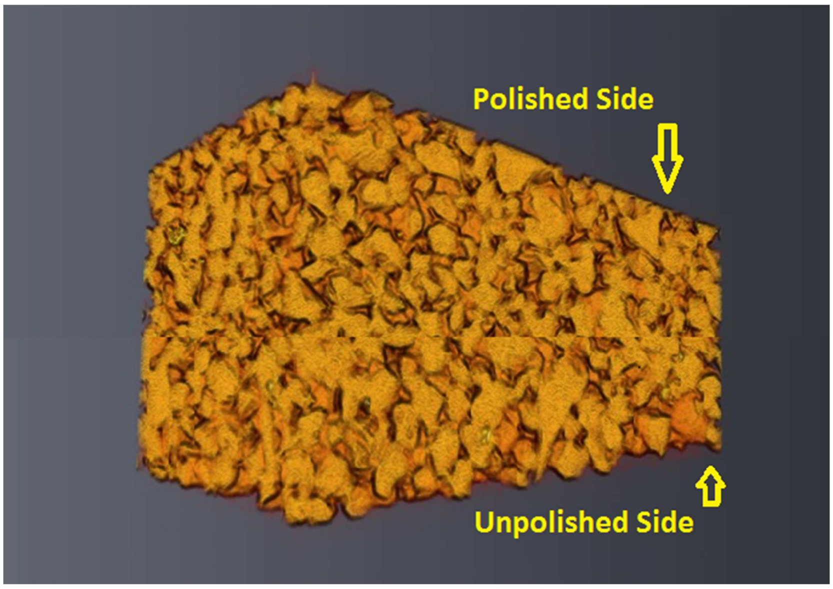

Figure 4.3. Three-dimensional view of side surfaces of the Bentheimer sample used. Note the sharp edge on the top side and many indentations on the bottom side (6 μm voxel size).

4.3.4. EXPERIMENTAL SET-UP AND PROCEDURE

In this study, the captive-bubble technique in a pendant-drop cell is used to capture CO_2 bubbles under different natural sandstone surfaces at varying pressures up to 15 MPa and a constant elevated temperature of 318 K. A schematic drawing of the experimental set-up is given in Fig. 4.4. The detailed description of the experimental setup and procedure can be found in Chapter 2.

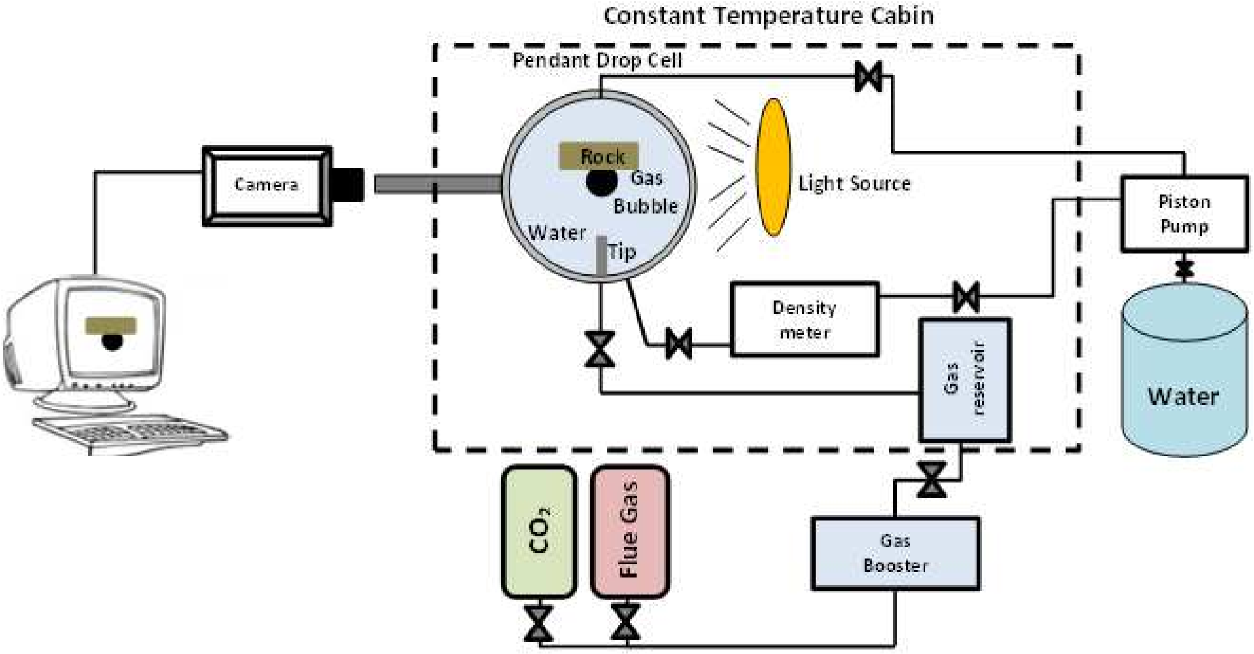

Figure 4.4. Schematic of the modified Pendant-Drop Cell (PDC) experimental set-up

4.4. RESULTS AND DISCUSSIONS

4.4.1. EXPERIMENTAL DETERMINATION OF INTERFACIAL TENSION

A modified version of the pendant-drop technique was used to experimentally determine the interfacial tension (IFT) between the gas bubble and the (pre-)saturated aqueous phase. A small gas bubble was released from a needle into the CO_2-saturated aqueous phase at various pressures and a temperature of 318 K. During the IFT experiment the bubble needs to stay attached to the needle. The IFT was determined from the analysis of the bubble shape and the density difference between the gas and the aqueous phase ($\Delta\rho$) using the DSA4 KRUESS© software (Chapter 2). To validate the experimentally determined IFT values of flue gas, the IFT of the CO_2/water system was first determined and thereafter compared to literature data [40, 42, 44] (Fig. 4.5). In this comparison, literature data which did not clearly indicate the experimental conditions were excluded. The IFT values of this study are in good agreement with those reported in literature in the pressure range investigated.

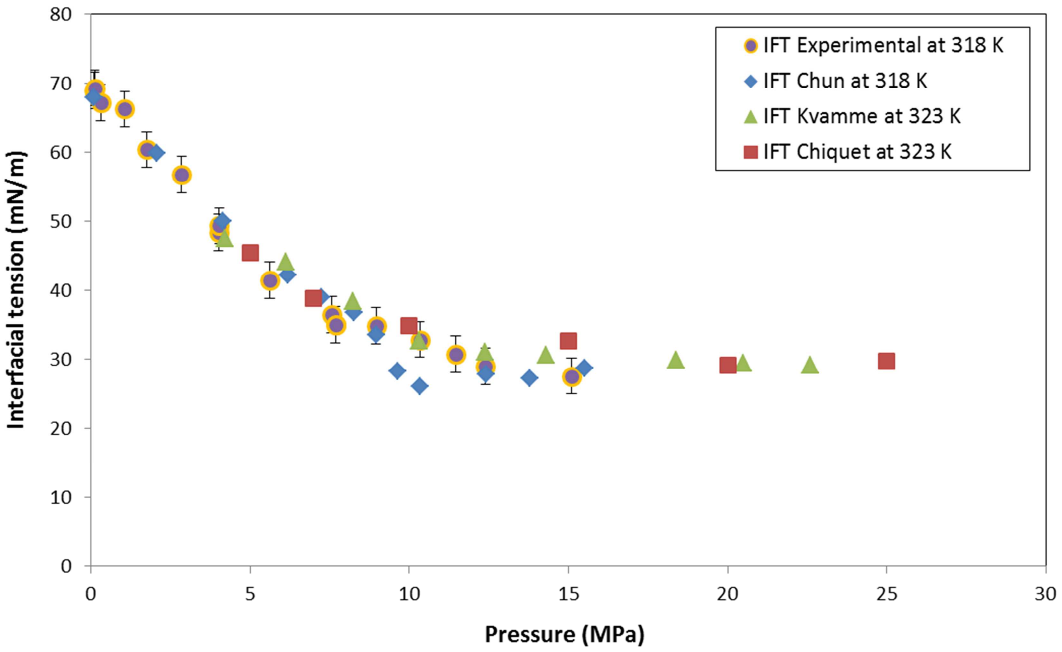

Figure 4.5. Interfacial tension as a function of pressure. Violet circle: IFT from this study at 318 K, blue rhombus: data of Chun et al. at 318 K [44], red square: data of Chiquet et al. at 323 K [40] and green triangle: data of Kvamme et al. at 323 K [42].

According to Fig.4.5, the IFT of the CO_2/water system decreases dramatically with increasing pressure up to 10 MPa. This behavior can be explained by increasing the density of the CO_2–rich phase and the aqueous phase due to an increased solubility of CO_2 in the aqueous phase (see also Fig. 4.6). The IFT is proportional to the density difference of the two coexisting phases. Thus, if the density difference decreases, the IFT decreases. Only when the solubility of CO_2 in the aqueous phase remains constant, along with the density of the aqueous phase, the IFT between the CO_2-rich and the aqueous phase appears to approach a stable value (see Figs. 4.5 and 4.6).

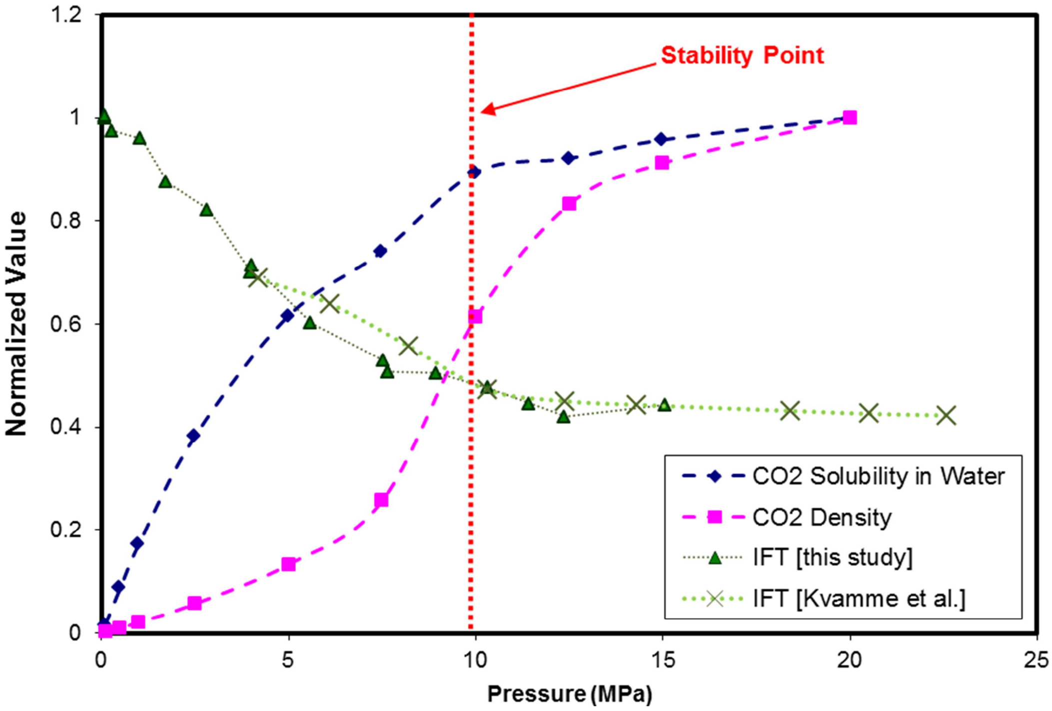

Figure 4.6. Normalized values of CO_2 density [48], the solubility of CO_2 in water [49] and IFT at a constant temperature of 318 K as a function of pressure. Dimensionless parameters are obtained by dividing the actual value by the respective maximum value in the given pressure range.

Fig. 4.7 illustrates the IFT data for synthetic flue gas/water, CO_2/water and N_2/water systems at a constant temperature of 318 K and various pressures. The IFT values of the nitrogen/distilled water system were obtained from Yan et al. (2001).

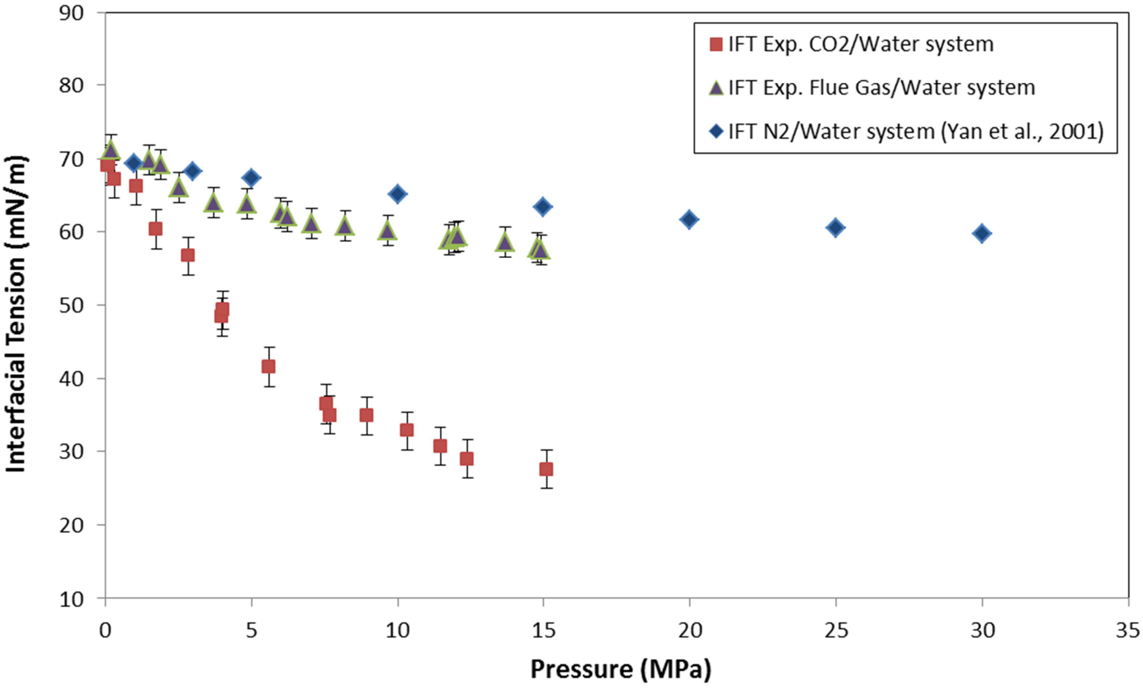

Figure 4.7. Comparison of experimentally determined IFTs for flue gas-water, CO_2/water and N_2/water systems at a constant temperature of 318 K.
Data of nitrogen/distilled water system are from Yan et al. (2001).

According to results in Fig. 4.7, the interfacial tension between flue gas and water is more similar to that of N_2 than to CO_2. This can be explained by the density data in Fig. 4.8, where, due to the high content of N_2 (80 mol%) in flue gas, the bulk density of flue gas is close to the density of nitrogen. Consequently, by considering the proportionality of IFT and the density difference (Young-Laplace equation), and from the density data (Fig. 4.8), it is expected that the IFT of a flue gas/water system behaves in a similar way to an N_2/water system. Accordingly, the IFT of these systems decreased smoothly with increasing pressure, because of the slight changes in densities with pressure (see Fig. 4.8).

Fig. 4.9 shows a buoyant bubble of CO_2 or flue gas in pre-saturated aqueous phase at various pressures. Fig. 4.9 (a) was taken at a pressure of 0.3 MPa, which is smaller than the critical pressure of CO_2, and Fig. 4.9 (b) at a pressure of 15.1 MPa, which is above the critical pressure of CO_2. The IFT of the latter is clearly smaller than that of the first one. However, the shape of the flue gas bubble showed no recognizable change from sub-critical (Fig. 4.9(c)) to super-critical (Fig. 4.9 (d)) pressure. This can also be seen in the way in which the bubbles are attached to the tip.

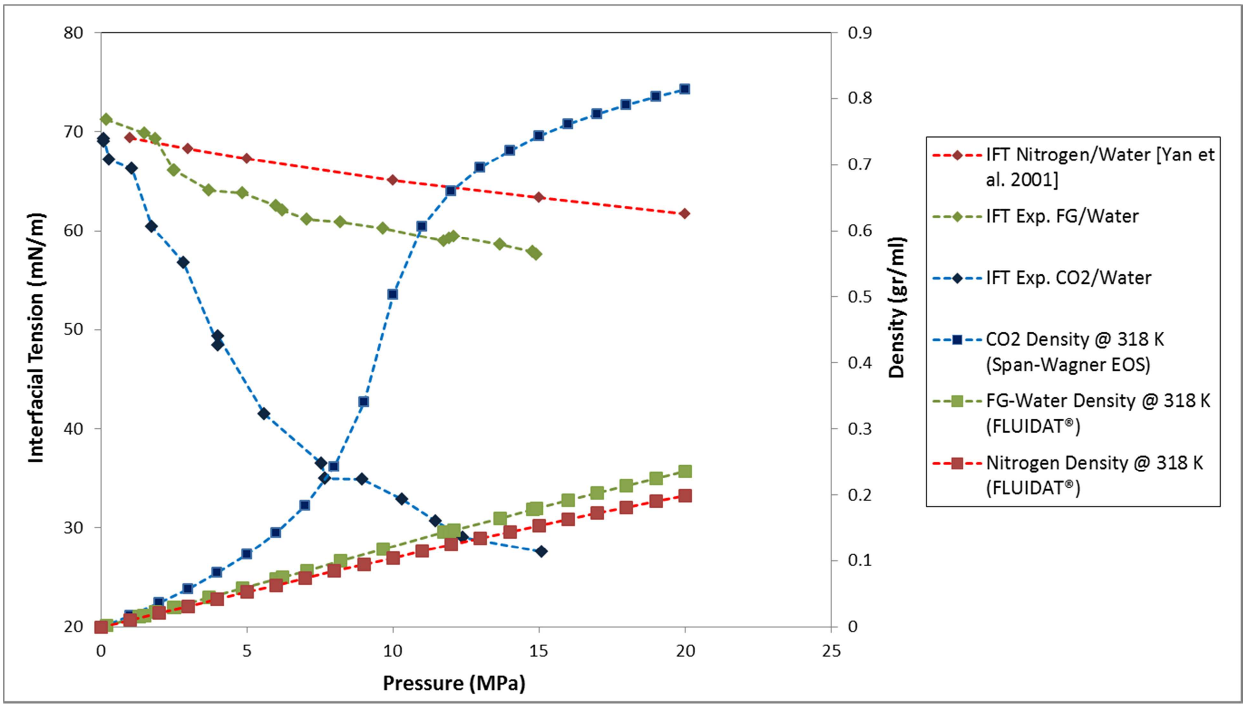

Figure 4.8. Density and interfacial tension variations with pressure in flue gas/water, CO_2/water and N_2/water systems at a constant temperature of 318 K.

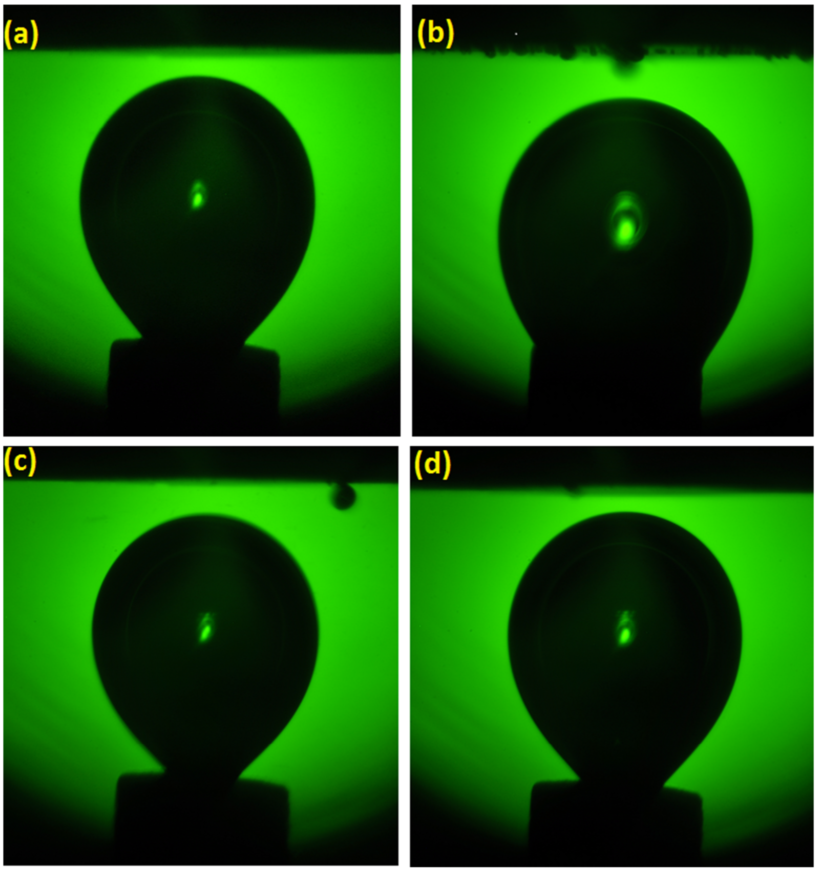

Figure 4.9. Digital images of a buoyant gas bubble in a pre-saturated aqueous phase at a constant temperature of 318 K (±0.1 K) and various pressures: (a) CO_2 bubble at 0.30 MPa, IFT=67.2 mN/m, (b) CO_2 bubble at 15.11 MPa, IFT=27.6 mN/m, (c) flue gas bubble at 1.32 MPa, IFT=69.9 mN/m and (d) flue gas bubble at 14.92 MPa, IFT=57.5 mN/m.

4.4.2. CONTACT-ANGLE DETERMINATION OF CO_2 IN UNSATURATED AQUEOUS PHASE

Two different types of contact-angle data are reported in the literature, namely stable (steady) and dynamic (transient or non-stable) contact angles [45, 47, 51]. Variation of the contact angle with time is generally regarded as indicating a ‘non-stable’ or ‘dynamic’ contact angle. If the contact angle experiment is conducted within the CO_2-saturated aqueous phase, variation of the contact angle over time is mainly due to the surface heterogeneity and roughness. In the case where the aqueous phase is not fully saturated with CO_2, the change in contact angle is related to the dissolution of CO_2 in the aqueous phase or water in the CO_2-rich phase [34, 47]. The second class of data provides important information on the interfacial interactions between the present phases, and more specifically, mass transfer between the liquid and the gas phase. In the unsaturated system, the change in contact angle is influenced by a number of mechanisms such as dissolution and bubble size variation, rather than by the wetting properties of the surface alone.

Fig. 4.10 shows the dynamic contact angles and CO_2 bubble radius at the apex as a function of time for different pressures. In the unsaturated system, the injected CO_2 bubble completely dissolves in the aqueous phase and disappears. In Fig. 4.10 (a), it can be seen that the bubble dissolution time depends on the initial radius of the bubble. However, comparison between experimental dissolution curves at 4.9 and 6.7 MPa reveals that if the initial bubble size is the same, pressure has no significant effect on the bubble dissolution behavior. This also confirms that the diffusion coefficient in the liquid phase is independent of pressure [52]. The change in the contact angle and droplet size over time (Fig. 4.10) can be divided into two regimes: the first regime (regime I) where a CO_2-rich bubble dissolves quickly in the aqueous phase and the second regime (regime II) where CO_2 gradually diffuses into the aqueous phase. For example, at 0.58 MPa after 180 seconds, 94% of the initial bubble volume dissolves in the fresh aqueous phase (Fig. 4.11), while dissolution of the rest of the bubble (6% of the bubble initial volume) takes 2300 seconds. This dissolution trend over time at 0.58 MPa is shown in the sequential digital images of the captive CO_2 bubble in Fig. 4.11. In the first regime, the contact angle increases continuously with time until it reaches a transition point. After this point and in regime II, the contact angle changes only slightly with time. The transition between fast and slow dissolution regimes is clearly visible, which allows the definition of a transition point, a transition time and a transition radius. The so-called transition point is the crossing point of the tangents to the curves in regime I and II which can be determined experimentally according to the evolution trend of the bubble size and contact angle with time at each specific pressure. According to Fig. 4.10, the transition from a strong change to an almost constant value (regime I to regime II) occurs at the same time for both contact angle and bubble radius, which can confirm the hypothesis that the contact angle depends on the bubble size.

The change in the contact angle over the time cannot be related to the wettability alteration of the surface from strongly to less water-wet. The wettability behavior of a surface is a material property. This means that the wettability does not change due to bubble shrinkage. The increase of contact angle with time, as seen in Fig. 4.10 (b), can be explained by bubble volume reduction (shrinkage) due to CO_2 dissolution in the aqueous phase. Because of the dependency of the contact angle on the bubble size (section 4.4.3), the bubble shrinkage has an effect on the change in the contact angles with time.

Table 4.3 summarizes the effect of pressure and initial bubble size on the contact angle and transition time. In this table, θ_{min} is the contact angle of the bubble with the initial bubble radius of R_{io} and θ_{max} is the last accurate detectable contact angle. For bubbles with a volume of less than 0.2 mm^3, the contact angle determination is not reliable due to the limited resolution and, thus, the high uncertainty in the bubble profile description. The data in Table 4.3 show that the transition time and radius at the transition zone for all experiments are in the range between 3 and 5 minutes, and 0.37 mm and 0.53 mm, respectively, regardless of the initial bubble size and pressure. Unfortunately, from the data at hand, the dependency of the contact angle at the initial bubble radius, θ_{min}, on the pressure cannot be deducted because the initial bubble sizes are not the same at different pressures.

Fig. 4.12 illustrates the evolution of the contact angle and the bubble parameters (i.e., bubble radius at apex, bubble height, diameter of the contact circle of three phases (base diameter), and aspect ratio (base diameter/bubble height)) with time at a pressure of 0.58 MPa and a temperature of 318 K. Only the curves at a pressure of 0.58 MPa are presented here, as the general behavior is the same at different pressures. As shown in Fig. 4.11 (a), the contact angle increases continuously to reach the transition zone after about 180 seconds. In this region, the bubble height, bubble radius at apex and base diameter decline at approximately the same rate (Fig. 4.12 (b)). The bubble shrinkage, represented by a continuous reduction in the contact length (base diameter) and bubble height, and due to the dependency of the contact angle on the bubble size, has an effect on the change in the contact angles with time. Consequently, if the contact-angle determination is performed in the first regime, the results are highly affected by the bubble size. In the second regime, the contact angle and bubble parameters vary with time at a much slower rate (Fig. 4.12). This confirms that a reliable experimental contact-angle determination has to be conducted in a saturated (fully or quasi) aqueous phase (Chapter 2, Fig. 2.4) to minimize the effect of dissolution (for a more detailed discussion see section 4.4.3).

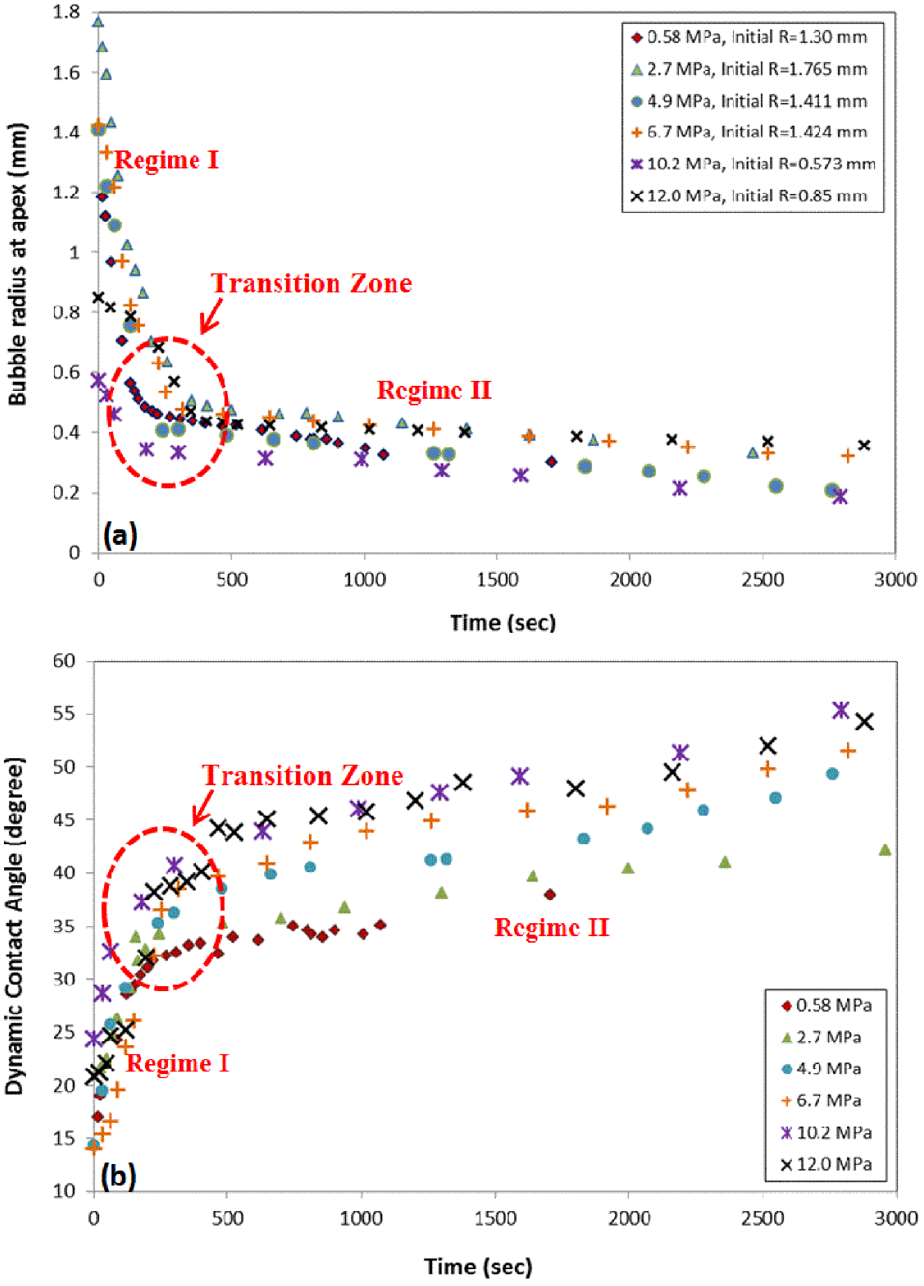

Figure 4.10. (a) Dynamic contact angle and (b) Bubble radius at apex over time for different pressures and at a constant temperature of 318 K.

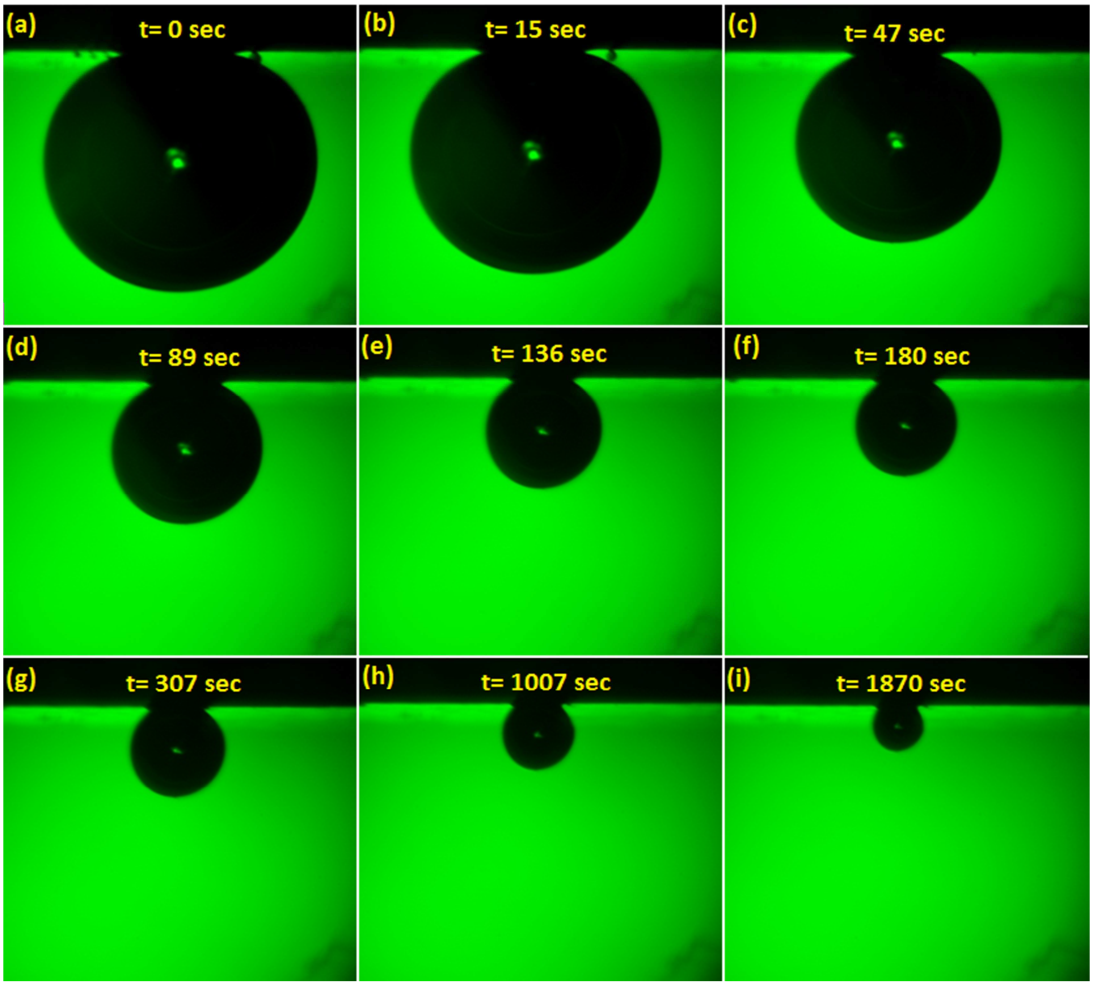

Figure 4.11. Sequential digital images of the captive CO_2–rich bubble on a Bentheimer surface at 0.58 MPa and 318 K: (a) t=1 sec, R_0=1.30 mm, V_b=7.71 μl, θ=16.3°, (b) t=15 sec, R_0=1.18 mm, V_b=5.99 μl, θ=17°, (c) t=47 sec, R_0=0.97 mm, V_b=3.36 μl, θ=22°, (d) t=89 sec, R_0=0.71 mm, V_b=1.37 μl, θ=24.3°, (e) t=136 sec, R_0=0.54 mm, V_b=0.621 μl, θ=28.9°, (f) t=180 sec, R_0=0.48 mm, V_b=0.46 μl, θ=30.4°, (g) t=307 sec, R_0=0.44 mm, V_b=0.35 μl, θ=32.5°, (h) t=1007 sec, R_0=0.35 mm, V_b=0.182 μl, θ=34.2°, (i) t=1870 sec, R_0=0.24 mm, V_b~0.053 μl,

θ=n.a. (due to the resolution limitation.)

Table 4.3. Contact angle and other parameters of CO_2 gas bubble at various pressures and a constant temperature of 318K

Pressure (MPa)	**R_{io} Bubble (mm)**	**θ_{min} (°)**	**θ_{max} (°)**	**Transition time (sec)**	**Radius at transition point (mm)**	**Initial CO_2 bubble mass (mgr)***	**CO_2 solubility in water (mol/kg)$^+$**
0.58	1.300	16.3	34.6	180	0.47	0.060	0.1219
2.7	1.765	14.4	47.8	200	0.50	1.018	0.5117
4.9	1.411	19.5	52.5	240	0.41	1.082	0.8193
6.7	1.424	15.4	59.8	250	0.53	1.783	1.0052
10.2	0.573	24.36	64.53	180	0.37	0.361	1.1923
12.0	0.850	20.85	66.37	320	0.47	1.472	1.2199

$^+$ Duan et al. [53]

* $m_b=\rho_{CO_2} \times V_b$

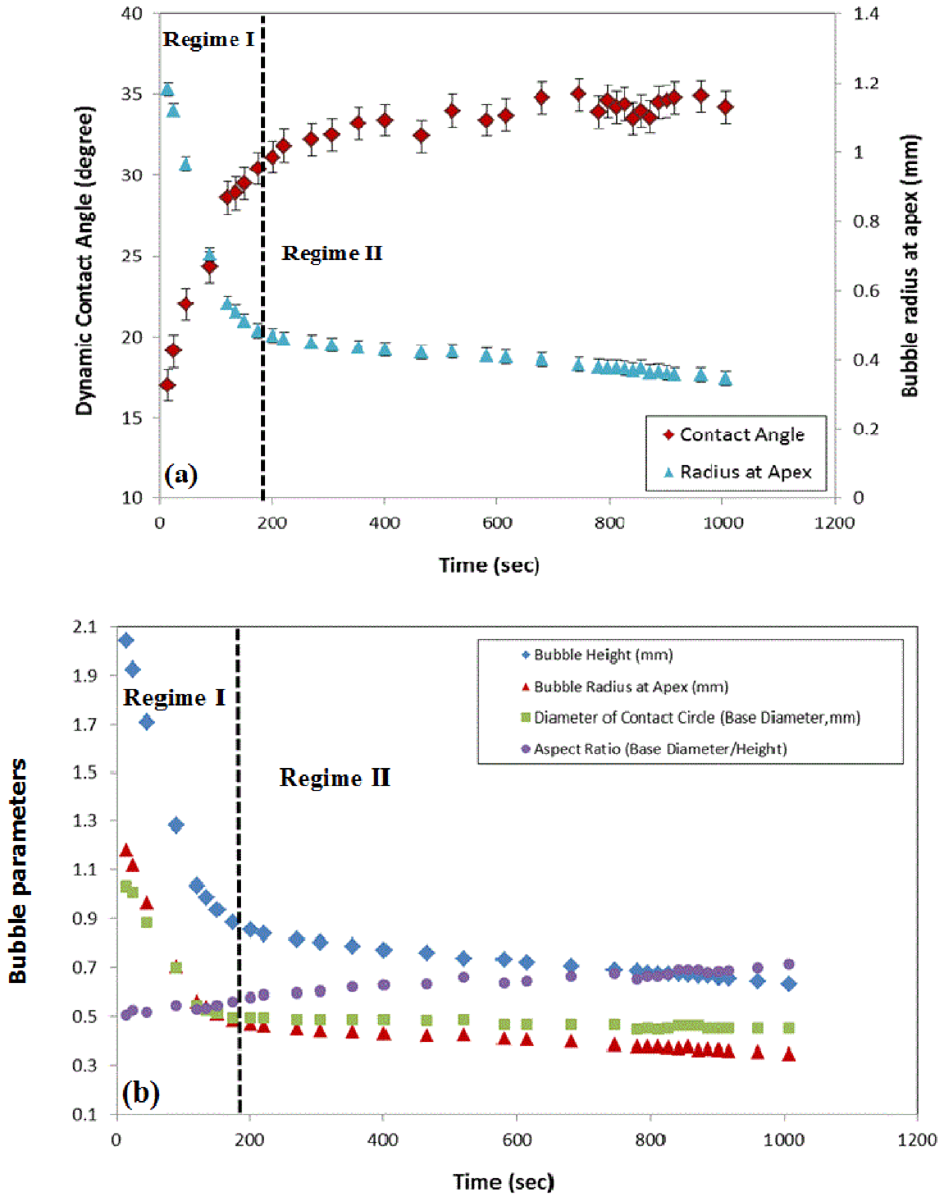

Figure 4.12. Evolution of (a) the contact angle and (b) bubble parameters with time at 0.58 MPa and 318 K.

4.4.2.1. CO_2 bubble dissolution

To better understand the origin of the two regimes observed at various pressures (Fig. 4.10 (a)), the mass transfer between the gas bubble and aqueous phase was calculated based on a mass balance of the bubble interface using Fick's law. The equations and their derivations are given in Appendix 4.1 and Appendix 4.2.

It becomes clear from Fig. 4.10 (a) that the bubble radius decreases significantly in regime I, i.e., has a sharp slope at early times of the experiment. However, the slope of the curve decreases with time, meaning that the mass-transfer rate decreases. The mass-transfer process experimentally observed over the complete time period (Fig. 4.10 (a)) cannot be described using a single mass-transfer or diffusion coefficient. Considering mass transfer separately in the two regimes, the curves could be represented with the general mass-transfer model using two different mass-transfer coefficients i.e., k_{L1} and k_{L2}.

The mass-transfer coefficients were obtained from fits of the model to the experimental data using Eq. A1.8. Comparison of the mass-transfer coefficients obtained (Fig. 4.13) reveals that the mass-transfer coefficient describing the behavior in regime I, k_{L1}, is about two orders of magnitude larger than the mass-transfer coefficient describing the second regime, k_2. Two different mass-transfer regimes were also detected by Vasconcelos et al. [54] in the dissolution of single bubbles of low-solubility gases in water with very little contamination. The results of the system at hand are in good agreement with the trend observed by Vasconcelos et al. [54], which quantitatively confirms the fast dissolution regime observed in the experiments.

Further, the diffusion of CO_2 into the aqueous phase is described using Fick's first law (Appendix 4.2). Fig. 4.14 shows the curves of the bubble radius as a function of time. The blue triangles display the experimental values and the red solid line is the description with Fick's law using a single diffusion coefficient of 3.07×10^{-9} m^2/s for both regimes and for all pressures at 318 K [55]. The two cases are described in Appendices 4.1 and 4.2, respectively. According to Fig. 4.14, Fick's law cannot represent the experimental data using a single effective diffusion coefficient; the experimental data of the bubble radius in regime I decrease much faster than predicted by the model. This is an indication of an accelerated mass transfer of CO_2 into the water in regime I, which cannot simply be explained by the diffusion process. However, by separately considering the short-term and long-term mass-transfer behavior, it is possible to describe the regimes individually with two effective diffusion coefficients.

Applying this method, the bubble radius as a function of time could be described very well with Fick's law (green dashed and dark blue dot-dashed lines in Fig. 4.14). All parameters, both obtained from the fit and taken from the literature, are summarized in Table 4. In this table, k_{L1} and k_{L2} are the mass-transfer coefficients determined from fits of the model to the experimental data and D_1 is the effective diffusion coefficient used for regime I obtained from a fit of Fick's law to the experimental data. $C_{co_2}^{s}$ is the concentration of CO_2 at the bubble interface, i.e., the solubility of CO_2 in water at the specific pressure taken from the literature [53]. $C_{co_2}^{b_2}$ gives the CO_2 concentration in the bulk phase in regime II and is obtained from the best fit of Fick's law to the experimental data. It is assumed that the CO_2 concentration in the bulk ($C_{co_2}^{b_1}$) is initially zero in regime I. Based on the slow dissolution rate of regime II, this regime is mainly considered to be a diffusion-dominant process. Therefore, the effective diffusion coefficient of regime II (D_2) is assumed to be 3.07×10^{-9} m^2/s, according to the diffusion coefficient of CO_2 into the water at 318 K [55].

Comparison of the data in Table 4.4 reveals that:

- The short-term mass-transfer coefficient (k_{L1}) is about 1½ to 2 orders of magnitude larger than the mass-transfer coefficient of CO_2 in regime II (k_{L2}). In addition, the adjusted short-term effective diffusion coefficients (D_1) is about three times larger than the molecular diffusivity of CO_2 in water (D_2) found in the literature [55]. These findings confirm quantitatively that, under the conditions considered, a second process in addition to the diffusion mechanism contributes to the CO_2 dissolution regimes.

- For bubbles with similar initial radii, the values obtained from fits for k_{L1} and D_1 increase with increasing pressure. This behavior is in agreement with the trend observed by Farajzadeh [56].

- From the data at hand, it can be concluded that the mass-transfer coefficient k_2 is not affected by pressure. This is in agreement with the fact that, in general, the diffusion of a gas into a liquid phase is independent of the pressure [52]. This pressure independency confirms the assumption of a diffusion-dominant process in regime II.

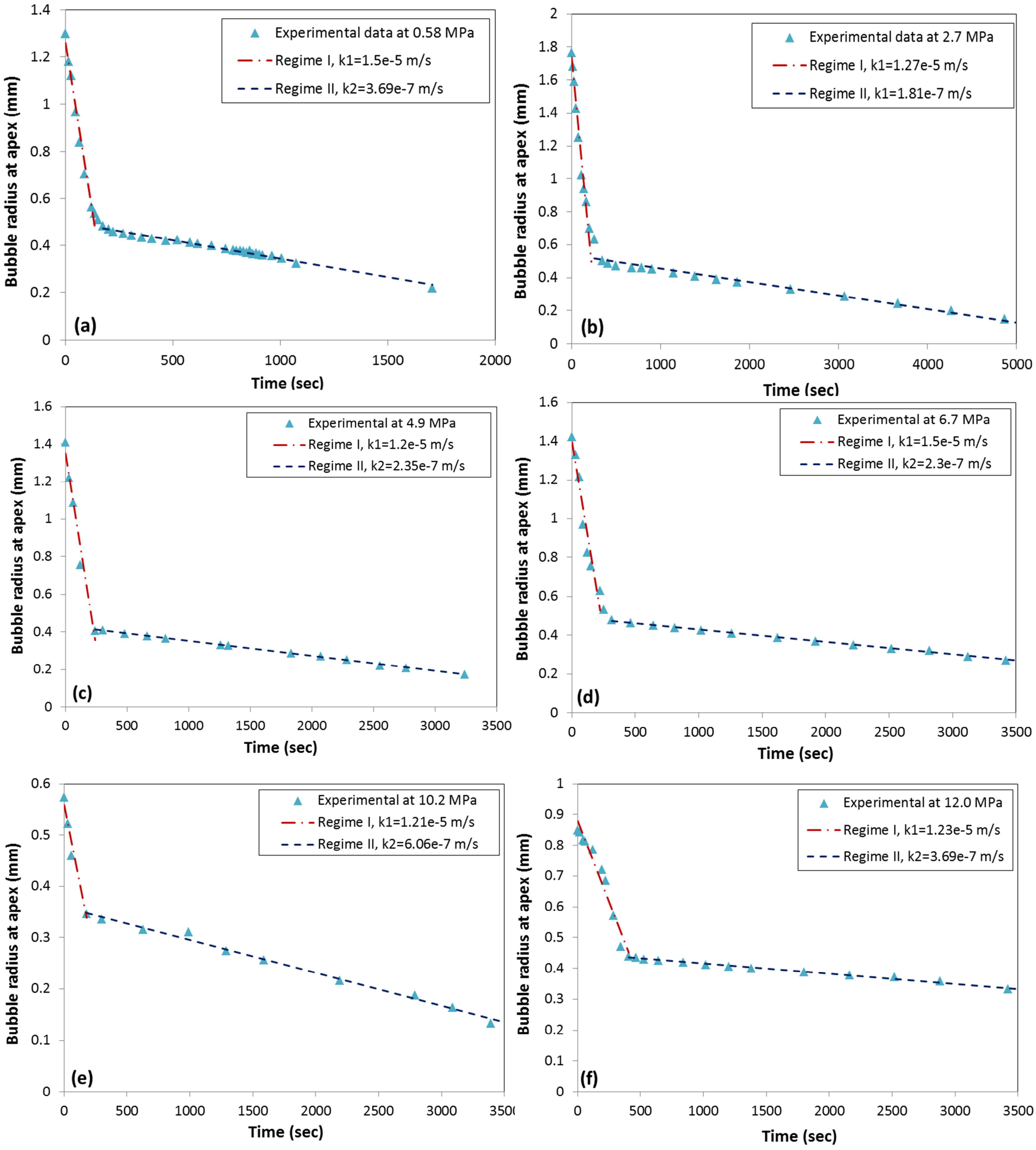

Figure 4.13. Bubble radius as a function of time at various pressures and a constant temperature of 318 K. The symbols display experimental data and the lines give the fit of the mass-transfer model (as given in Appendix 4.1) to the experimental data; red dot-dashed line: fit to data of regime I and the blue dashed line fit to data of regime II.

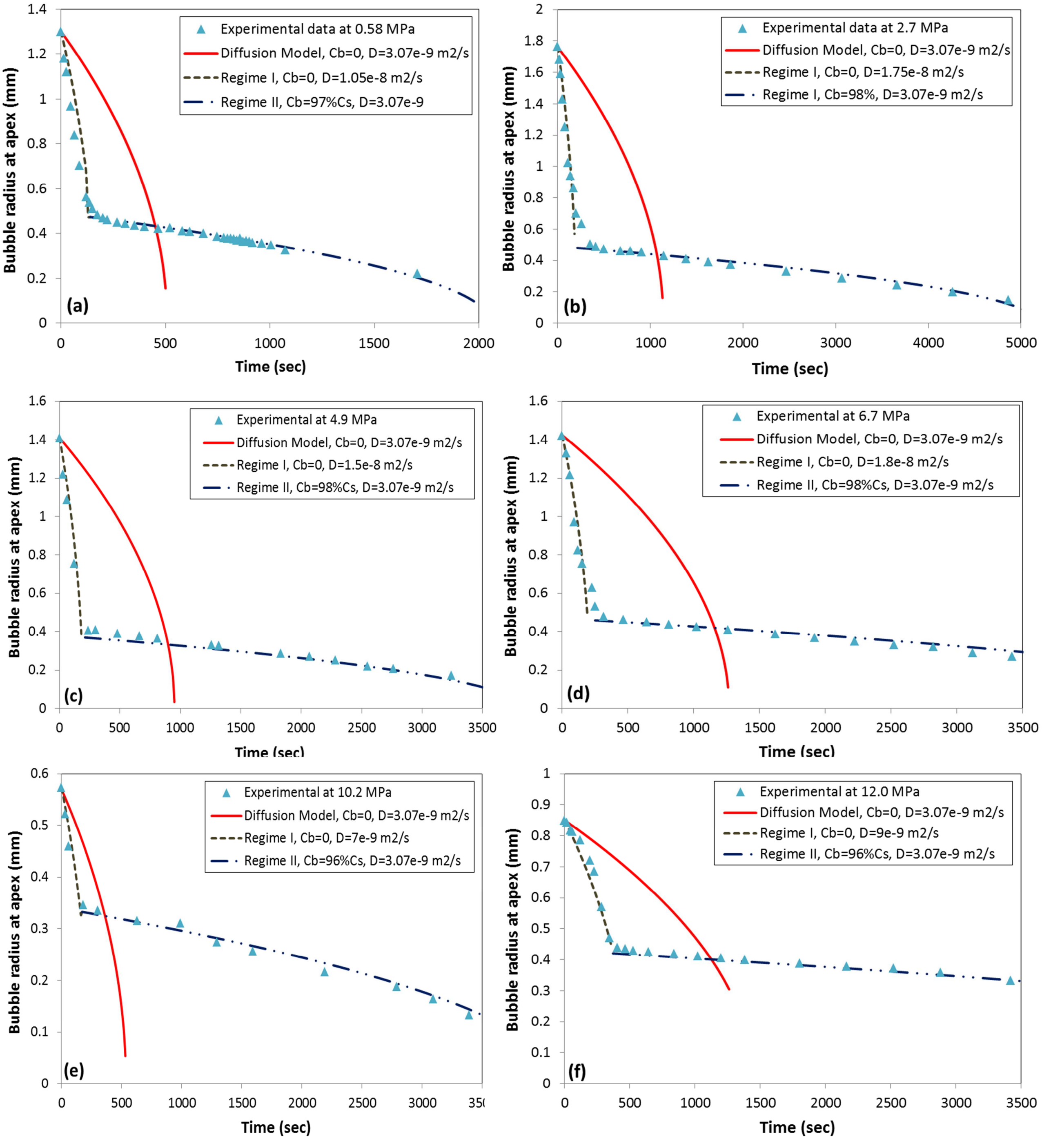

Figure 4.14. Bubble radius as function of time at various pressures and a constant temperature of 318 K. Blue triangles display experimental data and the lines give the description with Fick's law (see also Appendix 4.2); red line: description with Fick's law assuming a bulk phase of pure water (no CO_2 initially dissolved in the aqueous phase) and using a molecular diffusion coefficient of CO_2 in water, D, from [55]; green dashed line: description of regime I with Fick's law assuming a bulk phase of pure water. For regime I, D is obtained from the best fit with the experimental data; the blue dot-dot-dashed line: description of regime II with Fick's law with assumption of diffusion-dominant process (D from [55]). For regime II, the CO_2 concentration in the bulk is obtained from the best fit of the model to experimental data.

Table 4.4. Experimental and model parameters obtained from the description of the bubble radius as a function of time at various pressures and a temperature of 318 K.

Pressure (MPa)	**$k_{L1}\times10^5$ (m/s)**	**$k_{L2}\times10^7$ (m/s)**	**$D_1\times10^8$ (m^2/s)**	**$C_{co_2}^{b_2}$ (µmol/L)**	**$C_{co_2}^{b_2}/C_{co_2}^{s}$ (-)**	**R_{io} (mm)**	**Transition Time (sec)**	**Radius at Transition Time (R_{o2}) (mm)**
0.58	1.05	3.69	1.05	0.118	0.98	1.30	185	0.48
2.7	1.27	1.81	1.75	0.498	0.97	1.76	200	0.74
4.9	1.20	2.35	1.50	0.805	0.98	1.41	240	0.39
6.7	1.50	2.30	1.80	0.981	0.98	1.42	250	0.47
10.2	1.21	6.06	0.70	1.141	0.96	0.57	180	0.35
12.0	1.23	3.69	0.90	1.167	0.96	0.85	320	0.43

In order to explain the accelerated mass transfer observed in regime I, different mechanisms have been considered, i.e., spontaneous imbibition of CO_2 into the rock pores, density-driven natural convection [56-58], the effect of surface contamination (stagnant-cap model) [54], the relative motion between the bubble and the aqueous phase when a bubble rises through the aqueous phase (internal circulation theory) [52] and Marangoni effect [57, 58]. CO_2, as the least wetting phase, cannot overcome the capillary pressure and consequently penetrate into pore spaces [35], at least for this bubble size. Therefore, accelerated mass transfer, observed in regime I, cannot be originated by the spontaneous imbibition of CO_2 into the pores.

The onset of natural convection is determined by the Rayleigh number (*Ra*) and density-driven natural convection occurs in bulk solutions when *Ra*>2100. The calculation of this dimensionless number for the system at hand (Appendix 4.3) reveals that diffusion is accelerated by density-driven natural convection in regime I. Considering the dimensions and conditions of the system at hand, it is expected that the entire bubble dissolves quickly by natural convection since *Ra*>2100. However, after a certain time, known as the transition time, dissolution becomes less convection-dominated and more diffusion-dominated. The density difference in regime II is smaller, but according to this criterion (*Ra*>2100), natural convection should occur in regime II as well. Nonetheless, the results indicate that the rate of mass transfer is what one would expect for diffusion with no convection. The sudden change in the mass-transfer rate might be attributed to the presence of a small amount of impurities in the aqueous phase. The measured 273 ppm Ni and 64 ppm Cu may block the interface. After accumulation of the contaminant material at the bubble surface, the mass-transfer area of the bubble decreases, which causes a reduction of the mass transfer at the interface (stagnant-cap model) [54].

Finally, in regime II, molecular diffusion is the controlling mechanism for mass transfer between the CO_2-bubble and the aqueous phase. Due to the formation of a thin CO_2-saturated water film around the bubble, the driving force (concentration gradient) for diffusion reduces. Consequently, the dissolution of the bubble takes longer than the dissolution of the bubble in the pure water phase. According to the fit of Fick's law with the experimental data, the CO_2 concentration in the bulk phase in regime II ,$C_{co_2}^{b}$, is about 97%±1% of the maximum solubility of CO_2 in water at the given temperature and pressure. These findings are in good agreement with the experimental results of Farajzadeh [56].

4.4.3. CONTACT-ANGLE DETERMINATION OF CO_2 AND FLUE GAS IN PRE-EQUILIBRATED AQUEOUS PHASE

Fig. 4.15 shows the evolution of the bubble radius and contact angle with time at 0.58 MPa for different phase conditions and overall compositions of the CO_2/water system. To determine whether the system is in the one-phase or two-phase region, the phase diagram of the CO_2/water system is used from the literature (Chapter 2, Fig. 2.4). For an unsaturated system (one-phase region), the amount of CO_2 in the system is smaller than the maximum amount which can be dissolved in the aqueous phase at a given temperature and pressure. Hence, when adding a CO_2 bubble, the bubble dissolves completely in the aqueous phase (Fig. 4.15 (a)).

If the amount of CO_2 in the system, before releasing a new bubble, is such that the composition describes a point on the phase envelope (curve describing the border between one-phase and two-phase region), then the system is referred to as quasi-saturated in this work. In this system, by adding a CO_2 bubble, the pressure is initially slightly increased. Due to the fact that the amount of CO_2 which can be fully dissolved in the aqueous phase increases with pressure, the addition of CO_2 would mean that the overall system composition moves slightly from the phase envelope to the one-phase region (unsaturated case). Therefore, one refers to this case as ‘quasi-saturated’. The data show that, for this situation, the bubble dissolution rate is smaller than the dissolution rate in the unsaturated system. In the quasi-saturated system, the bubble initially dissolves slowly and the bubble size decreases. When equilibrium is established, the bubble size remains constant (Fig. 4.15 (b)). The time to reach equilibrium depends on the initial composition of CO_2 in the water-rich phase.

In the fully-saturated system, equilibrium is already established when injecting CO_2 into the system. Still, releasing CO_2 in the equilibrated system causes a slight disturbance, which can be recognized by an initial volume reduction of the bubble with time (Fig. 4.15 (c)). After introducing the CO_2 bubble, mass transfer occurs between the bubble and the aqueous phase. The driving force for this process is the difference in chemical potentials of each specific component in the two coexisting phases. The time required to reach a stable bubble size depends on the chemical potential gradients in the two phases. Since adding a CO_2 bubble to the equilibrated system only disturbs the equilibrium slightly, the mass transfer between the bubble and the aqueous phase is negligible and does not affect the contact angle so that the wetting properties of the substrate are determined. For such a system, any variation of the contact angle with time can be attributed to surface heterogeneity and roughness.

According to Fig. 4.15, the contact angle variation is proportional to the change in bubble volume which shows the dependency of the contact angle on the bubble size in the system at hand. These observations are in agreement with the results discussed in section 4.4.2. The error bars in these figures are given based on the standard error of the values which are calculated by:

$$S.E. = \frac{STDEV}{\sqrt{n}} \quad , \tag{4.7}$$

where S.E. is the standard error, *STDEV* is the standard deviation and n is the number of data points.

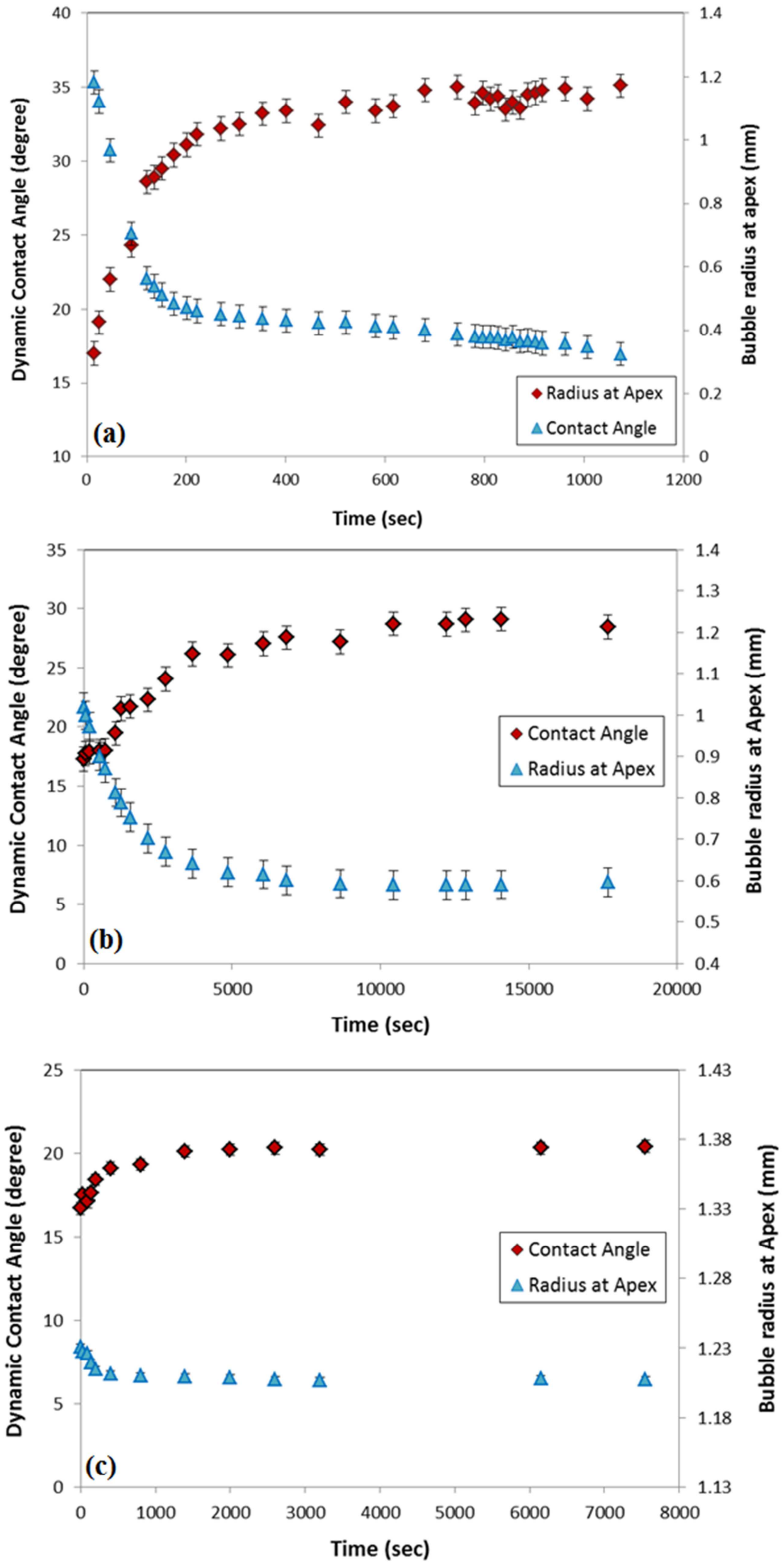

Figure 4.15. Evolution of bubble radius (shown as blue triangles at right y-axis) and contact angle (shown as red squares at left y-axis) over time at 0.58 MPa and 318 K in (a) unsaturated, (b) quasi-saturated and (c) fully-saturated aqueous phase. The error bars show the standard error of the values.

In Table 4.5, the basic parameters allowing the direct comparison of experiments in the unsaturated, quasi-saturated and fully-saturated system at 0.58 MPa are given. θ_{min} is the contact angle of the initial bubble with the radius of R_{io}. In the unsaturated system, the CO_2 bubble disappeared after 2700 seconds. In the quasi-saturated system the bubble first shrank and then became stable after 4800 seconds. In the fully-saturated system, the stable bubble was obtained after 180 seconds. In the two latter systems, R_{Final} and θ_{Final} are the bubble radius and the contact angle after establishing the equilibrated bubble.

Table 4.5. Parameters characterizing the experiments at 0.58 MPa in the unsaturated, quasi-saturated und fully-saturated system.

Aqueous Phase Condition	R_{io} **(mm)**	θ_{min} **(degree)**	R_{final} **(mm)**	θ_{final} **(degree)**	**Time (sec)**
Unsaturated (fresh water)	1.18	17	0	35.1	2700
Quasi-saturated with CO_2	1.02	17.3	0.62	26.06	4800
Fully-saturated with CO_2	1.23	16.7	1.21	20.4	180

From the data at hand, it can be concluded that a reliable contact-angle determination should be conducted in a pre-equilibrated (fully or quasi saturated) aqueous phase to eliminate dissolution effects. Dissolution affects the contact-angle determination due to the constantly changing bubble size; this means that the system continuously changes its conditions, thereby changing the contact line and the contact angle.

Therefore, all contact-angle determinations in this work were performed using a fully CO_2-saturated aqueous phase to evaluate the wetting properties of Bentheimer sandstone/water/CO_2 excluding dissolution effects. Fig. 4.16 illustrates the effect of pressure on the stable contact angle at a temperature of 318 K. The values of the contact angle in Fig. 4.16 are scattered so that the derivation of a relation between pressure and contact angle cannot be formulated in straightforward manner. The maximum variation of the contact angle of about 13 degrees was observed for experiments at 4.97 MPa. Another large variation of ca. 10 degrees was found for the experiments at 1.04 MPa. There is extensive experimental evidence in the literature confirming that the contact angle of a captive bubble/sessile droplet on a horizontal surface not only depends on the physical properties of the gas, liquid and solid phases but also varies with the bubble/droplet size [15-18]. In Fig 4.17, the stable contact angle is plotted as a function of bubble radius. It can be seen that the contact angle decreases with bubble size. Furthermore, since the bubble size does not depend on the pressure (Fig. 4.18), it explains the scattering of the contact angle as function of pressure (Fig. 4.16). Fig. 4.19 shows the sequential digital images of the CO_2–rich bubble captured on the Bentheimer rock at 4.97 MPa and 318 K. It can be seen that when the bubble size decreases, the bubble shape asymptotically approaches a spherical shape.

To understand the observed contact-angle dependency on the bubble size, different scenarios have been considered, i.e., surface roughness and hysteresis [15, 19], gravity effects on droplet geometry [21] and line tension [17, 20] (explanations in Chapter 4.2.1). Due to the contradictory results regarding the line-tension determination in the literature and following on from the results at 1.04 and 4.97 MPa, which are given in Appendix 4.4, the line-tension concept is not considered a proper method to describe the dependency of the contact angle on the bubble size for the system at hand, since surface non-ideality and roughness have a significant influence on the reliability of this method [15].

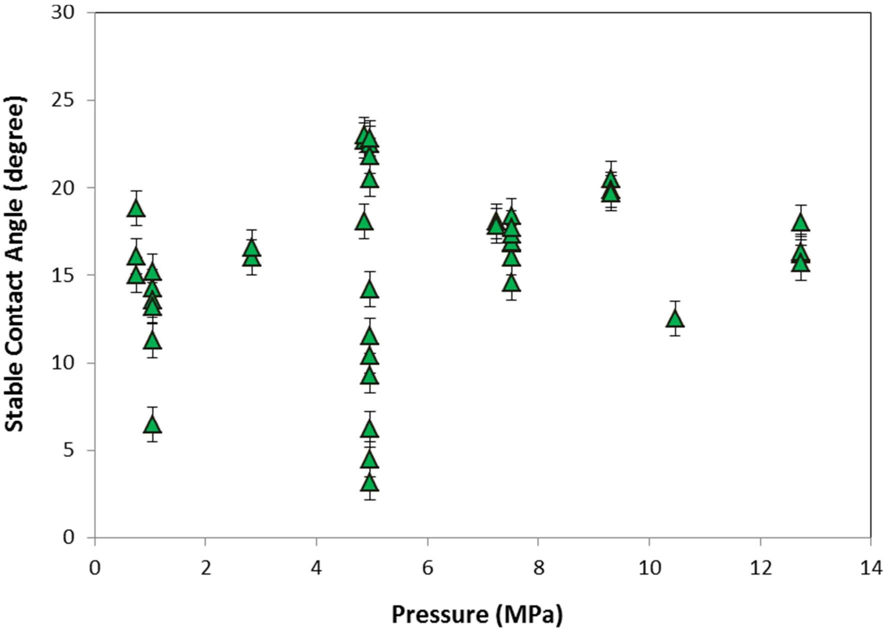

Figure 4.16. Stable contact angle (fully-saturated system) as a function of pressure at a temperature of 318 K. The error bars show the standard error of the values.

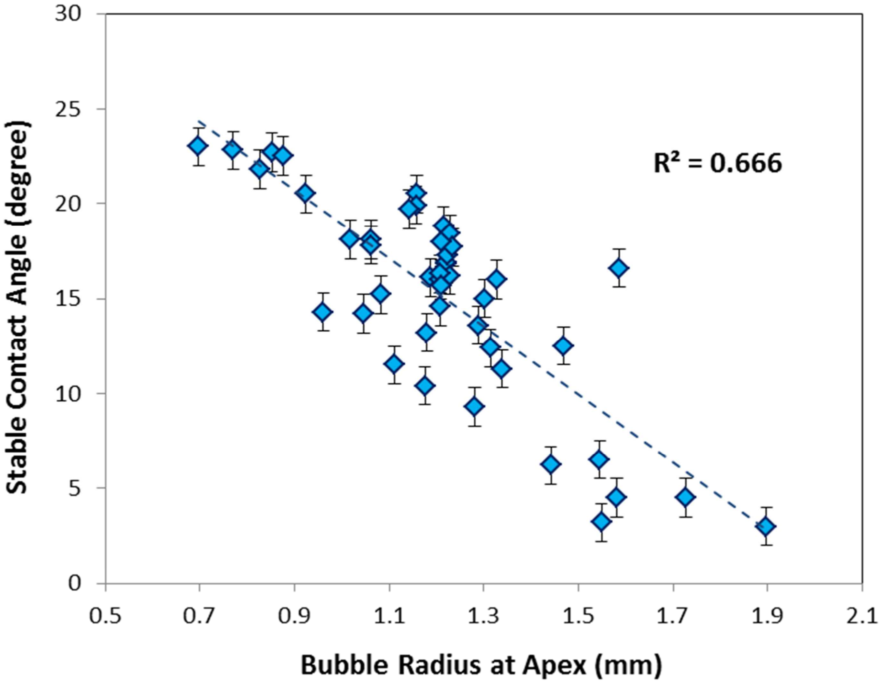

Figure 4.17. Stable contact angle as a function of the bubble radius at the apex at various pressures and a temperature of 318 K. The error bars show the standard error of the values.

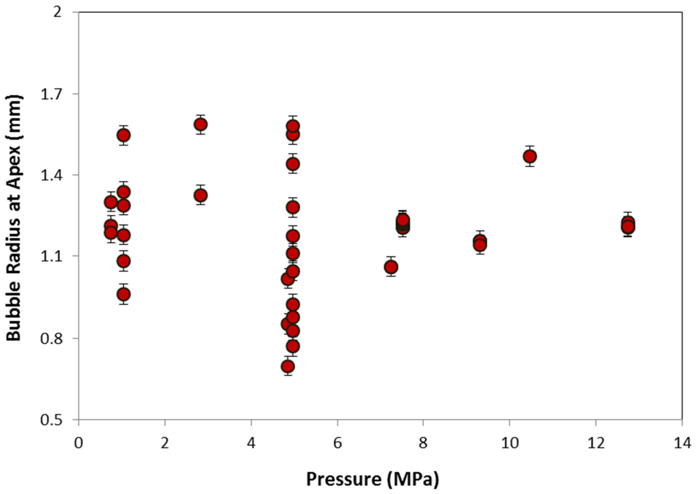

Figure 4.18. Bubble radius at the apex as a function of pressure at a temperature of 318 K.

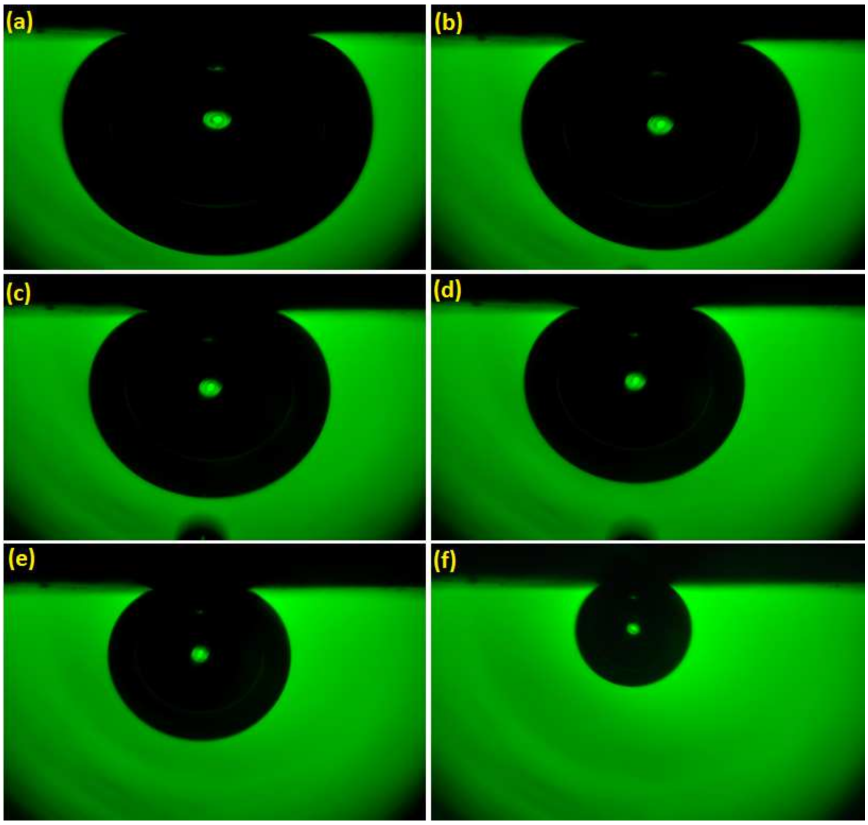

Figure 4.19. Sequential digital images of the captive CO_2–rich bubble on the Bentheimer rock at 4.97 MPa and 318 K: (a) R_0=1.90 mm, V_b=32 μl, θ=3.1°, (b) R_0=1.73 mm, V_b=23.56 μl, θ=4.5°, (c) R_0=1.55 mm, V_b=16.52 μl, θ=6.5°, (d) R_0=1.34 mm, V_b=11.97 μl, θ=11.3°, (e) R_0=1.08 mm, V_b=9.09 μl, θ=13.6°, (f) R_0=0.77 mm, V_b=1.93 μl, θ=22.8°.
Each picture was taken 30 seconds after the release of the bubble. When the bubble size reduces, the geometry of the bubble approaches a spherical shape.

4.4.3.1. Surface roughness

Surface roughness and/or heterogeneity decrease the accuracy of the contact-angle determination and increase the chance of hysteresis [59]. To minimize the effect of roughness in this work, fine-polished samples were used. The surface roughness was characterized using the so-called P_a factor which was determined using the Leica 3D stereo explorer (see section 4.3.2). The results in Figs. 4.16-19 were obtained by contact-angle determination on a sample with a P_a of 0.032 mm. However, to identify the contribution of roughness on the contact-angle and the bubble-size relation, the experiments were repeated using a sample which was only roughly polished (P_a=0.059 mm, see Fig. 4.2(b)).

Although the roughly polished sample is approximately two times rougher than the fine-polished sample, it is still significantly smoother than the original rock surface (P_a=0.272 mm). Figs. 4.20 (a) and (b) give the stable contact angles on the less-polished surface as a function of pressure and bubble radius, respectively. The range of the values of the contact angle is wider and contact-angle hysteresis increases: the contact angle scatters when plotted as a function of pressure (Fig. 4.20 (a)). The larger contact angle of the less-polished surface is attributed to the smaller size of the bubble in this system. However, the contact angle of the less-polished surface (Fig. 4.20(b)) behaves similar to the contact angle on the smooth, polished surface (Fig. 4.17) even though the square of the correlation coefficient for the linear regression, r^2, increases from 0.67 for fine-polished substrate (Fig. 4.17) to 0.86 for less-polished substrate (Fig. 4.20(b)). The comparison of the data allows the conclusion that surface roughness clearly affects the contact angle and its variation with the bubble size in the system at hand.

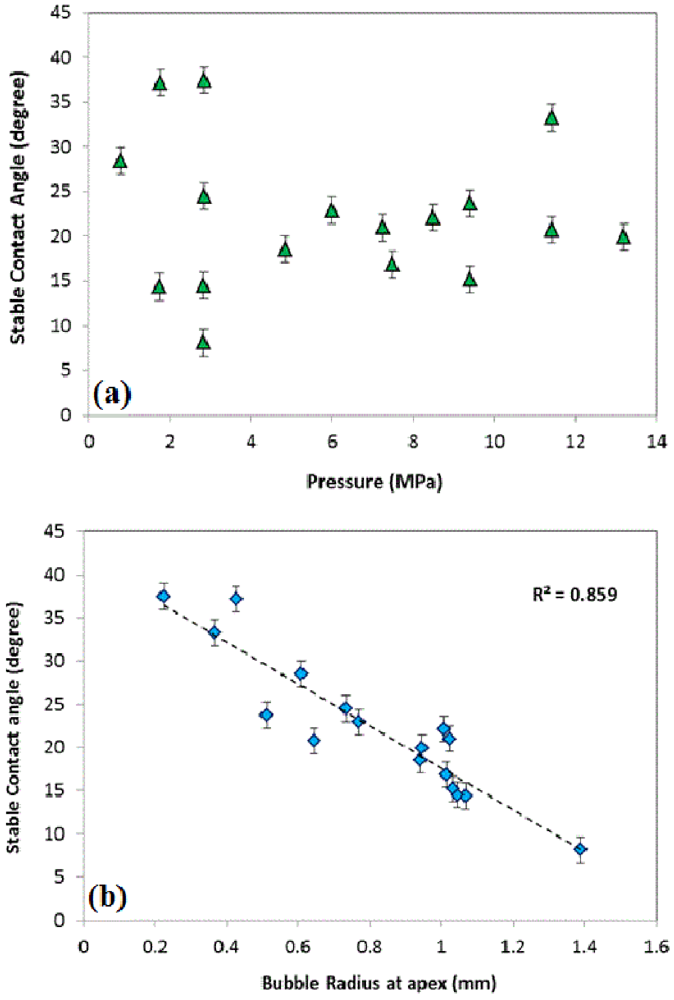

Figure 4.20. Stable contact angles for a less-polished surface as a function of (a) pressure and (b) bubble radius at apex at various pressures and a constant temperature of 318K. The dashed line is the best linear fit to the experimental data. The error bars show the standard error of the values.

4.4.3.2. Effect of gravity on bubble geometry

In this section, the contact-angle variation with bubble size is evaluated while the effect of gravity (buoyancy) on the bubble shape is taken into account [21, 24, 60, 61]. As a reference, the analytical model of Vafaei and Podowski (Eq. 4.4) was used, which allows the calculation of liquid droplet volume from a given contact angle (and radius of the contact area). This model has been adapted for a captive gas bubble system by considering the effect of buoyancy force on the bubble contour (Appendix 4.5). Figs. 4.21 (a) and (b) compare the bubble volumes calculated from the analytical expression (derived in Appendix 4.5) against the volumes computed from the experimentally captured images, at pressures of 1.04 and 4.97 MPa. The experimentally determined volumes (blue squares in Fig. 4.21) were obtained from the numerical solution and consecutively integrating the bubble profile based on the Young-Laplace description of the bubble image (KRUESS© Drop Shape Analysis [62]). The bubble radius at apex (R_0), obtained from the numerical solution of the bubble profile, along with the values of the contact angle (θ) and contact radius (R), were used to calculate the bubble volume in analytical expression, Eq. A4.8 (red triangle in Fig. 4.21). The contact angle (θ) and contact radius (R) were obtained from the intersection of a tangent line on the bubble profile and the base line describing the surface. As can be seen from Fig. 4.21, the results of experimentally and analytically determined volumes are in good agreement with each other, confirming that the contact-angle variation with the bubble volume can also be described with the analytical expression. There are slight differences between the experimentally determined volumes and the results of the analytical model for the large bubbles with small contact angles at 1.04 MPa. This difference might be attributed to: 1) the uncertainties in the contact-angle determination of a strongly water-wet system with very small contact angles, which directly influence the bubble volume calculations using an analytical model (Chapter 2), and/or 2) deviation of the actual bubble curvature from a circle at the horizontal cross sections for large bubbles (Appendix 4.5).

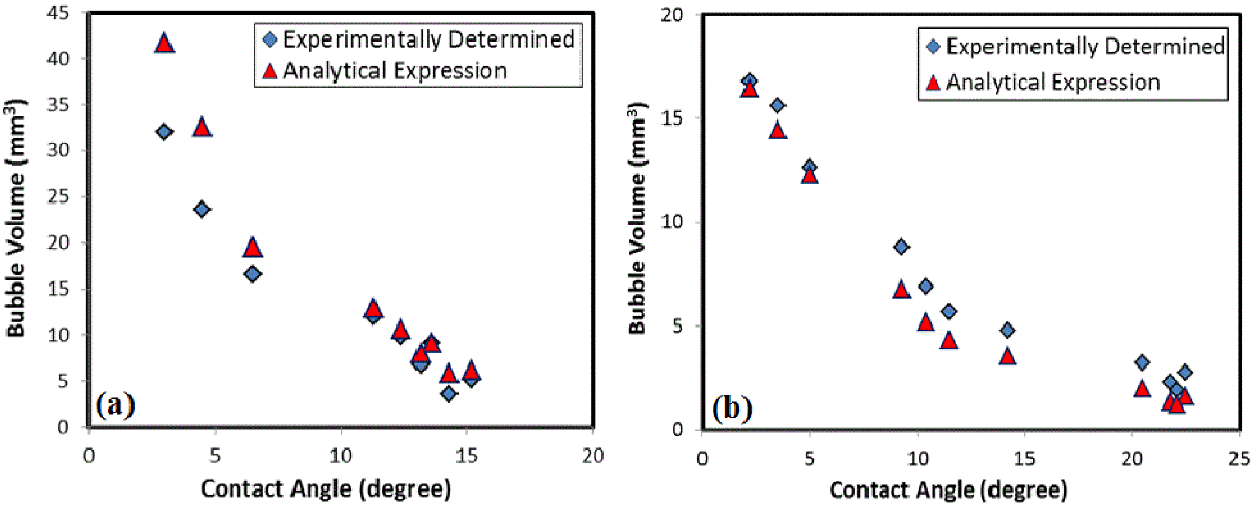

Figure 4.21. Bubble volume as a function of the contact angle at a constant temperature of 318 K and pressures of (a) 1.04 and (b) 4.97 MPa. Red triangles show the results obtained with the analytical model (Eq. A4.8) and blue squares are determined from the images of the bubble.

Based on the discussion with respect to the effect of gravity (buoyancy) on the bubble shape (section 4.2.1), it is expected that the bubble shape asymptotically approaches a spherical shape and, accordingly, the contact angle no longer depends on the bubble volume. This can also be seen in Figs. 4.19 a-f, where the variation of the contact angle with the bubble volume is given at a pressure of 4.97 MPa. These sequential digital images of the captive CO_2 bubble show that when the bubble size decreases, the contact angle increases and the bubble shape approaches a sphere. However, in order to identify whether surface forces or gravity (buoyancy) forces dominate, the Bond number (Eq. 4.6) is calculated and used for the presentation of the contact angle. In Figs. 4.22 (a) and (b), the stable contact angles are given as a function of the Bond number for various bubble sizes at pressures of 1.04 MPa and 4.97 MPa. The experimentally-determined IFT data (section 4.4.1) were used for calculation of the Bond numbers (Eq. 4.6). As mentioned in the experimental section, the density of the aqueous phase was determined with a vibrating-tube density meter (see schematic of the setup, Fig. 4.4). The Span-Wagner EOS was used to calculate the density of the CO_2–rich bubble assuming that the water concentration in the bubble is negligible. With this, the density difference between the aqueous phase and CO_2 bubble ($\Delta\rho$) at pressures of 1.04 and 4.97 MPa were calculated to be 1.046 and 0.957 g/ml, respectively. Following this, Bond numbers were calculated to range between 0.3 and 3.2.

Theoretically, Bond numbers smaller than one indicate that surface forces are dominant rather than gravity forces. Combining this knowledge with the fact that a decreasing bubble size results in a bubble shape approaching a sphere, it would be expected that the contact angle does not change with bubble size for small Bond numbers (smaller than one). In Fig. 4.22 (a), the contact angle as a function of the Bond number is given at two different pressures. When Bond numbers are larger than one, the contact angle significantly changes with the Bond number which means that, the gravity (buoyancy) force is more dominant than surface force. However, this variation decreases for Bond numbers less than 0.9. Based on the data from Fig. 4.22 (a), pressure has no effect on the contact angle of the bubbles with a Bond number larger than 1. However, the contact angle of the bubbles with a Bond number less than 0.9 increases by about 5^o when the pressure is increased from 1.04 MPa to 4.97 MPa. Fig. 4.22 (b) shows Bond number values as a function of the bubble radius at pressures of 1.04 and 4.97 MPa. For bubbles with a similar radius, the Bond number at a pressure of 4.97 MPa is larger than that at 1.04 MPa. Although the density difference of two coexisting phase decreases with increasing pressure, the influence of interfacial tension reduction is more highlighted; this resulted in the larger Bond number at 4.97 MPa. The variation of Bond number with bubble radius confirms that the influence of the bubble radius becomes less significant when the Bond number reduces.

According to the results presented in Fig. 4.22 and section 4.4.3.1, it can be concluded that the dependency of the contact angle on the bubble size in the system at hand can be explained by the effect of gravity (buoyancy) on bubble shape. However, the surface non-ideality and roughness have significant influence on the reliability of the contact-angle determination. This variation becomes insignificant for Bond numbers less than 0.9 (bubble maximum diameter of about 2.3 mm).

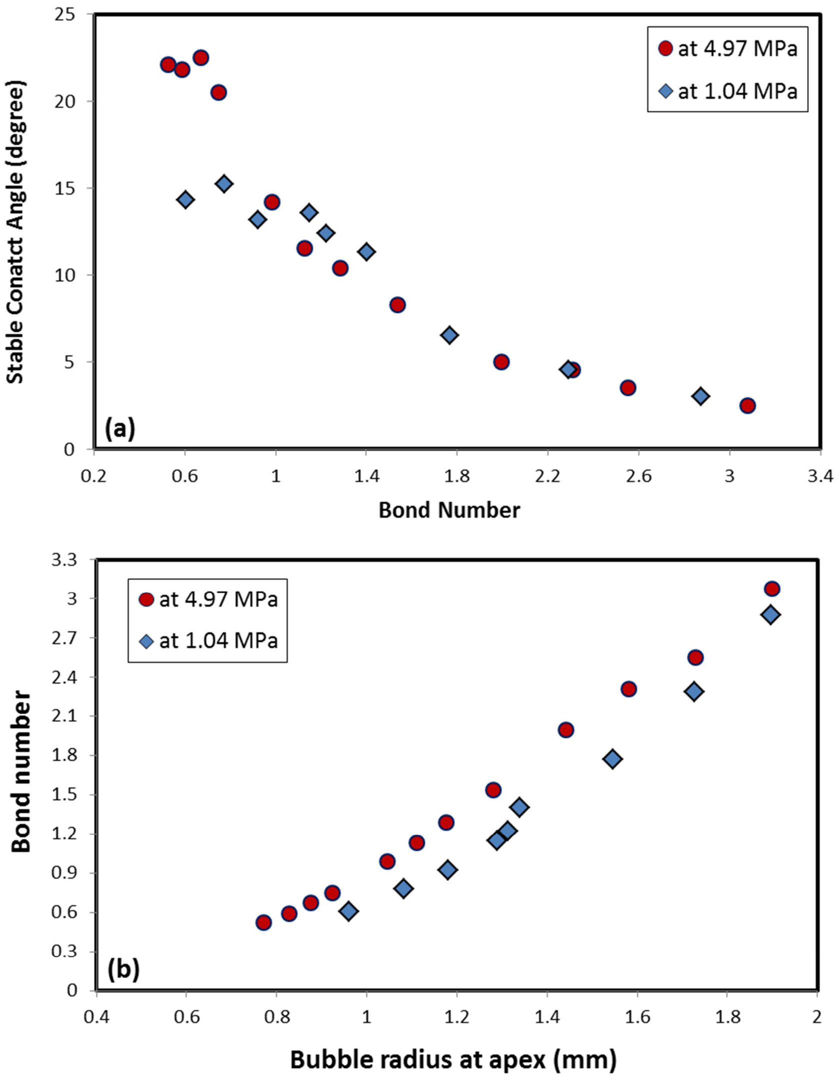

Figure 4.22. (a) Stable contact angle as a function of the Bond number for various bubble sizes, and (b) Bond number as a function of the bubble radius, at a constant temperature of 318 K and two pressures of 1.04 MPa (blue squares) and 4.97 MPa (red circles).

4.4.3.3. Effect of pressure on the contact angle in the Bentheimer/ CO_2/ water system

In the CCS field application, the amount of capillary-trapped CO_2 depends on the wettability of reservoir rocks at reservoir conditions, i.e. high pressures. To identify the effect of pressure on the contact angle, only those bubbles with a Bond number smaller than 0.9 were considered (see section 4.4.3.2). In this way, the effect of gravity could be excluded and the influence of the bubble size on the contact angle became insignificant. Fig. 4.23 represents the contact angle as a function of pressure for experiments which were characterized by Bond numbers of approximately 0.9 (±0.02).

Fig. 4.23 shows that the contact angle of the Bentheimer/CO_2/water system slightly increases with pressure. This slight rise (max. 5^o) might not be correlated to the effect of pressure, since it is within the experimental error range. This assumption is supported by the results of Espinoza and Santamarina [12], who observed that pressure does not have a significant effect of on the wettability of quartz surfaces. However, several studies have reported the wettability alteration of quartz surfaces from strongly to less water-wet in contact with supercritical CO_2 [6, 7, 36, 37, 63]. This inconsistency originates from differences in the surface charges of quartz and Bentheimer sandstone. Although Bentheimer sandstone is mainly composed of quartz, even a low content of clay (i.e. 2.5% Kaolinite and etc.) plays an important role in the surface charge of particles [64].

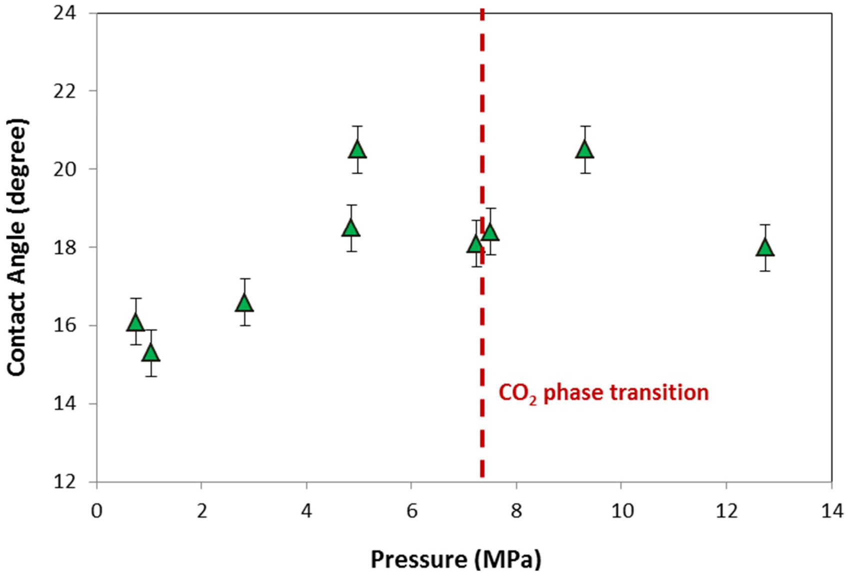

Figure 4.23. Contact angle as a function of pressure for bubbles with Bond numbers of about 0.9 (±0.02) for the Bentheimer/CO_2*/water system at 318 K.*

For the quartz surface, an increase in contact angle with pressure has been attributed to the decreased charge of the silica surface under the acidic pH of the CO_2–equilibrated aqueous phase [7, 63, 65]. The pH of the aqueous phase influences the surface charge of the particles. According to Tokunaga [65], the surface charge of a quartz particle is negative and approaches zero for a pH of 3. In water/CO_2 solutions, the pH decreases from 7 to 3 due to the dissolution of CO_2 in the aqueous phase [7]. The pH reduction results in a decline in the negative surface charge and thus, reduces the electrostatic repulsions. Consequently, the stability of the water film covering the surface decreases, which leads to a wettability alteration and thus an increase in contact angle (electric double layer effects, DLVO theory) [65].

Unlike quartz, the surface charge of Bentheimer sandstone approaches zero at a pH of 8 [62]. At low pH , the charge of a Bentheimer sandstone surface becomes more positive so that the stability of the water film increases [64]. This means that the pressure induced by the injection of a CO_2 bubble has no effect on the stability of the water film and thus the wettability of the Bentheimer sandstone (as seen in Fig. 4.23). Fig. 4.24 shows the sequential digital images of the CO_2 bubble with similar sizes on the Bentheimer rock at sub-critical (2.83 MPa), approximately critical (7.51 MPa) and super-critical (12.74 MPa) pressures. The comparison of the data allows the conclusion that CO_2 phase transition has no effect on the wettability of the Bentheimer sandstone/water system.

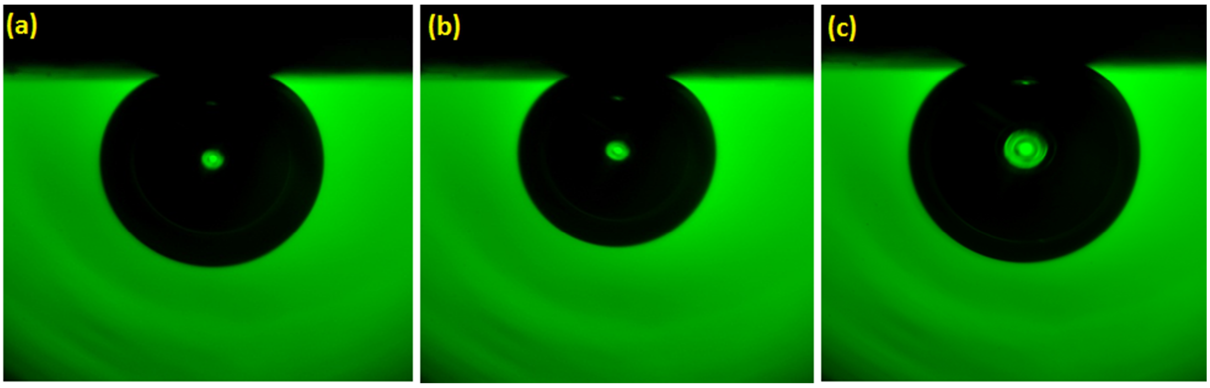

Figure 4.24. Sequential digital images of the captive CO_2 bubble with similar size on the Bentheimer rock at a constant temperature of 318 K and various pressures.

4.4.3.4. Effect of pressure on the contact angle in Bentheimer/flue gas/water system

The stable contact angles of the flue gas/Bentheimer/water system at a temperature of 318 K are presented in Figs. 4.25 and 4.26 as a function of pressure and flue gas bubble radius. As in the CO_2 system (Figs. 4.16 and 4.17), the contact angles in the flue gas/sandstone/water system are influenced more by bubble size than by pressure. However, the contact angle values of flue gas bubbles are all smaller than those of the CO_2 bubbles (see Figs. 4.16 and 4.25). This can be explained by the ratio of 20 mol% CO_2 to 80 mol% N_2 in the flue gas bubble and the higher IFT values in flue gas system (Fig. 4.8). To evaluate the effect of pressure on contact angle, the contact angle data at four specific pressures were extracted from Fig. 4.26 and shown in Fig. 4.27. The comparison between data reveals that the contact angle remains relatively unchanged, within the ranges of the error bars, with pressure variations (Fig. 4.27). Thus, it can be concluded that pressure has a negligible effect on the wettability of the flue gas/water/Bentheimer sandstone system.

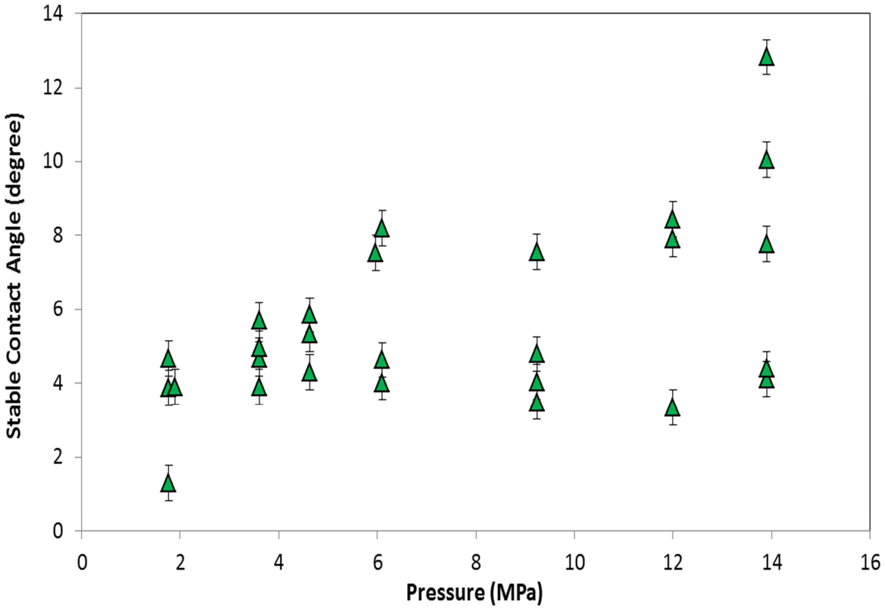

Figure 4.25. Stable contact angle (in pre-CO_2 saturated aqueous phase) as a function of pressure at a temperature of 318 K. The error bars show the standard error of the values.

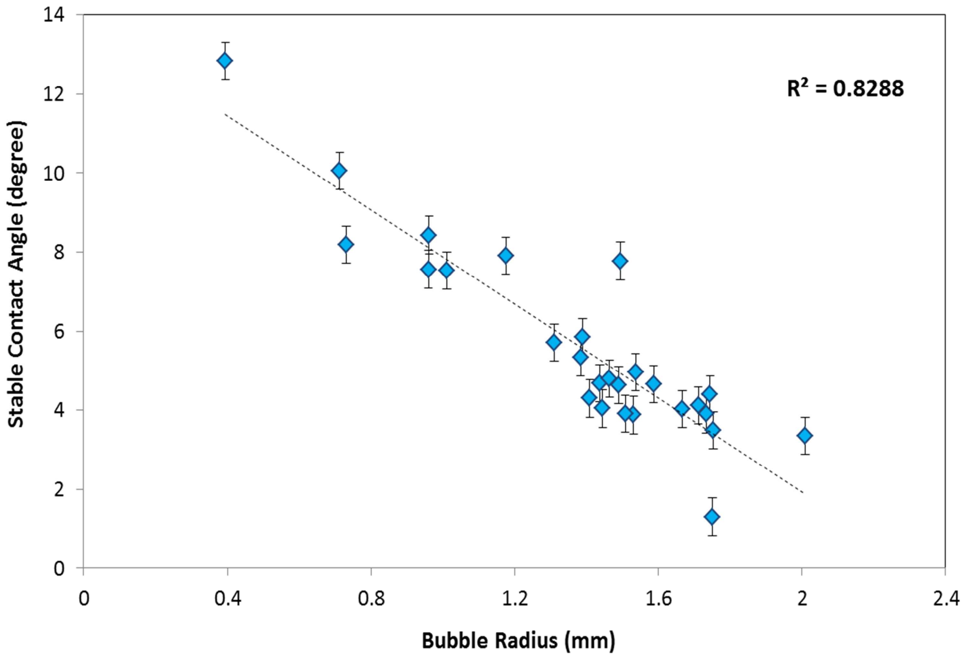

Figure 4.26. Stable contact angle as a function of the bubble radius at a constant temperature of 318 K and various pressures from 0.17 MPa to 13.9 MPa. The dashed line is the best linear fit to the experimental data. The error bars show the standard error of the values.

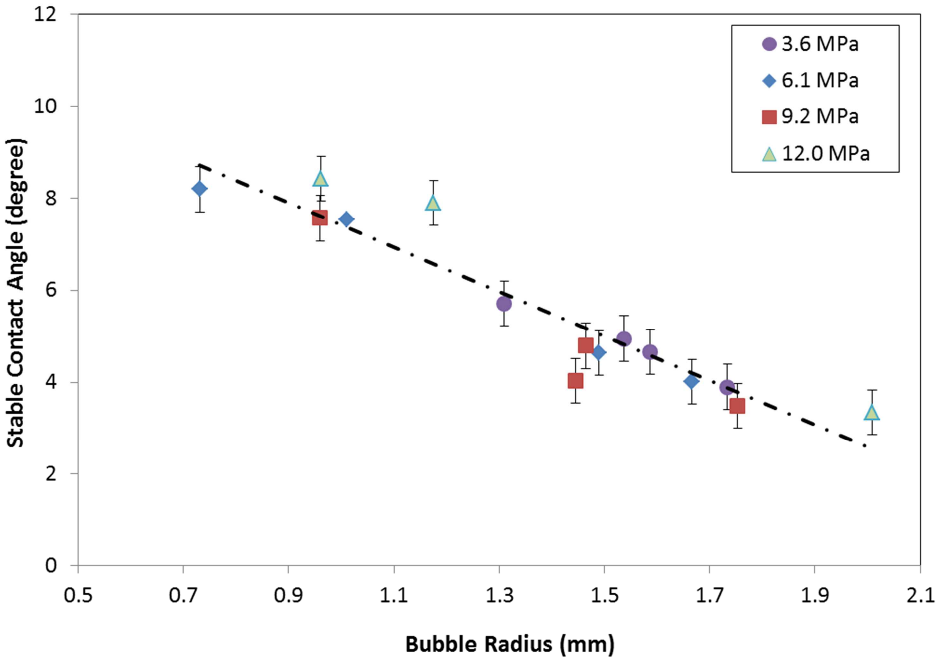

Figure 4.27. Stable contact angle vs. bubble radius at four specific pressures and a temperature of 318 K. The dashed line is the best linear fit to the experimental data.

4.5. CONCLUSIONS

In this work, wettability of the Bentheimer sandstone/water/CO_2 and/or flue gas system has been experimentally evaluated using the captive-bubble technique in a pressure range from 0.2 to 15 MPa (2 to 150 bar). The CO_2 experiments were conducted using different water-CO_2 mixtures, i.e. unsaturated and fully saturated, in order to evaluate the dissolution effects and wetting properties for short and long periods. In this study, contact-angle determinations were performed using natural rock surfaces which had not been treated chemically. The results of these experiments could be a step forward in understanding the displacement behavior of fluids in sandstone reservoirs. The results are summarized as follows:

- The CO_2/water interfacial tension decreases with increasing pressure. The considerable change occurs in the lower pressure range up to 10 MPa. At higher pressures, the interfacial tension decreases at a very slow rate. The flue gas/water IFT decreases slightly with pressure for all pressure ranges. The IFT trend for this system is similar to that of the nitrogen/water system and is attributed to the density variation with pressure.

- For experiments in the unsaturated aqueous phase, two dissolution regimes were observed: (1) the first regime where CO_2 dissolves quickly into the almost pure aqueous phase and (2) the second regime where CO_2 gradually diffuses into the aqueous phase. In the first regime, the contact angle increases continuously until it reaches the transition point. After this transition point, the contact angle changes slightly with time but is almost constant. Analysis of the data showed that this behavior cannot be caused by wettability alterations of the surface from strongly to less water-wet, but by bubble volume reduction due to CO_2 dissolution in the aqueous phase. Because of the dependency of the contact angle on the bubble size, the bubble shrinkage results in alterations of the contact angle over time.

- Results obtained from experiments with an unsaturated aqueous phase provide important information on the interfacial interactions and mass transfer between the aqueous and CO_2 phases. In the unsaturated system, the change in contact angle is influenced by a number of mechanisms such as dissolution and bubble size variation, rather than by the wetting properties of the surface alone.

- A reliable contact-angle determination should be conducted using a pre-equilibrated (fully or quasi-saturated) aqueous phase to eliminate dissolution effects. Due to dissolution, the bubble size continuously changes, so that a reliable and reproducible contact-angle determination is not guaranteed.

- Experiments in the fully-saturated system show that Bentheimer sandstone is (and remains) water-wet against either CO_2 or flue gas, even at supercritical pressures. However, all contact angles of the flue gas bubbles are smaller than those of CO_2. The data for the apparent contact angle of these systems show a strong dependence on the bubble size.

- Analysis of the experimental data shows that this dependency can be explained by the effect of gravity (buoyancy) on bubble shape. However, the surface non-ideality and roughness have significant influence on the reliability of the contact-angle determination. The influence of the bubble radius on the contact angle of the CO_2 system becomes insignificant for bubble diameters smaller than 2.3 mm (Bond numbers less than 0.9).

- The results of this study confirm previous findings by Vafaei and Podowski [21, 24] that axisymmetric droplets are size-dependent and cannot satisfy the original Young equation. In addition, it is in a good agreement with results of Sakai and Fujii [32], which shows that the apparent contact angle on rough surfaces can be changed by gravity.

- The surface roughness as used in this study can be improved. Its influence can be investigated in more details by using surfaces polished at different degrees.

- To identify the effect of pressure, only results with Bond numbers smaller than 0.9 (negligible dependency to the bubble size) were considered. From this, it could be deduced that there is no significant effect of pressure on the contact angle of the Bentheimer/CO_2/water system. Based on the literature data we concluded that this can be explained by the change in the charge of the rock due to interactions between components of the rock surface and the acidic aqueous phase containing CO_2.

- In the CCS field application, the amount of capillary-trapped CO_2 depends on the wettability of reservoir rocks. Results of this study show that there is no significant effect of pressure on the wettability of the Bentheimer/water/CO_2 or flue gas system. Even at high pressure, the Bentheimer sandstone remains water-wet to either CO_2 or flue gas.

APPENDICES:

Appendix 4.1: Mass-transfer model at the bubble interface

A mass balance on the bubble interface gives:

$$N_{CO_2}A_b = -\frac{d}{dt}\left(\rho_{CO_2}V_b\right) \ , \tag{A1.1}$$

where N_{CO2} is the molar flux of CO_2 [mol/(m^2.s)]. V_b and A_b are the CO_2–rich bubble volume and the gas-liquid interfacial area, respectively. ρ_{CO_2} is the density of CO_2 in the bubble pressure, P_b. The total pressure in the bubble is given by

$$P_b = P_L + \frac{2\gamma_{w,co_2}}{r_b} \ , \tag{A1.2}$$

where P_L is the pressure determined in the aqueous phase; γ_{w,co_2} is the water-CO_2 interfacial tension at pressure P_L and r_b is the bubble radius.

With the assumption of a spherical bubble, the bubble volume and the interfacial area between the liquid and the gas phase can be obtained from

$$V_b = \frac{\pi}{3}r_b^3[2 + 3\cos\theta_s - \cos^3\theta_s] \tag{A1.3}$$

$$A_b = 2\pi r_b^2(1 + \cos\theta_s) \tag{A1.4}$$

where θ_s is the contact angle for a spherical bubble. With assumption of a spherical bubble, θ_s is equal to the experimentally determined contact angle.

Mass transfer from CO_2–rich bubble to the aqueous phase can be determined by

$$N_{CO2} = k_L\left(C_{co_2}^s - C_{co_2}^b\right) \ , \tag{A1.5}$$

Where N_{CO2} is the molar flux of CO_2 [mol/(m^2.s)], k_L is mass-transfer coefficient in the aqueous phase [m/s]; $C_{co_2}^s$ is the concentration of CO_2 at the bubble interface [mol/m^3] given by Henry's law at the temperature and pressure of the system. $C_{co_2}^b$is CO_2 concentration in the aqueous phase and is assumed to be negligible.

Combining Eqs. A1.1 and A1.3-A1.5 yields

$$\frac{dr_b}{dt} = -\frac{k_L}{\rho_{CO_2}}C_{CO_2}^s \ , \tag{A1.6}$$

with the initial condition

$$t = 0,\ r_b = R_{io} \tag{A1.7}$$

Integration of Eq.(A1.6) with initial condition Eq. (A1.7) yields

$$r_b = R_{io} - \frac{C_{co_2}^s \times k_L}{\rho_{CO_2}}\ t \tag{A1.8}$$

Appendix 4.2: Steady-state diffusion through the bubble variable area

In this section I follow the derivation for steady-state diffusion through the spherical bubble variable area into an infinite body of liquid [66], and then scale the mass flux by the fraction of the full spherical surface represented by the CO_2 bubble against the solid surface. Diffusion of CO_2 from a CO_2-rich bubble into the aqueous phase is described using Fick's first law [66]. A mass balance is written at a thin spherical shell with the thickness of Δr around the bubble (Fig. 4.2A.1). Since the bubble dissolves in the liquid phase, the diffusion area cannot be considered constant and changes along the diffusion direction (r) and also with time [65]. In this case, at any instant in time, t, the CO_2 bubble radius is r_b.

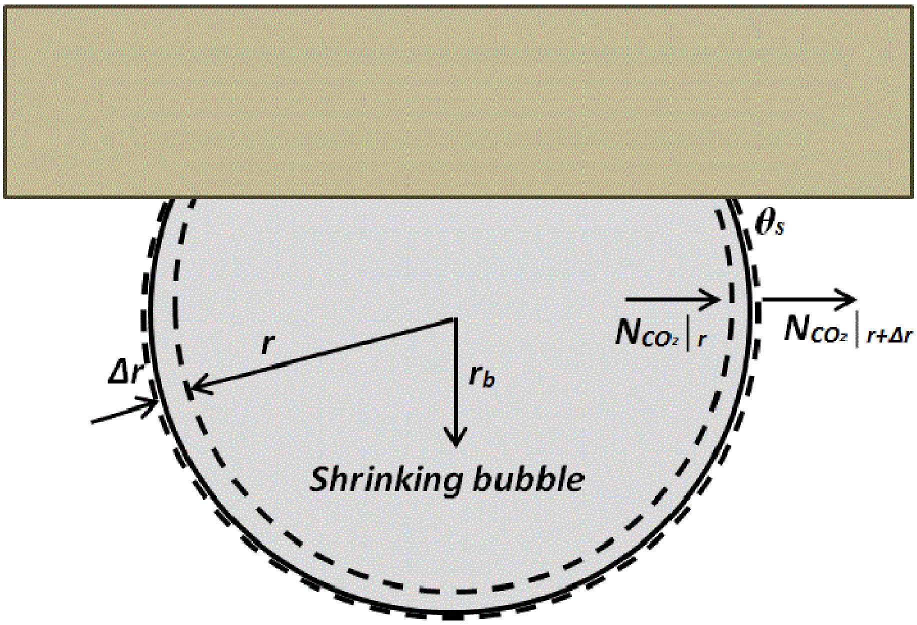

Figure 4.2A.1. Mass balance in the r-direction for a captive bubble through the variable area

A steady-state mass balance (zero accumulation rate) on the spherical shell (Δr) gives [66]

$$-\frac{d}{dr}\left(A_b \times N_{CO_2}\right)=0, \tag{A2.1}$$

which yields

$$A_b \times N_{CO_2} = Constant = W \tag{A2.2}$$

W is the constant molar rate of mass transfer. In this case, it is assumed that water diffusion into the CO_2-rich phase (bubble) is negligible because of the small diffusion coefficient of water into CO_2. Therefore, the system is considered as diffusion of CO_2 through non-diffusing water. According to Fick's law:

$$N_{CO_2}=-\,D\frac{dC_{CO_2}}{dr} \tag{A2.3}$$

where D is CO_2 diffusion coefficient into water. It should be noted that D depends on temperature but not greatly on pressure ($D=3.07\times10^{-9}$ m^2/s at 318 K) [52].

Combining Eq. A2.2 and A2.3 yields:

$$-A_b \times D\frac{dC_{CO_2}}{d\mathrm{r}} = W \qquad \text{(A2.4)}$$

In this case, initial and boundary conditions are:

$$C_{CO_2} = C_{co_2}^{s} \;\text{ at }\; r = r_b \qquad \text{(A2.5)}$$

$$C_{CO_2} = C_{co_2}^{b} \;\text{ at }\; r \to \infty \qquad \text{(A2.6)}$$

$$r \;= R_{io} \;\text{ at }\; t = 0 \qquad \text{(A2.7)}$$

By assuming a spherical shape for the bubble (truncated by the solid surface):

$$V_b = \frac{\pi}{3} r_b^3 [2 + 3\cos\theta_s - \cos^3\theta_s] \qquad \text{(A2.8)}$$

$$A_b = 2\pi r_b^2 (1 + \cos\theta_s) \qquad \text{(A2.9)}$$

Integrating Eq. A2.4 with boundary conditions (Eq. A2.5 and A2.6) yields

$$W = 2\pi(1 + \cos\theta_s)D\;(C_{co_2}^{s} - C_{co_2}^{b}) \times r_b \qquad \text{(A2.10)}$$

W is the constant molar rate of mass transfer (molar flux × area, Eq. A2.4) and is equal to the rate of dissolution of the bubble at any instant:

$$W = -\frac{dm_b}{dt} = -\frac{d}{dt}\left(\rho_{CO_2} V_b\right) \qquad \text{(A2.11)}$$

Combining Eqs. A2.8, A2.10 and A2.11 gives

$$-[2 + 3\cos\theta_s - \cos^3\theta_s]\pi \times \rho_{CO_2} r_b^2 \times \frac{dr_b}{dt} = 2\pi(1 + \cos\theta_s)D\;(C_{co_2}^{s} - C_{co_2}^{b}) \times r_b \qquad \text{(A2.12)}$$

Integrating Eq. A2.12 with initial condition (Eq. A2.7) yields

$${r_b}^2 = {R_{io}}^2 - 2\frac{(C_{co_2}^{s} - C_{co_2}^{b})\times \mathrm{D}}{\rho_{CO_2}}\left(\frac{2(1+\cos\theta_s)}{(2+3\cos\theta_s - \cos^3\theta_s)}\right)t \qquad \text{(A2.13)}$$

In regime I, it is assumed that the CO_2 concentration in the bulk ($C_{co_2}^{b}$) far from the bubble is zero. The CO_2 concentration in the bulk phase in regime II is obtained from the best fit of Eq. (A2.13) to the experimental data.

In this model, the bubble geometry is assumed to be spherical. This may have caused an error in calculations, in particular for larger bubbles. The average deviation for the volume of bubbles compared to spheres, at 0.58 MPa, was 5.31%.

Appendix 4.3: Rayleigh number calculation for a captive-bubble system

The onset of natural convection in the porous medium is determined by the Rayleigh number (*Ra*), which is dependent on the properties of the fluids and geometry of the system:

$$Ra = \frac{k\Delta\rho g L}{\phi\mu D} \tag{A3.1}$$

where k is the permeability of the porous medium; $\Delta\rho$ is the density difference between the boundary layer fluid and that far away; g is the local gravitational acceleration; L is the characteristic length-scale of convection; ϕ is the porosity; μ is the dynamic viscosity and *D* is the diffusivity of the characteristic that is causing the convection. In porous media the interfaces will be unstable for Rayleigh numbers above $4\pi^2 \approx 40$ [67].

For bulk solutions Eq. (A3.1) converts to:

$$Ra = \frac{\Delta\rho g L^3}{\mu D} \tag{A3.2}$$

In these systems, density-driven natural convection occurs when *Ra*>2100.

Accordingly, for the captive-bubble system at 0.58 MPa and 318K, Eq. A3.2 gives:

$$Ra = \frac{(1060-1000)\left({}^{kg}/_{m^3}\right)\times 9.8\left({}^{m}/_{s^2}\right)\times\left(2\times10^{-2}\right)^3(m^3)}{(0.65\times10^{-3})\left({}^{kg}/_{m.s}\right)\times(3\times10^{-9})\left({}^{m^2}/_{s}\right)} = 24\times10^{8} > 2100$$

Therefore, the calculation of this dimensionless number for the system at hand reveals that diffusion is accelerated by density-driven natural convection in regime I. The density difference in regime II is smaller, but according to this criterion, natural convection should occur in regime II as well. Nonetheless, the results indicate that the rate of mass transfer is what one would expect for diffusion with no convection (section 4.4.2.1).

Appendix 4.4: Line-tension determination for a CO_2/water/Bentheimer system

The line tension is determined using the contact-angle data as a function of bubble size and the length of the contact line (section 4.2.1). Due to the pressure dependency of the interfacial tension, the line tension is also a function of pressure. Therefore, to identify the dependency of the contact angle on the bubble size and line-tension determination, the pressure effect has been excluded by using only results of the contact angle at a constant pressure of either 1.04 or 4.97 MPa (Figs. 4.3A.1a and 4.3A.1b).

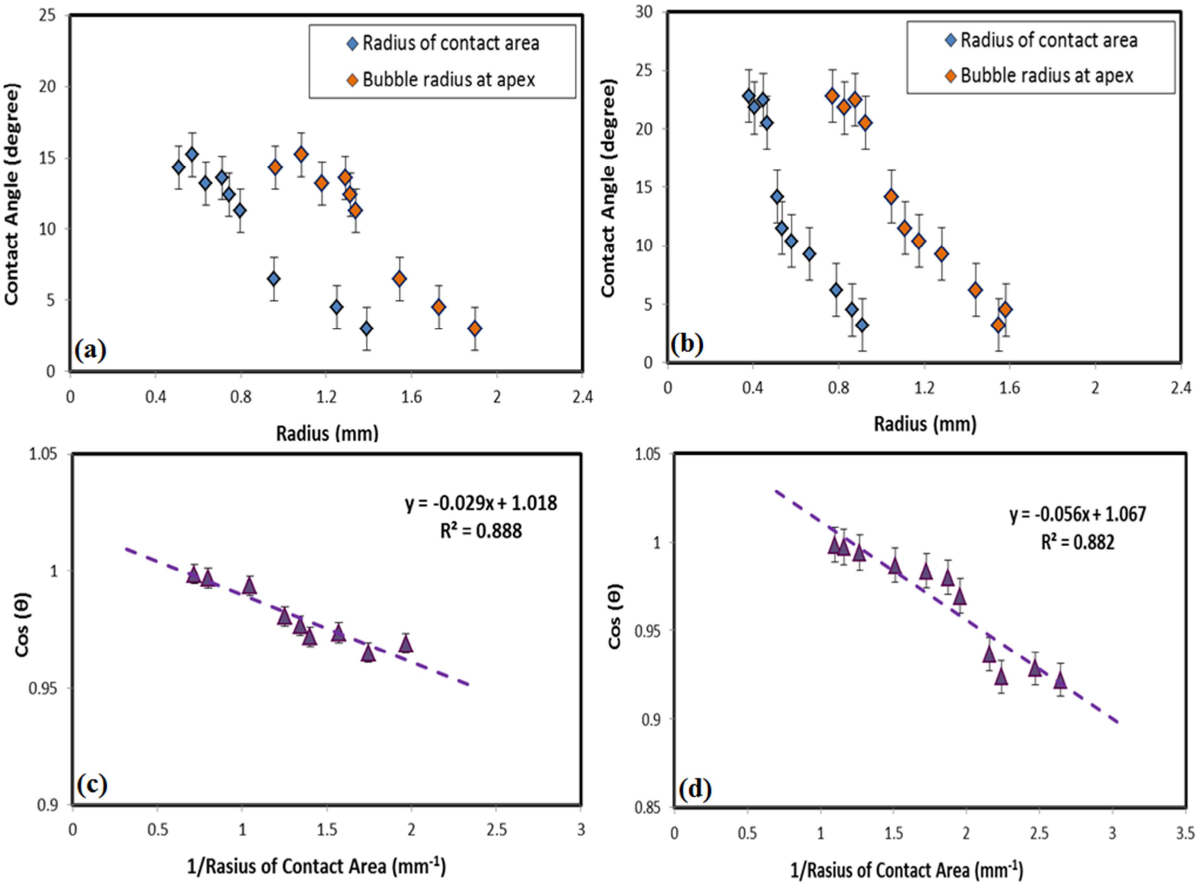

Figure 4.3A.1. Contact angle versus bubble radius or the inverse length of the contact line at two different pressures: (a, c) at 1.04 MPa and (b, d) at 4.97 MPa. Error bars are obtained based on the standard error calculation.

The line tension, σ, has been derived based on the data given in Figs. 4.3A.1c and 4.3A.1d and using Eq. 4.3. At constant pressures of 1.04 MPa and 4.97 MPa, the line tensions were 1.921×10^{-6} (J/m) and 2.46×10^{-6} (J/m), respectively. However the intercepts of the linear fit between $cos\theta$ and $1/R$, which give the contact angle for the infinite large bubble ($R \rightarrow \infty$), were more than one, i.e. 1.018 and 1.067 for constant pressures of 1.04 MPa and 4.97 MPa, respectively. A value of $cos\theta$ larger than one is mathematically impossible. It originates from: 1) the fact that the contact angle of the very large CO_2 bubble on Bentheimer sandstone is zero, which means that the system is absolutely water-wet and there is no three phase contact line in this case, and/or 2) the uncertainty in the determined values of the parameters used for the calculation of the line tension such as contact angle and length of the contact line.

Nevertheless, no data of line tension are found in the literature on Bentheimer sandstone to provide a comparison with previous studies.

In addition to the contradictory results regarding line-tension determination (section 4.2.1), for such a strongly water-wet system like Bentheimer sandstone with small contact angles (<20°), the bubble profiles near the solid surface are sometimes blurry and indistinct. In this system, even a small error in the detection of the bubble contact with the solid surface may cause errors in the determined contact angles (Chapter 2, section 2.3.4.1). This uncertainty may lead to overestimation in the infinite contact-angle determination. Following these results, it can be concluded that the line-tension concept may not be a proper method to describe the dependency of the contact angle on the bubble size for the system at hand, since surface non-ideality and roughness have a significant influence on the reliability of this method.

Appendix 4.5: Theoretical analysis of gas captive bubble on a horizontal substrate

The following theoretical analysis and derivations are based on the analytical model of Vafaei and Podowski [24], which allows the calculation of liquid droplet volume from a given contact angle (and radius of the contact area). In their approach, the droplet is circular in all its horizontal cross sections. This assumption does not apply to vertical sections. This model has been adapted for a captive gas bubble system surrounded by the aqueous phase by considering the effect of buoyancy force on the bubble contour. Forces in the z-direction acting on an axially symmetric captive bubble, as shown in Fig. 4.A4.1, should be considered.

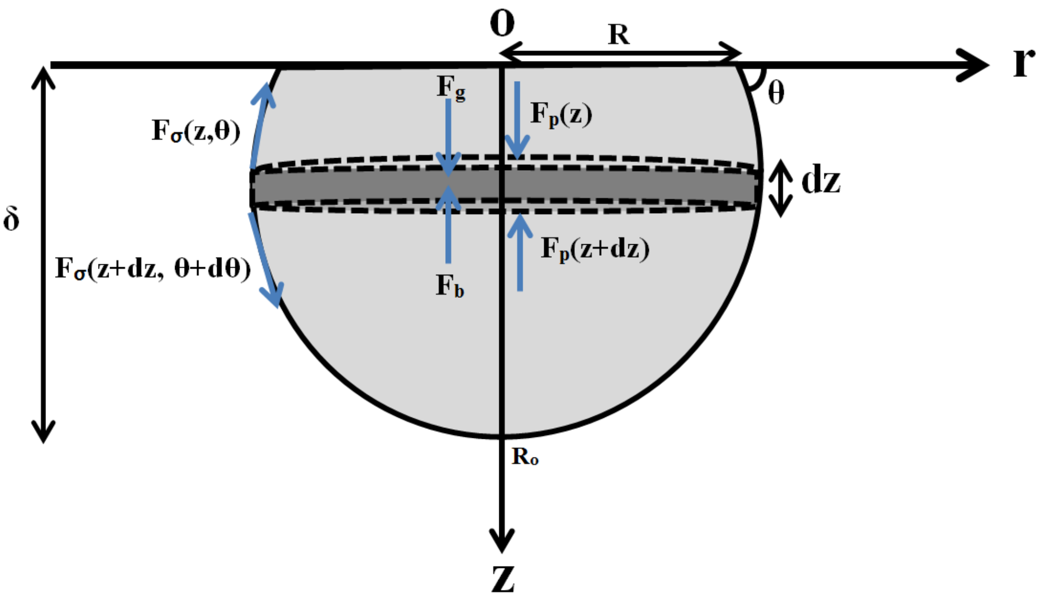

Figure 4.A4.1. Force balance in the z-direction for a captive bubble.

The force balance for a slice between z and z +dz is

$$dF_g - dF_b + F_p(z) - F_p(z+dz) - F_\sigma \sin\theta\,(z) + F_\sigma \sin(\theta + d\theta)\,(z+dz)$$

$$-P_L 2\pi r dr = 0 \quad \text{(A4.1)}$$

where the individual forces are:

the gravity force

$$dF_g = \rho_g g \pi r^2(z) dz \quad \text{(A4.2)}$$

the buoyancy force

$$dF_b = \rho_l g \pi r^2(z) dz \quad \text{(A4.3)}$$

the pressure force

$$F_p(z) = p(z) \pi r^2(z) \quad \text{(A4.4)}$$

the surface tension force

$$F_\sigma(z) = \gamma_{lv} 2\pi r(z) \tag{A4.5}$$

where the vertical pressure distribution is given by

$$p(z) = \rho_g g z + P_L + \frac{2\gamma_{lv}}{R_0} \tag{A4.6}$$

where P_L is the pressure determined in the aqueous phase; γ_{lv} is the liquid-vapor interfacial tension at pressure P_L; R_o is the bubble radius at apex and ρ_g is the density of the bubble.

By accounting the individual forces, Eq. (A4.1) gives

$$\left(\rho_l - \rho_g\right) g\pi r^2(z) = -\frac{d}{dz}\left[p(z)\pi r^2(z) - \gamma_{lv} 2\pi r(z) \sin\theta\,(z)\right] - P_L 2\pi r \frac{dr}{dz} \tag{A4.7}$$

Integrating both sides of Eq. (A4.7) yields

$$\begin{aligned} V_b = \int_0^\delta \pi r^2 dz &= \frac{\pi}{\Delta\rho g}\left[R^2\left(\rho_g g \times (0) + P_L + \frac{2\gamma_{lv}}{R_0}\right) - \gamma_{lv} 2R \sin\theta\right] - \frac{P_L R^2 \pi}{\Delta\rho g} \\ &= \frac{2\gamma_{lv}\pi R^2}{\Delta\rho g}\left(+\frac{1}{R_0} - \frac{\sin\theta}{R}\right) \end{aligned} \tag{A4.8}$$

where δ is the location of the apex; $\Delta\rho$ is the density differences between the bubble and aqueous phase; and R is the radius of the contact circle. Data of the contact angle (θ), the radius of the curvature at the apex (R_0) and the radius of the contact circle (R) are obtained using the numerical method from the Young-Laplace description of the bubble profile. $\Delta\rho$ and γ_{lv} are determined experimentally at the specific pressure and temperature.

REFERENCES

[1] Z. Li, M. Dong, S. Li, S. Huang, CO_2 sequestration in depleted oil and gas reservoirs--caprock characterization and storage capacity, Energy Conversion and Management, 47 (2006) 1372-1382.

[2] B. Basbug, F. Gumrah, B. Oz, Simulating the Effects of Deep Saline Aquifer Properties for CO_2 Sequestration, (2007).

[3] A. Shariat, R.G. Moore, S.A. Mehta, K.C.V. Fraassen, K.E. Newsham, J.A. Rushing, Laboratory Measurements of CO_2-H_2O Interfacial Tension at HP/HT Conditions: Implications for CO_2 Sequestration in Deep Aquifers, in: Carbon Management Technology Conference, Carbon Management Technology Conference, Orlando, Florida, USA, 2012.

[4] H. Salimi, K.-H. Wolf, J. Bruining, The influence of capillary pressure on the phase equilibrium of the CO_2–water system: Application to carbon sequestration combined with geothermal energy, International Journal of Greenhouse Gas Control, 11, Supplement (2012) S47-S66.

[5] C.H. Pentland, S. Al-Mansoori, s. iglauer, B. Bijeljic, M.J. Blunt, Measurement of Non-Wetting Phase Trapping in Sand Packs, in: SPE Annual Technical Conference and Exhibition, Society of Petroleum Engineers, Denver, Colorado, USA, 2008.

[6] J. Mills, M. Riazi, M. Sohrabi, Wettability of common rock-forming minerals in a CO_2-brine system at reservoir conditions, in: International Symposium of the Society of Core Analysts, Austin, Texas, USA, 2011.

[7] P. Chiquet, D. Broseta, S. Thibeau, Wettability alteration of caprock minerals by carbon dioxide, Geofluids, 7 (2007) 112-122.

[8] M. Akbarabadi, M. Piri, Geologic storage of carbon dioxide: an experimental study of permanent capillary trapping and relative permeability, in: International Symposium of the Society of Core Analysts, Austin, Texas, USA, 2011.

[9] M.B. Alotaibi, R.M. Azmy, H.A. Nasr-El-Din, Wettability Studies Using Low-Salinity Water in Sandstone Reservoirs, in, 2010.

[10] C. Chalbaud, M. Robin, S. Bekri, P. Egermann, Wettability impact on CO_2 storage in aquifers: visualisation and quantification using micromodel tests, pore network model and reservoir simulations, in: International Symposium of the Society of Core Analysts, Calgary, Canada, 2007.

[11] W. Jiamin, K. Yongman, J. Jongwon, Wettability alteration upon reaction with $scCO_2$: Pore scale visualization and contact angle measurements, in: Goldschmidt 2011, Prauge, Czech Republic, 2011.

[12] D.N. Espinoza, J.C. Santamarina, Water-CO_2-mineral systems: Interfacial tension, contact angle, and diffusion-Implications to CO_2 geological storage, WATER RESOURCES RESEARCH, 46 (2010).

[13] J.-Q. Shi, S. Durucan, Modelling of Mixed-Gas Adsorption and Diffusion in Coalbed Reservoirs, in: SPE Unconventional Reservoirs Conference, Society of Petroleum Engineers, Keystone, Colorado, USA, 2008.

[14] R. Puri, D. Yee, Enhanced Coalbed Methane Recovery, in: SPE Annual Technical Conference and Exhibition, 1990 Copyright 1990, Society of Petroleum Engineers, Inc., New Orleans, Louisiana, 1990.

[15] F.Y.H. Lin, D. Li, A.W. Neumann, Effect of Surface Roughness on the Dependence of Contact Angles on Drop Size, Journal of Colloid and Interface Science, 159 (1993) 86-95.

[16] J. Drelich, J.D. Miller, J. Hupka, The Effect of Drop Size on Contact Angle over a Wide Range of Drop Volumes, Journal of Colloid and Interface Science, 155 (1993) 379-385.

[17] J. Gaydos, A.W. Neumann, The dependence of contact angles on drop size and line tension, Journal of Colloid and Interface Science, 120 (1987) 76-86.

[18] R.J. Good, M.N. Koo, The effect of drop size on contact angle, Journal of Colloid and Interface Science, 71 (1979) 283-292.

[19] W.J. Herzberg, J.E. Marian, Relationship between contact angle and drop size, Journal of Colloid and Interface Science, 33 (1970) 161-163.

[20] R.J. Good, E. Elbing, Generalization of Theory for Estimation of Interfacial Energies, Industrial & Engineering Chemistry, 62 (1970) 54-78.

[21] S. Vafaei, M.Z. Podowski, Analysis of the relationship between liquid droplet size and contact angle, Advances in Colloid and Interface Science, 113 (2005) 133-146.

[22] D. Li, A.W. Neumann, Determination of line tension from the drop size dependence of contact angles, Colloids and Surfaces, 43 (1990) 195-206.

[23] J. Drelich, J.D. Miller, R.J. Good, The Effect of Drop (Bubble) Size on Advancing and Receding Contact Angles for Heterogeneous and Rough Solid Surfaces as Observed with Sessile-Drop and Captive-Bubble Techniques, Journal of Colloid and Interface Science, 179 (1996) 37-50.

[24] S. Vafaei, M.Z. Podowski, Theoretical analysis on the effect of liquid droplet geometry on contact angle, Nuclear Engineering and Design, 235 (2005) 1293-1301.

[25] R. Tadmor, Line energy and the relation between advancing, receding, and Young contact angles, Langmuir, 20 (2004) 7659-7664.

[26] Y. Liu, J. Wang, X. Zhang, Accurate determination of the vapor-liquid-solid contact line tension and the viability of Young equation, Scientific Reports, 3 (2013) PMC3684806.

[27] B.A. Pethica, P.J.C. Pethica, in: 2nd International Congress of Surface Activity, London: Butterworths, 1957, pp. 131.

[28] J. Leja, W. Poling, in: International Mineral Process congress, 1960, pp. 325.

[29] H. Löwe, S. Hardt, Chemical Micro Process Engineering, John Wiley & Sons, 2004.

[30] E.M. Blokhuis, Y. Shilkrot, B. Widom, Young's law with gravity, Molecular Physics, 86 (1995) 891-899.

[31] H. Fujii, H. Nakae, Effect of gravity on contact angle, Philosophical Magazine A, 72 (1995) 1505-1512.

[32] H. Sakai, T. Fujii, The Dependence of the Apparent Contact Angles on Gravity, Journal of Colloid and Interface Science, 210 (1999) 152-156.

[33] P. Letellier, A. Mayaffre, M. Turmine, Drop size effect on contact angle explained by nonextensive thermodynamics. Young's equation revisited, Journal of Colloid and Interface Science, 314 (2007) 604-614.

[34] D. Yang, Y. Gu, P. Tontiwachwuthikul, Wettability Determination of the Reservoir Brine−Reservoir Rock System with Dissolution of CO_2 at High Pressures and Elevated Temperatures, Energy & Fuels, 22 (2008) 504-509.

[35] N. Shojai Kaveh, C. Berentsen, S.E.J. Rudolph-Floter, K.H. Wolf, W.R. Rossen, Wettability Determination by Equilibrium Contact Angle Measurements: Reservoir Rock- Connate Water System With Injection of CO_2, in: SPE Europec/EAGE Annual Conference, Society of Petroleum Engineers, Copenhagen, Denmark, 2012.

[36] J.-W. Jung, J. Wan, Supercritical CO_2 and Ionic Strength Effects on Wettability of Silica Surfaces: Equilibrium Contact Angle Measurements, Energy & Fuels, 26 (2012) 6053-6059.

[37] S. Saraji, L. Goual, M. Piri, H. Plancher, Wettability of Sc-CO_2/Water/Quartz Systems: Simultaneous Measurement of Contact Angle and Interfacial Tension at Reservoir Conditions, Langmuir, (2013).

[38] C. Chalbaud, M. Robin, J.M. Lombard, F. Martin, P. Egermann, H. Bertin, Interfacial tension measurements and wettability evaluation for geological CO_2 storage, Advances in Water Resources, 32 (2009) 98-109.

[39] C. Chalbaud, M. Robin, J.-M. Lombard, H. Bertin, P. Egermann, Brine/CO_2 Interfacial Properties and Effects on CO_2 Storage in Deep Saline Aquifers, Oil & Gas Science and Technology – Rev. IFP, 65 (2010) 541-555.

[40] P. Chiquet, J.-L. Daridon, D. Broseta, S. Thibeau, CO_2/water interfacial tensions under pressure and temperature conditions of CO_2 geological storage, Energy Conversion and Management, 48 (2007) 736-744.

[41] A. Georgiadis, G. Maitland, J.P.M. Trusler, A. Bismarck, Interfacial tension measurements of the (H_2O + CO_2) system at elevated pressures and temperatures, Journal of Chemical and Engineering Data, 55 (2010) 4168-4175.

[42] B. Kvamme, T. Kuznetsova, A. Hebach, A. Oberhof, E. Lunde, Measurements and modelling of interfacial tension for water+carbon dioxide systems at elevated pressures, Computational Materials Science, 38 (2007) 506-513.

[43] A. Hebach, A. Oberhof, N. Dahmen, A. Kögel, H. Ederer, E. Dinjus, Interfacial tension at elevated pressures-measurements and correlations in the water + carbon dioxide system, Journal of Chemical and Engineering Data, 47 (2002) 1540-1546.

[44] B.-S. Chun, G.T. Wilkinson, Interfacial tension in high-pressure carbon dioxide mixtures, Industrial & Engineering Chemistry Research, 34 (1995) 4371-4377.

[45] A. Ameri, N. ShojaiKaveh, E.S.J. Rudolph, K.H. Wolf, R. Farajzadeh, J. Bruining, Investigation on Interfacial Interactions among Crude Oil–Brine–Sandstone Rock–CO_2 by Contact Angle Measurements, Energy & Fuels, 27 (2013) 1015-1025.

[46] N. Shojai Kaveh, K.H. Wolf, S.N. Ashrafizadeh, E.S.J. Rudolph, Effect of coal petrology and pressure on wetting properties of wet coal for CO_2 and flue gas storage, International Journal of Greenhouse Gas Control, 11, Supplement (2012) S91-S101.

[47] N. Shojai Kaveh, E.S.J. Rudolph, K.-H.A.A. Wolf, S.N. Ashrafizadeh, Wettability determination by contact angle measurements: hvbB coal–water system with injection of synthetic flue gas and CO_2, Journal of Colloid and Interface Science, 364 (2011) 237-247.

[48] R. Span, W. Wagner, A New Equation of State for Carbon Dioxide Covering the Fluid Region from the Triple-Point Temperature to 1100 K at Pressures up to 800 MPa, Journal of Physical and Chemical Reference Data, 25 (1996) 1509-1596.

[49] V.I. Baranenko, L.N. Fal'kovskii, V.S. Kirov, L.N. Kurnyk, A.N. Musienko, A.I. Piontkovskii, Solubility of oxygen and carbon dioxide in water, Atomic Energy, 68 (1990) 342-346.

[50] W. Yan, G.-Y. Zhao, G.-J. Chen, T.-M. Guo, Interfacial Tension of (Methane + Nitrogen) + Water and (Carbon Dioxide + Nitrogen) + Water Systems, Journal of Chemical & Engineering Data, 46 (2001) 1544-1548.

[51] D. Yang, Y. Gu, P. Tontiwachwuthikul, Wettability determination of the crude oil-reservoir brine-reservoir rock system with dissolution of CO_2 at high pressures and elevated temperatures, Energy and Fuels, 22 (2008) 2362-2371.

[52] E.L. Cussler, Diffusion: mass transfer in fluid systems, Cambridge University Press, 2009.

[53] Z. Duan, R. Sun, C. Zhu, I.M. Chou, An improved model for the calculation of CO_2 solubility in aqueous solutions containing Na^+, K^+, Ca^{2+}, Mg^{2+}, Cl^-, and SO_4^{2-}, Marine Chemistry, 98 (2006) 131-139.

[54] J.M.T. Vasconcelos, S.P. Orvalho, S.S. Alves, Gas–liquid mass transfer to single bubbles: Effect of surface contamination, AIChE Journal, 48 (2002) 1145-1154.

[55] M.J.W. Frank, J.A.M. Kuipers, W.P.M. van Swaaij, Diffusion Coefficients and Viscosities of $CO_2 + H_2O$, $CO_2 + CH_3OH$, $NH_3 + H_2O$, and $NH_3 + CH_3OH$ Liquid Mixtures, Journal of Chemical & Engineering Data, 41 (1996) 297-302.

[56] R. Farajzadeh, Enhanced transport phenomena in CO_2 sequestration and CO_2 EOR, in: Geoscience and Engineering, Delft University of Technology, The Netherlands, 2009.

[57] A. Okhotsimskii, M. Hozawa, Schlieren visualization of natural convection in binary gas–liquid systems, Chemical Engineering Science, 53 (1998) 2547-2573.

[58] B. Arendt, D. Dittmar, R. Eggers, Interaction of interfacial convection and mass transfer effects in the system CO_2–water, International Journal of Heat and Mass Transfer, 47 (2004) 3649-3657.

[59] W.G. Anderson, Wettability Literature Survey- Part 2: Wettability Measurement, SPE Journal of Petroleum Technology, 38 (1986) 1246-1262.

[60] A.K. Das, P.K. Das, Equilibrium shape and contact angle of sessile drops of different volumes-Computation by SPH and its further improvement by DI, Chemical Engineering Science, 65 (2010) 4027-4037.

[61] H. Ren, S. Xu, S.T. Wu, Effects of gravity on the shape of liquid droplets, Optics Communications, 283 (2010) 3255-3258.

[62] B. Song, J. Springer, Determination of Interfacial Tension from the Profile of a Pendant Drop Using Computer-Aided Image Processing: 1. Theoretical, Journal of Colloid and Interface Science, 184 (1996) 64-76.

[63] J.L. Dickson, G. Gupta, T.S. Horozov, B.P. Binks, K.P. Johnston, Wetting phenomena at the CO_2/water/glass interface, Langmuir, 22 (2006) 2161-2170.

[64] A.E. Peksa, P.L.J. Zitha, K.H.A.A. Wolf, Role of Rock Surface Charge in the Carbonated Water Flooding Process, in: 75th EAGE Conference & Exhibition incorporating SPE EUROPEC 2013, EAGE, London, UK, 2013.

[65] T.K. Tokunaga, DLVO-Based Estimates of Adsorbed Water Film Thicknesses in Geologic CO_2 Reservoirs, Langmuir, 28 (2012) 8001-8009.

[66] B.K. Dutta, Principles of mass transfer and separation processes, Phi Learning, 2009.

[67] E.R. Lapwood, Convection of a fluid in a porous medium, Mathematical Proceedings of the Cambridge Philosophical Society, 44 (1948) 508-521.

CHAPTER 5

Evaluation of Interfacial Interactions between Crude Oil-Water-Sandstone with CO_2 or Flue Gas using Surface Free Energy Analysis[*]

ABSTRACT

Wettability plays a significant role on the performance of enhanced oil recovery techniques because of its effect on fluid saturations and flow behavior in porous media. This study is directed towards determining contact angles, i.e. wettability, in systems with water, an oil-saturated rock, and carbon dioxide or synthetic flue gas. Two situations are considered: Rock system I is partially water-wet, whereas rock system II is effectively oil-wet. Contact angles have been determined experimentally as a function of pressure using pendant-drop shape analysis. The experiments were carried out at a constant temperature of 318 K and pressures varying between 0.1 and 16.0 MPa in a pendant-drop cell.

For rock system I, i.e., partially water-wet substrate/water/CO_2 or flue gas, the dependence on pressure is very small. The results show that both carbon dioxide and flue gas are the non-wetting phase in the pressure range studied. This behavior can be quantitatively understood in terms of the expected dependencies of the three interfacial energies in Young's equation on pressure.

For Rock system II, i.e., effectively oil-wet substrate/water/CO_2, the dependency of contact angle on pressure is considerable. This study proves that carbon dioxide becomes the wetting phase at pressures higher than 10.0 MPa. Beyond 10.0 MPa, i.e. in the supercritical region, the contact angle remains practically constant. However, rock system II is intermediate-wet with water and synthetic flue gas (20 mol% CO_2 and 80 mol% N_2) at low pressures. In this system, the contact angle increases slightly with pressure. These behaviors can again be quantitatively understood based on expected trends of the three interfacial energies that determine the contact angle.

To describe the wetting properties of the surface as a function of pressure, a surface-free-energy analysis is used based on an equation of state (EOS). Following this approach, a modified equation of state is proposed to describe the contact angle of a liquid/gas/solid system at various pressures. It is also shown that use of the equation of state method makes it possible to approach the experimental data quantitatively, if a number of reliable contact-angle and interfacial-tension data are available for a system of interest.

KEYWORDS: Wettability; Contact angle; Surface free energy analysis; Equation of state; Oil recovery; CO_2 storage; Synthetic flue gas.

---

[*] ***Published partly in:***

- *Journal of Energy and Fuels, 27 (2013) 1015-1025.*

5.1. INTRODUCTION

Carbon dioxide injection, either miscible or immiscible, has been recognized as an efficient method to enhance oil recovery and to reduce CO_2 emission [1-3]. By performing an exergy analysis Eftekhari et al. [4] showed that the cost of separation of CO_2 from flue gas and re-injection is comparable to the benefit from oil recovery. Therefore, to make the CO_2-based oil enhanced oil recovery process economically more efficient, the recovery process should be optimized to maximize oil recovery and to minimize storage costs. CO_2 injection is typically applied after water flooding where a significant volume of oil is left behind due to capillarity. However, the unfavorable gas-oil mobility ratio and the rock heterogeneity contribute to fingering and channeling, which results in poor volumetric sweep efficiency. To improve the mobility ratio between the injected fluid and the oil, water and CO_2 are usually injected in alternating slugs [5, 6]. It has been shown by different studies that the chemical composition of the aqueous phase has significant effect on the performance of such a process [7-9]. At the same time this may lead to trapping of a significant volume of oil in the form of ganglia surrounded by thin water films. Consequently, the injected gas may not directly contact the trapped oil [10]. For such a condition, the interactions between oil, water, CO_2 and the rock surface determine the flow characteristics of the system. One practical approach to analyze and understand the flow behavior of such a complex system is through investigation of the dynamic interfacial interactions between rock, brine, CO_2, and oil at reservoir conditions. In this study, rock wettability is investigated, which controls the transport properties, viz. the relative permeability, the capillarity, and the residual saturations of brine, CO_2, and oil in the reservoir rock. This is important for the control of the performance of any CO_2 injection process.

The wettability is determined by the relative surface energy of, e.g., two fluids on a solid surface [11]. Contact-angle determination is the most widely accepted method for determining the average wettability of a specific surface at reservoir conditions [12]. Although this method is strongly influenced by several parameters including surface roughness, viscous effects, contact line fluctuations, and vibrations, it is relatively easy to conduct and can be applied at high pressures and temperatures. By definition the contact angle is determined through the densest phase. A reservoir rock is considered to be water-wet when the contact angle of a water droplet on the rock surface is in a range between 0° and 70°. If the water droplet has a contact angle in the range between 75° and 105° the surface is considered to be intermediate-wet. Finally, when the contact angle is in the range between 105 and 180° the rock is oil-wet.

In general, for a CO_2-liquid-solid system, CO_2 is assumed to be the non-wetting phase. For most practical conditions, the injected CO_2 is in its supercritical state. Therefore, disregarding the possibility of partial wetting of CO_2 may lead to an underestimation of the efficiency for oil recovery and storage implementation. Recent experiments and observations for different fluid-solid combinations reveal that CO_2 can be considered as wetting or partially wetting phase with partial water saturation [13-15]. Yang et al. [16, 17] addressed the effect of temperature, pressure, CO_2 dissolution and diffusion on the wetting properties of the system of reservoir crude, reservoir brine, reservoir rock, and CO_2. The authors showed that CO_2 injection can alter the wettability of a limestone rock slice and thus will significantly influence the oil recovery and CO_2 storage efficiency. Chalbaud et al. [18, 19] conducted interfacial tension experiments for brine-CO_2 systems at different pressures, temperatures and salinity conditions representing a CO_2 storage operation. The authors concluded that for a strong hydrophilic porous medium, the CO_2 does not wet the solid surface, whereas if the porous medium is less hydrophilic the CO_2 significantly wets the surface. Chiquet et al. [20] conducted a series of contact-angle experiments with various brine solutions and CO_2 as the fluid phases, and as solid substrates mica or quartz which are water-wet in the presence of hydrocarbons. The experimental data revealed that the wetting properties of mica changes from water-wet towards intermediate-wet at pressures higher than 10.0 MPa. In addition, the wettability alteration is a consequence of CO_2 dissolution, which leads to a decrease in the pH of the aqueous phase. Shojai Kaveh et al. [21, 22] proved that CO_2 can change the wetting properties of a medium rank high volatile Bituminous (hvBb) coal from intermediate-wet to gas-wet. For the injection of a synthetic flue gas, 20 vol. % CO_2 and 80 vol. % N_2, a change from water-wet to intermediate-wet was observed. For the high rank semi-anthracite coal, the wettability alteration from intermediate-wet to gas-wet with CO_2 injection was observed at pressures above 5.7 MPa.

Moreover, direct injection of flue gas into a reservoir eliminates the need for CO_2 separation prior to its injection into the field. Flue gas injection in heavy-oil reservoirs is investigated as an option to enhance oil recovery [23, 24]. In light-oil reservoirs, this process may be a cost-effective gas displacement method, particularly in low-porosity and low-permeability reservoirs [24]. Despite its importance for improved oil recovery and CO_2 storage, there are limited experimental data in literature concerning the wettability behavior of the system consisting of crude oil, rock, water, and CO_2 and/or flue gas at reservoir conditions. Most of the previous studies on this topic concerned the wetting behavior of the system consisting of rock, brine, and CO_2 as function of pressure, temperature and salinity. However, even though the system including crude oil with rock, aqueous phase, and CO_2 is more realistic for the industry, only limited experimental data on these systems are available in literature and hardly any data exists with flue gas. To our knowledge, the work conducted by Yang et al. [17] is the only published research that attempts to identify the interfacial interactions between crude oil, carbonate, brine, and CO_2.

The main purpose of this study is to extend the research of the previous studies. To this end, different substrates with different wetting properties are studied experimentally. A modified experimental procedure, which simulates the real conditions in CO_2 injection process, is applied to evaluate the wetting properties of a system consisting of crude oil, water, rock, CO_2 and/or flue gas. Equilibrium contact-angle experiments were conducted using a modified pendant-drop cell (PDC) technique at high pressures and elevated temperature using oil-wet and water-wet sandstone rock slabs. The contact-angle data are then described using an equation of state approach which is the subject of numerous studies, being carried out mostly by Neumann et al. [25-27]. Following this approach, a modified equation of state is proposed to describe the contact angle of a liquid/gas/solid system at various pressures.

5.2. EXPERIMENTAL

5.2.1. MATERIALS

Two rock slabs were obtained from a Bentheimer sandstone block. Each slab has dimensions of 30 × 12 × 6.0 mm^3. The Bentheimer sandstone is composed of 95% quartz, 3% of clay, and less than 2% feldspars and is naturally water-wet. The average porosity is 21% and the permeability is around 1.5 Darcy. Carbon dioxide (purity 99.7 %) is obtained from Linde Gas Benelux. Two crude oil samples, crude A and B, with different physical properties (Table 5.1) were used.

Table 5.1. Physical properties of the oil samples used in the experiments

Oil	**MW (g/gmol)**	**Density (g/ml)**	**Acid Number (mg KOH/g oil)**	**Base Number (mg KOH/g oil)**	**C_{7+} (wt. %)**	**C_{11+} (wt. %)**
A	223.04	0.8376	0.24±0.02	0.294±0.01	96.38	77.57
B	223.98	0.8532	3.52±0.05	1.46±0.05	95.42	78.44

5.2.2. METHODOLOGY

In this subsection the experimental procedure that is used to determine the wetting properties of the system rock, oil, water, CO_2 and/or synthetic flue gas is explained. Thereby, typical in-situ conditions that might be encountered in CO_2-injection processes are established. The main advantage of the proposed procedure is that the experiments can be conducted at realistic conditions of the most common CO_2 injection scenarios, i.e., tertiary gas injection after water flooding and water-alternating-gas injection processes.

Prior to the experiments, one side of each rock slab was polished to mitigate the effect of surface roughness on the contact-angle determination. The characterization of the roughness of the surface is based on the calculation of the so-called P_a factor (a more detailed description is in Chapter 2). Then the rock slabs were dried in an oven at 333 K for 48 hours. SB-1 was saturated with crude A without any treatment and filtration. The substrate was then aged at room temperature for at least six weeks. Crude B was used to saturate the substrate SB-5. This substrate was aged with crude B for 22 months at 333K (Table 5.2). This was done to allow investigating the effect of aging time and oil properties on the wetting properties of the surface. It is expected that the Bentheimer sandstone sample that was only “briefly” exposed to crude A, i.e., SB-1, is no longer completely water-wet, but exhibit a finite contact angle in the water-CO_2-oil saturated substrate system. The substrate consists of patches of oil and rock. The sample that was exposed to crude B for much longer times, i.e., SB-5, is considered to be completely oil-wet, i.e., an oil film has formed between the rock and CO_2.

For each run, a saturated rock slab was placed inside the cell and leveled horizontally (Fig. 5.1) before the cylinder was closed and made leak-free. Subsequently, the cell was placed in the oven and was aligned with the camera, the endoscope and the light source. Next, the cell was vacuumed to remove air. Then, the gas buffer cell was filled and pressurized with gas to make sure that enough gas is available for a complete experimental run. The whole set up was then pre-heated to a temperature of 318 K. After reaching the desired temperature, the temperature in the oven was kept constant at 318 K for all experiments. Thereafter, the cell was filled with distilled water. Subsequently, the system pressure was increased to the test pressure by injecting CO_2 into the cell from the gas buffer cell at a low flow rate. Based on the decrease in pressure in the gas buffer cell the number of moles of CO_2 added to the cell is calculated using the Span-Wagner reference equation of state [28]. The compositional information is necessary to make sure that the aqueous phase has been fully saturated with CO_2. Moreover, a density meter inside the oven monitors the density of the mixture. A stable density value at constant pressure and temperature shows that the system is in equilibrium. Once equilibrium had been reached, a gas bubble, either CO_2 or flue gas, was injected into the cell via the capillary tip which is positioned at the bottom of the cell (Fig. 5.1). Successive images of the bubble captured on the surface were taken and then used as input of image-analysis procedure to determine the contact angle. For the image analysis, the Young-Laplace equation was used to describe the bubble profile. The details of the image processing and contact-angle determination can be found in Chapter 2.

Having completed the test at the first pressure level, more CO_2 was injected into the cell to increase the system pressure to the next pressure level. The system was allowed to settle for at least 6 hours to reach the new equilibrium state. After equilibration, a gas bubble was injected into the cell, placed against the rock surface and the contact angle determined with image analysis. This procedure was repeated in pressure steps around 1.5 MPa, up to the maximum pressure of 16.0 MPa, at a constant temperature of 318 K. This procedure was repeated for all experiments conducted in this study (Table 5.2).

Table 5.2. Summary of the experiments

Sample	**Wettability**	**Crude Oil**	**Aging time**	**Aging temperature (K)**	**Gas Phase**	**Aqueous Phase**
SB-1	water-wet	A	six weeks	298	CO_2 and/or flue gas	distilled water
SB-5	oil-wet	B	22 months	333	CO_2 and/or flue gas	distilled water

In this study all contact-angle determinations were performed using a fully CO_2-saturated aqueous phase, so that the mass transfer involved in the process is negligible and the contact-angle determination is not affected by dissolution.

Figure 5.1. Digital photograph of the inside of the modified pendant-drop cell with a Bentheimer Sandstone sample mounted inside.
At the bottom the injection tip with an outer diameter of 1.8 mm is observed.

5.3. RESULTS AND DISCUSSIONS

5.3.1. EFFECT OF PRESSURE

Fig. 5.2 shows the CO_2 stable contact-angle data as a function of pressure for partially water-wet (SB-1) and oil-wet (SB-5) substrates. It can be observed from Fig. 5.2 that for a partially water-wet sample the contact angle remains nearly constant and is less than 75° in the pressure range studied. The contact angle never exceeds 70° and the surface remains partially water-wet when the pressure increases from 0.5 to 14.0 MPa. These results are not in agreement with the data from the work of Espinoza et al. [14] for a hydrophilic-quartz surface. This disagreement is attributed to the presence of oil patches on the surface which make the wetting properties of clear and untreated sandstone different than that of briefly-aged substrate.

Three different regions can be identified for the contact-angle data of an oil-wet system. (1) For pressures up to 4.0 MPa the contact angle increases slightly from 95° to 100°. This pressure range corresponds to gaseous CO_2 at 318K. This region is called the sub-critical region. (2) In the pressure range between 4.0 MPa and 9.0 MPa, i.e., near-critical conditions for CO_2 at 318K, the contact angle increases sharply from 100° to 140° and the substrate turns from intermediate-wet to CO_2-wet. This phenomenon could be attributed to the formation of a layer of dense CO_2 on the solid and a large decrease in the γ_{lv} [29]. Because high-energy fluids, for example water, tends not to spread on low-energy surfaces, the presence of a low-energy CO_2 layer on the surface will cause the CO_2 contact angle to increase in order to reduce contact between these two phases. In addition, the decrease in γ_{lv} will cause θ to increase further above 90° to increase the interfacial area between water and CO_2. (3) For pressures higher than 9.0 MPa, the contact angle slightly increases with pressure from 140° to 145°. This region corresponds to supercritical conditions of CO_2 at 318K. These results are in agreement with the experimental data from Dickson et al. [13] for a hydrophobic glass surface where the authors showed that the CO_2 contact angle remains almost constant with pressure even if the system pressure increases to above 20.0 MPa.

Fig. 5.3 illustrates the synthetic flue gas contact angles for partially water-wet (SB-1) and oil-wet (SB-5) substrates as a function of pressure at a temperature of 318 K. In both systems, i.e. SB-1 and SB-5, the contact-angle values of flue gas bubbles are all smaller than those of the CO_2 bubbles. For a partially water-wet sample (SB-1), the oil/sandstone/water/flue gas system is (and remains) water-wet even at high pressures. The experimental results show that the pressure has no significant effect on the wettability of this system (rhombus in Fig. 5.3). For the hydrophobic sample (SB-5), the oil/rock/water/synthetic flue gas system is intermediate-wet at low pressures. In this system, the contact angle increases slightly with increasing the pressure and the substrate turns from intermediate-wet to flue gas-wet at pressures above 14 MPa. The wettability behavior of these systems, i.e., SB-1 and SB-5, with synthetic flue gas can be explained by considering the wetting properties of these samples with CO_2 and the ratio of 20 mol% CO_2 to 80 mol% N_2 in the flue gas bubble. In addition, the interfacial tension (IFT) between water and synthetic flue gas changes slightly with increasing the pressure (Chapter 4, Fig. 4.7). Accordingly, less impact of pressure on the wettability of the flue gas system can be expected. This trend is also observed experimentally (Fig. 5.3).

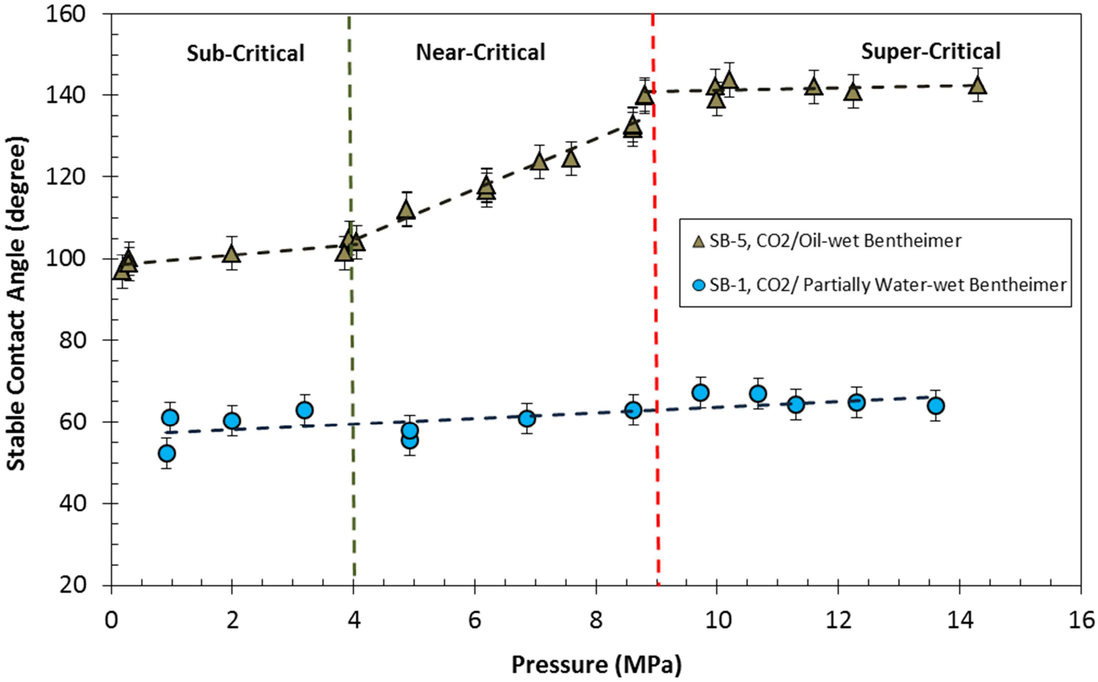

Figure 5.2. CO_2 contact angles for partially water-wet substrate, SB-1, and the oil-wet substrate, SB-5, as a function of pressure at a temperature of 318 K. The dashed lines give the best linear fit through the respective data.

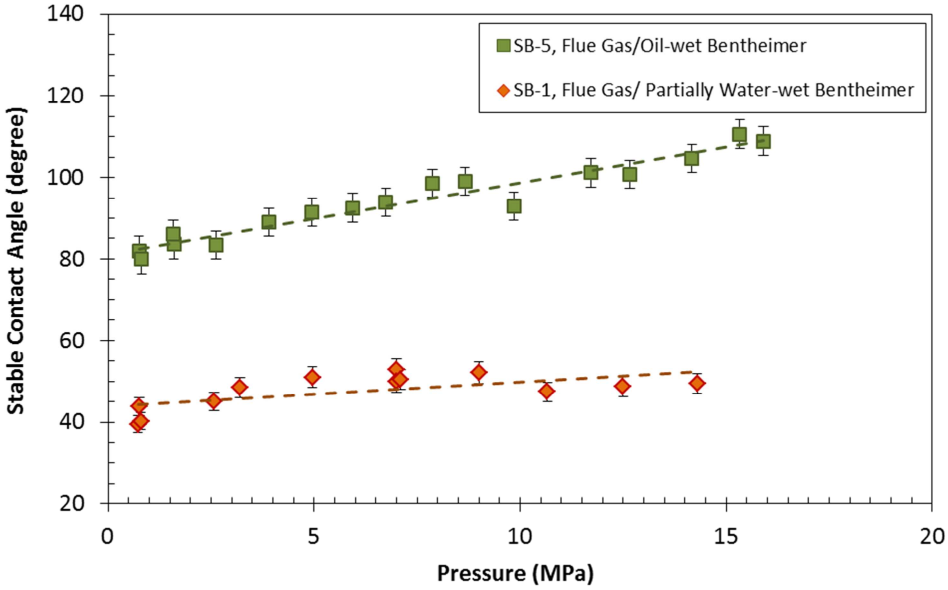

Figure 5.3. Synthetic flue gas contact angles for partially water-wet substrate, SB-1, and the oil-wet substrate, SB-5, as a function of pressure at a temperature of 318 K. The dashed lines give the best linear fit through the respective data.

The primary objective of the SB-5 experiments was to examine the effect of aging time on the contact-angle measurements. To this end, a rock substrate, viz., SB-5, was saturated with Crude B and aged for 22 months at a constant temperature of 333 K. As a result of the aging procedure the wettability of the substrate changed from strongly water-wet to effectively oil-wet. The change in the initial wettability was examined by immersing the substrates in distilled water to allow them to produce oil spontaneously. For this rock slab, i.e., SB-5, no oil production was observed even after one month. In addition, digital images along with the mass balance of the oil-wet and water-wet substrates before and after the experiments revealed that for the oil-wet substrates no oil was liberated during the spontaneous imbibition test (see Fig. 5.4).

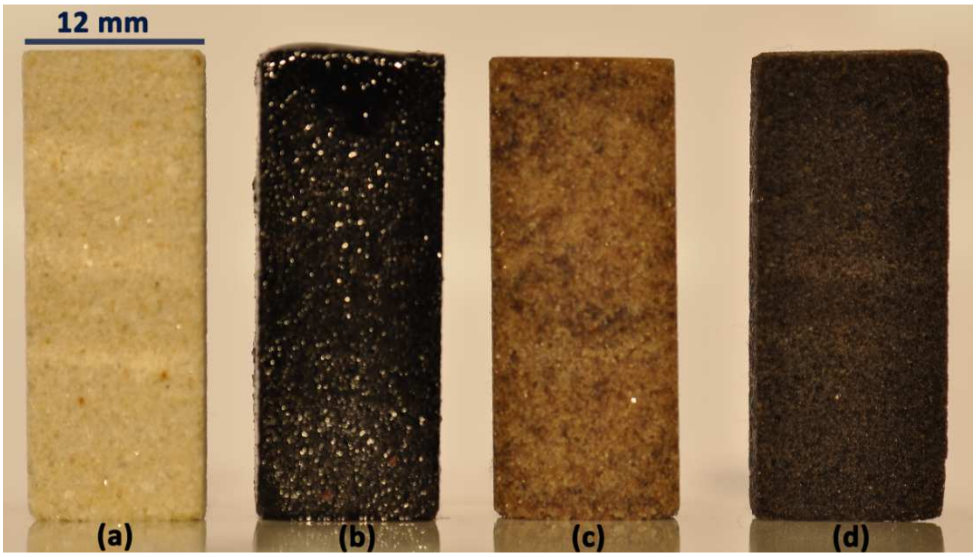

Figure 5.4. Bentheimer Sandstone samples: (a) initial sample, (b) sample saturated with oil before experiment, (c) partially water-wet sample (SB-1) after experiment, and (d) effectively oil-wet sample (SB-5) after experiment.

The contact-angle data show that even at low pressures, the SB-5 system is intermediate-wet. However, the wettability alters from intermediate-wet to CO_2-wet at pressures higher than 9.0 MPa. This means that CO_2 is able to enter the small pores, due to the sign change of capillary pressure, and come into contact with the oil that has been trapped by water after the initial water flooding. The results of three-dimensional random network model [30, 31] show the implications of the oil-wet substrate experiment. Suicmez et al. [30, 31] showed that for an oil-wet porous medium, the gas relative permeability is lower in the presence of water than oil because the gas is no longer the most non-wetting phase. For practical purposes this means that an initially oil-wet substrate becomes CO_2-wet at pressures relevant for CO_2-based oil recovery processes.

In Fig. 5.5 the digital images of the captured CO_2 bubbles on the oil-wet and water-wet surfaces are compared. The images were taken at approximately the same pressure and temperature and in presence of CO_2-saturated aqueous phase. It is obvious that for the oil-wet surface, carbon dioxide can wet the surface while for the water-wet sample CO_2 is the non-wetting phase even at high pressures. From an operational point of view, it is preferable to inject CO_2 at lower pressures because of compression and injection costs. Because of improved phase behavior with oil with increasing pressure, CO_2 is usually injected at supercritical conditions for EOR [32]. The results of this study indicate another advantage of injection at supercritical conditions: it is expected that CO_2 flooding of an oil-wet porous medium, in the presence of water, results in more-direct contact with the oil when the CO_2 is injected at near-critical conditions. At these conditions the rock is CO_2-wet and the contact angle hardly changes if the pressure increases further.

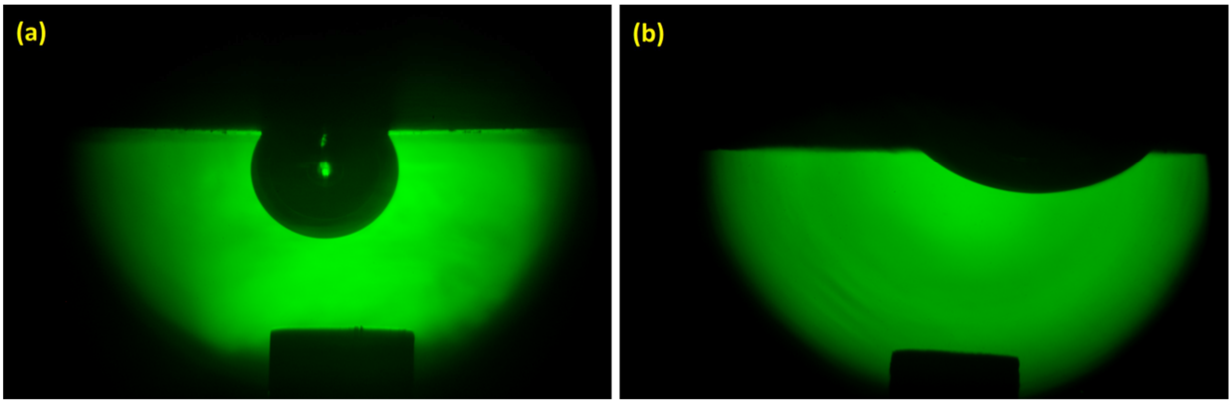

Figure 5.5. Digital images of CO_2 bubbles on an oil saturated-Bentheimer surface in the presence of CO_2-saturated aqueous phase at 318 K; (a) partially water-wet (SB-1) sample at $P=8.62$ MPa, $\theta=63.02°$ and (b) effectively oil-wet (SB-5) sample at $P=8.80$ MPa, $\theta=139.70°$.

5.3.2. EVALUATION OF CONTACT ANGLES BY SURFACE-FREE-ENERGY ANALYSIS

The dependence of the contact angle on pressure can be explained using surface-free-energy analysis by investigating the dependency of the three interfacial energies in Young's equation (Chapter 1, Eq. 1.2), i.e., γ_{sv}, γ_{sl}, and γ_{lv}, on the pressure. In Young's equation, γ_{lv} and θ are parameters, which can be determined experimentally. However, γ_{sv} and γ_{sl} remain unknown. In order to determine the unknowns, an additional correlation between γ_{lv}, γ_{sl} and γ_{sv} is required. The most common method to derive such a correlation is based on a surface-free-energy analysis (SFEA), which is the subject of numerous studies mostly carried out by Neumann et al. [25-27]. This relation is called an equation of state and is described by:

$$f(\gamma_{lv}, \gamma_{sv}, \gamma_{sl}) = 0 \tag{5.1}$$

where γ_{lv}, γ_{sv} and γ_{sl} are the interfacial tensions or surface energies between the aqueous phase and the gas phase, the solid and the gas phase, and the solid and the aqueous phase, respectively. Surface energy is usually defined as the amount of the required work to create a unit area of surface of the object in its environment. In other words, surface energy indicates the work required to split a bulk sample to two surfaces [33] in its environment. In case the surfaces are not identical, the work of adhesion (W) is considered as the energy of cleaving species 1 from species 2 in a medium of species 3:

$$W_{12} = \gamma_{13} + \gamma_{23} - \gamma_{12} \tag{5.2}$$

where γ_{13} and γ_{23} are the surface energies of the two new species in medium 3, and γ_{12} is the interfacial tension between species 1 and 2. Based on the definition of cleavage work, the cleavage energy of a single species ($W_{11} = W_{22}$) [33], the surface energy of each surface can be written as:

$$W_{11} = 2\gamma_{13} \tag{5.3}$$

$$W_{22} = 2\gamma_{23} \tag{5.4}$$

For a captive-bubble system, free energy of adhesion per unit area of a solid-vapor pair ,W_{sv}, is equal to the work required to separate a unit area of the solid-vapor interface [34] ($v=1$, $s=2$, $l=3$), which presented schematically in Fig. 5.6:

$$W_{sv} = \gamma_{lv} + \gamma_{sl} - \gamma_{sv} \tag{5.5}$$

By using Eqs. (5.3) and (5.4):

$$W_{ss} = 2\gamma_{sl} \tag{5.6}$$

$$W_{vv} = 2\gamma_{lv} \tag{5.7}$$

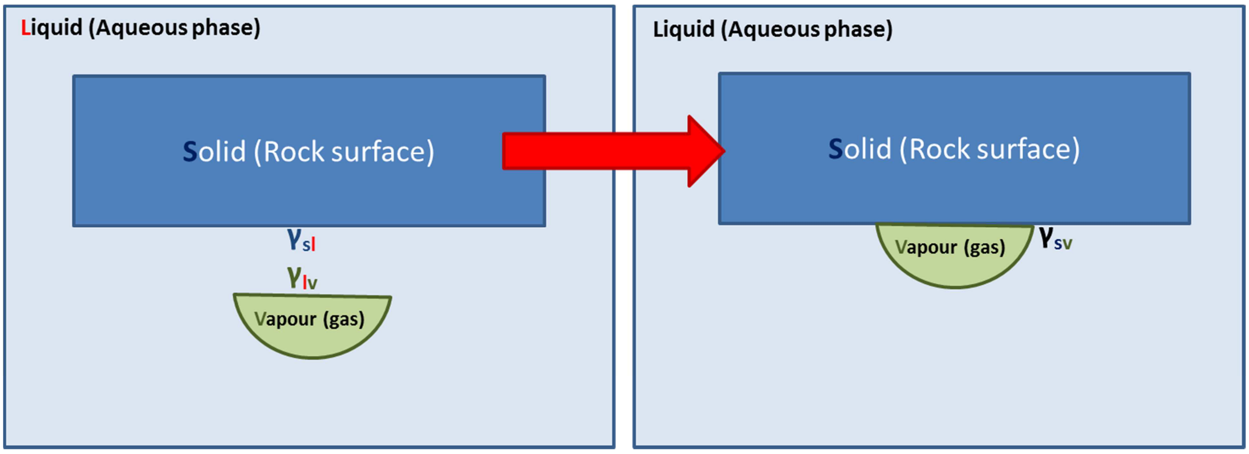

Figure 5.6. Schematic representation of work of adhesion in captive-bubble system.

The interfacial adhesion work can be approximated using the cohesion work of a solid and the cohesion work of the relevant gas phase. This idea was proposed for the first time by Antonow [35] and Berthelot [36]. Unlike Antonow's rule, Berthelot's combing rule has a theoretical background and accounts for molecular interactions of like pairs in terms of London dispersion [36]:

$$\varepsilon_{ij} = \sqrt{\varepsilon_{ii}\varepsilon_{jj}} \tag{5.8}$$

where ε_{ij} is the potential energy parameter of unlike-pair interactions; ε_{ii} and ε_{jj} are the potential energy parameters of like-pair interactions. The free energy is directly proportional to the energy parameter, ε [37, 38], so that based on the Berthelot's combing rule, the interfacial adhesion work, W_{sv}, can be described by the geometric mean of the cohesion work of the solid phase, W_{ss}, and the cohesion work of the relevant gas phase, W_{vv}:

$$W_{sv} = \sqrt{W_{ss}W_{vv}} \tag{5.9}$$

By further modification of the Berthelot hypothesis, Kwok and Neumann [25] proposed an alternative formulation of this combination rule:

$$\varepsilon_{ij} = (1-\kappa(\varepsilon_{ii}-\varepsilon_{jj})^2)\sqrt{\varepsilon_{ii}\varepsilon_{jj}} \tag{5.10}$$

where κ is a fitting parameter.

In this study, the same approach as was applied by Neumann et al. is followed to determine γ_{sv} versus pressure [26]. Based on the alternative formulation of combining rule, Eq. (5.10), the free energy of adhesion for a solid-vapor pair Eq. (5.9) can be written as:

$$W_{sv} = (1-\alpha_2(W_{vv}-W_{ss})^2)\sqrt{W_{ss}W_{vv}} \tag{5.11}$$

where α_2 is a constant. Replacing Eqs. (5.6) and (5.7) in Eq. (5.11) gives:

$$W_{sv} = 2\left[1-\beta_2(\gamma_{lv}-\gamma_{sl})^2\right]\sqrt{\gamma_{lv}\gamma_{sl}} \tag{5.12}$$

Using Eq. (5.5) and (5.12) an alternative equation of state can be obtained to determine the solid-vapor interfacial tension, γ_{sv} :

$$\gamma_{sv} = \gamma_{lv} + \gamma_{sl} - 2\sqrt{\gamma_{lv}\gamma_{sl}}\left[1 - \beta_2(\gamma_{lv} - \gamma_{sl})^2\right] \tag{5.13}$$

Combining this equation with Young's equation (Chapter1, Eq. 1.1,) yields:

$$\cos\theta = 1 - 2\sqrt{\frac{\gamma_{sl}}{\gamma_{lv}}}\left[1 - \beta_2(\gamma_{lv} - \gamma_{sl})^2\right] \tag{5.14}$$

where β_2 is a constant. The basic assumption in this method is that γ_{sl} remains practically unchanged and γ_{sv} only depends on the properties of the solid surface and the gas phase used in the contact-angle determination. The constant β_2 and γ_{sl} are determined using Eq. (5.14) by a least square fit of a given set of θ and γ_{lv} data measured on one and the same type of solid surface. It is important to note that this approach can only be applied for the same liquid phase and if the solid phase is not altered due to swelling, chemical reaction or mineral dissolution so that the assumption of a constant γ_{sl} is fulfilled. Once γ_{sl} and β_2 are determined, they can be used to determine the contact angle for the same surface and different liquid-vapor pairs. Then it is possible to estimate the theoretical contact angle and to provide a validation method for contact-angle measurements.

In this study, a pair of experimental $\theta - \gamma_{lv}$ data for the oil-wet system, SB-5, at low (0.5 MPa) and high (10.0 MPa) pressures were used to calculate γ_{sl} and the constant β_2 using Eq. (5.14). For these calculations, the interfacial-tension data have been interpolated from the experimentally determined IFT values (Chapter 4) at relevant pressures and temperature. With these data and Eq. (5.14), the γ_{sl} and fitting parameter β_2 for substrate SB-5/CO_2 system were calculated to be 25.48 mN/m and 1.057×10^{-4} $(m/mN)^2$, respectively. For the SB-5/Flue gas system, γ_{sl} and β_2 are 25.13 mN/m and 1.114×10^{-4} $(m/mN)^2$, respectively. The small variation between γ_{sl} values in CO_2 and flue gas systems can be attributed to the difference in composition of the CO_2-saturated aqueous phase in the corresponding experiments.

These values, i.e., γ_{sl} and β_2, were then used to compute the CO_2 and synthetic flue gas contact angles of the oil-wet substrate SB-5 at the experimental temperature of 318K and experimental pressures. Tables 5.3 and 5.4 summarize the experimental and predicted CO_2 and synthetic flue gas contact angles for the oil-wet substrate SB-5/water/gas system. It can be seen from these tables that Eq. (5.14) can reproduce the whole set of contact-angle data within an acceptable range of accuracy (<5%). The comparisons between predicted and experimental contact angles of CO_2 and synthetic flue gas for the substrate SB-5 are shown in Figs. 5.7 and 5.8. According to Figs. 5.7 and 5.8, the model equation is able to reproduce the contact-angle data in the range of pressures studied. In other words, the equation-of-state method can be used to evaluate the wetting properties of a specific surface, if a number of reliable contact-angle and interfacial-tension data are available for the system under consideration. It is worthwhile to note that any deviation between the contact angles predicted by Eq. (5.14) and the experimental contact-angle values can be caused by the non-ideality of the rock surface, i.e., roughness, heterogeneity, and/or the small changes in the γ_{sl} with pressure.

Table 5.3. Results of the contact-angle prediction using the equation of state approach for the oil-wet substrate (SB-5)/ CO_2/ distilled water system

Pressure (MPa)	γ_{lv} **(mN/m)**[§]	**Exp. CA**[§§]	γ_{sv} **(mN/m)**[*]	**Model CA**[**]
0.18	68.12	96.9	26.29	89.31
0.30	67.56	100.1	25.60	89.90
0.30	67.56	98.8	25.60	89.90
1.99	59.69	101.3	16.82	98.33
3.93	51.39	105.1	9.64	107.95
4.88	47.75	112.0	7.13	112.60
6.20	43.20	116.7	4.53	119.01
6.20	43.20	117.9	4.53	119.01
7.07	40.56	123.8	3.29	123.17
7.59	39.11	124.6	2.70	125.63
8.61	36.62	132.4	1.81	130.26
8.81	36.19	139.7	1.67	131.12
8.81	36.19	140.1	1.67	131.12
9.97	33.95	142.3	1.05	136.00
10.00	33.90	139.1	1.04	136.13
10.20	33.57	143.8	0.96	136.91
11.60	31.71	142.1	0.57	141.76
12.25	31.10	140.9	0.47	143.54
14.30	30.60	142.5	0.39	145.08
15.50	30.20	144.5	0.33	146.38

[§] Experimental data from Chapter 4

[§§] CA- contact angle

[*] Calculated using Eq. (5.13)

[**] Calculated using Eq. (5.14)

Table 5.4. Results of the contact-angle prediction using the equation of state approach for the oil-wet substrate (SB-5)/ synthetic flue gas/ distilled water system

Pressure (MPa)	γ_{lv} **(mN/m)**[§]	**Exp. CA**[§§]	γ_{sv} **(mN/m)**[*]	**Model CA**[**]
0.75	70.50	82.0	30.76	85.42
0.82	70.33	79.9	30.52	85.60
1.60	68.57	83.6	28.13	87.49
1.58	68.61	86.0	28.19	87.45
2.62	66.60	83.4	25.59	89.61
3.90	64.61	89.0	23.15	91.76
4.95	63.32	91.5	21.64	93.16
5.94	62.35	92.5	20.53	94.23
6.74	61.71	93.9	19.82	94.94
7.87	60.98	98.6	19.03	95.74
8.66	60.56	99.1	18.59	96.20
9.85	60.04	92.9	18.04	96.79
11.72	59.32	101.2	17.29	97.60
12.66	58.93	100.8	16.90	98.03
14.17	58.17	104.7	16.14	98.89
15.33	57.40	110.6	15.39	99.77
15.90	56.94	108.9	14.94	100.31

[§] Experimental data from Chapter 4

[§§] CA- contact angle

[*] Calculated using Eq. (5.13)

[**] Calculated using Eq. (5.14)

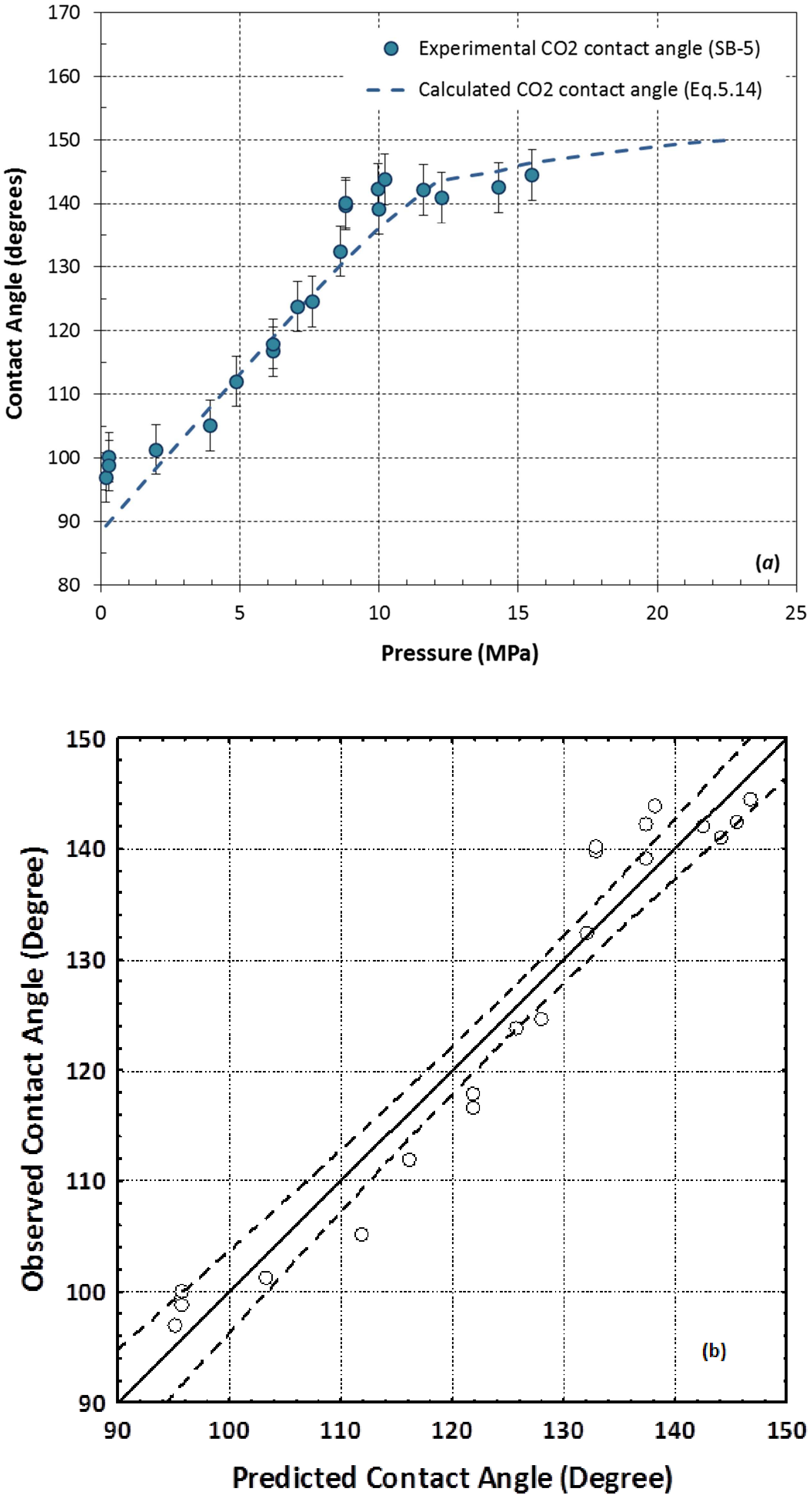

Figure 5.7. (a) CO_2 Contact angle as function of pressure for the oil-wet sample (SB-5) and water at a temperature of 318 K. Symbols display the experimental data; the line the prediction using Eq. (5.14). (b) Point-by-point comparison. The dashed lines show the 95% confidence interval.

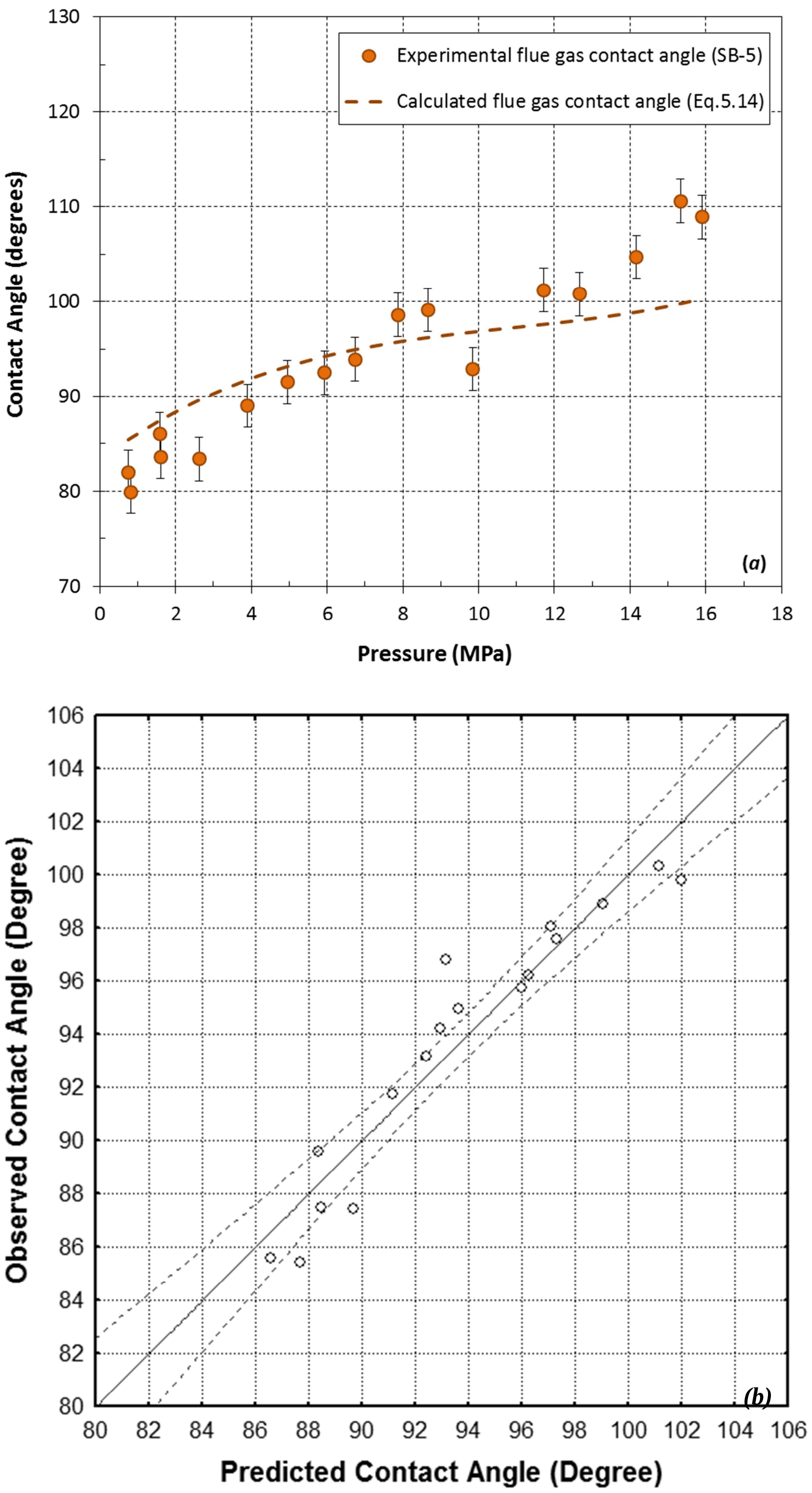

Figure 5.8. (a) Synthetic flue gas contact angle as function of pressure for the oil-wet sample (SB-5) and water at a temperature of 318 K. Symbols display the experimental data; the line the prediction using Eq. (5.14). (b) Point-by-point comparison. The dashed lines show the 95% confidence interval.

Having determined γ_{sl} and β_2, Eq. (5.13) was used to calculate γ_{sv}. The results are depicted in Fig. 5.9 and show that for both CO_2 and flue gas, γ_{sv} decreases with increasing the pressure. However, the variation of γ_{sv} with pressure for the flue gas system is smaller than those for CO_2, which is correlated to the change of γ_{lv} with pressure in these systems. The decrease in γ_{sv} and a constant value of γ_{sl} makes the numerator of Young's equation more negative at increasing pressures. The decrease in γ_{lv} will also make $\cos\theta$ more negative. Thus, both the numerator and denominator of Young's equation contribute to negative values of $\cos\theta$ (increase in θ) as the CO_2 pressure increases. Fig. 5.9 also shows that for CO_2 system above 10.0 MPa both γ_{lv} and γ_{sv} remain almost constant with increasing the pressure. This, a constant γ_{sl} explains the nearly constant θ for the CO_2/ oil-wet substrate SB-5/water system as the pressure increases above 10.0 MPa. In addition, a low value of γ_{sv} at pressures higher than 10.0 MPa indicates that the surface becomes CO_2-wet.

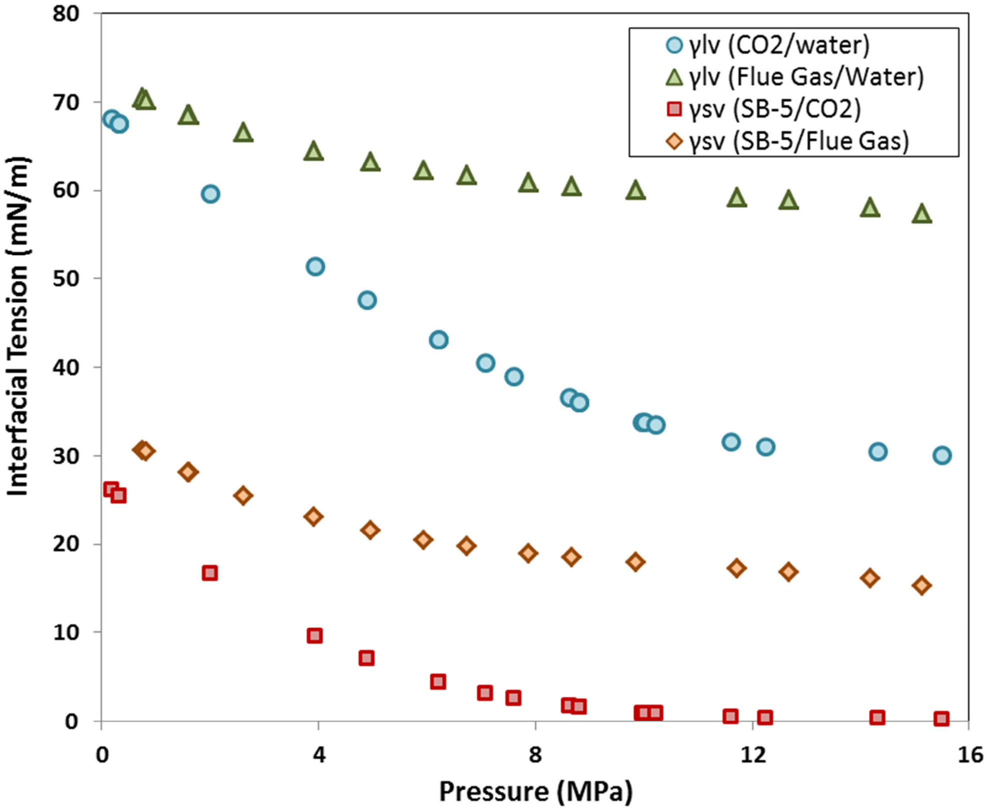

Figure 5.9. Calculated IFT-values versus pressure for CO_2/water/SB-5 system. γ_{lv} from Chapter 4, Fig. 4.7 and γ_{sv} from Eq. (5.13) vs. pressure. γ_{sv} was calculated for the oil-wet substrates (SB-5) using Eq. (5.13).

The evolution of the contact angle of the "partially" water-wet surface can be explained in the same way. Eq. (5.4) was used with a pair of experimental $\theta - \gamma_{lv}$ data for the partially water-wet substrate SB-1 at low (2.0 MPa) and high (12.0 MPa) pressures to calculate γ_{sl} and the constant β_2. The γ_{sl} and constant β_2 for the substrate SB-1/CO_2 system were determined to be 2.88 (mN/m) and 2.371×10^{-5} $(m/mN)^2$, respectively. The average deviation (error) and the standard deviation are 4.04% and 5.89%, respectively. For the SB-1/Flue gas system, γ_{sl} and β_2 are 2.45 mN/m and 4.730×10^{-5} $(m/mN)^2$, respectively. The small variation between γ_{sl} values in CO_2 and flue gas systems can be attributed to the difference in composition of the CO_2-saturated aqueous phase in the corresponding experiments.

For a strongly water-wet surface γ_{sl} is considered to be zero. The low value of γ_{sl} reveals that the surface is partially water-wet. Thereafter, γ_{sv} for SB-1/CO_2 system was calculated using Eq. (5.14) and is shown in Fig. 5.10 as triangles. It can be seen that γ_{sv} for the partially water-wet substrate SB-1/CO_2 decreases from 22.05 to 14.03 (mN/m) as the pressure increases from 1.0 to 15.0 MPa. The data for γ_{sl} and γ_{sv} reveal that γ_{sl} is negligible when compared to γ_{sv}. Consequently, the main controlling interfacial tensions in Young's equation for the partially water-wet system (SB-1) are γ_{sv} and γ_{lv}.

The ratio between γ_{sv} and γ_{lv}, i.e., γ_{sv}/γ_{lv}, is also shown in Fig. 5.10 as squares (2nd y-axis). It is obvious that in the pressure range studied, γ_{sv}/γ_{lv} slowly increases from 0.0 to 10.0 MPa. Consequently, the contact angle remains almost constant (Young's equation). The experimental results of CO_2 reported in this study are in agreement with the experimental and theoretical data from Dickson et al. [13] for a hydrophilic surface/CO_2/water system. The authors showed that even if both γ_{sv} and γ_{lv} decrease with pressure the ratio between γ_{sv} and γ_{lv} remains approximately constant in the pressure range between 0.1 MPa to 14.0 MPa and hence the contact angle remains nearly constant with pressure.

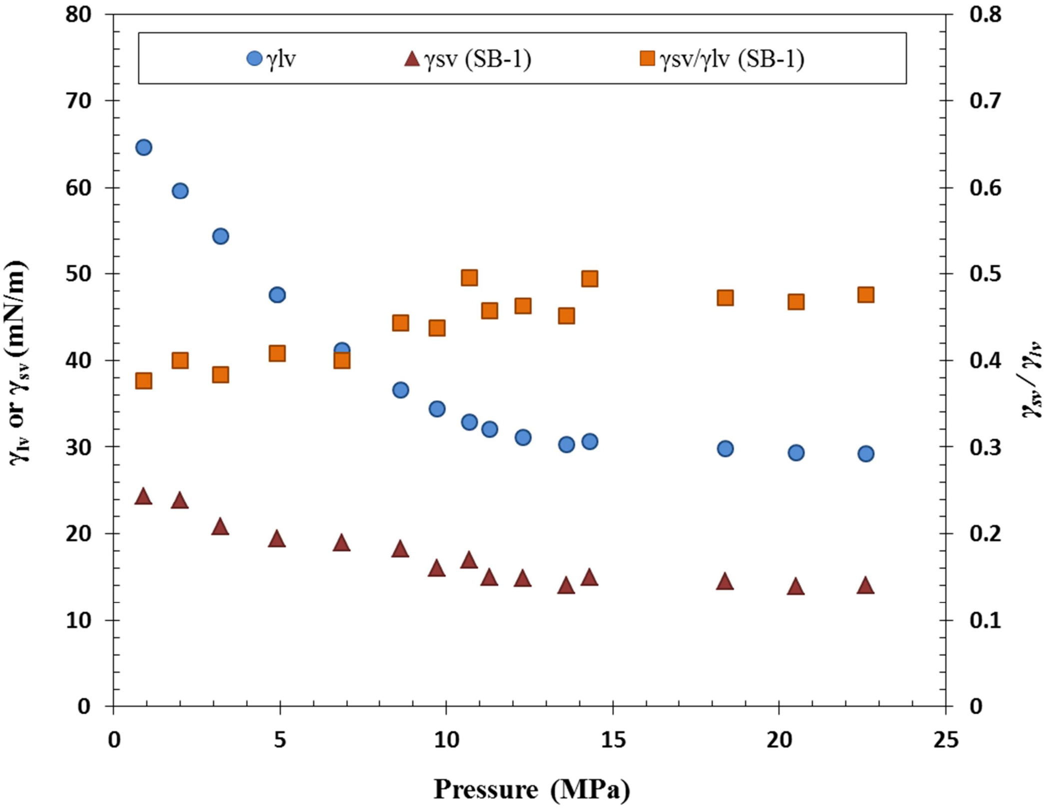

Figure 5.10. Calculated IFT-values vs. pressure for CO_2/water/SB-1 system. γ_{lv} data are from Chapter 4 and γ_{sv} was calculated for the partially water-wet substrate (SB-1)/CO_2/water using Eq. (5.13).

The wettability behavior of the oil-wet substrate, water, and CO_2 might be correlated to CO_2 solubility in water, the CO_2 density, and the interfacial tension between the CO_2-rich gas phase and the aqueous phase. Fig. 5.11 shows the dimensionless solubility, density, interfacial tension, and contact angle of the oil-wet sample/water/CO_2 system vs. pressure. These dimensionless parameters are obtained by dividing each value by its respective maximum value within the given pressure range. This maximum occurs at the highest pressure for all of the quantities, except for the IFT for which the maximum occurs at the lowest pressure. According to Fig. 5.11, the contact angle becomes constant in the same pressure range in which the interfacial tension, the density, and the CO_2 solubility become nearly constant. Present data do not allow determining the degree of importance of each of these parameters separately.

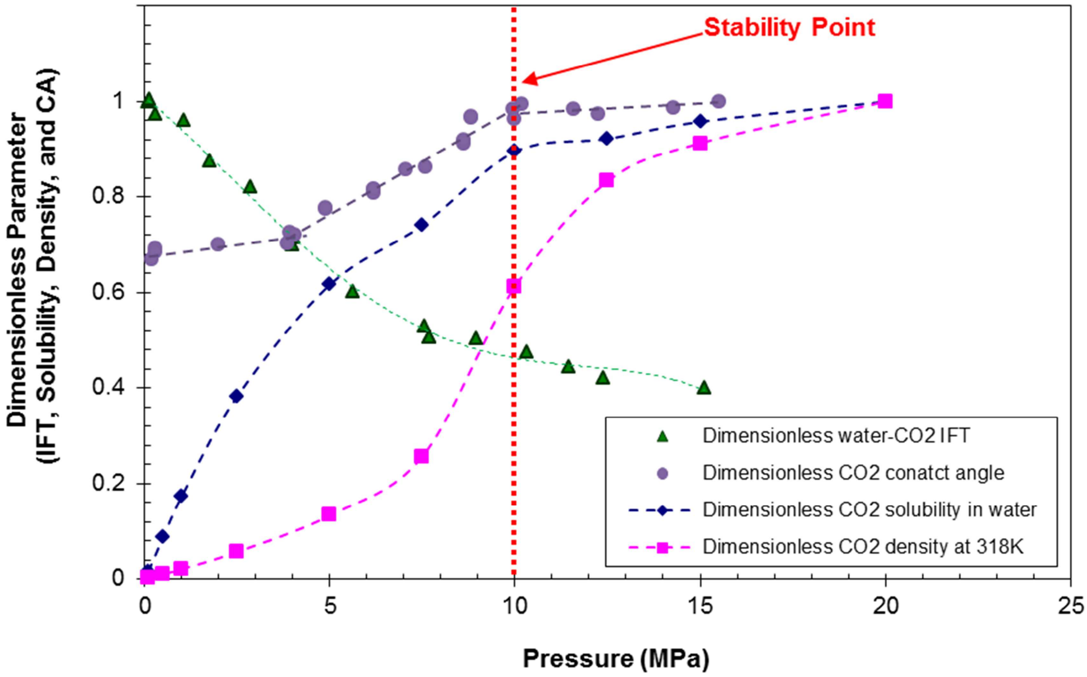

Figure 5.11. Dimensionless density [28], CO_2 solubility in water [39], IFT between CO_2 and water and the stable contact angle on oil-wet Bentheimer sandstone at a constant temperature of 318 K as function of pressure. The stability point is the point above which the contact angle remains constant.

Table 5.5 summarizes the fitting parameters of Eq. (5.14), i.e. γ_{sl} and β_2, calculated for the effectively oil-wet (SB-5) and partially water-wet (SB1) substrates with the average error and standard deviation between the experimental and predicted contact angles (see Appendix 5.1 and Tables 5.3, 5.4).

Table 5.5. The calculated γ_{sl} *and* β_2 *parameters with error analysis for oil-wet and water-wet systems*

Case	γ_{sl} (mN/m)	β_2 (m/mN)^2	Average Error* (%)	Std. Dev. * (%)
CO_2/ SB-1 (water-wet)	2.88	2.371×10^{-5}	4.04	5.89
Flue gas / SB-1 (water-wet)	2.45	4.730×10^{-5}	5.25	6.81
CO_2/ SB-5 (oil-wet)	25.48	1.057×10^{-4}	3.41	4.61
Flue gas/ SB-5 (oil-wet)	25.12	1.114×10^{-4}	3.92	4.69

* Appendix 5.1

5.3.4. EFFECT OF BUBBLE SIZE

The effect of bubble size on the contact-angle determinations has been addressed by different studies [40, 41]. However, the conclusions are not generally in agreement (Chapter 4, section 4.2.1). Drelich et al. [40] derived advancing and receding contact angles by analyzing the shapes of sessile drops and captive bubbles. The authors showed that for a smooth and homogeneous solid surface the contact angle does not change with respect to the bubble size. Analysis of the experimental data in Chapter 4 shows that this dependency can be explained by the effect of gravity (buoyancy) on bubble shape. However, the surface non-ideality and roughness have significant influence on the reliability of the contact-angle determination. In this chapter, the effect of bubble size on the contact-angle determination is examined for three different substrates with different degrees of roughness. Fig. 5.12 shows the contact angle vs. bubble radius for different sandstone systems. The contact-angle determinations were all performed at a temperature of 318 K. The contact-angle data for the water-wet substrate with zero-oil saturation was already obtained in Chapter 4. It can be seen from Fig. 5.12 that the contact angle is more dependent on the bubble size for the surface with a higher P_a (roughness) factor (section 5.2.2 and Chapter 2). This relation is highly pronounced for the water-wet substrate with zero-oil saturation with roughness factor of 0.32 mm. However, for partially water-wet and intermediate-wet substrates with P_a values of 0.16 mm and 0.21 mm, the contact angle does not change much with the bubble radius. Therefore, it can be concluded that the effect of bubble radius on contact-angle determination becomes more important as the surface becomes rougher. These considerations confirm the observations by Drelich et al. [40] for a smooth and homogeneous solid surface and also are in agreement with the results of Sakai and Fujii [32], which shows that the apparent contact angle on rough surfaces can be changed by gravity (more details are in Chapter 4).

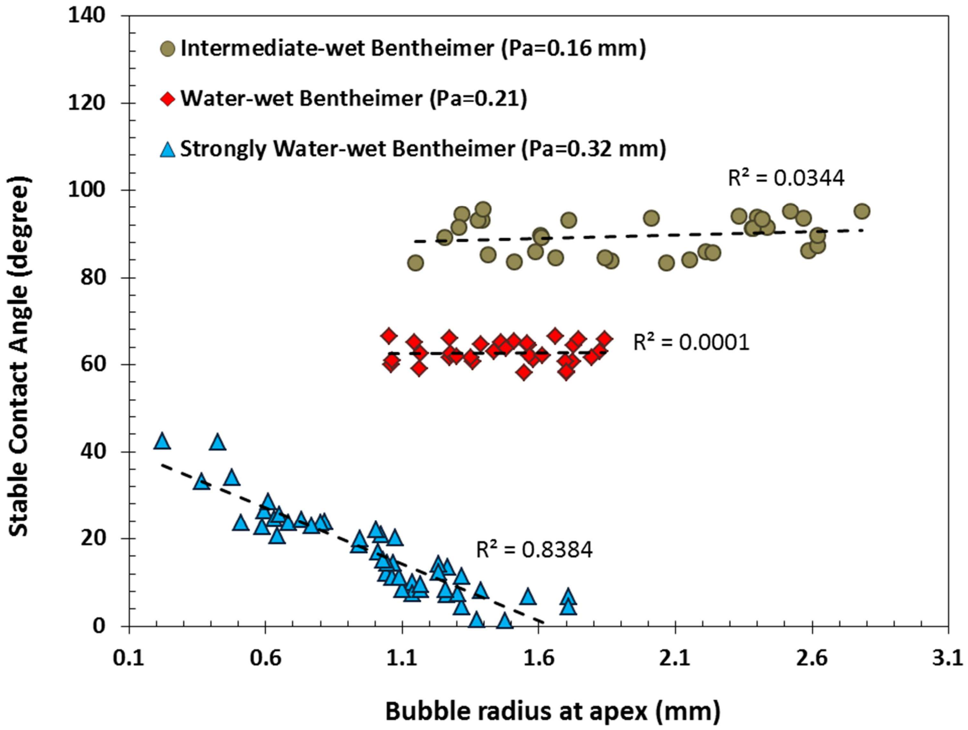

Figure 5.12. Dependence of the stable contact angle as a function of bubble radius for pure (Chapter 4) and oil-wet sandstone systems at a temperature of 318 K.

5.4. CONCLUSIONS

From this study it was found that:

- It is possible to prepare both water-wet and oil-wet substrates by ageing Bentheimer sandstone with appropriately chosen crude oils. The water-wet sample, which was obtained after short exposure to the oil, is called rock system I and the oil-wet sample obtained after long exposure is called rock-system II. Rock system I is partially water-wet, whereas rock system II is effectively oil-wet.
- For rock system I, i.e., a partially water-wet surface, the dependence of the contact angle with pressure is very small for either CO_2 or synthetic flue gas. Both carbon dioxide and synthetic flue gas are the non-wetting phase. This behavior can be quantitatively understood in terms of the expected dependencies of the interfacial tension on the pressure (Fig. 5.9).
- For rock system II, i.e. an effectively oil-wet surface, the dependence on pressure is more considerable with CO_2. The CO_2 becomes the wetting phase at high pressures. The contact angle is initially 95^o and increases only slightly in the range 0-4.0 MPa. Between 4.0 MPa and 10.0 MPa the contact angle increases more or less linearly until it reaches a value of 150^o (Fig. 5.2). Beyond 10 MPa, i.e. in the supercritical region, the contact angle remains constant. The behavior can again be quantitatively understood based on expected trends of the three interfacial tensions that determine the contact angle.

- For the hydrophobic sample, the oil/rock/water/synthetic flue gas system is intermediate-wet at low pressures. In this system, the contact angle increases slightly with increasing the pressure and the substrate turns from intermediate-wet to flue gas-wet at pressures above 14.0 MPa.

- The wettability behavior of both hydrophilic and hydrophobic systems with synthetic flue gas can be explained by considering the wetting properties of these samples with CO_2 and the ratio of 20 mol% CO_2 to 80 mol% N_2 in the flue gas bubble. In addition, the interfacial tension between water and synthetic flue gas changes slightly with increasing pressure. Accordingly, less impact of pressure on the wettability of the flue gas system can be expected. This is also observed experimentally (Fig. 5.3).

- To describe the wetting properties of the surface as a function of pressure, a surface-free-energy analysis can be implemented. Use of the equation-of-state method makes it possible to approach the experimental data quantitatively. However, the improved EOS model used in this thesis has to be validated for different brine salinities. Using a reliable relevant IFT and contact-angle data is essential.

Appendix 5.1: Error analysis

Average deviation and standard deviation in percentages are calculated using Eqs. (A1.1) and (A1.2), respectively.

$$\text{Average Deviation (\%)} = \frac{1}{n}\sum_{i=1}^{n}\left[\frac{\text{ABS}(\text{CA}^{i}_{\text{exp.}} - \text{CA}^{i}_{cal.})}{\text{CA}^{i}_{\text{exp.}}}\right]\times 100 \qquad \text{(A1.1)}$$

$$\text{Standard Deviation (\%)} = \pm\sqrt{\frac{\frac{1}{n}\sum_{i=1}^{n}\left[\frac{\text{ABS}(\text{CA}^{i}_{\text{exp.}} - \text{CA}^{i}_{\text{cal.}})}{\text{CA}^{i}_{\text{exp.}}}\right]^{2}\times 100}{n-1}} \qquad \text{(A1.2)}$$

REFERENCES

[1] P. Bedrikovetsky, A. Evtjukhin, Mathematical Model and Laboratory Study of the Miscible Gas Injection in Fractured-Porous Reservoirs, in: SPE Latin America/Caribbean Petroleum Engineering Conference, Port-of-Spain, Trinidad, 1996.

[2] A. Ameri, R. Farajzadeh, V.S. Suicmez, J. Bruining, Experimental and Numerical Investigation on the Performance of Gas Oil Gravity Drainage at Different Miscibility Conditions, SPE 154170, in: SPE Improved Oil Recovery Symposium, Society of Petroleum Engineers, Tulsa, Oklahoma, USA, 2012.

[3] S.N. Ashrafizadeh, A. Ameri Ghasrodashti, An investigation on the applicability of Parachor model for the prediction of MMP using five equations of state, Chem. Eng. Res. Des., 89 (2011) 690–696.

[4] A.A. Eftekhari, H. Van Der Kooi, H. Bruining, Exergy analysis of underground coal gasification with simultaneous storage of carbon dioxide, Energy, 45 (2012) 729-745.

[5] S. Chen, H. Li, D. Yang, P. Tontiwachwuthikul, Optimal Parametric Design for Water-Alternating-Gas (WAG) Process in a CO_2-Miscible Flooding Reservoir, J. Can. Pet. Technol., 49 (2010) pp. 75-82.

[6] T.C. LaForce, Insight from analytical solutions for improved simulation of miscible WAG flooding in one dimension, Computational Geosciences, (2012) 1-14.

[7] A.A. Aleidan, D.D. Mamora, $SWACO_2$ and $WACO_2$ Efficiency Improvement in Carbonate Cores by Lowering Water Salinity, in: Canadian Unconventional Resources and International Petroleum Conference, Society of Petroleum Engineers, Calgary, Alberta, Canada, 2010.

[8] H. Jiang, L. Nuryaningsih, H. Adidharma, The Effect of Salinity of Injection Brine on Water Alternating Gas Performance in Tertiary Miscible Carbon Dioxide Flooding: Experimental Study, in: SPE Western Regional Meeting, Society of Petroleum Engineers, Anaheim, California, USA, 2010.

[9] R. Farajzadeh, R.M. Muruganathan, W.R. Rossen, R. Krastev, Effect of gas type on foam film permeability and its implications for foam flow in porous media, Adv. Colloid Interface Sci., 168 (2011) 71-78.

[10] B. Bijeljic, A. H. Muggeridge, M. J. Blunt, Multicomponent mass transfer across water films during hydrocarbon gas injection, Chemical Engineering Science, 58 (2003) 2377-2388.

[11] G.J. Hirasaki, Wettability: Fundamentals and Surface Forces, SPE Formation Evaluation, 6 (1991) 217-226.

[12] N. Siemons, H. Bruining, H. Castelijns, K.-H. Wolf, Pressure dependence of the contact angle in a CO_2–H_2O–coal system, Journal of Colloid and Interface Science, 297 (2006) 755-761.

[13] J.L. Dickson, G. Gupta, T.S. Horozov, B.P. Binks, K.P. Johnston, Wetting Phenomena at the CO_2/Water/Glass Interface, Langmuir, 22 (2006) 2161-2170.

[14] D.N. Espinoza, J.C. Santamarina, Water-CO_2-mineral systems: Interfacial tension, contact angle, and diffusion-Implications to CO2 geological storage, Water Resour. Res., 46 (2010) W07537.

[15] D. Yang, P. Tontiwachwuthikul, Y. Gu, Interfacial Tensions of the Crude Oil + Reservoir Brine + CO_2 Systems at Pressures up to 31 MPa and Temperatures of 27 °C and 58 °C, Journal of Chemical & Engineering Data, 50 (2005) 1242-1249.

[16] D. Yang, Y. Gu, P. Tontiwachwuthikul, Wettability Determination of the Reservoir Brine-Reservoir Rock System with Dissolution of CO_2 at High Pressures and Elevated Temperatures, Energy & Fuels, 22 (2008) 504-509.

[17] D. Yang, Y. Gu, P. Tontiwachwuthikul, Wettability Determination of the Crude Oil-Reservoir Brine-Reservoir Rock System with Dissolution of CO_2 at High Pressures and Elevated Temperatures, Energy & Fuels, 22 (2008) 2362–2371.

[18] C. Chalbaud, M. Robin, J.M. Lombard, F. Martin, P. Egermann, H. Bertin, Interfacial tension measurements and wettability evaluation for geological CO_2 storage, Advances in Water Resources, 32 (2009) 98-109.

[19] C. Chalbaud, M. Robin, J.-M. Lombard, H. Bertin, P. Egermann, Brine/CO_2 Interfacial Properties and Effects on CO_2 Storage in Deep Saline Aquifers, Oil Gas Sci. Technol. – Rev. IFP, 65 (2010) 541-555.

[20] P. Chiquet, D. Broseta, S. Thibeau, Wettability alteration of caprock minerals by carbon dioxide, Geofluids, 7 (2007) 112-122.

[21] N. Shojai Kaveh, E.S.J. Rudolph, K.-H.A.A. Wolf, S.N. Ashrafizadeh, Wettability determination by contact angle measurements: hvbB coal–water system with injection of synthetic flue gas and CO_2, Journal of Colloid and Interface Science, 364 (2011) 237-247.

[22] N. Shojai Kaveh, K.H. Wolf, S.N. Ashrafizadeh, E.S.J. Rudolph, Effect of coal petrology and pressure on wetting properties of wet coal for CO_2 and flue gas storage, International Journal of Greenhouse Gas Control, 11 (2012) S91-S101.

[23] M. Dong, S. Huang, Flue Gas Injection for Heavy Oil Recovery, Journal of Canadian Petroleum Technology, 41 (2002).

[24] O.S. Shokoya, S.A. Mehta, R.G. Moore, B.B. Maini, M. Pooladi-Darvish, A. Chakma, The Mechanism of Flue Gas Injection for Enhanced Light Oil Recovery, Journal of Energy Resources Technology, 126 (2004) 119-124.

[25] D.Y. Kwok, A.W. Neumann, Contact angle interpretation in terms of solid surface tension, Colloids and Surfaces A: Physicochemical and Engineering Aspects, 161 (2000) 31-48.

[26] D.Y. Kwok, A.W. Neumann, Contact angle measurement and contact angle interpretation, Advances in Colloid and Interface Science, 81 (1999) 167-249.

[27] D. Li, A.W. Neumann, Equation of state for interfacial tensions of solid-liquid systems, Adv. Colloid Interface Sci., 39 (1992) 299-345.

[28] R. Span, W. Wagner, A New Equation of State for Carbon Dioxide Covering the Fluid Region from Triple-Point Temperature to 1100 K at Pressures up to 800 MPa, J. Phys. Chem. Ref. Data, 25 (1996) 1509-1597.

[29] Y. Sutjiadi-Sia, P. Jaeger, R. Eggers, Interfacial tension of solid materials against dense carbon dioxide, Journal of Colloid and Interface Science, 320 (2008) 268-274.

[30] V. Suicmez, M. Piri, M. Blunt, Pore-scale Simulation of Water Alternate Gas Injection, Transport in Porous Media, 66 (2007) 259-286.

[31] V.S. Suicmez, M. Piri, M.J. Blunt, Effects of wettability and pore-level displacement on hydrocarbon trapping, Advances in Water Resources, 31 (2008) 503-512.

[32] L.W. Lake, Enhanced Oil Recovery, Prentice Hall Incorporated, 1989.

[33] J.N. Israelachvili, Intermolecular and Surface Forces with Applications to Colloid and Biological Systems, Academic Press, Orlando, 1985.

[34] M.E. Schrader, Young-Dupre Revisited, Langmuir, 11 (1995) 3585-3589.

[35] G. Antonow, Surface tension at the limit of two layers, Journal of Chemical Physics, 5 (1907) 372-385.

[36] D. Berthelot, Sur le mélange des gaz, Compt. Rend., 126 (1989) 1857-1858.

[37] L.A. Girifalco, R.J. Good, A Theory for the Estimation of Surface and Interfacial Energies. I. Derivation and Application to Interfacial Tension, The Journal of Physical Chemistry, 61 (1957) 904-909.

[38] R.J. Good, E. Elbing, Generalization of Theory for Estimation of Interfacial Energies, Industrial & Engineering Chemistry, 62 (1970) 54-78.

[39] V.I. Baranenko, L.N. Fal'kovskii, V.S. Kirov, L.N. Kurnyk, A.N. Musienko, A.I. Piontkovskii, Solubility of oxygen and carbon dioxide in water, Atomic Energy, 68 (1990) 342-346.

[40] J. Drelich, J.D. Miller, R.J. Good, The Effect of Drop (Bubble) Size on Advancing and Receding Contact Angles for Heterogeneous and Rough Solid Surfaces as Observed with Sessile-Drop and Captive-Bubble Techniques, Journal of Colloid and Interface Science, 179 (1996) 37-50.

[41] J. Drelich, J.D. Miller, The Effect of Solid Surface Heterogeneity and Roughness on the Contact Angle/Drop (Bubble) Size Relationship, J. Colloid Interface Sci., 164 (1994) 252-259.

CHAPTER 6

Conclusion

The results of this thesis give insight into the interfacial interactions and wettability of different rocks in the presence of water and CO_2 and/or synthetic flue gas. Experiments were performed at reservoir conditions: high pressures and elevated temperature. To describe the wetting properties of the surface as a function of pressure, a surface-free-energy analysis has been used based on an equation of state (EOS). Moreover, the dissolution and mass transfer behavior of a CO_2 bubble in a water/Bentheimer sandstone system have been obtained at various pressures. The observed behaviors have been incorporated into mass transfer models to indicate the dominant mass transfer mechanism. This thesis consists of three main chapters. The conclusions of each chapter are summarized here.

6.1. PART I: CO_2 ENHANCED COAL BED METHANE

Two coal types, i.e. hvBb and semi-anthracite, were studied with respect to their wetting properties when injecting CO_2 or flue gas at various pressures, ranging from 0.1 to 16 MPa, at a constant temperature of 318 K. The results show that at a given temperature and pressure the non-stable contact angle increases with time up to a constant value; the latter is the stable contact angle. The aging time (time to reach stability) was much shorter for the synthetic flue gas bubbles than for CO_2 bubbles.

- In general, the stable contact angles of CO_2 as well as the synthetic flue gas increase with pressure. The rate of increase is influenced by the coal rank and the gas bubble composition.
- When injecting CO_2, the wettability of the semi-anthracite coal surface changed from intermediate-wet to CO_2-wet at a pressure around 5.7 MPa. The implication on field scale could be that, for CO_2 storage in semi-anthracite coal, the reservoir pressure has to overcome a pressure threshold of 5.7 MPa to wet the surface and thereby to enhance the storage capacity.
- Results with injection of synthetic flue gas revealed that Selar Cornish coal is intermediate-wet at the investigated pressures and that the contact angle only slightly increases with pressure. For field-scale applications this implies that there is no pressure threshold to wet the surface with the flue gas.
- For both coal samples the contact angles of the flue gas bubbles are smaller than those of the CO_2 bubbles. Based on this wetting behavior, injection of pure CO_2 into SC and WL coal could be more efficient than injection of flue gas.
- For the synthetic flue gas, the contact angle trend is dominated by the CO_2 behavior. Nitrogen does not dissolve in water and sorbs into the coal to a lesser degree than CO_2.

The behavior of the synthetic flue gas system at a certain CO_2 partial pressure is comparable to the behavior of the CO_2 system at the same (total) pressure.

- The pressure has less effect on the contact angles on the semi-anthracite sample than on those on the Warndt Luisenthal sample regardless of whether CO_2 or flue gas has been injected.
- In general, the hydrophobicity of the coal samples increases with coal rank and pressure. This behavior can be related to the different surface chemistry and electrochemical properties of the two coal samples used.
- The fact that the wettability of different coal ranks changes differently reveals that on the field scale coal wettability is definitely important for the evaluation of the efficiency of CO_2 storage process.

It is thus expected that the behavior found in this study is generally applicable to coals with the same rank and with similar compositions and maceral content. However, other coal types and/or coal ranks may show a different behaviour due to different mineral, aliphatic and/or aromatic surface compositions.

6.2. PART II: AQUIFERS AND DEPLETED GAS RESERVOIRS

Wettability and interfacial interactions of the system Bentheimer sandstone/water/CO_2 and/or flue gas has been experimentally evaluated using different water-CO_2 mixtures, i.e. unsaturated and fully saturated, in order to evaluate the dissolution effects and wetting properties for short and long periods.

- The CO_2/water interfacial tension decreases with increasing pressure. The largest change occurs in the lower pressure range up to 10 MPa. At higher pressures, the interfacial tension decreases at a very slow rate. The flue gas/water IFT decreases slightly with pressure for all pressure ranges. The IFT trend for this system is similar to that of the nitrogen/water system and is attributed to the density variation with pressure.
- For experiments with an unsaturated aqueous phase, two dissolution regimes were observed: (1) the first regime where CO_2 dissolves quickly into the almost pure aqueous phase and (2) the second regime where CO_2 gradually diffuses into the aqueous phase. In the first regime, the contact angle increases continuously until it reaches the transition point. After this transition point, the contact angle changes slightly with time but is almost constant. Analysis of the data showed that this behavior cannot be caused by wettability alterations of the surface from strongly to less water-wet, but by bubble volume reduction due to CO_2 dissolution in the aqueous phase. Because of the dependency of the contact angle on the bubble size, the bubble shrinkage results in alterations of the contact angle over time.
- Results obtained from experiments with an unsaturated aqueous phase provide important information on the interfacial interactions and mass transfer between the aqueous and CO_2 phases. In the unsaturated system, the change in contact angle is influenced by a number of mechanisms such as dissolution and bubble size variation, rather than by the wetting properties of the surface alone.
- A reliable contact-angle determination should be conducted using a pre-equilibrated (fully or quasi-saturated) aqueous phase to eliminate dissolution effects. Due to dissolution, the bubble size continuously changes, so that a reliable and reproducible contact-angle determination is not guaranteed.

- Experiments in the fully-saturated system show that Bentheimer sandstone is (and remains) water-wet against either CO_2 or flue gas, even at supercritical pressures. However, all contact angles of the flue gas bubbles are smaller than those of CO_2. The data for the apparent contact angle of these systems show a strong dependence on the bubble size.
- Analysis of the experimental data shows that this dependency can be explained by the effect of gravity (buoyancy) on bubble shape. However, the surface non-ideality and roughness have significant influence on the reliability of the contact-angle determination. The influence of the bubble radius on the contact angle of the CO_2 system becomes insignificant for bubble diameters smaller than 2.3 mm (Bond numbers less than 0.9).
- The results of this study confirm that axisymmetric droplets are size-dependent and cannot satisfy the original Young equation. In addition, they are in a good agreement with the current literature that the apparent contact angle on rough surfaces can be changed by gravity.
- To identify the effect of pressure, only results with Bond numbers smaller than 0.9 (negligible dependency to the bubble size) were considered. From this, it could be deduced that there is no significant effect of pressure on the contact angle of the Bentheimer/CO_2/water system. Based on the literature data we concluded that this can be explained by the change in the charge of the rock due to interactions between components of the rock surface and the acidic aqueous phase containing CO_2.

In the CCS field application, the amount of capillary-trapped CO_2 depends on the wettability of reservoir rocks. Results of this study show that there is no significant effect of pressure on the wettability of the Bentheimer/water/CO_2 or flue gas system. Even at high pressure, the Bentheimer sandstone remains water-wet to either CO_2 or flue gas.

6.3. PART III: OIL RESERVOIR

In Chapter 5, both water-wet and oil-wet substrates were prepared by ageing Bentheimer sandstone with appropriately chosen crude oils. The water-wet sample, which was obtained after short exposure to the oil, is called rock-system I and the oil-wet sample, obtained after long exposure, is called rock-system II. Rock-system I is partially water-wet, whereas rock-system II is effectively oil-wet.

- For rock system I, i.e., a partially water-wet surface, the dependence of the contact angle with pressure is very small for either CO_2 or synthetic flue gas. Both carbon dioxide and synthetic flue gas are the non-wetting phase. This behavior can be quantitatively understood in terms of the expected dependencies of the interfacial tension on the pressure.
- For rock system II, i.e. an effectively oil-wet surface, the dependence on pressure is more considerable with CO_2. The CO_2 becomes the wetting phase at high pressures. The contact angle is initially 95^o and increases only slightly in the range 0-4.0 MPa. Between 4.0 MPa and 10.0 MPa the contact angle increases more or less linearly until it reaches a value of 150^o. Beyond 10 MPa, i.e. in the supercritical region, the contact angle remains constant. The behavior can again be quantitatively understood based on expected trends of the three interfacial tensions that determine the contact angle.
- For the hydrophobic sample, the oil/rock/ water/synthetic flue gas system is intermediate-wet at low pressures. In this system, the contact angle increases slightly with increasing

pressure and the substrate turns from intermediate-wet to flue gas-wet at pressures above 14 MPa.

- The wettability behavior of both hydrophilic and hydrophobic systems with synthetic flue gas can be explained by considering the wetting properties of these samples with CO_2 and the ratio of 20 mol% CO_2 to 80 mol% N_2 in the flue gas bubble. In addition, the interfacial tension between water and synthetic flue gas changes slightly with increasing pressure. Accordingly, less impact of pressure on the wettability of the flue gas system can be expected which also observed experimentally.
- To describe the wetting properties of the surface as a function of pressure, a surface-free-energy analysis can be implemented. Use of an equation-of-state method makes it possible to approach the experimental data quantitatively, if a number of reliable contact-angle and interfacial-tension data are available for a system of interest.

The results of this study prove that CO_2 can wet an oil-wet substrate in the presence of water. CO_2 is and remains the non-wetting phase in the case of a water-wet substrate and in the presence of water.

6.4. RECOMMENDATIONS

In this study, contact-angle determinations were performed using natural rock surfaces, which were not treated chemically. The output of this study is a step forward in understanding the displacement behavior of multiple phases in reservoirs. The results presented in this thesis can be used as input parameters in reservoir simulations dealing with CO_2 or flue gas storage. Additional research can be built on the results of this thesis. Relevant issues are:

- The presence of impurities in flue gas, like NO_x and SO_x, and their effects on the wettability. These have to be determined and compared with the existing data on pure CO_2 and synthetic flue gas.
- The wettability of different gases that are involved in CCS, like CH_4 and N_2, has to be determined through a similar procedure presented in this thesis.
- The improved EOS model used in this thesis has to be validated for different brine salinities. Using reliable relevant IFT and contact-angle data is essential.
- The rock surface roughness as used in this thesis can be changed. Its influence can be investigated by using surfaces polished to different degrees.
- More investigations on the zeta potential and surface charge determination of these samples versus pH are needed.
- This thesis discussed the wettability of rock surface, fluid and gas. However, these experiments need to be combined with additional data such as zeta potential and core flooding measurements to provide information regarding the displacement behavior of fluids in porous media.

NOMENCLATURE

CCS	Carbon dioxide Capture and Storage
CA	Contact Angle
DSA	Drop Shape Analysis
ECBM	Enhance Coal-Bed Methane
EGR	Enhance Gas Recovery
EOR	Enhance Oil Recovery
EOS	Equation of State
hvBb	High Volatile Bituminous (hvBb)
IFT	Interfacial tension
PDC	Pendant Drop Cell
SC	Selar Cornish
SFEA	Surface Free Energy Analysis
S.E.	Standard error
STDEV	Standard deviation
WL	Warndt Luisenthal

A_b	Gas-liquid (bubble) interfacial area
Bo	Bond number
C_{co_2}	CO_2 concentration
$C_{co_2}^{s}$	CO_2 concentration at the bubble interface
$C_{co_2}^{b}$	CO_2 concentration in the aqueous phase (bulk)
$C_{co_2}^{b_1}$	CO_2 concentration in the bulk phase in regime I
$C_{co_2}^{b_2}$	CO_2 concentration in the bulk phase in regime II
D	CO_2 molecular diffusion coefficient into water
D_1	Effective diffusion coefficient in regime I
D_2	Effective diffusion coefficient in regime II
F_b	Buoyancy force
F_g	Gravity force
F_p	Pressure force

F_σ	Surface tension force
g	Local gravitational acceleration
H	Contact angle hysteresis
k	Permeability of the porous medium
k_L	Mass-transfer coefficient in the aqueous phase
k_{L1}	Mass-transfer coefficient in regime I
k_{L2}	Mass-transfer coefficient in regime II
L	Characteristic length-scale of convection
n	Number of data points
N_{ca}	Capillary number
N_{CO_2}	Molar flux of CO_2
r	*in Chapter 3*: Dimensionless bubble radius at apex
l_p	Sampling length
m_b	Bubble mass
MD	Bubble maximum diameter
$p(z)$	Vertical pressure distribution
P_a	Characterization factor of the surface roughness
P_b	Total pressure in the bubble
P_c	Capillary pressure
P_L	Pressure of the aqueous phase
P_{nw}	Pressure of the non-wetting phase
P_w	Pressure of the wetting phase
R	*in Chapter 1*: an effective pore radius corresponding to the narrowest pore throat along the entire CO_2 flow path *in Chapter 4:* contact radius; the radius of the contact circle
r_b	Bubble radius
R_0	Radius of curvature at apex
R_{i0}	Initial radius of bubble at apex
R_{02}	Radius of bubble at apex at transition time
R_{final}	Bubble radius after establishing the equilibrated bubble
Ra	Rayleigh number
t	Time

V	Volume of a droplet
V_b	Volume of a bubble
W	*in Chapter 4:* Constant molar rate of CO_2 *in Chapter 5:* Work of adhesion
W_{sv}	Free energy of adhesion per unit area of a solid-vapor pair; Interfacial adhesion work
W_{ss}	Cohesion work of the solid phase
W_{vv}	Cohesion work of the vapor phase
Z	Absolute ordinate value (height)
α_2	A constant in Eq. 5.11
β_2	A constant in Eq. 5.12
ε	Energy parameter
ε_{ij}	Potential energy parameter of unlike-pair interactions
ε_{ii}	Potential energy parameters of like-pair interactions
κ	Fitting parameter in Eq. 5.10
θ	Apparent contact angle (experimentally determined contact angle)
θ_Y	Young's contact angle
θ_a	Advancing contact angle
θ_r	Receding contact angle
θ_s	Contact angle for a spherical droplet/bubble
θ_∞	Contact angle for the bubble with infinite radius of the solid-liquid contact circle
θ_{min}	Contact angle of the bubble with the initial bubble radius of R_{io}
θ_{max}	Last accurate detectable contact angle
θ_{final}	Contact angle after establishing the equilibrated bubble
ϕ	Porosity of the porous medium
μ	Dynamic viscosity
ρ_{CO_2}	Density of CO_2 in the bubble pressure
ρ_g	Density of the gas phase (bubble)
ρ_l	Density of the liquid phase
$\Delta\rho$	Density difference between the bubble and aqueous phase

γ_{aq,CO_2}	Interfacial tension between the aqueous phase and the CO_2– rich phase
γ_{w,CO_2}	Interfacial tension between water and CO_2
γ_{lv}	Interfacial tensions between the aqueous phase and the gas phase
γ_{wg}	Interfacial tensions between CO_2 and water
γ_{sv}	Surface energy between the solid and the gas phase
γ_{sl}	Surface energy between the solid and the aqueous phase
σ	Line tension
δ	Bubble height; Location of the apex
υ	*in Chapter 3:* Injection velocity of the gas

Acknowledgement

> *"To get the full value of joy you must have someone to divide it with."* ***- Mark Twain***

"*Time is flying…*" this phrase stuck in my mind all the time, from the beginning of my PhD. During these four years, I have experienced different ups and downs, and it is still hard for me to believe that all of them have passed and now I'm writing the last sentences of my dissertation- the part that gives me the full value of this joy! This dissertation for sure is not only the result of my own work, but it mirrors all the support, help and best wishes that I have received during these years. I feel extremely lucky to have had great supervisors and many wonderful friends and colleagues, who made me feel very welcome in Delft. And now is the time to express my deepest gratitude to these people, without whom the successful completion of this work would never have been possible.

I'm undoubtedly indebted to my promoter, **Prof. Bill Rossen**, who was always there for me, to answer my questions and to give me invaluable ideas for my research. I appreciate all his contributions and I am so proud that I have had a chance to work with him. I truly enjoyed our discussions and admire his open views on different things, his critical vision, technical and scientific knowledge, and many other qualities, which have made him an example for me.

My deepest gratitude goes to my advisor, **Dr. Karl-Heinz Wolf**, for his amazing support. Particularly in the last months of my PhD, when I was going through the most difficult moments of my life, he was always there. He supported me and taught me how I should cope with it. His kind attention, encouragement, support and guidance during that period helped me a lot to find myself again and to finalize my thesis. Dear Karl-Heinz, I learned a lot from you, not only for my work but also for my personal life. I have been very fortunate to have your supervision during my PhD. The freedom that I had during these years of research, the trust that you had in my work and your persuasiveness were important in making me an independent researcher. Karl-Heinz, *bedankt voor alles!*

I would like to express my warmest thanks to **Dr. Susanne Rudolph**, who was not only my supervisor but also a fabulous friend. Without her help in starting this PhD project, it would have been impossible. Her endless energy and enthusiasm were always encouraging, and her valuable and precise comments as well as the extensive and useful discussions we had were always lighting my way during these years. Despite geographical distance, she was always available for me, patiently spending time discussing work as well as non-work matters. She taught me to be persevering and patient, not only in doing research but also in all aspects of life. Susanne: I deeply thank you for believing me and my competence and for supporting me in the hard moments. *I miss you very much!*

My wholehearted thanks go to **Prof. Hans Bruining** for providing me an opportunity to work on this interesting topic, funded by the GRASP European Project. I was always welcomed for discussion, even with his busy agenda, and I appreciated all his contributions during my PhD research.

I would like to sincerely thank **Dr. Cas Berentsen**, who was my advisor for a time. Cas: I am extremely happy that I had a chance to work with you, even for such a short period. I appreciate all your efforts and wish you all the best.

I would like to express my appreciation to the rest of the **dissertation committee** including Dr. Christopher Pentland, Prof. Hans Geerlings, Prof. Pacelli Zitha and Prof. Jan Dirk Jansen for taking time and participating in my PhD defence and carefully reviewing my thesis. Their constructive comments and valuable suggestions helped me to improve my dissertation in the final stage.

I acknowledge the sponsors of **CATO2** for their financial support and positive feedback. They provided me a nice opportunity to meet great researchers and find cool colleagues. I would like to particularly thank Jan Brouwer, Jan Hopman, Sander van Egmond, Marlies Verlinde and Marie-Louise De Leijer.

I am grateful to **Dr. Patrick van Hemert** for all the valuable discussions we had and for helping me to improve the image-analysis procedure.

I would like to offer my special thanks to all the **technical staff** of the "Laboratory of Geoscience and Engineering", particularly Jan Etienne, Marc Friebel, Karel Heller and Joost van Meel. Without their kind support and help, I could never have succeeded in collecting my experimental results. **Jan and Marc:** your technical expertise and help were fundamental and so priceless. I really enjoyed working with you and learned a lot from you. *Hartstikke bedankt!*

Without the **supporting staff** of the Geoscience and Engineering Department, life would have been very hard! I thank them all, especially Margot Bosselaar for always being available and for her lovely support, Hannie Zwiers for her kind attention, and Lydia Broekhuijsen and Marlijn Ammerlaan, Ralf Haak, Asha Doergaram, Marijke Schillemans, and Marja Roep, and Maarten Mulder from ICT department.

My warmest thanks go to **Dr. Janice Rossen** who is such a great, energetic and enthusiastic friend. I’m so grateful for all her wholehearted attention, support, care; for so much trust in me and for the inspiring emails that she sent me.

I gratefully thank the marvellous support of my former teacher and supervisor, **Dr Nezamedin Ashrafizadeh**, who also taught me “Engineering Ethics”. Dr Ashrafizadeh: I appreciate all your valuable contributions in my growth. You had your own unique style of coaching. Now, when I look back, I see the effects and benefits. For me, you are not only a remarkable teacher, but also a much-respected “MASTER”.

I am truly grateful to my dearest **friends** and colleagues, Ania, Chris, Saskia and Elisa for all their friendship and lovely support. I especially thank Chris for translating my summary and propositions into Dutch and for proof-reading of part of my thesis, and Ania for her always heart-warming presence. I am thankful to all my friends and colleagues at the Geoscience and Engineering Department and YoungDelft, especially to Andreas, Christian, Araz, Farzad, Amin, Ehsan, Ali, Tianqi, Jiakun, Durgesh, Eduardo, Jakolien, Leon, Rahul, Elham, Hua, Siavash, Farid, Mojtaba, Mohammad, Nikita, Bander, Grigori, Alex, Carlos, Asiya, Rudy, Azadeh, Samira, Chunman, Rohit, Zhe, Eveline, Janneke and Gijs for letting me have unforgettable, great memories during my PhD studies.

I would like to express my appreciation of my **Iranian friends** in the Netherlands, who helped me in settling abroad and offered me their support, especially Hamidreza and Maryam, Hamid and Fatemeh, Mohammad Simjoo, Mohammad Reza Kamali, Ali Vakili, and many others.

When I look back, there was one person who was always standing behind me; who gave me her unconditional love and support; the one inspiring me the most during my education, and watching me grow step-by-step; who taught me how to *love* and how to *live*: My lovely **Mother**. Every moment of my life you offered us your true love and you sacrificed yourself for our happiness. I cannot remember anything from you except love and kindness, truth and trust. There are no words big enough to explain my endless love and gratefulness to you. But only couple of months before finishing my PhD, when I was planning to dedicate my thesis to you, suddenly you left me alone….and I lost my chance to express my gratitude to you, and share my joy and happiness with you. Now, I am dedicating this thesis to your memory, to who are and remain in my heart forever…..Peace upon you, my dear “MADAR”!

And my beloved **Dad**, the legend of my life, who taught me how to *think* and how to *behave*, how to love people unconditionally, how to prefer others than yourself and how to be strong. I’m extremely grateful to you for everything. Without you, I would not have achieved what I have today. Thanks for all your encouragement and interest in my work and progress, for all your support, kindness and lessons…. “سپاسگزارم“.

My heartfelt thanks and love go to my amazing **family**; my sweet sister, Hanieh, my father in-law and mother in-law, my lovely grandmother and grandfather, Aunt Nasrin, Uncle Ardeshir, Aunt Nastaran and Uncle Ardalan, who are inspiring and trusting in me. *Thank you all, I love you!*

The last sentences are for the dearly-loved of my life, my hero, my best friend, colleague and spouse, **Amin**. Thanks for your true love and your true support, for listening to me and for your constantly heart-warming presence, your extreme trust in me and your unconditional help. I also appreciate all your scientific help and all discussions that we had which made our personal life as well as and the career full of joy. *Thanks, sweetheart!*

My final word of thanks is for you, the “Lord”, wherever you are. Thanks for being with me at all times!

Narjes (Maryam) Shojai Kaveh
Delft, February 2014

LIST OF PUBLICATIONS

Journal articles:

1. N. Shojai Kaveh, E. S. J. Rudolph, K-H. A. A. Wolf, S. N. Ashrafizadeh, "Wettability Determination by Contact Angle Measurements: hvbB Coal – Water System with Injection of Synthetic Flue Gas and CO_2", *Journal of Colloid and Interface Science*, Vol. 364, pp. 237-247, 2011.
2. N. Shojai Kaveh, K-H. A. A. Wolf, S. N. Ashrafizadeh, E. S. J. Rudolph, "Effect of Coal Petrology and Pressure on Wetting Properties of Wet Coal for CO_2 and Flue Gas Storage", *International Journal of Greenhouse gas Control*, V. 11S, pp. 91-101, 2012.
3. A. Ameri, N. Shojai Kaveh, E. S. J. Rudolph, K-H. A. A. Wolf, R. Farajzadeh, J. Bruining, "Investigation on Interfacial Interactions among Crude Oil- Brine- Sandstone Rock- CO_2 by Contact Angle Measurements", *Energy Fuels*, Vol. 27, pp. 1015–1025, 2013.
4. N. Shojai Kaveh, E. S. J. Rudolph, P. van Hemert, W. R. Rossen, K-H. A. A. Wolf, “Wettability Evaluation of CO_2-Water-Bentheimer Sandstone System: Dissolution, Contact Angle and Bubble Size”, Just Accepted, *Energy Fuels*, 2014.

Conference articles:

1. N. Shojai Kaveh, E.S.J. Rudolph, W.R. Rossen, K-H. Wolf, “Contact Angle Interpretation of CO_2-Water-Oil-Sandstone System by Surface Free Energy Analysis”, 27th Conference of the European Colloid and Interface Society (ECIS), 1-6 September 2013, Sofia, Bulgaria.
2. N. Shojai Kaveh, E.S.J. Rudolph, W.R. Rossen, P. van Hemert, K-H. Wolf, “Interfacial Tension and Contact-Angle Determination in Water-Sandstone Systems with Injection of Flue Gas and CO_2”, 17th IOR/EOR conference-From Fundamental Science to Deployment, 16-18 April 2013, Saint Petersburg, Russia.
3. N. Shojai Kaveh, C.W.J. Berentsen, E.S.J. Rudolph, K-H. Wolf, W.R. Rossen, “Wettability Determination by Equilibrium Contact Angle Measurements Reservoir Rock–Connate Water System with Injection of CO_2” (SPE 154382), 74th EAGE Conference and Exhibition incorporating SPE EUROPEC 2012, 4-7 June 2012, Copenhagen, Denmark.

4. N. Shojai Kaveh, E.S.J. Rudolph, K-H. Wolf, S.N. Ashrafizadeh, “The Effect of Coal Rank on the Wettability Behavior of Wet Coal System with Injection of Carbon Dioxide and Flue Gas”, 74th EAGE Conference and Exhibition incorporating SPE EUROPEC 2012, 4-7 June 2012, Copenhagen, Denmark.
5. N. Shojaikaveh, E. S. J. Rudolph, J. Bruining, S. N. Ashrafizadeh, "Wettability Determination of HVBB Coal – Water System with Injection of Model Flue Gas and CO_2", 73nd EAGE Conference & Exhibition Incorporating SPE EUROPEC 2011, 23-26 May 2011, Vienna, Austria.
6. N. Shojaikaveh, E. S. J. Rudolph, J. Bruining, S. N. Ashrafizadeh, Karl-Heinz Wolf, "Experimental study of Carbon dioxide/Nitrogen injection to wet coal", 8th EUROPEAN COAL CONFERENCE (Geodarmstadt), 10-13 October 2010, Darmstadt, Germany.
7. N. Shojaikaveh, E. S. J. Rudolph, S. N. Ashrafizadeh, "Influence of N_2/ CO_2 injection to the wettability behavior of the coal-water-gas system", 72nd EAGE Conference & Exhibition Incorporating SPE EUROPEC 2010, 14-17 June 2010, Barcelona, Spain.

ABOUT THE AUTHOR

Narjes (Maryam) Shojai Kaveh was born on August 28, 1983 in Tehran, Iran. In 2001, after having obtained her high school diploma in “Mathematics and Physics” at “Nedaye Azadi High School”, she started studying Process Engineering at Iran University of Science and Technology in Tehran.

In 2005, Narjes obtained her BSc. degree and immediately after continued her MSc. studies in Chemical Engineering at Iran University of Science and Technology in Tehran. Her master thesis was about process parameters of Chlor-Alkali Membrane cells under the supervision of Dr. S.N. Ashrafizadeh and Dr. Fereydoon Mohammadi. In 2007, she graduated with Cum Laude in Chemical Engineering. One month later in 2007, Narjes started her doctoral studies in the field of interfacial phenomena and effects of wettability on capillary pressure and permeability in porous medium and reservoir rock in the Chemical Engineering department of Iran University of Science and Technology. In 2008, Narjes received the scientific award of the Iranian National Elite Foundation. In January of 2010, Narjes was granted a research fellowship of "Marie Curie Actions" through the GRASP program and she left Iran to continue her research in the Department of Geoscience and Engineering at Delft University of Technology. In January of 2011, she officially started her doctoral research there. During this period, she explored the interfacial interactions and wetting properties of the rock surfaces for CO_2 storage under supervision of Prof. Bill Rossen, Dr. Karl-Heinz Wolf and Dr. Susanne Rudolph.